

Ultrafast photoinduced processes in metal - containing molecular complexes and in proteins

THÈSE N° 6739 (2015)

PRÉSENTÉE LE 11 SEPTEMBRE 2015
À LA FACULTÉ DES SCIENCES DE BASE
LABORATOIRE DE SPECTROSCOPIE ULTRARAPIDE
PROGRAMME DOCTORAL EN PHOTONIQUE

ÉCOLE POLYTECHNIQUE FÉDÉRALE DE LAUSANNE

POUR L'OBTENTION DU GRADE DE DOCTEUR ÈS SCIENCES

PAR

Roberto MONNI

acceptée sur proposition du jury:

Prof. J.-E. Moser, président du jury
Prof. M. Chergui, directeur de thèse
Prof. A. Vıcek, rapporteur
Dr J. Helbing, rapporteur
Prof. K. Johnsson, rapporteur



ÉCOLE POLYTECHNIQUE
FÉDÉRALE DE LAUSANNE

Suisse
2015

*“Qualunque vetta tu sia riuscito a scalare
ricorda sempre da dove sei partito
e la strada che hai percorso per arrivare”*

Dedicato ai miei genitori

Abstract

The aim of this thesis is to investigate the ultrafast inter- and intra-molecular processes, occurring in both metal-containing molecular complexes and in proteins, by means of ultrafast Transient Absorption (TA) spectroscopy.

The first part of the thesis focuses on understanding the origin of the solvent dependent Intersystem Crossing (ISC), from the lowest excited singlet state ($^1A_{2u}$) to the lowest excited triplet state ($^3A_{2u}$), in $[Pt_2(P_2O_5H_2)_4]^{4-}$ (**Pt(pop)**) and its perfluoroborated derivative $[Pt_2(P_2O_5(BF_2)_2)_4]^{4-}$ (**Pt(pop)-BF₂**). Our UV pump-Visible probe TA experiments (exciting both in the $^1A_{2u}$ state and in higher-lying states) highlight the presence of an intermediate state, in agreement with the previous hypothesis of Milder and Brunschwig. The energy of the latter state is strongly modulated by both the solvent and the ligands present in the *pop* cage, causing the large difference in ISC timescales (upon excitation in the $^1A_{2u}$ state) between Pt(pop) in acetonitrile (**MeCN**) (< 1 ps), Pt(pop) in water (~13 ps) and Pt(pop)-BF₂ in MeCN (1.6 ns). Excitation at higher-lying excited states populates both the $^1A_{2u}$ and the $^3A_{2u}$ state in different ratios, depending on the investigated system. Finally, we report on the presence of wave-packets in the ground and excited states, as well as the coherence transfer from the initially excited state to the $^3A_{2u}$ state.

The second part focuses on the photo-excited tryptophan (***Trp**) quenching by metal complexes in protein systems, such as ferrous Myoglobins (**Mbs**) and Prion Proteins (**PrPs**). Mb is a small globular protein composed by 153 amino acids and containing two Trp residues (positions 7 and 14). Trp⁷ is ~20 Å far away from the heme and its fluorescence is only quenched via Förster energy transfer (**FRET**), while Trp¹⁴ is closer (~15 Å) and it is quenched via both FRET and electron transfer to the heme. Our results demonstrate that *Trp¹⁴-to-heme electron transfer process occurs, surprisingly, also in ferrous Mbs (e.g. deoxy-Mb and MbCO) and highlight the generation of a long-lived product, namely a Fe^{II}-porphyrin^{•-}. We also report the interesting case of MbNO, in which the *Trp¹⁴ transfers the electron on the NO instead of the heme.

Prion proteins are also globular proteins composed of 209 amino acids (in humans) and involved in metal binding. Even though a large amount of experiments and theoretical work have been performed on these proteins their main physiological role is not completely determined, but it is clear that the formation of a scrapie isoform (**PrP^{Sc}**) of the cellular PrPs (**PrP^C**) is the infectious

agent and functions as a template for the PrP^C → PrP^{SC} conversion. Our UV pump–Visible probe TA experiments aim to unravel the ultrafast processes occurring in the octarepeat region of PrPs and fill the gap between ultrashort and biological timescales. We find that both the minimum Cu binding sequence HGGGW (**OPS**) and the total octarepeat region (PHGGGWGQ)₄ (**OP4**) display a non–exponential quenching of the Trp residues, which was assigned to *Trp–to–nearby amino acids (H, G or Q) in different peptide’s conformations. Upon Cu²⁺ complexation by OPS, a feature related to the formation of a Cu⁺ complex was detected. The same was not detected upon Cu²⁺ complexation by OP4, showing longer quenching timescales than the free peptide. Our results highlight the relationship between structural conformation of the peptide and quenching timescales of the *Trp.

Keywords: *Ultrafast Processes, Wave–packets, Metal Complexes, Myoglobin, Energy Transfer, Electron Transfer, Transient Absorption Spectroscopy, Intersystem Crossing, Prion Proteins.*

Prefazione

Questo lavoro consiste nell'investigare processi inter–ed intra–molecolari, attivi sia in complessi molecolari metallici che in proteine, tramite la spettroscopia ultrarapida d'assorbimento transiente (TA).

Nella prima parte della tesi discuteremo la dipendenza dal solvente dell'Intersystem Crossing (ISC), dal primo stato eccitato di singoletto ($^1A_{2u}$) a quello di tripletto ($^3A_{2u}$), in sistemi quali $[Pt_2(P_2O_5H_2)_4]^{4+}$ (Pt(pop)) ed il suo perfluoroborato derivato $[Pt_2(P_2O_5(BF_2)_2)_4]^{4+}$ (Pt(pop)–BF₂). Dai risultati ottenuti eccitando nell'UV (sia nello stato $^1A_{2u}$ che in stati a più alta energia) e sondando il campione nel visibile, si evince la presenza di uno stato intermedio, come già ipotizzato da Milder e Brunschwig, la cui energia è modulata sia dal solvente che dal ligando *pop*. Di conseguenza, eccitando il sistema (Pt(pop) in acetonitrile (MeCN), in acqua e Pt(pop)–BF₂ in MeCN) in $^1A_{2u}$, si osservano forti variazioni nei tempi di ISC i cui valori sono < 1 ps, ~13 ps e 1.6 ns, rispettivamente. Se si eccita il campione a stati con più alta energia, si ha un rilassamento a stati aventi minore energia ($^1A_{2u}$ ed $^3A_{2u}$) la cui popolazione dipende dal solvente e dal ligando. Infine, in tutte le misure sono stati dettati dei pacchetti d'onda, sia nello stato fondamentale che in $^1,3A_{2u}$, con conseguente trasferimento di coerenza tra lo stato inizialmente eccitato e $^3A_{2u}$.

La seconda parte della tesi tratta l'interazione del triptofano eccitato (*Trp) con complessi metallici presenti in proteine, come la Mioglobina (Mb) ferrosa ed i Prioni (PrPs). La Mb è una piccola proteina globulare costituita da 153 residui e contenente due Trp (posizioni 7 e 14). La fluorescenza del Trp⁷, che dista 20 Å dell'eme, viene smorzata esclusivamente tramite trasferimento d'energia di Förster (FRET), mentre nel caso del Trp¹⁴ (che dista 15 Å) la suddetta fluorescenza viene smorzata da due meccanismi (in Mb ferriche), ossia il FRET ed il trasferimento di carica. I nostri risultati mostrano come il trasferimento di carica sia operativo anche in Mb ferrose, rivelando la formazione di prodotti con tempo di vita particolarmente lungo, quali Fe^{II}–porphyrin^{•-}. Inoltre mostreremo il caso della MbNO, in cui l'elettrone viene trasferito sul ligando e non sull'eme.

Il trasferimento di carica è fondamentale anche nei prioni, proteine globulari costituite da 209 residui (negli umani) e coinvolte nella coordinazione di metalli divalenti. Nonostante la grande quantità di informazioni sui prioni, sia sperimentali che teoriche, vi è ancora insicurezza nel ruolo principale dei prioni, la cui isoforma dei prioni cellulari (PrP^C), cosiddetta “scrapie”

(PrP^{SC}), funge da base per la conversione PrP^C→PrP^{SC}. I nostri esperimenti TA, eccitando nell'UV e sondando il campione nel visibile, mirano a comprendere i processi ultrarapidi nella regione "ottaripetuta". Sia la minima sequenza coordinante il Cu, HGGGW (OPS), che tutta la regione ottaripetuta, (PHGGGWGQ)₄ (OP4), mostrano uno smorzamento della fluorescenza del *Trp rispetto al *Trp in acqua, che è stata assegnata ad un trasferimento di carica dal *Trp a residui vicini. I risultati del complesso OPS–Cu mostrano la formazione di un complesso contenente Cu⁺; effetto non presente nel complesso OP4–Cu, dove la fluorescenza del *Trp viene smorzata in tempi più lunghi del corrispettivo peptide. I nostri risultati mostrano la correlazione tra la struttura del peptide e le scale di tempi dello smorzamento della fluorescenza del *Trp.

Parole chiave: *Processi Ultrarapidi, Pacchetti d'onda, Complessi Metallici, Mioglobina, Trasferimento d'energia, Trasferimento di carica, Spettroscopia d'Assorbimento Transiente, Intersystem Crossing, Prioni.*

Table of Contents

Shining light on metal-complexes	1
1 Spectroscopy and Inter-/Intra-Molecular processes: an introduction	5
1.1 Ultrafast Transient Absorption	5
1.2 Ultrafast phenomena.....	8
1.2.1 Intramolecular processes	8
1.2.2 Intermolecular processes: Energy and electron transfer	12
1.2.3 Wave-packet dynamics.....	18
2 Experimental Set-up and data treatment	21
2.1 Experimental Set-ups	21
2.1.1 Two-Dimensional Transient Absorption.....	21
2.1.2 ULTRA beam-line at Rutherford Appleton Laboratory (RAL)	33
2.2 Data Treatment	34
3 Solvent and ligand effects on Pt(pop) intramolecular relaxation	39
3.1 $d^8 - d^8$ complexes and Pt(pop): an introduction	39
3.2 Steady state spectra.....	44
3.3 Solvent dependence	46
3.3.1 Sample preparation.....	46
3.3.2 Experimental results.....	46
3.4 Ligand dependence	52
3.4.1 Sample preparation.....	52
3.4.2 Experimental results	52
3.5 Summary of the GF results.....	57
3.6 Discussion.....	58
3.7 Conclusions	61

4	Electron and Energy Transfer in Myoglobins	63
4.1	Myoglobin and tryptophan	64
4.2	Deoxy–Myoglobin.....	70
4.2.1	UV pump–visible probe	70
4.2.2	UV pump–IR probe	79
4.2.3	Deoxy–Mb conclusions.....	83
4.3	Carboxy–myoglobin (MbCO)	84
4.3.1	UV pump–IR probe	85
4.3.2	MbCO conclusions	89
4.4	Nitrosyl–myoglobin (MbNO).....	90
4.4.1	UV pump–visible probe	91
4.4.2	UV pump–IR probe	96
4.4.3	MbNO conclusions.....	100
4.5	Cyano–myoglobin (MbCN).....	102
4.5.1	UV pump–IR probe	102
4.5.2	Application of Marcus’ theory of electron transfer on MbCN.....	106
4.5.3	MbCN conclusions	108
4.6	General conclusions.....	108
5	Prion proteins and their biological role	111
5.1	Sample preparation	115
5.2	Static spectra of PrPs	117
5.3	Transient absorption experiments on HGGGW (OPS)	118
5.3.1	Investigation of OPS dynamics	118
5.3.2	Investigation of OPS–Cu dynamics	121
5.4	Transient absorption experiments on (PHGGGWGQ) ₄ (OP4).....	124
5.4.1	Investigation of OP4 dynamics	124
5.4.2	Investigation of OP4–Cu dynamics.....	126
5.5	Discussion.....	128

5.6	Conclusions	131
6	Conclusions and Perspectives	133
	List of abbreviations.....	139
	Acknowledgements.....	143
	Bibliography.....	145
	Appendix A (Pt(pop)).....	161
	Curriculum Vitae.....	165

Introduction

Shining light on metal–complexes

Metals have an extremely important role in nature and applications, being in their metallic form, as metal complexes, or in living organisms either as free cations (e.g. Na^+ or K^+) or incorporated in proteins as cofactors (e.g. Fe^{3+} , Cu^{2+} or Mg^{2+} metal–complexes). The physical and chemical properties of metal complexes can vary strongly depending on the ligands and the metal center used, leading to a wide variety of possible applications.

From the technological application point of view, the catalytic properties of molecular complexes are indeed of interest, as well as the capability to inject electrons on a given substrate upon absorption of light. Some metal complexes show particularly interesting catalytic properties when in their excited state, as in the case of di–metallic Rh^{II} , Pd^{II} and Pt^{II} complexes (e.g. $\text{Rh}^{\text{II}}_2(\text{dppm})_2\text{Cl}_2(\text{CO})_2$, $\text{Pd}^{\text{II}}_2(\text{dppm})_2\text{Cl}_2$ (where $\text{dppm} = 1, 1\text{-bis (diphenylphosphino) methane}$) and Tetrakis (μ –pyrophosphito) diplatinate(II) ($[\text{Pt}^{\text{II}}_2(\text{P}_2\text{O}_5\text{H}_2)_4]^{4-}$, hereafter addressed as $\text{Pt}(\text{pop})$).[1] However, to obtain the maximum performances of a photo–catalyst, as well as to improve its performances, a deep knowledge of the system is required. Primarily, it is important to understand which state has the catalytic activity, to know its lifetime as well as to investigate which ligands could improve the lifetime of that (or another) state. Upon irradiation several processes can occur: the system can stay in the initially populated state and live long enough to react or it can populate other low–lying states via Intersystem Crossing (ISC) or Internal Conversion (IC) mechanisms. In order to find new photo–catalysts it is necessary to better understand the properties of suitable metal–complexes, not only on the reactive timescales (seconds to minutes) but also on the ultrafast timescales, in order to comprehend the photo–cycle of the used molecular complex and its properties. In this regards, the case of $\text{Pt}(\text{pop})$ is quite interesting, being part of a large family of di–metallic $d^8\text{--}d^8$ molecular complexes with the peculiarity of generating a metal–metal σ –bond in the excited state.[2] $\text{Pt}(\text{pop})$ caught interest as photo–catalyst in hydrogen production because of its capability to abstract non–acidic hydrogen atoms from alcohols, together with its easy synthesis and high stability.[1] Even though several experimental and theoretical studies were performed on $\text{Pt}(\text{pop})$, its photo–cycle is still not completely determined and its high–lying excited states have never been investigated experimentally.

On top of this, because of the ultrafast generation (10s ps) of its reactive state (the lowest excited triplet) the reactivity of the lowest excited singlet states has never been tested. For this reason several derivatives were synthesized with the sole purpose of slowing down the ISC and have the possibility to investigate the excited states of the molecular complex, such as the perfluoroborated derivative ($[\text{Pt}^{\text{II}}_2(\text{P}_2\text{O}_5(\text{BF}_2)_2)_4]^{4-}$ hereafter addressed as Pt(pop)-BF₂).[3] Beside this, the peculiar formation of a Pt-Pt bond in the excited state, together with the high harmonicity of the potential energy curves in the lowest excited singlet and triplet states, drew the attention of scientists to the point of becoming a case-study.

Metal-complexes are often synthesized in order to mimic the properties of a given cofactor present in a specific protein, giving the possibility to investigate its role and the influence of the protein scaffold. As a matter of fact, in living organisms metals are involved in several processes, e.g. bone formation (Ca), neural signal transmission (Na and K), oxygen transport in tissues as well as a wide variety of redox processes (Fe).[4] Metal-complexes are usually embedded in the protein's structure and they act as cofactors in the protein's physiological function. Of particular interest is the function of the cofactor in heme proteins, which are involved in a wide variety of physiological functions, ranging from electron transfer (Cytochrome b and c) to catalysis (Cytochrome P450, Peroxidase), and oxygen transport/storage (Hemoglobin and Myoglobin).[5] Although these proteins have different physiological roles, they share the cofactor, the heme, which is composed by a Fe-porphyrin complex connected to the protein via one of the axial coordination sites of the Fe ion. The sixth coordination site is either bound to another amino acid residue or used to perform the physiological function, e.g. binding molecular oxygen [6-8] or nitrogen monoxide to convert it in nitrite.[7, 8] The heme is involved in a series of inter-molecular processes that can either be part of an electron transport chain or quench nearby residues in order to rapidly dissipate excess energy. An example of heme protein involved in the electron transport chain in mitochondria is Cytochrome c (Cyt c). Its main role is to accept electrons from the Cytochrome bc₁ and transfer them to the so called Complex IV (Cytochrome c oxidase). The electron transport process is possible because of the Fe ion in the heme, which can assume several oxidation states (commonly Fe²⁺ and Fe³⁺) allowing the electron flow between proteins. Recently, Chauvet *et al* [9] reported an ultrafast transient absorption (TA) study of the Cytochrome bc₁, showing the different behavior of hemes *b* and *c* contained in the protein.

Another protein that has been widely studied is Myoglobin (Mb), which is considered the hydrogen atom of biology. This fairly small globular protein (153 residues) is involved in the oxygen storage [6–8] as well as in the physiological regulation of bioactive NO.[7, 8] This protein is also quite interesting from the photo–physical point of view, showing different ligand behaviors upon photo–excitation and highlighting the affinities of diatomic ligands both for the porphyrin and the protein environment. As an example in MbCO the ligand is photo–detached from the heme and is docked within 1 ps in a nearby pocket that hinders its recombination (occurring on μs [10, 11]), while in MbNO the ligand (after photolysis) recombines non exponentially to the heme on 10–30 ps and 120–250 ps.[12] Ligand dynamics are not the sole interesting photo–induced processes related to the heme, which is capable of effectively quench the fluorescence of various amino acids constituting the protein structure. An interesting example is given by the quench of excited tryptophan (*Trp) fluorescence, which previously was reported to occur via *Trp–to–heme energy transfer.[13, 14] However, recent 2D–UV TA experiments demonstrated that, in ferric Mbs, the quenching of *Trp is due to two competing processes, namely *Trp–to–heme energy and electron transfer.[15]

The electron transfer processes in proteins often involve metal complexes, occurring not only in heme proteins but also in prion proteins. Discovered by Prusiner in 1970s,[16] the main physiological function of prion proteins is not completely understood yet, even though their involvement in transmissible spongiform encephalopathies (TSE) is clearly determined.[16–18] Prion proteins are involved in Cu^{2+} binding,[19] even if they were reported to bind other metal ions, e.g. Mn^{2+} , Fe^{2+} and Zn^{2+} . Furthermore, Ruiz *et al* [20] suggested the generation of Cu^+ due to an electron transfer from the tryptophan residue present in the Cu–binding tail sequence.

On these basis, in this thesis we study the ultrafast inter–and intra–molecular processes in metal–complexes, not only in catalytically interesting complexes, such as Pt(pop) and Pt(pop)– BF_2 , but also in physiologically relevant proteins, such as Myoglobin and Prion proteins. This thesis is structured in six chapters. Chapter 1 gives a brief introduction on the theoretical concepts that underlie the main ideas of this work, which are necessary to understand the presented experimental results. Chapter 2 focuses on the technical side of the work, giving the details of the set–ups used to perform the experiments and a concise summary of the most important tools used in the data analysis. Chapters 3 to 5 are dedicated to the main experimental results obtained.

Chapter 3 focuses mainly on ultrafast phenomena in molecular complexes, investigating the ISC mechanism from the lowest excited singlet state to the lowest excited triplet state of Pt(pop) and its perfluoroborated derivative Pt(pop)-BF₂. These complexes also display wave-packet dynamics both in the ground and excited states, showing transfer of coherence between states of different multiplicity.

Chapters 4 and 5 are dedicated to the study of biological samples, which share the presence of electron transfer from the *Trp to a suitable acceptor. Chapter 4 is entirely focused on the electron transfer process in ferrous Mbs, which is investigated by using tryptophan as a naturally occurring probe. Comparing selective heme excitation with excitation of both Trp and heme we examine the Trp photo-cycle and its relationship with the heme, the ligands bound to it and the amino acids present between the Trp and the heme. Therefore, in this chapter we investigate different ferric and ferrous Mbs, both ligated and un-ligated ones, addressing the generation of low-valent hemes upon electron transfer from the *Trp under physiologically relevant conditions. In chapter 5 we report on the ultrafast phenomena occurring in a specific portion of prion proteins, the N-terminal part of the peptide sequence known as the octarepeat region. The latter is involved in Cu²⁺ binding, therefore we focus on the quenching kinetics of *Trp, which shows different time decays before and after Cu²⁺ complexation.

Finally, Chapter 6 briefly summarizes the results obtained in this work, followed by prospective experiments that could be performed in the future to answer the still open questions.

Chapter 1

1 Spectroscopy and Inter-/Intra-Molecular processes: an introduction

The field of spectroscopy extends from steady state techniques to the more modern ultrafast time-resolved ones. This chapter focuses on describing the basic concepts of both techniques (Section 1.1), and on introducing the basic ultrafast inter- and intra-molecular processes (Section 1.2) needed to understand the discussions presented in the following chapters.

1.1 Ultrafast Transient Absorption

Anders Jonas Angstrom was one of the pioneers in the field of spectroscopy in 1850s. Nowadays, absorption and emission spectroscopies are common tools used both in research as well as in the industrial production and quality control. The absorption of a given solution, containing an absorbing molecule (chromophore), is a dimensionless quantity related to the light intensity before (I_0) and after (I) the solution itself. Lambert and Beer described the absorption as function of the optical path-length (l) [cm], the concentration of the absorber (c) [mol L^{-1}] and the molar extinction coefficient (ϵ) [$\text{mol}^{-1} \text{L cm}^{-1}$], as shown in Equation (1.1).

$$(1.1) \quad A(\lambda) = \epsilon(\lambda) \cdot c \cdot l = \log_{10}\left(\frac{I_0}{I}\right)$$

The molar extinction coefficient value is typical of the chromophore in a specific solvent and it is strictly connected to the microscopic characteristics of the system (solvent + solute) under study. Static spectroscopy probes only $S_0 \rightarrow S_n$ transitions (S_0 is the ground state and S_n indicates various excited states) giving no information on the excited states dynamics; however, sampling the system at given time-delays allows to study also the evolution of different species in solution. If the system is perturbed before probing its response, it is possible to study the dynamics related to other states than the ground state. This procedure was proposed by Norrish, Eigen and Porter, which implemented flash photolysis technique and received the Nobel Prize in 1967.[21] This technique allowed to prepare the studied system in an energetically higher state by a flash-lamp and to probe its evolution in time, with a time-resolution in the order of micro- (μs), nano- (ns) and picoseconds (ps), therefore allowing the investigation of several fast processes such as electron transfer in protein systems [22, 23] and Intersystem Crossing (ISC).

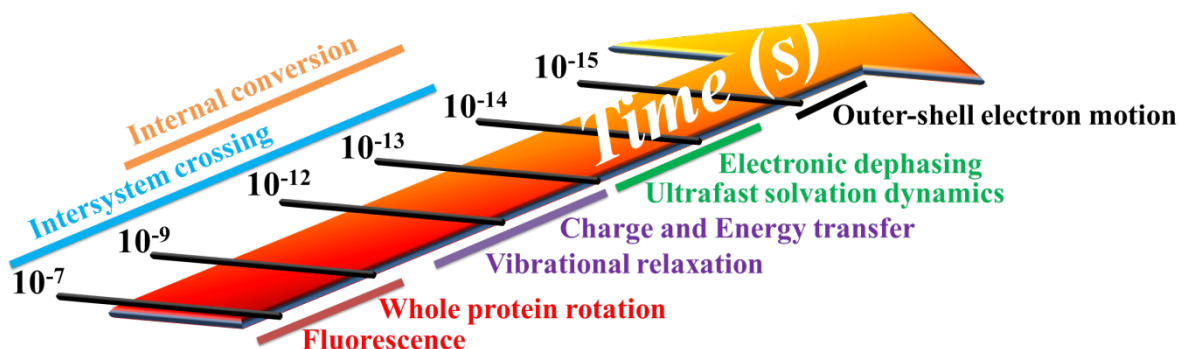


Figure 1-1 Schematic representation of dynamic intervals for some fast and ultrafast processes.

The natural extension of the flash photolysis technique came with the advent of pulsed lasers, which allowed reaching time-resolutions in the femto- (fs) and atto-seconds (as) range.[24–26] These improvements allow one to investigate processes such as ultrafast Internal Conversion (IC), charge and energy transfer, solvation dynamics and wave packet dynamics, which occur on ultrafast timescales, as shown in Figure 1-1. Several ultrafast time-resolved techniques were implemented in the last decades, such as Fluorescence Up-Conversion [27] and Transient Absorption.[28, 29] Here we focus on the latter, since it is the main technique used to perform the experiments presented in the next chapters. A general scheme for Transient Absorption (TA) spectroscopy is presented in Figure 1-2: a fs pump pulse generates a perturbation in the system under study, which is then detected via a probe pulse (spatially overlapped with the pump pulse on the sample). By changing the time-delay between pump and probe pulses it is possible to gather information on the temporal evolution of the system from fs to ns (even ms in some systems[30]). In the geometry shown in Figure 1-2 the transient signal will have the same direction of the transmitted probe, thus being heterodyne detected with the probe light. The signal is usually ~1% of the absorption, or even smaller, and it is calculated by subtracting the probe without pump (I_u) to the probe in the presence of the pump (I_p) as shown in the following equation:

$$(1.2) \quad \Delta OD = -\log_{10}\left(\frac{I_p}{I_u}\right) \cong \frac{1}{\ln(10)}\left(\frac{I_p - I_u}{I_u}\right)$$

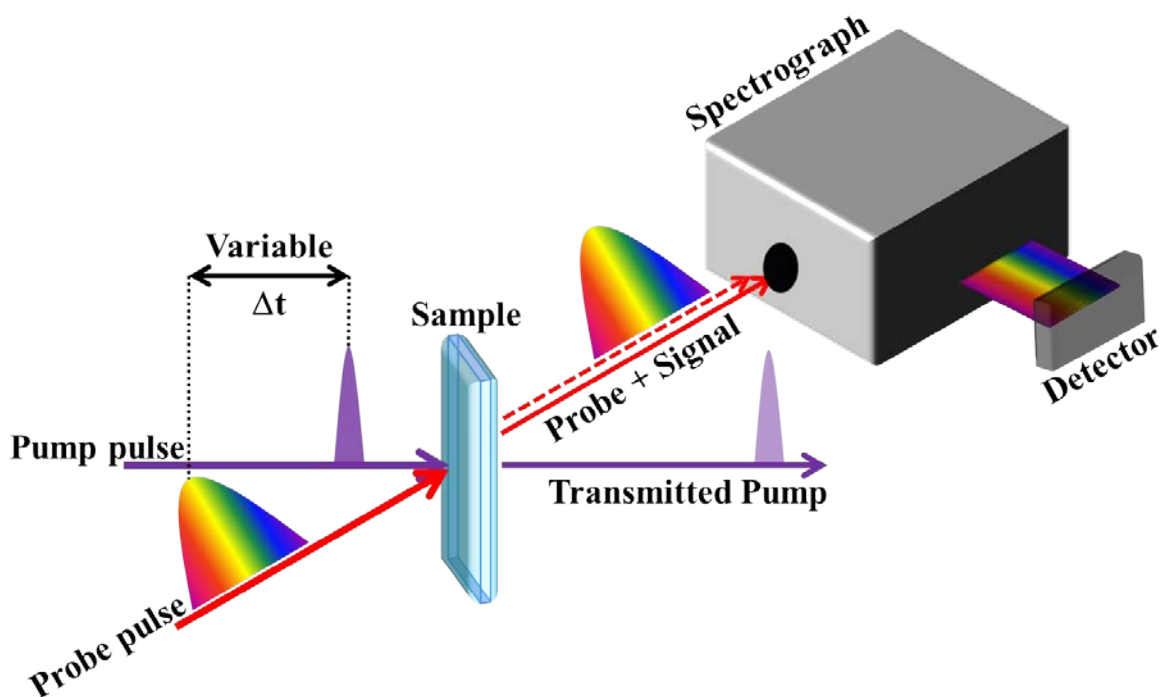


Figure 1-2 Schematic representation of a Transient Absorption set – up. After the sample position are drawn two probe arrows: the dotted red arrow represents the transient signal and the solid red represents the transmitted probe.

The final result shown in equation (1.2) is obtained by expressing $I_p = I_u + x$, where x is a small perturbation of I_u , and then expanding the base ten logarithm in a Taylor series truncated at the first term. As a consequence of equation (1.2), when the probe pulse arrives on the sample before the pump there will be no signal; however, when the probe pulse arrives after the pump, a transient signal appears. Typically, a transient signal is composed by the following contributions: Ground State Bleach (GSB), Stimulated Emission (SE) and Excited State Absorption (ESA). The scheme in Figure 1-3 displays a simplistic example of these features in a four level system and their representation in the UV–visible region. The GSB is a pump–induced depletion of the amount of molecules in the ground state, thus causing less absorption with respect to the unpumped probe and leading to a negative transient signal. Further, the molecules excited by the pump pulse are in the S_1 state (in the simple picture of Figure 1-3), thus their interaction with the probe pulse can either cause them to absorb or emit light. In the former case the excited molecules will absorb one photon and (depending on its energy) they will end up in S_2 (ESA_1) or S_3 (ESA_2), thus resulting in an increased absorption and a positive transient signal. The emission of light upon interaction with the probe pulse leads to SE, which gives a negative transient signal because the emitted photons add to the transmitted probe light, thus the detector will collect more light.

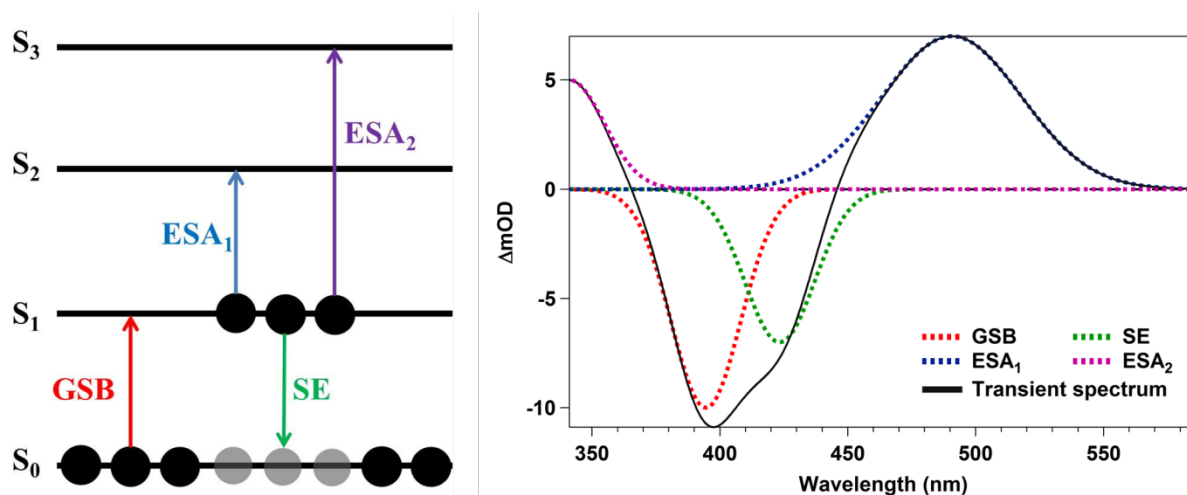


Figure 1-3 Simulated example of a typical transient spectrum in the visible region with several components overlapping (right). On the left is shown a diagram with the meaning of the different components.

All these features are shown in the calculated transient spectrum of Figure 1-3, where the single GSB, SE and ESA features are displayed (dotted colored lines), together with the resulting transient signal (black solid line). The presence of several overlapping features in the probe region is a rather common result when performing transient absorption experiment probing in the UV and visible regions, because of the wider absorption bands with respect to the IR region.

When pump and probe pulses interact with the sample at the same time ($\Delta t = 0$) the optical phase of the probe is changed by the interaction of the latter with the pump pulse, thus generating an artifact.[31] This phenomenon is called cross-phase modulation and it is due to a change of the refractive index of the non-linear medium proportional to the pump pulse intensity. The Full-Width at Half Maximum (FWHM) of the time-zero artifact is related to the pump pulse-length, as previously demonstrated by Polli *et al.*[32]

1.2 Ultrafast phenomena

This section introduces the most important ultrafast processes that will be used throughout this work. A description of the intra-molecular processes is given in Section 1.2.1, followed by inter-molecular processes in Section 1.2.2. The final part (Section 1.2.3) is dedicated to wave-packet generation and coherence transfer.

1.2.1 Intramolecular processes

As mentioned above, the advent of pulsed lasers allowed the investigation of several processes occurring on fast and ultrafast timescales; thus leading to a better understanding of inter- and intra-molecular relaxation process.

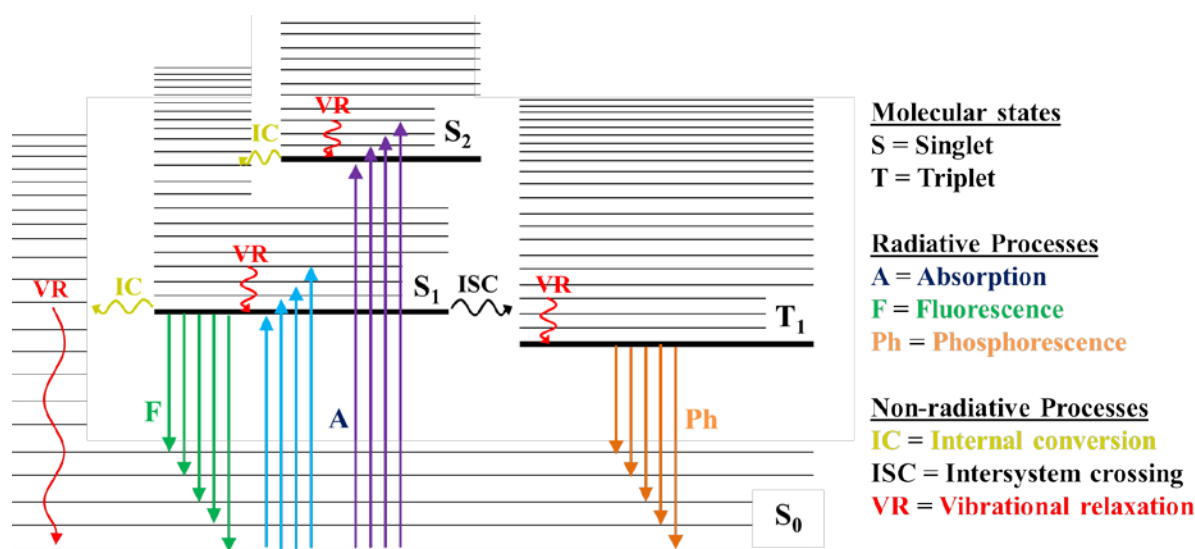


Figure 1-4 Jablonski diagram for a three level molecular system. The ground state is S_0 , the two excited singlet states are S_1 and S_2 and the lowest triplet excited state is T_1 . The curved arrows represent non-radiative deactivation mechanisms while straight arrows represent radiative deactivation mechanisms. Horizontal lines represent iso-energetic processes.

In Figure 1-4 is shown the Jablonski diagram, which represents the possible intramolecular radiative and non-radiative processes occurring in a molecule upon absorption of a photon possessing enough energy to populate higher electronic excited states. The non-radiative processes, such as Vibrational Relaxation (VR), IC and ISC, are represented by curved arrows, while radiative processes, e.g. fluorescence and phosphorescence, are represented by straight arrows. Depending on the spectral width of the excitation pulse, several vibrational states can be excited contemporarily. The excess energy is dissipated through VR on the ps timescale [33, 34] and mainly depend on how fast the system (excited molecule + solvent) can dissipate the extra energy through vibrational modes.[33] If the molecules are excited in the S_2 state, it is most likely for them to undergo IC to the S_1 state (within 10s of fs),[35] followed by VR in order to lose excess energy and stabilize on $v' = 0$ vibrational state. The ultrafast non-radiative deactivation of highly excited electronic states to the lowest excited state ($S_n \rightarrow S_1$ transition) of the same spin multiplicity (from which it fluoresces) is known as Kasha's rule.[36, 37] However, after its postulation in 1950 by Kasha,[36] several exceptions were reported, such as the azulene,[38, 39] pyrene,[40] naphthalene,[41, 42] carbon nanotubes,[43, 44] as well as diplatinum complexes (discussed in Chapter 3).

The non-radiative transition from an excited singlet state to a triplet state is known as ISC. The latter occurs through a spin-flip process that strongly depends on the electron exchange and it is responsible for the coupling of electron spin vectors.

When the exchange interaction J between two coupled spins is strong, the energy separation between singlet and triplet states is very large and the two spins are said to be strongly coupled. This interaction energy is given by the spin Hamiltonian H_{IE} , which is proportional to J as shown in equation(1.3):

$$(1.3) \quad H_{IE} = J \cdot \mathbf{S}_1 \cdot \mathbf{S}_2 = J_0 \cdot \exp(-R)$$

Where \mathbf{S}_1 and \mathbf{S}_2 are the spin systems, J_0 is a parameter that depends on the orbitals and R is the orbital separation in space. For ISC to occur, the J value must be small and comparable to that of magnetic torque available in the system, which can be of three types: i) coupling with the magnetic moment of an applied laboratory magnetic field (Zeeman coupling); ii) coupling with the magnetic moment of a nuclear spin (hyperfine coupling) and iii) coupling with the magnetic moment due to orbital motion (spin-orbit coupling). In the latter case the spin-orbit coupling energy can be written as $E_{SO} = \langle \psi_1 | \mathbf{H}_{SO} | \psi_2 \rangle$, where \mathbf{H}_{SO} is the spin-orbit coupling operator and ψ_1 and ψ_2 are the initial and final orbitals, respectively. Moreover the spin-orbit coupling operator can be described as the interaction between spin (\mathbf{S}) and angular momentum (\mathbf{L}), and thus as the interaction of their annexed magnetic momenta $\boldsymbol{\mu}_S$ and $\boldsymbol{\mu}_L$, respectively, as shown in equation(1.4).

$$(1.4) \quad \mathbf{H}_{SO} = \eta_{SO} \cdot \mathbf{S} \cdot \mathbf{L} \cong \eta_{SO} \cdot \boldsymbol{\mu}_S \cdot \boldsymbol{\mu}_L$$

In equation (1.4) η_{SO} is the spin-orbit coupling constant, which is due to the nuclear charge that the electron “feels” as it orbits along key atoms involved in the ISC process. It is important to recall that the spin-orbit coupling constant (η_{SO}) is proportional to the fourth power of the atomic number of the atom involved in the ISC. Therefore, the presence of heavy atoms in the molecule has a direct impact on the ISC timescale (heavy-atom effect).[45] The ISC rate constant can be estimated by using equation (1.5), which is function of the activation energy (E_a) and temperature (T):

$$(1.5) \quad k_{ISC} = k_0 + A e^{\left(-\frac{E_a}{RT}\right)}$$

Where k_0 is a temperature independent rate constant, A is a probability factor and the exponential represents the T-dependent part of the rate constant. However, the availability of ultrafast techniques led to a deeper study of the metal complexes, showing the inadequacy of the text-book notions in the ultrafast time domain.

Even if the presence of a heavy-atom in the molecule undoubtedly causes spin-changes that are orders of magnitude faster than in organic molecules, recent results in the field of ultrafast spectroscopy highlight that the large spin-orbit coupling constant of the metal is not the only parameter playing a role in the ISC rate.[46–52] Recent TA and Fluorescence Up-Conversion measurements reported by Chergui *et al*, described $^1\text{MLCT} \rightarrow ^3\text{MLCT}$ (MLCT = Metal-to-Ligand Charge Transfer) ISC time constants < 30 fs in $[\text{M}^{\text{II}}(\text{bpy})_3]^{2+}$ complexes (M = Fe, Ru; bpy = 2,2'-bipyridine).[49, 53–55] The latter results show faster ISC with respect to Osmium (Os) complexes, for which ISC of 100 fs ($\text{Os}(\text{dmbp})_3$) and < 50 fs ($\text{Os}(\text{bpy})_2(\text{dpp})$) were reported (dmbp = 4,4'-dimethyl-2,2'-bipyridine and dpp = 2,3-dipyridyl pyrazine).[56] The observed difference in ISC times, between the two Osmium complexes, was explained in terms of higher density of states in the $\text{Os}(\text{bpy})_2(\text{dpp})$ with respect to the $\text{Os}(\text{dmbp})_3$. [56, 57] Going to even higher atomic numbers, the ISC timescale of Pt(pop) ($[\text{Pt}_2(\text{P}_2\text{O}_5\text{H}_2)_4]^{4-}$) lies in the 10–30 ps range, showing a strong solvent dependence.[52] The ISC time constants presented above show an opposite trend with respect to the one predicted from the heavy-atom effect; as a matter of fact the spin-orbit coupling constant of the metal ions (reported in parentheses) are: Fe (0.05 eV) $<$ Ru (0.10 eV) $<$ Os (0.37 eV) $<$ Pt (0.58 eV).[57] Following the latter values the ISC rate should be higher in Pt-complexes than in Fe-complexes, while it is exactly the opposite. Hence, the presence of a high spin-orbit coupling constant is a necessary but not sufficient condition to achieve fast ISC timescales, which are influenced also by the density of states, crossing of potential energy surfaces and structural rearrangements of the investigated molecules. Therefore, ultrafast techniques enable us to explore new scenarios that question basic rules found in textbooks resulting in a better understanding of processes such as ISC, IC, Kasha rule and heavy-atom effect.[46, 57]

The last item present in the Jablonski diagram shown in Figure 1-4, is related to the radiative processes, namely fluorescence (emission from excited singlet states) and phosphorescence (emission from the excited triplet states), whose natural timescales lie in the range 10^{-9} s– 10^{-7} s and 10^{-4} s– 10^2 s, respectively.[58] The radiative rate constant of a molecule is related to the absorption extinction coefficient in the following way:[59]

$$(1.6) \quad k_e^0 = 3 \times 10^{-9} \nu_0^2 \int \epsilon d\nu \cong \nu_0^2 f$$

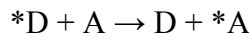
Where ν_0 is the maximum absorption wavelength (in wavenumbers) and the integral corresponds to the area of the band's extinction coefficient (ϵ) plotted versus the wavenumbers.

The latter product is about equal to the oscillator strength (f) multiplied by the square of the central absorption wavelength (in wavenumbers), recalling that the oscillator strength is described, in the classical theory, by equation (1.7).

$$(1.7) \quad f = 4.3 \times 10^{-9} \int \varepsilon d\nu$$

1.2.2 Intermolecular processes: Energy and electron transfer

The Jablonski diagram, shown in Figure 1-4, is adequate for intra-molecular process but it does not contain the presence of multiple deactivation channels related to the interaction of several chromophores. In presence of different species that can interact, the energy absorbed by a chromophore D (Donor) can be transferred to a second molecule A (Acceptor) through dipole-dipole interaction or charge exchange. These mechanisms are of particular importance in biological systems, being at the basis of their functionality.[60] Some of the most striking cases that exemplify the central role of energy exchange in proteins are the photosynthetic systems. Considering an energy transfer process where *D is the excited donor:



This process can occur via two main mechanisms: the electron exchange mechanism and the dipole-dipole interaction mechanism, named Dexter and Förster mechanisms in honor to the scientists that formulated them, respectively. These two mechanisms are schematically depicted in Figure 1-5, summarizing the different nature of the two processes together with the initial and final states. The rate constant in the Förster mechanism [61, 62] (hereafter FRET) is described in equation (1.8):

$$(1.8) \quad k_{FRET} = \frac{2\pi}{h} \int d\varepsilon |sV^{ed}|^2 J(\varepsilon)$$

where s is the screening of the electrodynamic interaction V^{ed} (assumed in Förster theory to be $1/n^2$, with n being the solvent's index of refraction), $J(\varepsilon)$ is the spectral overlap between the emission spectrum of the donor and the absorption spectrum of the acceptor and V^{ed} is given by equation (1.9):

$$(1.9) \quad V^{ed} = \frac{e^2}{4\pi\varepsilon_0} \int \frac{P_D(r_1)P_A(r_2)}{|r_1 - r_2|} dr_1 dr_2 \approx \frac{1}{4\pi\varepsilon_0} \frac{\kappa\mu_D\mu_A}{R^3}$$

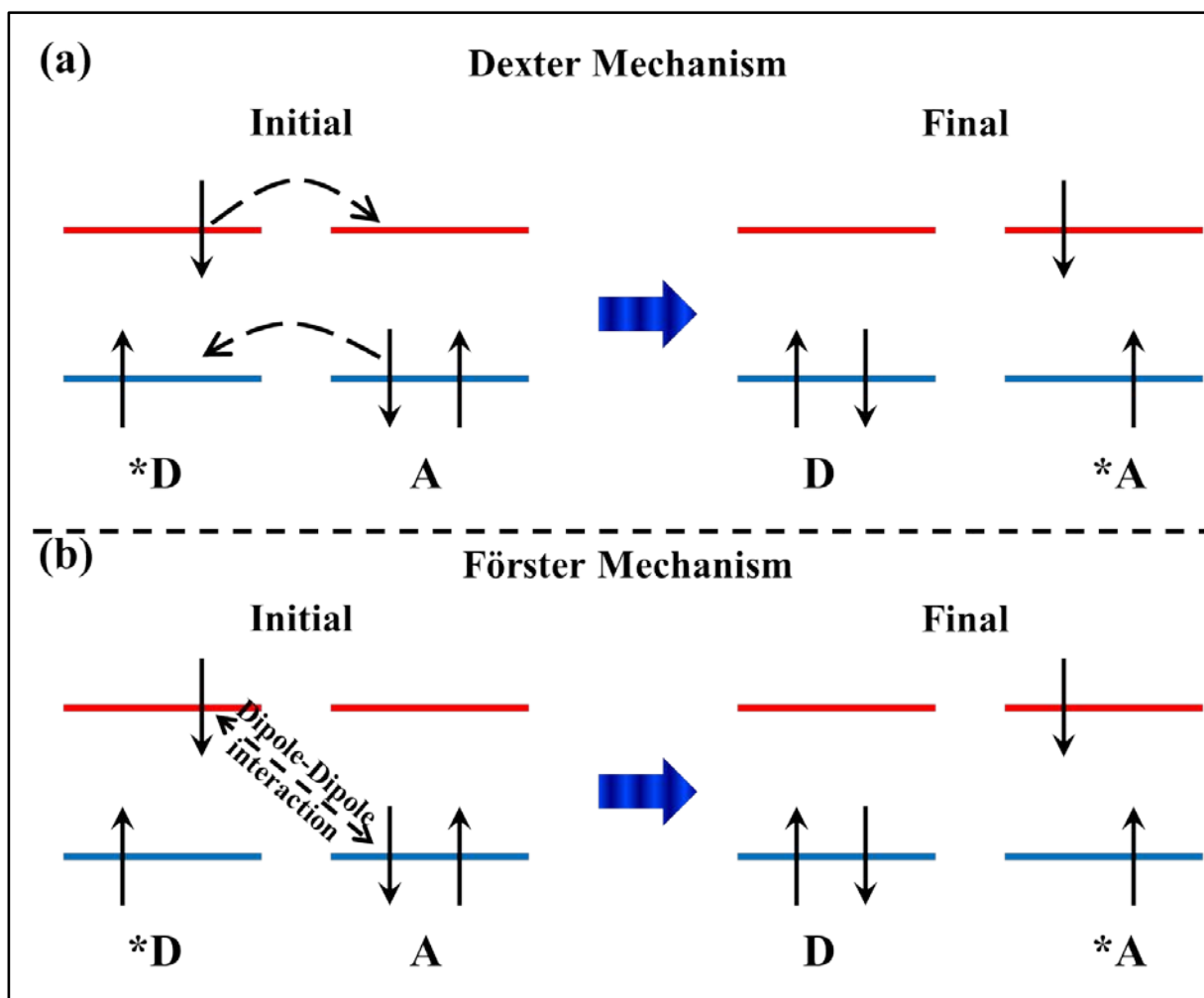


Figure 1-5 Schematic Dexter energy transfer mechanism (a) and Förster energy transfer mechanism (b) between an excited donor molecule (*D) and a ground state acceptor molecule (A).

Where P_D and P_A are the transition densities of donor and acceptor, respectively, κ is an orientation factor, μ the transition dipole moments and R is the center-to-center distance. From equations (1.8) and (1.9) it is possible to get three main information: i) the FRET efficiency is related to the distance in a $1/R^6$ fashion; ii) the reciprocal donor/acceptor orientation plays a crucial role and iii) by the spectral overlap between donor's emission and acceptor's absorption.[61]

The rate constant of the Dexter energy transfer mechanism [63] can also be described by equation (1.8), but using a different operator (V^{EX}), as shown in equation (1.10):

$$(1.10) \quad V^{ex} = \frac{2\beta_{ET}\beta_{HT}}{A} \approx Ae^{-2\alpha R}$$

Where β_{ET} and β_{HT} (both proportional to $\exp(-\alpha R)$) are the electron and hole transfer matrix elements, respectively, A is the energy difference between charge transfer configurations and the locally excited donor configuration, α is a modulation factor of the distance (usually in the 1.2 – 2.0 \AA^{-1} range) and R is the distance between donor and acceptor.[61] Hence, the rate constant for this process can be expressed as:

$$(1.11) \quad k_{Dexter} = \frac{2\pi}{h} A^2 J e^{(-4\alpha R)}$$

In this case J indicates the normalized spectral overlap integral (donor emission and acceptor absorption area set to unity) and the rate falls exponentially with the D–A distance, indicating that this process will be important at short distances and will become quickly negligible as the donor–acceptor distance increases.[61] One of these two processes will prevail depending on the donor–acceptor distance, thus combining in a total operator V^{TOT} that is given by the sum of V^{ed} and V^{ex} . Due to the exponential distance dependence of V^{ex} , the Dexter mechanism will be more important at short distances ($\sim 5\text{--}10 \text{\AA}$) after which its importance decays strongly. The Dexter mechanism is also important in triplet–triplet energy transfer, where the transition dipole moments (and thus FRET) are small. On the other hand FRET will be more important at donor–acceptor distances $> 10 \text{\AA}$, as in the case of protein systems in which is one of the main quenching mechanisms in the fluorescence of several naturally present chromophores. Due to the strong relationship between FRET efficiency and donor–acceptor distance, in 1978 this mechanism was proposed by Stryer as a “*spectroscopic ruler*”,[62, 64–66] due to the possibility of measuring distances between a given donor–acceptor pair inside diverse systems (such as proteins and cells). This technique is widely used nowadays in fluorescence imaging techniques as well as time–resolved techniques;[65–69] however, recent measurements on ferric myoglobins[15] showed that other deactivation channels can be operative and compete with FRET, thus leading to the possibility of wrong donor–acceptor distance estimates. In biological systems, an additional deactivation pathway, which can compete with FRET, is electron transfer between two chromophores,[15] thanks to the presence of amino acid residues that can act as intermediates for hopping or reducing the tunneling energy.[15, 70]

Electron transfer displays a central role in biological systems and can occur over longer distances ($\sim 20 \text{\AA}$),[71–75] contrarily to Dexter energy transfer that is active only at very short distances. Several important works were performed to understand the role of electron transfer in proteins and to correlate the distance with the efficiency of the process.[71, 73, 74, 76–83]

Most of them focused on binding of a Ru(bpy)₂(Im) (where Im = Imidazole) to an histidine present in the protein, (usually azurins,[75–77] myoglobin [77, 84, 85] or cytochrome c,[77, 78, 86]) while Giese *et al* studied mostly the importance of amino acid residues in the electron transfer process within peptides.[72, 73, 81] Depending on the amino acid residues present between donor and acceptor molecules, the electron transfer can occur via tunneling through space [82] or via “*hopping*” through different residues.[72, 82, 83] When the donor–acceptor distance increases, the hopping process becomes faster with respect to the direct tunneling; nonetheless the presence of residues can reduce the energy needed for the tunneling process, as will be briefly discussed in the chapter dedicated to the tryptophan–heme electron transfer in myoglobins.

The electron transfer process was described for the first time by Rudolph Marcus [87–90] on the basis of previously reported Libby’s hypothesis,[91] defining the donor–acceptor system with two parabolas (assigned to reactants and products) as function of a general reaction coordinate (Figure 1-6). Marcus describes the rate constant as function of the reorganization energy (λ), the free energy of the reaction (ΔG°), the temperature (T) and the electronic coupling between donor and acceptor (H_{AB}), as shown in equation (1.12):

$$(1.12) \quad k_{et} = \sqrt{\frac{4\pi^3}{h^2 \lambda k_B T}} H_{AB}^2 e^{-\frac{(\Delta G^\circ + \lambda)^2}{4\lambda k_B T}}$$

$$(1.13) \quad \Delta G^\circ = O x_D - Red_A - E_{D^*} + E_{Prod.} - \frac{e^2}{\epsilon} (d_{AD})$$

Equation (1.13) shows the dependence of the free energy change to parameters like the oxidation potential of the donor in the excited state (given by the term: $O x_D - E_{D^*}$), the reduction potential of the acceptor (Red_A), the energy of the product pairs ($E_{Prod.}$) and finally the Coulombic interaction between the generated radical pairs, with e being the electron charge, ϵ the dielectric constant and d_{AD} the donor–acceptor distance. As can be seen in equation (1.12), the electron transfer rate constant is dependent on the reorganization energy (both in the pre–exponential and in the exponential factors), which is composed of two terms: the solvent reorganization λ_s and the internal reorganization λ_i .

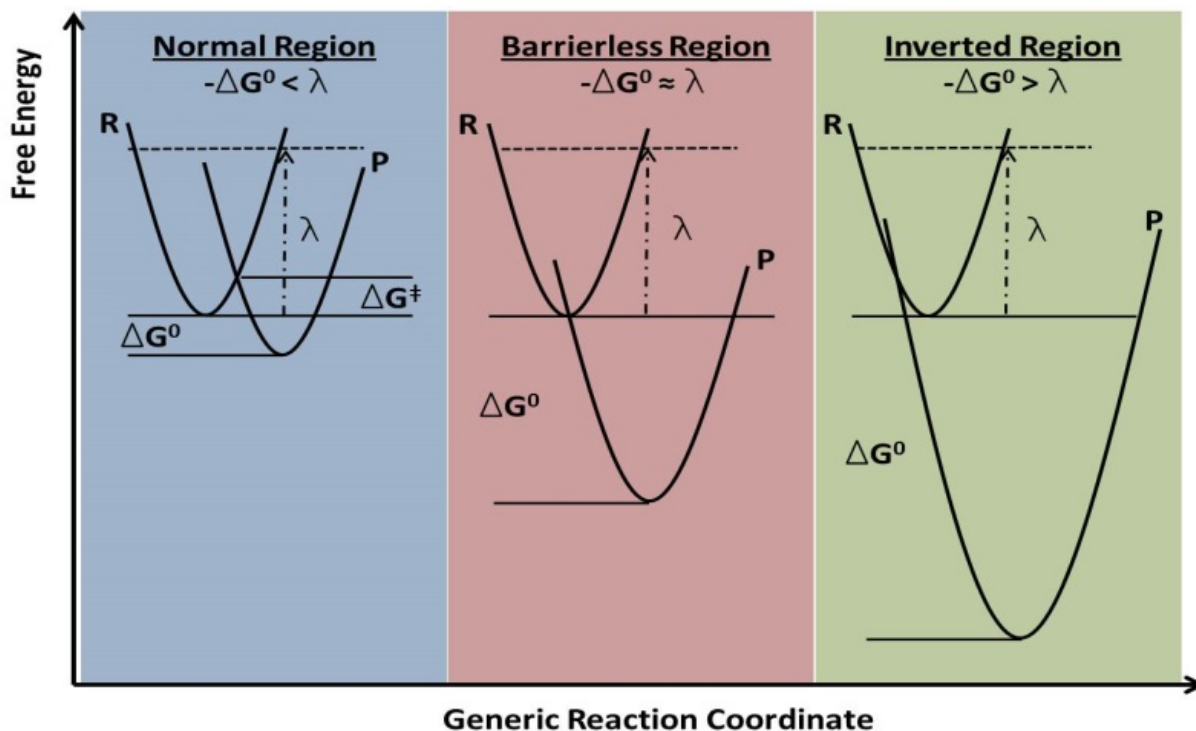


Figure 1-6 Schematic representation of the three main regions expected from Marcus' theory. ΔG° is the difference in Gibbs free energy of the two parabolas, λ is the total reorganization energy and ΔG^\ddagger is the activation energy for the electron transfer reaction.

The solvent reorganization energy (λ_s) can be expressed as function of the center-to-center distance R , the optical (D_{op}) and static (D_{st}) dielectric constants of the solvent and the charge transferred during the process Δe , if the reactants are approximated to spheres with ionic radii a_1 and a_2 , respectively:

$$(1.14) \quad \lambda_s = (\Delta e)^2 \left(\frac{1}{2a_1} + \frac{1}{2a_2} - \frac{1}{R} \right) \left(\frac{1}{D_{op}} - \frac{1}{D_s} \right)$$

The internal reorganization energy instead, is related to the changes in bond-length of the reactants:

$$(1.15) \quad \lambda_i = \frac{1}{2} \sum_j k_j (Q_j^r - Q_j^p)^2$$

Where Q_j^r and Q_j^p are equilibrium values for the j^{th} normal mode coordinate Q_j in the reactant and product, respectively and k is a reduced force constant given by: $2 \cdot k^r \cdot k^p / (k^r + k^p)$ in which k^r is the force constant for the reactants and k^p is the force constant for the products.

The total reorganization energy of each reactant (defined as λ_{AA} for the acceptor and λ_{DD} for the donor) is obtained by the so-called self-exchange reaction, namely the change in total reorganization energy upon a reaction in which donor and acceptor species are equal molecules with different charge, e.g. $\text{Fe}_1^{2+} + \text{Fe}_2^{3+} \rightarrow \text{Fe}_1^{3+} + \text{Fe}_2^{2+}$ (usually described as $\text{Fe}^{3+/2+}$ and generically $\text{D}^{+/0}$ and $\text{A}^{0/-}$ for donor and acceptor, respectively). The latter parameters are then used to calculate the total reorganization energy for the entire reaction (λ_{DA}), which is obtained through Marcus' cross-relation, as shown in equation (1.16):

$$(1.16) \quad \lambda_{DA} \cong \frac{1}{2}(\lambda_{AA} + \lambda_{DD})$$

The determination of the λ and ΔG° values allows identifying the three main regions that are expected from Marcus theory, which give the final value of the exponential function reported in equation (1.12): i) the normal region, ii) the barrier-less region and iii) the inverted region, as shown in Figure 1-6. The terms ΔG^0 , ΔG^\ddagger ($\Delta G^\ddagger = (\Delta G^0 - \lambda) / 4\lambda$) and λ identify the energy difference of the two parabola's minima, the activation energy and the total reorganization energy, respectively. As shown in Figure 1-6 the normal region (blue panel) is identified by the reactants and products parabolas close in energy, so that the electron transfer reaction is only slightly exoergonic. The larger the energy difference between the two parabolas, the more exoergonic will be the reaction and the lower the activation energy, till the point in which $\Delta G^\ddagger = 0$ and $-\Delta G^0 = \lambda$ that is identified as the barrier-less region (red panel), in which the electron transfer rate is maximum. If the electron transfer reaction becomes even more exoergonic (green panel), the parabola of the products will cross the one of the reactants on the other side of its minimum, thus increasing again the activation energy required for the reaction to occur and slowing down its rate. This region, usually called Marcus inverted region, was observed experimentally only ~30 years [92] after Marcus proposed his theory.[87] The reason is that, in a solution, the diffusion of the donor and acceptor molecules becomes the rate limiting step, leading to the impossibility of investigating this region. The existence of the latter was proven by synthesizing molecules containing both the electron donor and acceptor moieties separated by molecular spacers of different dimensions, allowing the characterization of the inverted region for several donor-acceptor pairs.[93, 94]

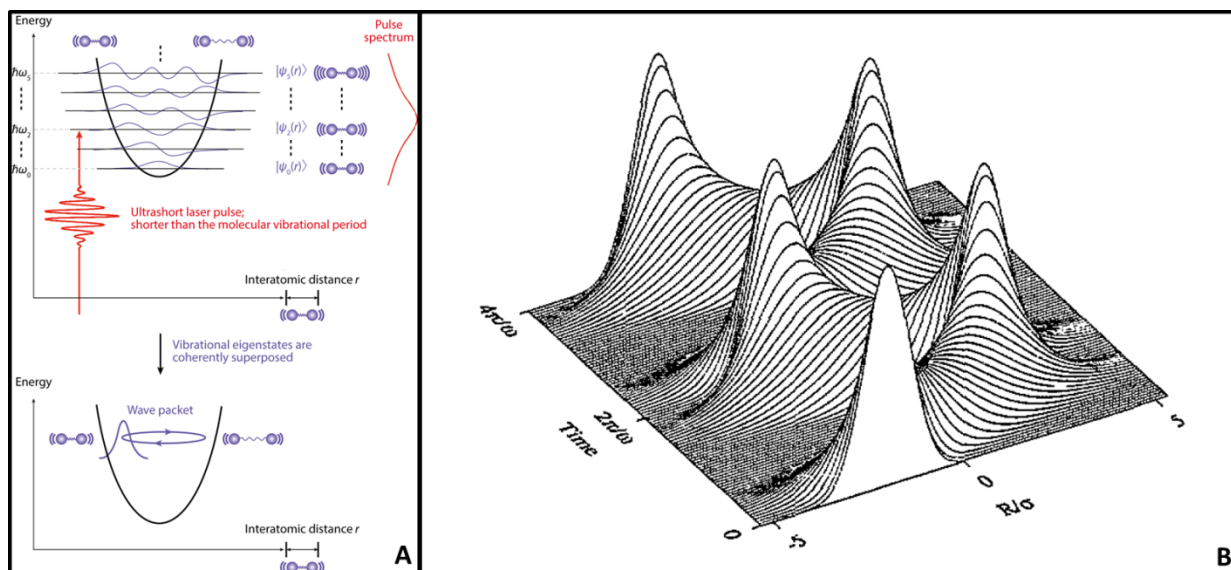


Figure 1-7 Schematic representation of the generation of a wave-packet via an ultrashort laser pulse (A) and example of wave - packet breathing in a perfectly harmonic potential. The scheme presented in (A) is adapted from ref.[95], while the wave-packet breathing is adapted from ref.[96]

1.2.3 Wave-packet dynamics

When performing time-resolved experiments with short excitation pulses, it is possible to coherently superpose vibrational eigenstates of the system thus generating a wave-packet. More precisely, if the pulse duration is shorter than the vibrational period of the molecule, the bandwidth is broad enough to excite several vibrational states impulsively, as shown in Figure 1-7A.[95, 96] The excited eigenstates are coherently superposed, thus leading to interference (both constructive and destructive) as function of time and space that generates a localized wave function of the type shown in equation (1.17):

$$(1.17) \quad |\Psi(r, t)\rangle = \sum_n c_n |\psi_n(r)\rangle e^{-i(\omega_n t - \phi_n)}$$

Where $\psi_n(r)$ and ω_n are the eigenfunction and the transition frequency of the n -th vibrational level, respectively; c_n and ϕ_n represent the amplitude and phase of the n^{th} vibrational level and r is the inter-nuclear distance of the atoms involved in the vibration. This superposition of vibrational states represents the so-called wave-packet. [95, 96] If the excitation pulse used to generate the wave-packet is not short enough, two main problems can arise: i) the wave-packet may evolve during the excitation pulse and ii) the excitation pulse does not bring the two potential energy surfaces in a clear resonant condition.

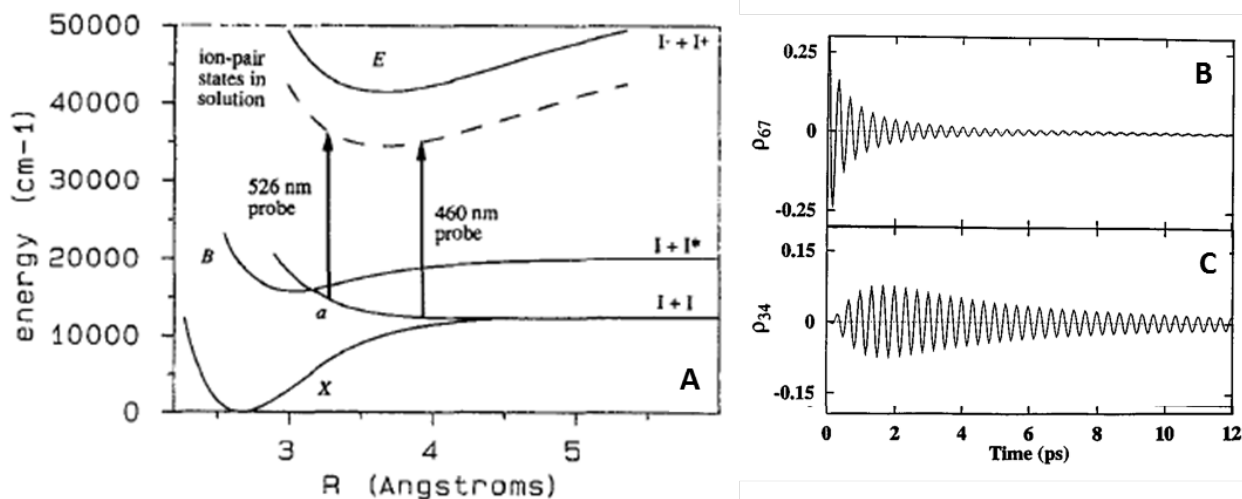


Figure 1-8 In (A) is shown the experimental examples of coherence transfer of the I_2 case, adapted from ref. [106]. The X indicates the ground state, while B and a indicate two excited state. In (B), (C) are shown the results of a theoretical prediction of coherence transfer between two states, adapted from ref. [107], with ρ indicating the chosen density matrix element.

When the wave-packet is generated in the ground state, it is static and it starts moving only when it is transferred to another potential energy, in which it is not at equilibrium. If the latter potential energy surface has exactly the same shape of the ground state but displaced in some coordinate axis, the wave-packet simply oscillates without changing shape. However, if the potential of the excited state is different with respect to the one in the excited state, the wave-packet starts “breathing” as shown in Figure 1-7B. The presence of a weak anharmonicity in the excited state potential energy surface influences dramatically the dynamics of Gaussian wave-packets, which initially oscillates similarly to the harmonic potential case, but after a given time the wave-packet breaks into pieces and spreads over the potential energy surface. In the latter cases, it exist the possibility of revival or fractional revival of the wave-packet.[97–100]

In pump-probe spectroscopy, wave-packets are prepared by the interaction with the pump pulse and their evolution is investigated through the interaction with the probe pulse. Pollard *et al* [101] reported one of the first pump-probe experiments that studied wave-packet motion in Nile blue dye, which was excited with 6-fs pulses and probed in the entire visible range (580–700 nm). Zewail *et al*[102–105] reported notable experiments on both wave-packets dynamics and coherence transfer upon surface crossing, e.g. the photo-dissociation of sodium iodide (NaI).[102, 104] In the latter case, the ground state and first excited state potential energy curves cross in a point leading either to an ionic dissociation or to a covalent one. They generated a wave-packet in the first excited electronic state, which leaked through the crossing of the curves and allowed detection of dissociated sodium.[102, 104]

Scherer *et al* [106] reported a similar case on the I₂ dissociation in hexane via time-resolved dichroism. They reported the frequencies of the wave-packets generated in the ground and excited states, together with oscillations arising from coherence transfer from the wave-packet in the *B* state to the *a* state, as shown in the schematic representation of Figure 1-8A. Further, they suggested that curve crossing occurs via solvent cage-induced electric dipole transitions between electronic states, highlighting that the coherence of the excited state wave-packet motion is not perturbed or destroyed by the interaction with the solvent.[106] Consani *et al* [55] reported the first example of coherence transfer in [Fe^{II}(bpy)₃]²⁺ upon 530 nm excitation of the latter. In this case the wave-packet was not generated by the laser pulse, but by an impulsive structural change of the complex's geometry from the low-spin to the high-spin geometry, namely in the transition from the first excited singlet state to the excited triplet state. The wave-packet generated in this way is then transferred to the quintet state, thus providing an interesting case of coherence transfer in organometallic complexes.[55]

Jean and Fleming [107] reported a theoretical investigation of the coherence transfer process between states by using the Redfield formalism. They generated some coherence in a high-lying state involving levels $n = 6$ and $n = 7$ (ρ_{67}), as shown in Figure 1-8B, whose only allowed dephasing mechanism is the one-photon relaxation. As the population relaxes to a lower-lying state (ρ_{34}) also the coherence is transferred, as shown in Figure 1-8C, with an efficiency that is maximal in harmonic potentials. As a matter of fact, the harmonicity of the potential guarantees exact frequency matching between pairs of levels that differ by the same amount of quanta ($\rho_{67} = \rho_{34} = 1$ quantum), contrarily to the anharmonicity that results in frequency mismatch and thus a less efficient coherence transfer.

Chapter 2

2 Experimental Set-up and data treatment

This chapter is divided in two main sections: the description of the set-ups used for the experiments and the data treatment. The former part is itself divided in two sub-sections: the Two-Dimensional (2D) UV Transient Absorption set-up and the ULTRA beam-line situated in the Rutherford Appleton Laboratories in UK. In the section dedicated to the data treatment are discussed the techniques used in data analysis, such as GVD correction, as well as data fitting and coherent oscillations analysis.

2.1 Experimental Set-ups

In this technical section are discussed the details of the set-ups used to perform the experiments that are presented in the following chapters. Nevertheless, most of the attention is dedicated to the 2D-UV TA set-up, on which most experiments were performed.

2.1.1 Two-Dimensional Transient Absorption

Figure 2-1 shows a schematic table layout of the Transient Absorption setup, based on a 20 kHz laser system.[28, 29] The Ti:sapphire oscillator (Halcyon, KMLabs) is pumped by a continuous wave (CW) Nd:YVO₄ single frequency ($\lambda = 532$ nm) single mode laser, delivering ~ 5 W. The output of the oscillator (~ 400 mW, 80 MHz, 790 nm, ~ 40 nm FWHM) seeds a cryogenically cooled regenerative amplifier (Wyvern500 KMLabs), which is tandem-pumped by three Q-switched (20 ns pulses ~ 1 mJ at 532 nm, 10–50 kHz) Nd:YVO₄ lasers (DS20HE532, Photonics Industries). The amplifier's repetition rate can be tuned between 10 and 50 kHz by tuning the pump lasers' repetition rate and then fine-tuned by tuning the oscillator's repetition rate through remotely controlled variation of its cavity length. Cooling at cryogenic temperatures (liquid nitrogen temperature) the amplifier's crystal increases the thermal conductivity of the Ti:sapphire, thus reducing thermal lensing that would influence cavity alignment as function of pump power. The amplifier delivers 790 nm pulses (~ 40 nm FWHM) at 20 kHz repetition rate, with 0.6 mJ per pulse and typical pulse duration of 50 fs. The output of the amplifier passes through a telescope, which reduces the beam diameter by 3 times. After the telescope the beam is split in two arms: 70% of the energy is directed to the Topas-White, while the rest is used for another experiment.

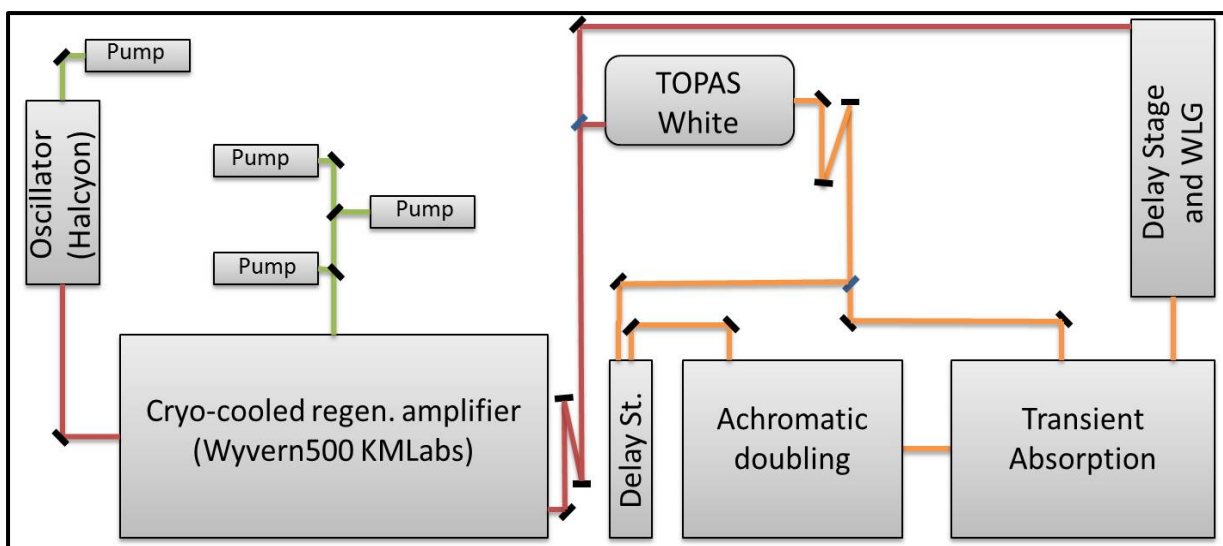


Figure 2-1 Schematic representation of the laser components on the table. The black rectangles represent mirrors while the blue ones represent beam-splitters.

The Topas-White system (developed by Light Conversion) is a two-stage Non-collinear Optical Parametric Amplifier (NOPA), which converts the 800 nm pulses in tunable visible pulses in the 450–750 nm range. The use of a pulse shaper and a Fused Silica wedges inside the Topas allows pulse compression of the output, obtaining nearly Fourier Transform pulses. The Topas-White output is split in 60:40 ratio: the most intense part is used to generate the pump pulses, while the remaining is used to produce UV probe pulses, as shown in Figure 2-1.

The pump pulses can be either in the visible range (450–760 nm) or in the UV (250–380 nm), by frequency doubling the visible pulses through a non-linear crystal (100 μm -thick β -Barium Borate, BBO). The remaining 40% of the Topas-White output passes through a 30 cm remotely controlled delay-line (Aerotech, BMS60) and then is used to generate UV probe pulses via achromatic frequency doubling.[108, 109]

The remaining intensity (30%) of the amplifier's output is split again: ~80% is sent to another experimental set-up, while the remaining 20% passes twice through a 30 cm remotely controlled delay-line and it is focused on a 5 mm-thick CaF_2 plate, in order to generate a white-light super-continuum (operational in case of visible probe measurements).[110, 111] The pump and probe pulses are focused (and spatially overlapped) on the sample, with typical diameters of 100 μm and 40 μm , respectively. After passing the sample the probe is focused into a 100 μm multi-mode fiber (Avantes FC-UV 100-2), which couples the light into a 0.25 m imaging spectrometer with a 150 grooves per mm grating. The latter images the spectrum of the probe pulses onto the detector surface, where it is spectrally resolved detected.

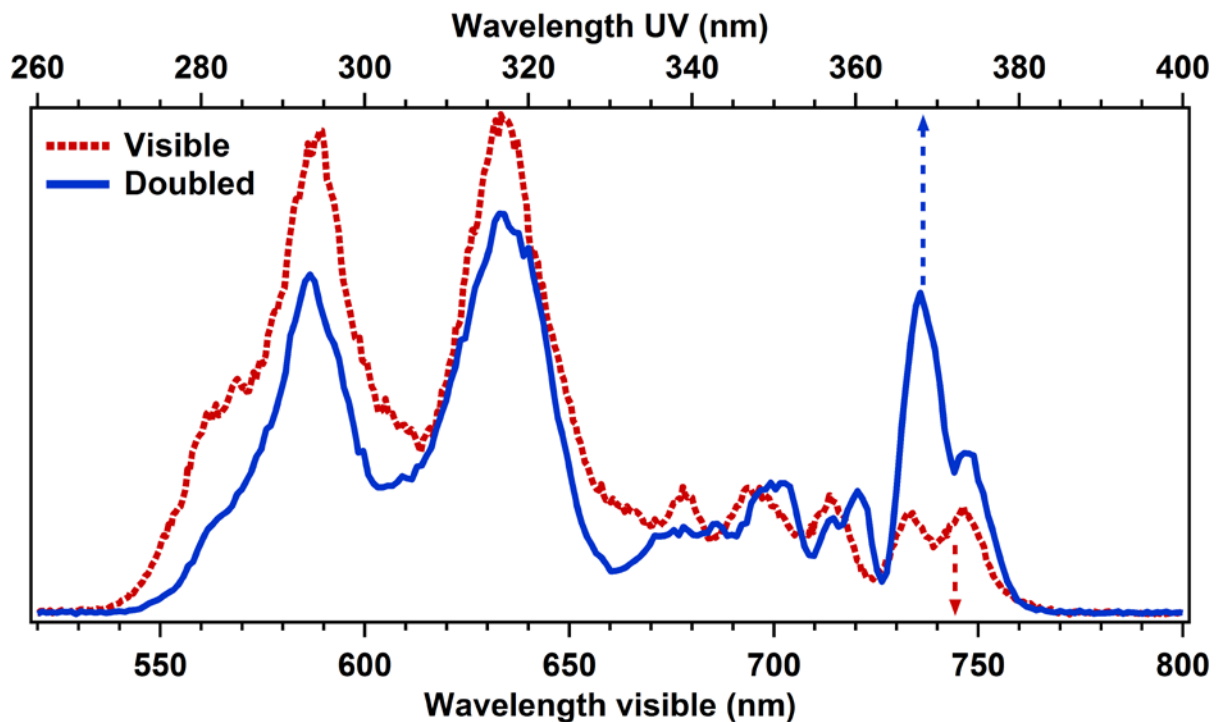


Figure 2-2 Typical broadband TOPAS output and its frequency doubled spectrum. The colored arrows point the wavelength axis used in both cases.

The following sections will give a detailed description of the most important parts of the set-up, namely the Topas-White, the achromatic doubling, the tunable UV pump and the detection system.

2.1.1.1 Topas-White

This two stage NOPA developed by Light Conversion is the main light source of the set-up. The system is designed to be compact and deliver near Fourier Transformed intense pulses (25 μJ) in the visible region (450–750 nm), supplying more energy with respect of the typical output of a “classical” NOPA, in the order of few μJ . This difference is due to the double-pass in the non-linear medium (BBO), having a pre-amplification stage followed by a second amplification stage that strongly increases the energy output of the first one. The Topas-White was developed to solve the main problems that affect a “classical” NOPA, namely limited applicable pump energy and dispersion matching over broad wavelength ranges.

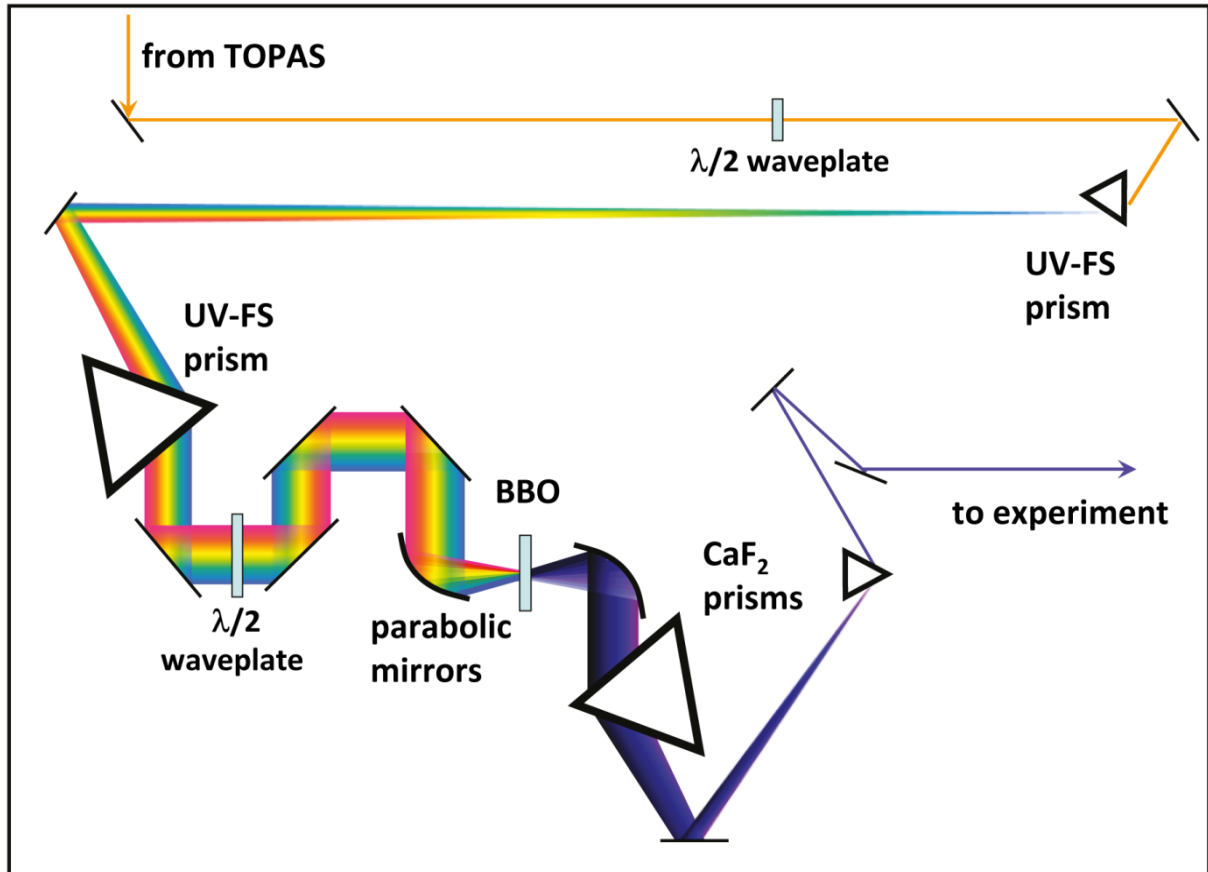


Figure 2-3 Schematic view of the achromatic doubling The UV grade fused silica prisms (UV-FS) have a low dispersion in the visible region, while the CaF₂ prisms have low dispersion in the UV region.

The first issue is improved by applying an appropriate wave-front tilt through a combination of reflective optics and a telescope. The second issue is solved by the introduction of a pulse-shaper in the white-light super-continuum pathway, before the pre-amplification stage.

This pulse-shaper consists of several components, namely: a diffraction grating, a spherical mirror, a folding mirror and a phase mask (namely a cylindrical aspheric lens). By controlling the distance between the grating and the phase mask it is possible to control the chirp of the seed beam, thus compensating for the second and third-order dispersion due to the optics in the Topas pathway. The latter, together with a movable glass wedge, allows obtaining nearly Fourier limited ($< 15\text{--}20$ fs) pulses in the selected region of operation. By tuning the alignment of the seed and pump beams it is possible to choose spectrally narrow (~ 30 nm FWHM) or broad (~ 200 nm FWHM) output signals. The latter has strong relevance when using the achromatic doubling to probe in the UV region, where ~ 100 nm probing window is necessary, as shown in Figure 2-2.

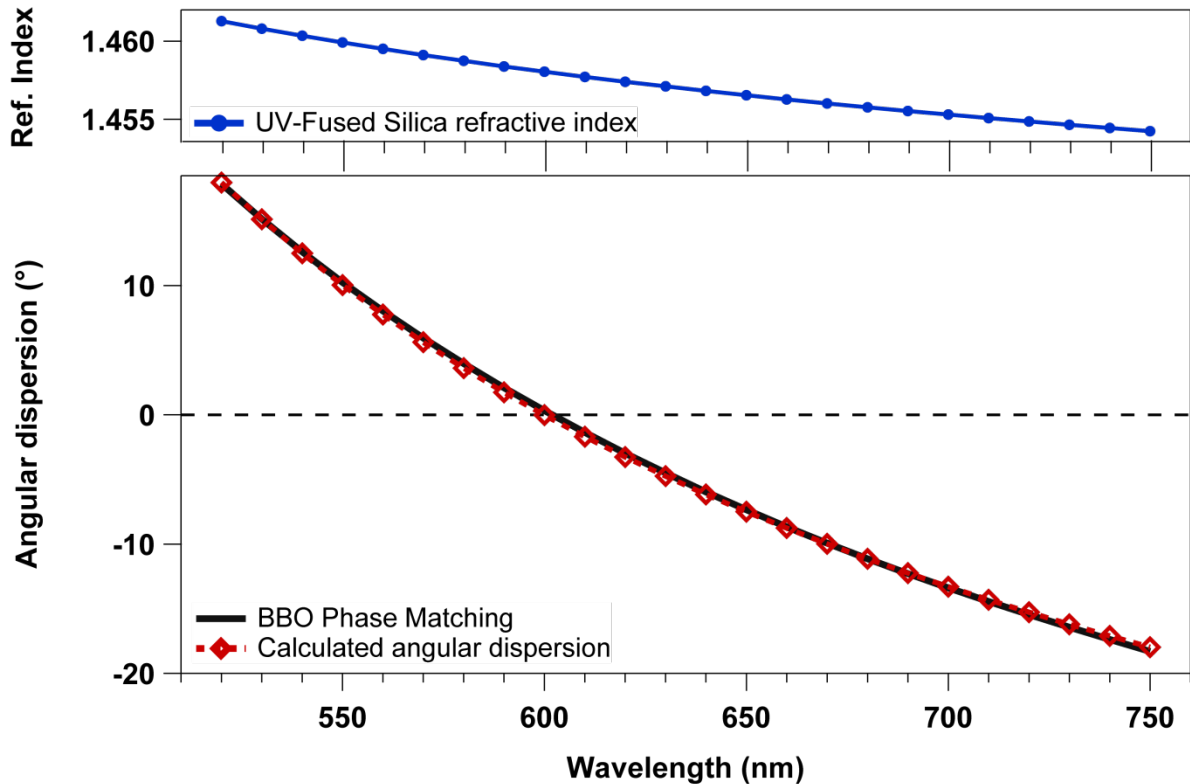


Figure 2-4 Comparison of the phase matching angle of a BBO cut at 40.5° with the calculated angular dispersion induced by UV-FS prisms. In the upper panel is shown the refractive index change of UV-FS in the wavelength range of interest.

2.1.1.2 Achromatic doubling

The set-up was built to work in the UV region, thus allowing both exciting and probing in the 250–380 nm range. This was achieved by the implementation of achromatic frequency doubling (Figure 2-3), the scheme of which was inspired by the work of Baum *et al.*[108, 109]

As can be seen in Figure 2-3, the achromatic doubling resembles a prism compressor with a frequency doubling stage in its center. The visible pulses generated from the TOPAS are angularly resolved by a first UV grade Fused Silica (UV-FS) prism, and collimated by a second one. At this stage all the frequencies are spatially separated and collimated. By focusing them with the right focal length on a doubling crystal, it is possible to achieve the phase matching condition for each single frequency, thus achieving an achromatic second harmonic generation. In our experimental set-up the incoming light from the TOPAS is focused on a 200 μm -thick BBO crystal (cut at 40.5°) through a 90° off-axis parabolic mirror with Effective Focal Length (EFL) of 2 cm, thus obtaining a doubling efficiency of 10–15 % in the entire spectral region (500–700 nm), as shown in Figure 2-2.

A second 90° off-axis parabolic mirror, with equal EFL, is used to collimate the generated UV light, whose frequencies are spatially re-composed via two CaF₂ prisms. The latter have also the function of removing the undoubled visible light that co-propagates with the generated UV light. Figure 2-4 shows the refractive index change of UV-FS in the visible region and a comparison of the external phase matching angle for frequency doubling in a BBO crystal (cut at 40.5°) with the calculated angular dispersion induced by a pair of UV-FS prisms (apex angle 68.7° and prism distance ≈ 77 cm) in the 550–750 nm region.

The wavelength-dependent angular dispersion produced by a pair of UV-FS prisms and a focusing element with focal length f was calculated with equation (2.2), which is derived by the application of Snell's Law (equation (2.1)) to the prism-air system:

$$(2.1) \quad n_1 \sin \theta_1 = n_2 \sin \theta_2$$

$$(2.2) \quad \theta(\lambda) = \left[\alpha - A + \arcsin \left(\sin(A) \sqrt{n^2(\lambda) - \sin^2(\alpha)} - \cos(A) \sin(\alpha) \right) \right] d/f$$

In equation (2.1) n_1 and n_2 are the refractive indexes of the medium 1 and 2, while θ_1 is the angle of the light (with respect to the normal of the surface determined by the two media) inside the medium 1 and θ_2 is the same angle but for medium 2. In equation (2.2) α is the light's incidence angle with respect to the normal to the prism's face, A is the apex angle, $n(\lambda)$ is the refractive index of the prism's material and d the prisms distance (the d/f term determines the spatial width of the frequency resolved beam). The $n(\lambda)$ was obtained by applying Sellmeier equation, as shown in equation (2.3):

$$(2.3) \quad n^2(\lambda) = 1 + \frac{B_1 \lambda^2}{\lambda^2 - C_1} + \frac{B_2 \lambda^2}{\lambda^2 - C_2} + \frac{B_3 \lambda^2}{\lambda^2 - C_3}$$

Where λ is the wavelength expressed in μm , while $B_{1,2,3}$ and $C_{1,2,3}$ are experimentally determined constants that are typical of the material.[112–114] Figure 2-2 displays a typical TOPAS spectrum, obtainable when operating in broadband mode (dotted red), together with its frequency doubled output (solid blue). As can be seen in Figure 2-2 the entire TOPAS spectrum (200 nm) has been efficiently doubled, leading to a UV probe spanning more than 100 nm in the 275–385 nm region.

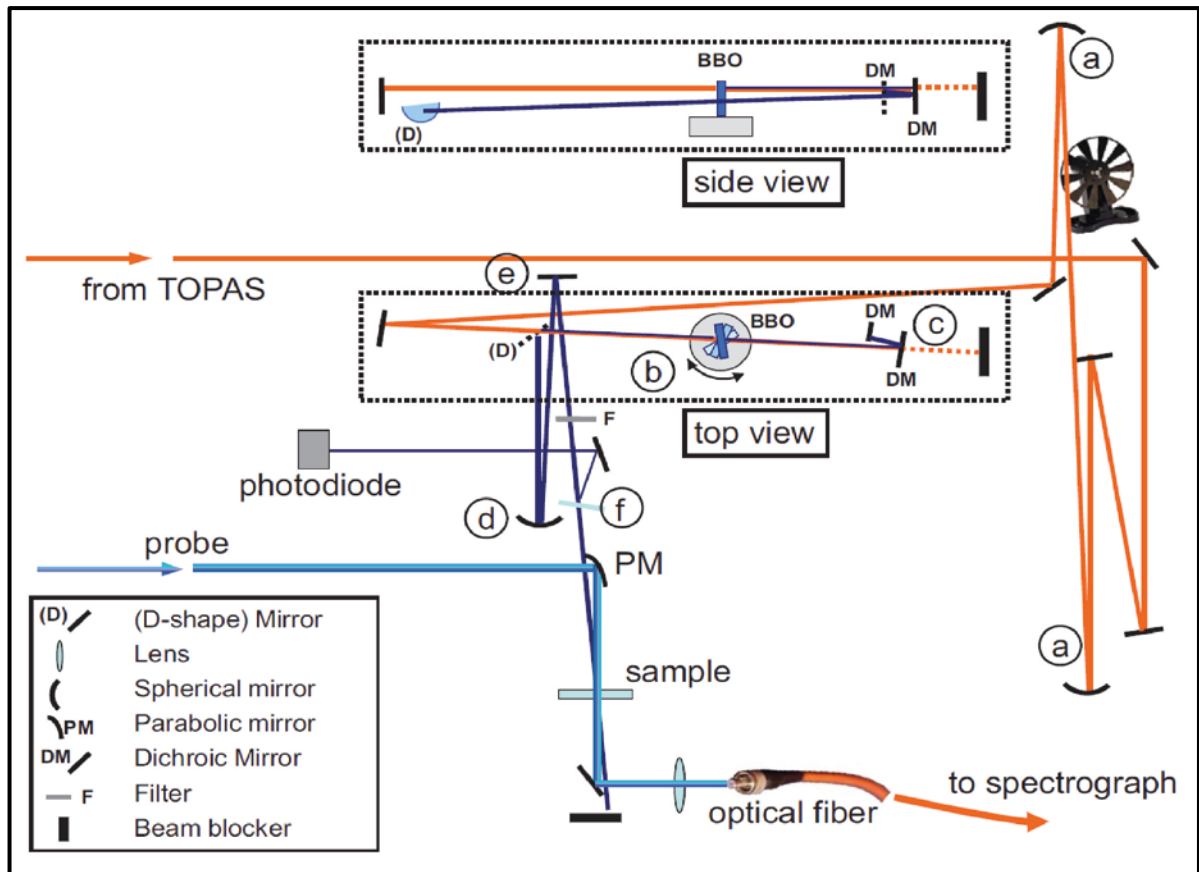


Figure 2-5 Schematic view of the tunable pump pulse generation. Regions identified with letters (a-f) are discussed in details in the text.

2.1.1.3 Tunable Pump pulses

Figure 2-5 shows a schematic view of the UV tunable pump pulses generation. The visible pulses generated in the Topas–White pass through a telescope realized with reflective optics (a). Between the two spherical mirrors (where the beam is focused) is placed a stable phase–lockable mechanical chopper (Thorlabs, MC2000 with 100 slot blade), which runs phase–locked at a frequency $F_{\text{Chop.}} = F_{\text{Ampl.}}/2$. The distance between the mirrors constituting the telescope (a) can be adjusted by a micrometric translation stage positioned under the first mirror, and is set in such a way that the beam will be slightly focusing at the BBO position (b).

The BBO crystal is set on a computer–controlled motorized rotation stage (Thorlabs, CR1/M–Z7E), which can rotate on the plane of the input beam, in order to get the phase–matching angle for different input wavelengths. To obtain the best compromise for both frequency and time resolution, the system is aligned to get pump pulses with 2 nm spectral band–width (FWHM), as shown in Figure 2-6.

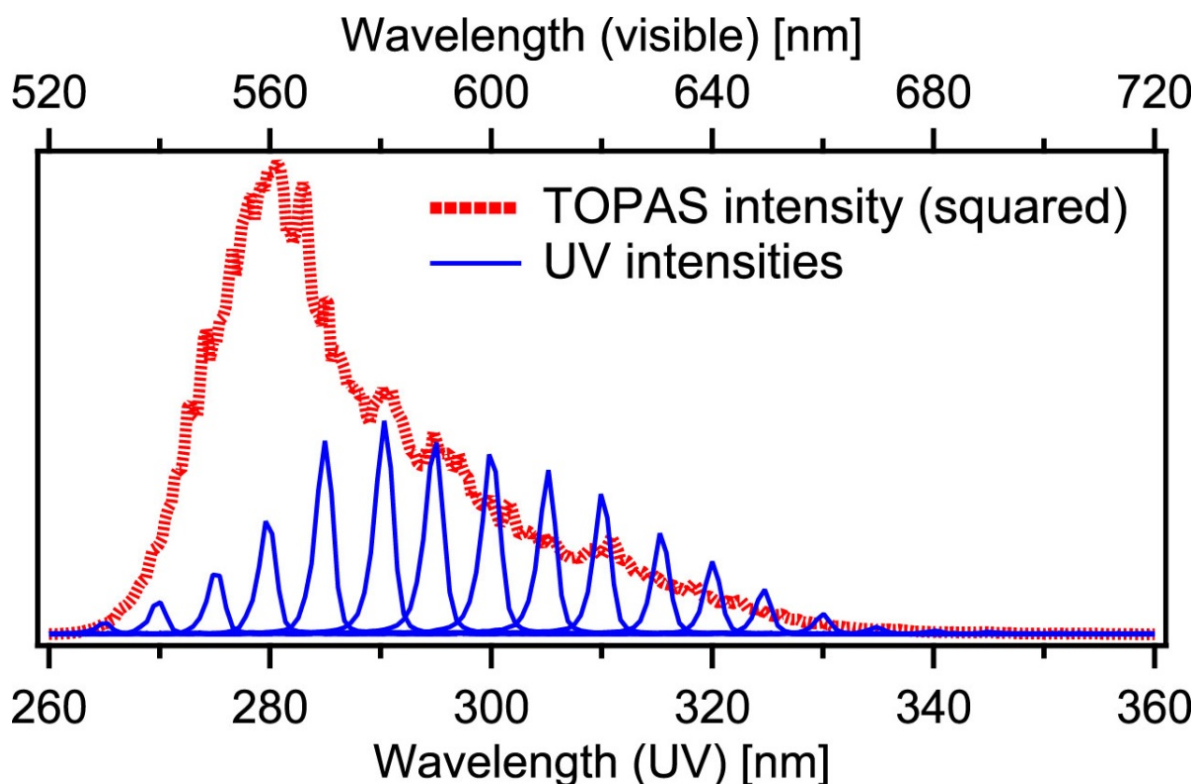


Figure 2-6 Example of the spectral profile of the UV pump (blue solid lines) with respect to the Topas output squared (red dotted lines). Typical spectral width of the UV pump pulses is 2 nm FWHM.

This would not be a problem on a single pump wavelength pump–probe measurement, while it becomes very important in 2D experiments in which the excitation wavelength is scanned to generate a 2D map for each time–delay. The rotation of the BBO (when scanning the pump wavelength) introduces a displacement of the beam as function of the crystal’s rotation angle, leading to a drift of the pump spot on the sample. This issue was solved by introducing two mirrors after the BBO crystal (c), in order to have the doubled beam retro–reflected through the BBO and thus compensating for the pump beam shift. Taking advantage of this geometry, two dielectric mirrors (Layertech, P1010047), with high reflectance in the 260–340 nm region (> 90%) and high transmittance in the entire visible range, were used in (c) to filter out the residual visible light mixed with the generated UV.

The UV pulses are then extracted by a D–shaped mirror and focused on the sample via a spherical mirror (d). Before reaching the sample, the UV pump is reflected on another dielectric mirror (e), in order to remove the remaining visible light that was not removed by the two dielectric mirrors in (c). In Figure 2-5 is also shown a side–view of the doubling crystal and the D–shaped mirror. The angle in the scheme is amplified; however, in the set–up the visible light passes on the edge of the D–shaped mirror and the generated UV is reflected near the edge, minimizing the beam–height variation.

Finally a thin silica window (**f**) is used to pick-up a small percentage of the pump light intensity that is sent on a photo-diode (PD). This is used as a diagnostic for the pump intensity but also to define the presence of the pump onto the sample (parity), which is necessary for the pump-probe measurements.

When the pump wavelength is set in the visible region (directly using the Topas-White output), the BBO crystal is removed and protected silver coated mirrors (Thorlabs, PF10-03-P01) are used instead of dielectric mirrors. In the case of visible pump light the IRF is shorter (reaching values of 40-50 fs) because of the larger band-width with respect to the UV case.

2.1.1.4 The detection system

As mentioned above, the probe pulses are focused into a 100 μm multi-mode fiber after the interaction with the sample. The probe pulses are then sent into a 0.25 m imaging spectrograph, where they are dispersed by a 150 grooves per mm holographic grating and imaged onto the detector. Two different detectors have been used in the set-up: the first was a Hamamatsu S11105 and the second was a Hamamatsu S10453. The Hamamatsu S11105 is a multichannel detector consisting of a 512 pixels (pixel size: 12.5 x 250 μm) Complementary Metal-Oxide Semiconductor (CMOS) linear sensor. This CMOS allows reading out each pixel up to 50 MHz (meaning 100 kHz per spectrum) with a read out noise of 3 mV rms over a saturation output of 1.5 V. The signal obtained from the detector is read by a fast 14 bits ADC (Spectrum M2i.4022, 4 parallel operating channels) and then processed by a Lab Windows acquisition program developed in our group.

The Hamamatsu S10453 is still a multichannel detector with 512 pixels CMOS linear sensor, but the pixels have a larger surface (20 x 500 μm). The maximum read out rate for each pixel is 10 MHz, leading to a maximum reading rate per spectrum of 20 kHz. However, the bigger pixel size brings the advantage of detecting a larger spectral region (~250 nm against ~150 nm of the former) even if losing in spectral resolution. Moreover, the Hamamatsu S10453 has better noise performances displaying a noise level of 1.1 mV rms over a saturation output of 3.2 V.

2.1.1.4.1 Noise considerations

As explained in the previous chapter, in transient absorption experiments are detected very small changes in the absorption spectrum (in the order of 1% or less). For this reason, reducing the experimental noise is crucial in order to obtain a good signal-to-noise ratio (S/N), as previously reported by Moon.[115]

In the experiments considered in this work there are two main sources of noise, namely the laser's energy fluctuations and the detection noise. The energy fluctuations of the laser pulses start with the oscillator and propagate to the generation of pump and probe pulses. As mentioned above the oscillator is pumped by a CW Nd:YVO₄ laser, whose noise level is negligible. The most important source of noise in the amplifier is given by the three Q-switched pump lasers, whose noise level is ~0.3% rms each. The noise of each pump laser is independent, implying that the noise contribution can be calculated as the square root of the sum of the squared values as shown in equation (2.4):

$$(2.4) \quad Noise_{Ampl.} = \sqrt{\sum Noise_{pump}^2} = \sqrt{0.3^2 + 0.3^2 + 0.3^2} = 0.52 \% rms$$

The value obtained by equation (2.4) is then divided by the number of pump lasers, since they are three independent noise sources, thus leading to a final value of 0.17% rms.[28, 29] The result shows that, by pumping the crystal of the amplifier with three pump lasers, it is possible to introduce more energy on the system but getting a lower noise level than the sum of each pump laser's noise. This result can be still improved by running the amplifier in saturation, which allows gaining a factor of two on the amplifier's noise and leading to a value of ~0.1% rms. The noise introduced by the Topas-White is (from the manual) < 2.5% rms in the 530–700 nm region, while it raises to < 9% rms below 530 nm (depending on the stability of the input light). However, the latter values depend strongly on the noise of the laser seeding the Topas-White system. In our system we estimated that the noise of the Topas-White is typically 0.5% when operating at large bandwidth (200 nm) and < 0.3% when operating at narrow bandwidth (50 nm). Frequency doubling of the Topas-White output introduces more sources of noise, leading to a final noise level < 1%. Moreover, in a typical transient absorption experiment the noise level before and after time-zero is comparable,[28, 29] indicating that the pump pulses play a marginal role while the probe noise is the most important for the measurements. As mentioned above, the probe pulses can be obtained by achromatic doubling (when probing the UV region) or by generating a white-light super-continuum (when probing in the visible), and leading in both cases a probe noise level in the order of 1%.

The detection of the probe light is another source of noise, consisting of the electronic noise (EN independent of the signal intensity) and shot noise (statistical noise associated with measuring N photons). Photodiode arrays have been the typical choice for multi-channel detection, due to their typical saturation charge corresponding to the detection of $\sim 5 \times 10^8$ photons and readout noise of $\sim 10^4$ electrons, represented by the yellow solid line in Figure 2-7 (EN ≈ 10000).

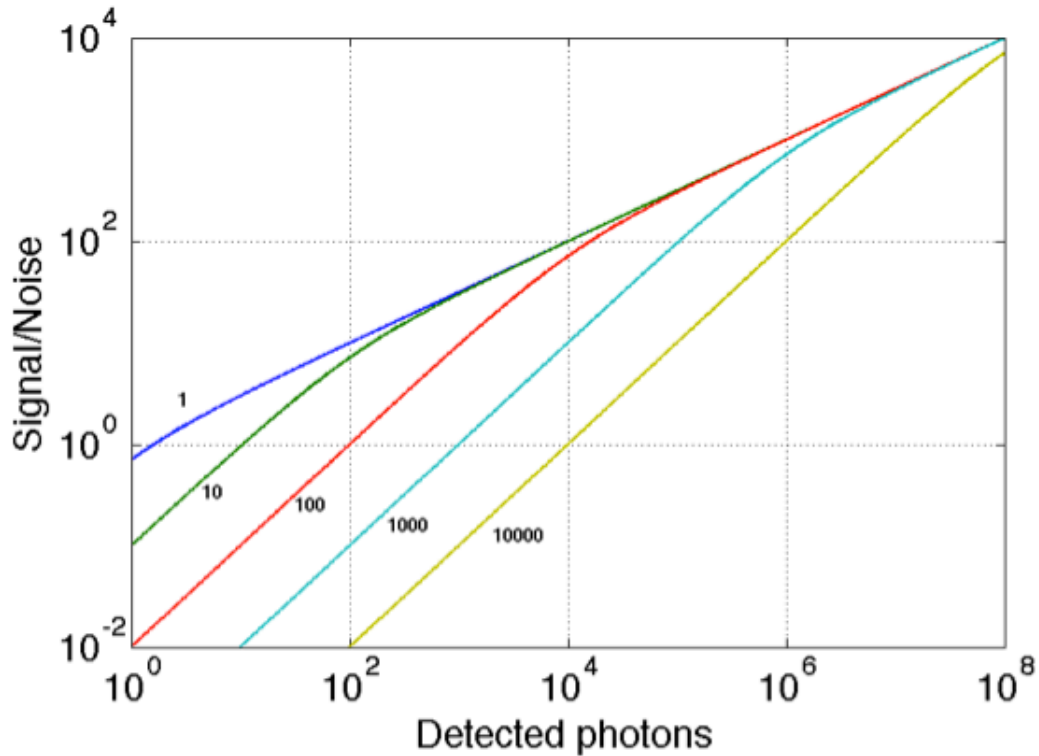


Figure 2-7 Detector limited signal to noise ratio as function of detected photons for different value of electronic noise (EN) (written near the curves). The EN = 1 represents the ideal detector while the detector used in our experiments has an EN = 2000.

The amount of photons detected by a diode array is three orders of magnitude bigger than the single pixel full well capacity of a CCD, which is in the order of $3\text{--}5 \times 10^5$ electrons and it is represented by the red solid line (EN ≈ 100) in Figure 2-7. A typical CCD detector has a readout noise of 1–10 electrons, thus performing better than photodiode arrays in low-intensity regimes, which is often the case when dealing with broadband probe pulses.

In the last decade CMOS have been strongly implemented, showing a saturation charge of $\sim 8 \times 10^5$ electrons and readout noise of ~ 2000 electrons rms. The detector used in the present version of the set-up (Hamamatsu S10453) has a saturation charge of $1.5\text{--}2 \times 10^6$ electrons and electronic noise of 690 electrons rms, with maximum pixel readout rate of 10 MHz, as shown in Figure 2-7 close to the solid turquoise line (EN ≈ 1000). To estimate the detection noise and the total noise of the set-up, it is important to take into account several parameters (e.g. electronic noise, shot noise and probe fluctuations) as shown in equation (2.5) and (2.6), respectively.

These equations allow understanding how the S/N can be improved in a given transient absorption system.

$$(2.5) \quad \text{Detection noise} = \sqrt{EN^2 + \text{shot}^2}$$

$$(2.6) \quad \text{Noise}_{\text{Tot}} = \sqrt{EN^2 + \text{shot}^2 + \text{probe noise}^2}$$

In fact, in time-resolved experiments it is important having the best S/N, which can be achieved in different ways: i) increase the number of measurements in order to remove the stochastic noise by averaging (increasing the repetition rate of the laser system decreases the time per acquisition, allowing more averaging) and ii) introducing a reference for the probe, which corrects for the energy fluctuations and shape changes of the probe spectrum. Averaging of M measurements increases the S/N, reducing the noise by a factor of \sqrt{M} (where M is the number of measurements) and it is always necessary. Contrarily, the presence of a reference beam is not always needed, but depends sensitively on the system itself. The use of a reference beam means dividing the intensity of the probe light in two arms, thus fewer photons on the main detector as well as the presence of another source of electronic noise (reference detector). Hence, in some cases the use of a reference deteriorates the S/N of the set-up. To determine whether or not a reference beam could improve the S/N in the above-presented 20 kHz set-up, we leave momentarily aside the pulse-to-pulse energy fluctuations of the probe light (probe noise in equation (2.6)) from the noise equation and express the shot noise in terms of number of detected photons. The S/N of a measurement of N photons is then given by equation (2.7):

$$(2.7) \quad \frac{S}{N} = \frac{N}{\sqrt{EN^2 + N}}$$

The addition of a reference implies a reduction of the number of photons arriving on the detector, since the same amount of probe light has to be used to illuminate two detectors. The signal in presence of a reference is calculated by subtracting the signals read by the two detectors. Since these events are statistically independent, the total noise will add again as the square root of the sum of each contribution squared. To evaluate the regime where referencing is useful, it is necessary to consider two limit cases, namely when $EN \gg \sqrt{N}$ and $EN \ll \sqrt{N}$. In the shot noise limited case, namely $EN \ll \sqrt{N}$, a 50% splitting of the probe beam means half of the signal light on the detector, thus increasing the noise by $\sqrt{2}$ per detector. The same noise will be present in the reference detector, implying that the S/N in the reference-corrected measurement will be half the S/N of the measurement without referencing.

When the readout noise is dominating, namely $EN \gg \sqrt{N}$, the S/N per detector is halved (since the noise is independent of the intensity) and combining the result for the two detectors leads to a decrease of the total S/N by a factor of $2\sqrt{2}$. Therefore, it is clear that introducing a reference is useful only if the shot noise of the source is $\gg 2$ times the detector noise. Beside this, Dobryakov *et al* [116] reported on the importance of a reference beam in pump–probe systems that use intense probe light.

To give an estimate of the detection noise in our case, we can take a value of N that is half the detector’s saturation value. This because the probe spectrum is usually not flat and, if using white–light super–continuum the amount of light in the bluest region of the spectrum has typically one or two orders of magnitude less in counts. Since the saturation of the Hamamatsu S10453 is 1.5×10^6 we can take an average value of $N = 10000$, which means that the shot noise will be $\sqrt{10000} \approx 100$, thus a relative shot noise of 1%. Since the noise level in the probe is typically $< 1\%$ and the introduction of a reference is useful only if the shot noise is at least twice the readout noise, our system does not need referencing. Therefore, in our system the use of referencing would only decrease the performances in terms of noise and the amount of detected light in the signal arm.

2.1.2 ULTRA beam–line at Rutherford Appleton Laboratory (RAL)

The ULTRA beam–line is based on a 10 kHz synchronized dual–arm fs and ps laser system that allows performing high–sensitivity time–resolved infrared and Raman measurements, being able to detect $\Delta OD = 10^{-5}$ in 1 s.[30] Briefly, two cryogenically cooled Ti:sapphire chirped pulse amplifier (Thales Lasers) are pumped by three 55 W Nd:YAG lasers and seeded from a single oscillator (Femtolaser, < 20 fs, > 50 nm bandwidth). One amplifier generates 40–80 fs, 0.8 mJ, 800 nm pulses at 10 kHz repetition rate, while the other delivers 1–3 ps, 0.8 mJ, 800 nm pulses at 10 kHz repetition rate. The timing between the output pulses of the two amplifiers is synchronized to < 50 fs through sharing the same oscillator source, while long–term drifts are removed by applying a slow feedback control on the ps amplifier cavity length. The shot–to–shot noise for both the fs and ps outputs is 1% rms energy. The output of the fs amplifier is divided in four portions to seed two fs OPAs, one fs NOPA, one fs Harmonic Generation (HG) and (< 10 μ J) to generate a white–light super–continuum. The output of the ps amplifier is divided in three parts to seed two ps OPAs and one ps HG. Two experimental stations are available for pump–probe measurements, in which the pump and probe beams are focused onto the sample with typical diameters of 100 μ m and 50 μ m, respectively.

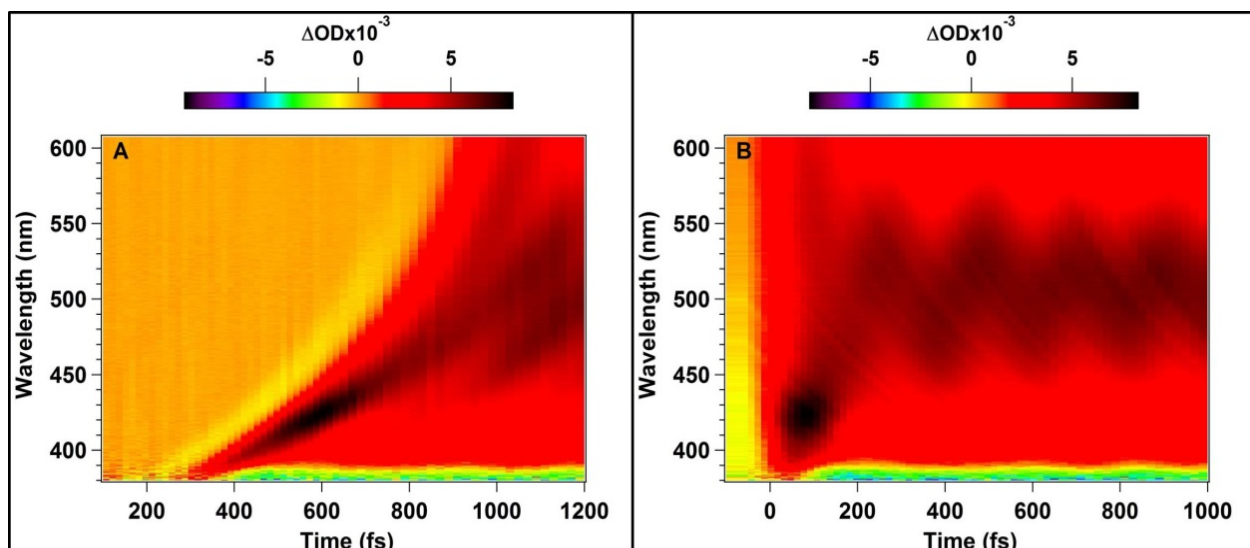


Figure 2-8 Example of GVD correction for a diplatinum complex (Pt(pop)). In (A) is displayed the t - λ plot as obtained from the experiments and in (B) is shown the GVD corrected plot.

The samples are placed in Harrick cells and, in order to avoid photo-damage, both flowing of the sample and rastering of the cell are applied. After passing through the sample the probe beam is sent into a 0.25 m spectrograph (DK240, Spectra Products) containing several diffraction gratings in order to control the spectroscopic window as well as the spectral resolution. The detection system is composed by three different detectors, in order to be able to probe spectral regions spanning from the UV to the IR: a Silicon (Si) array detector (512 pixels, Quantum Detectors, QD), an Indium-Gallium Arsenide (InGaAs) array detector (256 pixels, QD) and Mercury Cadmium Telluride (MCT) array detectors (128 and 64 pixels, IR Associates). When probing in the Mid-IR region, which is the case for the experiments presented here, two 128 pixels MCT detectors were used to detect the probe light and two 64 pixels MCT detectors were used as reference.

2.2 Data Treatment

As mentioned in previous paragraphs the probe pulses are spectrally resolved and detected allowing broad-band detection. The result is a matrix containing the transient signal vs time and wavelength (hereafter t - λ matrix). Due to the refractive index change inside the material each wavelength will move with its own speed through any transmissive optics (including the flow-cell and solvent, thus generating a Group Velocity Dispersion (hereafter GVD) and leading to a different time-zero for each wavelength as shown in Figure 2-8A. The GVD can be corrected after the experiment and after averaging of different scans (as shown in Figure 2-8B) by interpolating the time points in each wavelength column.

Since the GVD is due to the variation of the refractive index in the solvent as well as in the flow-cell material, it will be usually less severe in the IR region and will become more and more important while shifting the detection to the UV region. This effect can also be noticed by the curvature of the time-zero vs λ curve in Figure 2-8A, which becomes steeper as long as λ decreases. The second step in the data treatment is to retrieve the decay times of the different features present in the investigated spectral region. In order to retrieve the timescales two main methods, which lead to the same results, are widely used: Global Fitting (GF) of several kinetic traces and Singular Value Decomposition (SVD) of the entire data matrix.

The GF process implies the best-fit of several kinetic traces with a function obtained by the sum of exponential decay functions, which are convoluted with the experimental Instrumental Response Function (IRF) and multiplied by a Heaviside step function ($H(t)$), as shown in equation (2.8).

$$(2.8) \quad f(\lambda, t) = H(t) * (IRF \otimes \sum_i A_i(\lambda) \exp(-\frac{t}{\tau_i}))$$

The exponential decay functions present in equation (2.8), include the decay constant τ_i and the wavelength-dependent amplitude, which give information about the weight of the given τ_i at each wavelength. The amplitudes of each exponential decay functions can be plot as function of the wavelength in order to obtain the Decay Associated Spectra (DAS), allowing understanding the evolution of the spectral transient features on the τ_i timescale. However understanding the DAS could be complicated in presence of several spectral features. In general, the DAS obtained by an exponential decay τ is compared with a transient spectrum at delay time τ ; if the DAS shows the same sign of the transient spectrum at a given λ then the investigated feature is decaying, otherwise if the DAS has opposite sign the feature is rising.

When studying a system in which wave-packets are generated, equation (2.8) is not enough to describe the entire time-course, thus needing an exponentially damped sine function convoluted with the experimental IRF, as shown in equation (2.9).

$$(2.9) \quad f(\lambda, t) = H(t) * [IRF \otimes (\sum_i A_i(\lambda) e^{-\frac{t}{\tau_i}} + \sum_j A_j(\lambda) e^{-\frac{t}{\tau_{Dj}}} A_j(\lambda) e^{-\frac{t}{\tau_{Rj}}} \sin(\omega_j t + \phi_j))]$$

In this way it is possible to account for the population times, through the sum over “ i ”, and for the exponentially damped oscillatory pattern, through the sum over “ j ”. The damped oscillatory pattern is described by the $\sin(\omega t + \phi)$ multiplied by the damping exponential (first exponential term inside the sum) and another exponential that accounts for the rise (second exponential inside the sum). The rising exponential is used only if the amplitude of the oscillatory pattern is increasing with time; when it is not necessary its amplitude is set to zero, removing it from the equation.

The SVD procedure uses the entire data matrix, reducing the fit dimensionality and acting as a noise filter.[117–119] This procedure starts from the data matrix $M(\lambda, t)_{m \times n}$ and it decomposes the latter in the product of three matrices, as shown in equation (2.10):

$$(2.10) \quad M(\lambda, t) = S_{m \times m}(\lambda) \times W_{m \times n} \times T(t)_{n \times n}^T$$

Two main conditions have to be fulfilled in order to have the SVD procedure working: i) the data matrix can be described by a discrete linear combination of terms and ii) the noise in the data has to be purely stochastic. Under these conditions the columns present in the $S(\lambda)_{m \times m}$ and $T(t)_{n \times n}^T$ matrices are known as singular spectra (also called “eigenspectra”) and singular kinetic vectors (also called “eigen-traces”) respectively. $W_{m \times n}$ is a diagonal matrix, thus having $w_{ij} = w_{ji} = 0$ while $w_{ii} \neq 0$. The diagonal entries are also called “singular values” and represent the contribution of each eigenspectrum (and the corresponding eigen-trace) to the data matrix. In the case of noise-free data there are N non-vanishing singular values, while the presence of noise acts as a perturbation of the latter and of the respective singular vectors.[117–119] The eigen-traces are then globally fit to retrieve the important timescales and thus the amplitudes can be used to obtain the DAS’s, as shown in equation (2.11):

$$(2.11) \quad DAS_k(\lambda) = \sum_k a_{ik} w_{ii} U_k(\lambda)$$

Where $U_k(\lambda)$ is the eigenspectrum related to the k -th eigen-trace. Both the GF and SVD procedures retrieve the same information; however, each of them has strong and weak points. The GF of several kinetic traces becomes increasingly computationally expensive, thus increasing the probability to get trapped in local minima of the used fitting function. Nevertheless, it can describe well changes in shape of transient features (narrowing and broadening) and it is necessary when fitting transient signals containing wave-packets.

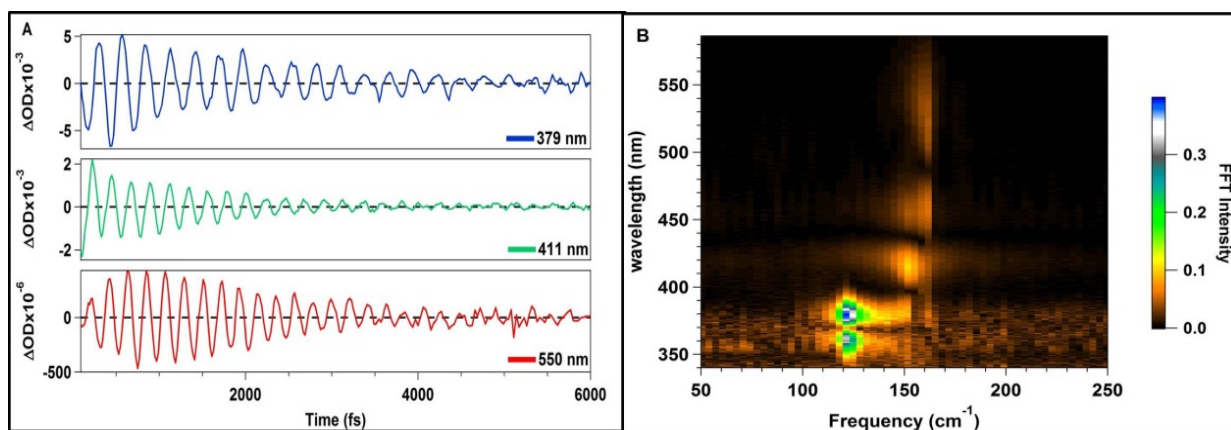


Figure 2-9 Example of oscillatory pattern at selected wavelengths after removal of the exponential decay (A) and final result of the FFT map (B). This dataset was taken from the results of Pt(pop) upon 360 nm photo-excitation.

On the other hand, the SVD suppresses stochastic noise and it is computationally less expensive but it has several drawbacks: i) the shifts of transient features are not well describe; ii) kinetics with weak amplitude can be mixed with the noise and; iii) oscillatory patterns are not well described. In the presence of oscillatory patterns the GF of relevant kinetic traces become immediately computationally expensive, requiring up to one day converging on the result. Moreover, the big amount of parameters in the fitting function increases sensibly the probability of trapping in local minima.

The SVD procedure is limited in this case, implying the possibility to obtain wrong results. In order to double-check the retrieved central frequencies and to know the wavelength at which every frequency is appearing, a Fast Fourier Transform (FFT) map can be used. This method is based on three steps: i) removing the oscillatory pattern (e.g. by smoothing the data or performing an SVD and reconstructing the data matrix only with exponential decays); ii) subtract the exponential decays from the original data matrix and iii) performing an FFT for each wavelength along the time axis. Figure 2-9A shows a set of kinetic traces obtained after removal of the exponential decay from the transient signal of Pt(pop), in order to be sure of the sole presence of the oscillatory pattern. In Figure 2-9B is displayed the FFT map, showing the presence of FFT peaks as function of wavelength and frequency.

By comparing the results obtained by the two methods we can highlight some important points: i) GF of selected kinetic traces gives information on both the frequency of the oscillation and its damping time, but it is a computationally expensive and long process (simultaneous fit of the population and coherence times); ii) the FFT map is less time consuming and less computationally expensive, giving a map of the frequencies as function of the wavelength, but it

does not supply any information on the damping times of the observed frequencies; and iii) the FFT map allows an immediate recognition of the wavelength range in which an oscillatory pattern is present. Therefore, we see GF of single kinetic traces and FFT map as two complementary methods to obtain information on the oscillatory pattern present in TA results. Hence, both approaches will be used in the analysis of wave-packets, as it is shown in the case of Pt(pop) and Pt(pop)-BF₂ reported in Chapter 3.

Chapter 3

3 Solvent and ligand effects on Pt(pop) intramolecular relaxation

This chapter focuses on both solvent and ligand effects on the ISC timescales in Pt(pop). After a brief introduction on Pt(pop) and bimetallic complexes (Section 3.1), we analyze the static spectra of Pt(pop) in different solvents (Section 3.2). To investigate the solvent dependent ISC (Section 3.3), we compare the results of TA experiments of Pt(pop) dissolved in acetonitrile (MeCN) and water (at two different excitation wavelengths). Our experimental results are then compared with previous ones, in which Pt(pop) was dissolved in Ethanol (EtOH), Ethylene Glycol (Et-Gly) and Dimethylformamide (DMF). Section 3.4 is entirely dedicated to the ligand dependence, comparing the TA results of Pt(pop) in MeCN with the ones of the perfluoroborated derivative Pt(pop)-BF₂. The latter possesses a stiffer *pop* cage that shows a weaker interaction with the solvent due to the BF₂ bridges binding the terminal oxygen atoms. The obtained results are used together in Section 3.6 to propose a photo – cycle for both Pt(pop) and Pt(pop)-BF₂.

3.1 d⁸ – d⁸ complexes and Pt(pop): an introduction

Understanding the intramolecular energy relaxation pathways of metal complexes and how they are affected by the environment is crucial for applications in chemistry, biology, solar energy conversion and luminescent materials. In this respect, bimetallic Pt^{II}, Rh^I and Ir^I d⁸-d⁸ complexes are particularly interesting due to their remarkable photo-chemical and photo-physical properties.[2, 120–123] In these complexes, the HOMO is an anti-bonding d-σ* orbital while the LUMO is a p-σ bonding orbital along the intermetallic axis (see Figure 3-1).[120, 121] Thus, the photo-induced HOMO → LUMO transition generates a highly reactive biradical complex with a σ-bond between the two metal ions, which can exist in both its singlet or triplet state.[2, 120–122, 124, 125] The lowest excited singlet state (¹A_{2u}) of these complexes undergoes ISC to the lowest excited triplet state (³A_{2u}) with near unity quantum yield [126] on the ps timescale.[52, 127] The biradical character of the ³A_{2u} state and its long life-time (from 30 ns to several μs [121]) make it reactive and capable of abstracting non-acidic hydrogens from alcohols,[128] hydrocarbons [129–131] and organo-silanes,[129] as well as halogens from organic halides.[128, 132]

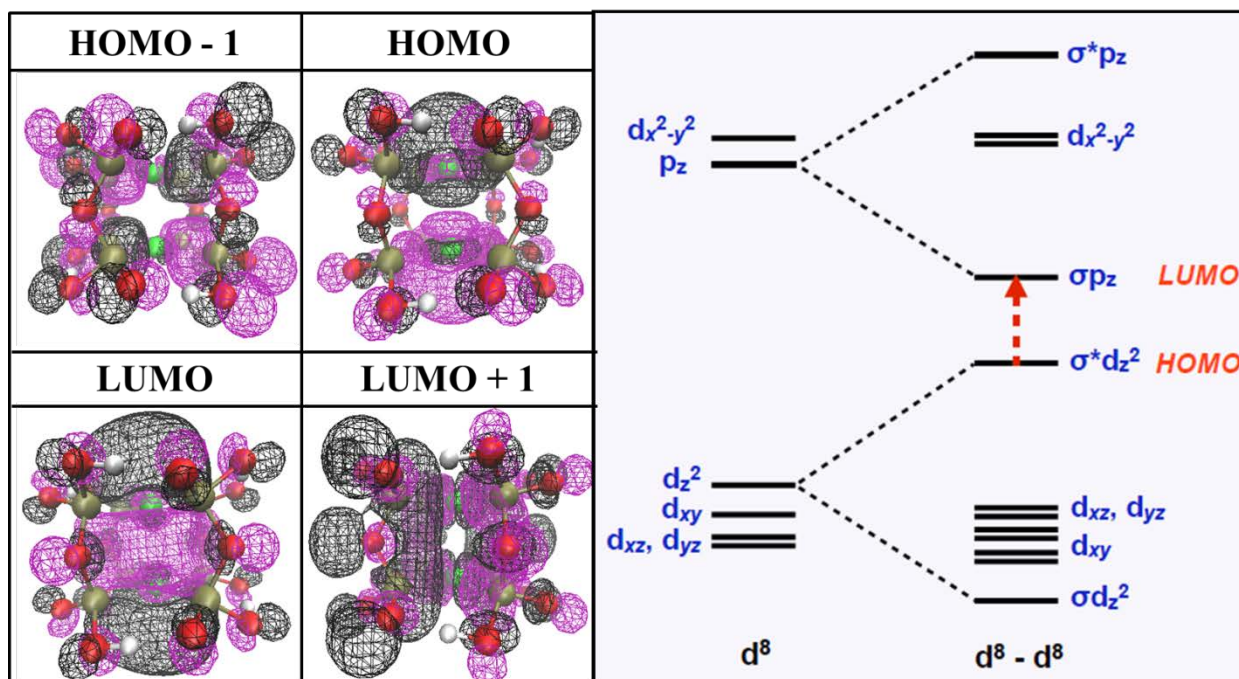


Figure 3-1 shows a qualitative molecular orbital diagram for a $d^8 - d^8$ complex resulting from the interaction of the two face - to - face square planar d^8 ions. The z - direction is along the Metal - Metal axis and the red arrow represents the HOMO \rightarrow LUMO transition. On the left side are shown the molecular orbitals of Pt(pop) simulated by Gloria Capano with the DFT method, using the B3LYP exchange and correlation function and the TZVP basis set. Relativistic effects were described by the ZORA scalar method, while the solvent was included using the implicit COSMO model. In the structure the oxygen atoms are depicted in red, the phosphorous atoms in silver, the hydrogen atoms in white and the platinum atoms in green. The negative regions of the wavefunction are depicted in black while the positive are illustrated in purple.

In the case of the di-platinum complexes, this high triplet state reactivity is thought to be crucial for the photo-catalytic implementation of H_2 production from alcohols.[1] Among all the d^8-d^8 complexes Pt(pop) is the most studied, since its synthesis [120, 125, 133] is easier than Rh^I and Ir^I complexes.[125] As shown in Figure 3-1 (and in Figure 3-2C) Pt(pop) consists of two PtP_4 parallel planes, held together by four bridging oxygen, and eight terminal $P(O)(OH)$ moieties, which are strongly exposed to the solvent and can actively participate in hydrogen bonding. In Figure 3-1 is represented a qualitative molecular orbital diagram for a generic d^8-d^8 complex, which arises from the interaction of two face-to-face square planar d^8 metal complexes. Figure 3-1 shows also the simulated frontier molecular orbitals of Pt(pop) in ethanol, displaying the anti-bonding character of the HOMO and the σ -bonding character of the LUMO. Beside these, also the HOMO-1 and LUMO +1 are shown in Figure 3-1, showing the importance of the ligand together with the negligible amplitude on the Pt ions.

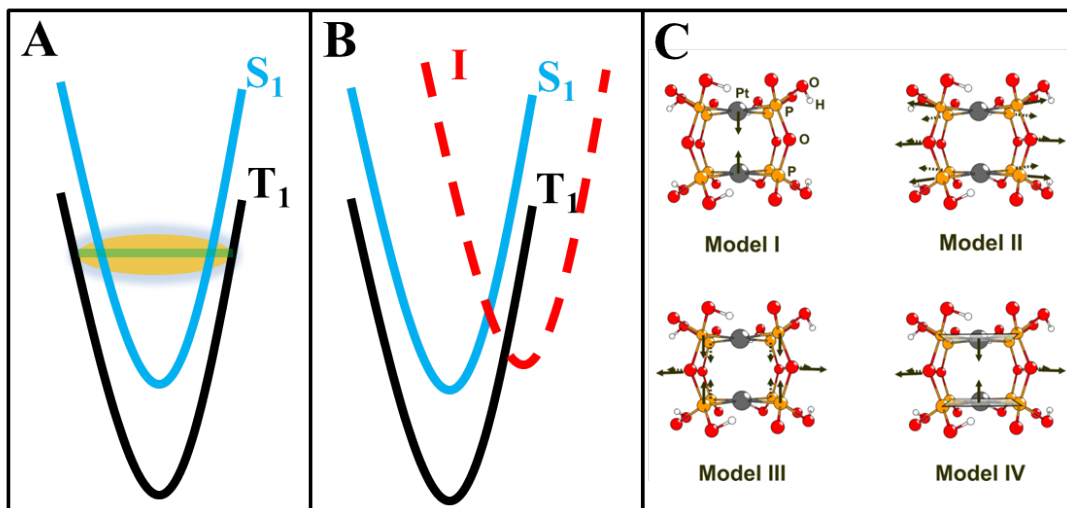


Figure 3-2 Scheme of the two possible pathways for the ISC process from S_1 to T_1 in Pt(pop). In (A) a region of strong electronic coupling induced by the excitation of low-frequency skeletal modes could allow the ISC between the S_1 and T_1 states and in (B) a third state (addressed as I), shown as a dotted red line, acts as an intermediate in the ISC process. In (C) are shown some models that account for different deformations, as can be seen by the arrows. Model I shows only the displacement of the Pt ions, Model II and Model III show different cage distortions and Model IV displays a concerted motion of the PtP4 plane with the bridging oxygens. Panel (C) is reproduced from ref. [138].

Analysis of Pt(pop) low temperature absorption and emission Frank–Condon progressions,[134–136] showed Pt–Pt stretching frequencies of 120 cm^{-1} , 150 cm^{-1} and 155 cm^{-1} for the $^1A_{1g}$ ground state and the $^1A_{2u}$ and the $^3A_{2u}$ excited states, respectively. Beside these strong amplitude modes, also a weak 40 cm^{-1} mode was reported, which was assigned to the *pop* cage deformation.[134] The results of the Frank–Condon analysis also showed a contraction by 0.21 \AA of the Pt–Pt bond distance for the excited states ($^{1,3}A_{2u}$) relative to the equilibrium value of 2.92 \AA for the ground state, suggesting that the singlet and triplet ($^{1,3}A_{2u}$) states have nested parallel potential curves along the Pt–Pt coordinate, as shown in Figure 3-2. These trends were confirmed by recent time–resolved X–ray absorption experiments, showing an additional 0.01 \AA expansion of the *pop* cage in the triplet state.[52, 137, 138] The latter expansion goes hand in hand with the weak 40 cm^{-1} mode, that was addressed as one of the possible mechanisms inducing ISC in Pt(pop), as shown in Figure 3-2A.

Milder and Brunschwig [127] investigated in detail the solvent and temperature (T) dependence of the $^1A_{2u} \rightarrow ^3A_{2u}$ ISC in Pt(pop), by means of ps time–resolved fluorescence.

They described the non-radiative decay of the system with a two-channel expression, as shown in equation (3.1).

$$(3.1) \quad k_{obs} = k_0 + k(T) = k_0 + \frac{A}{\sqrt{RT}} \exp\left(-\frac{E_a}{RT}\right)$$

Where k_0 is the weak coupling temperature-independent contribution and $k(T)$ is the strong coupling temperature-dependent contribution, in which $A = (H_{AB}^2 \pi^{1/2})/(\hbar\lambda^{1/2})$ and $E_a = (\Delta E + \lambda)^2/4\lambda$. In the expressions of the amplitude and the activation energy, H_{AB} is the electron coupling between involved states, ΔE the energy difference between the two states and λ is the total reorganization energy. They found $k_0 \approx 1.5 \times 10^{-9} \text{ s}^{-1}$, which was assigned to the direct $^1A_{2u} \rightarrow ^3A_{2u}$ ISC assisted by both intramolecular and solvent modes (sensitive to the protonation/deuteration state of the solvent). Indeed, direct spin-orbit coupling between the singlet and triplet states of Pt(pop) is symmetry forbidden.[136, 139] Furthermore, they reported values of the T-dependent rate ($k(T)$) in the $(10 \text{ ps})^{-1}$ range at room temperature, which reflect a strong coupling case. They proposed that this ISC rate is mediated by a first $^1A_{2u} \rightarrow ^3B_{2u}$ ISC, which needs to overcome a barrier (as shown in Figure 3-2B), followed by an ultrafast $^3B_{2u} \rightarrow ^3A_{2u}$ IC. Interestingly, the reported T-dependent ISC rates are 2–3 orders of magnitude slower than in other transition metal complexes, such as $M^{II}(\text{bipy})_3$ ($M = \text{Fe, Ru}$ and bipy = 2,2' - bipyridine),[53, 55] Re^I carbonyl-diimine complexes,[48, 51, 57, 140] or mono-Pt^{II} acetylides.[74]

In a recent study, using ultrafast fluorescence and TA measurements, we reinvestigated the solvent dependence of the ISC in solution at 300 K,[52] finding times ranging from 30 ps in Ethylene glycol to 11 ps in DMF (see Table 3–1 in Section 3.3).[52] In this case, the T-independent rate is overwhelmed and the same mechanism as described by Milder and Brunschwig [127] should be operative. Our study also revealed a rich wave packet pattern due to the Pt–Pt vibration, which is created by the impulsive bond formation upon excitation from the HOMO to the LUMO. The demonstration of wave-packet upon impulsive bond formation in Pt(pop) triggered several ultrafast studies on other d^8 – d^8 complexes. Cho *et al* [141] investigated the di-platinum complex $[\text{Pt}(\text{ppy})(\mu\text{-tBu}_2\text{pz})_2]$ (ppy = 2-phenyl pyridine and $\mu\text{-tBu}_2\text{pz}$ = 3,5-di-terButyl pyrazolate) by anisotropy TA, finding Pt–Pt wave packet oscillations in opposite phase for parallel and perpendicular polarization. They also reported a much faster ISC time than Pt(pop) ($< 150 \text{ fs}$), while the dephasing time of the wave packet was found to be 2.4 ps. The latter observations were explained by the occurrence of two energetically close and strongly coupled singlet and triplet states.

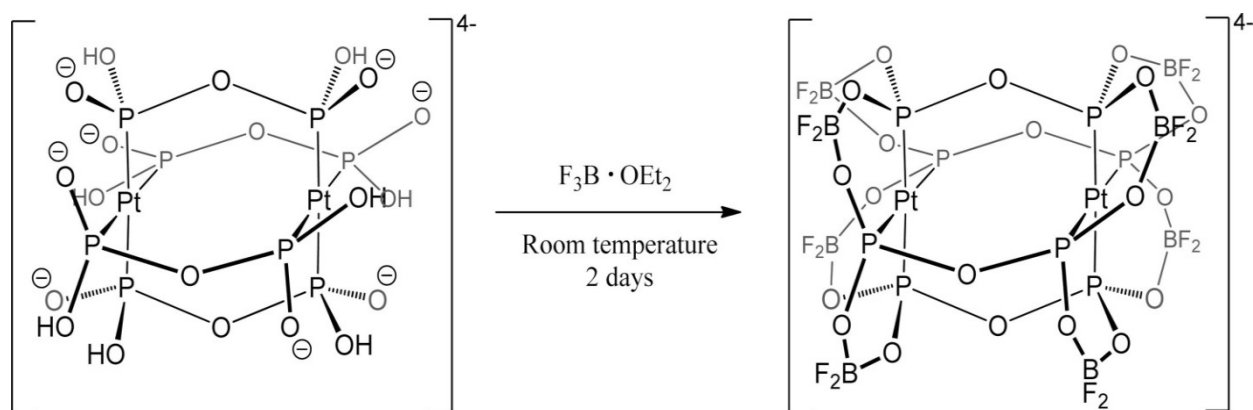


Figure 3-3 Synthesis of Pt(pop)-BF₂ with the structures of both Pt(pop) and Pt(pop)-BF₂. This Figure was reproduced from ref. [3]

In this case the wave packet bounces back and forth between the two states (followed by an IC to the lowest triplet state [141]), with the anisotropy arising from the different nature of the ESA transitions from the singlet and the resonant triplet state. This picture is fully consistent with the Milder and Brunschwig's hypothesis of an ISC mediated by the ³B_{2u} state.[127] Hartsock *et al* [142] investigated the [Ir₂(dimen)₄]²⁺ (dimen = 1,8-diisocyno-p-menthane) complex by ultrafast TA and Density Functional Theory (DFT). From the wave-packet patterns they concluded that it possesses two singlet ground state isomers in solution at room temperature. The latter results were recently confirmed by quantum mechanics/molecular mechanics (QM/MM) multiscale MD simulations by Dohn *et al* [143]

Recently, Durrell *et al* [3] functionalized Pt(pop) with bridging BF₂ groups between the terminal oxygen atoms in the P(O)(OH) moieties (Pt(pop)-BF₂), whose synthesis and structural sketches are shown in Figure 3-3. This perfluoroboration makes the ligand cage stiffer, thus reducing the capability of symmetry breaking and making the interaction with the solvent weaker. They found that the ¹A_{2u} radiative lifetime is prolonged by 3–4 orders of magnitude with respect to that of Pt(pop). Beside this, its T-independent (k₀) and T-dependent intersystem crossing (ISC) pathways are at least 18 and 142 times slower than those of Pt(Pop). The slowdown in the T-independent ISC channel was attributed to two factors: i) reduced spin-orbit coupling between the ¹A_{2u} state and the mediating triplet (³B_{2u}), owing to increases of Ligand-to-Metal Charge Transfer (LMCT) energies (see bands at 315 nm, 285 nm and 246 nm in Figure 3-4B) relative to the excited singlet and; ii) less access to solvent, which reduces dissipation of the excess energy to solvent vibrational modes.

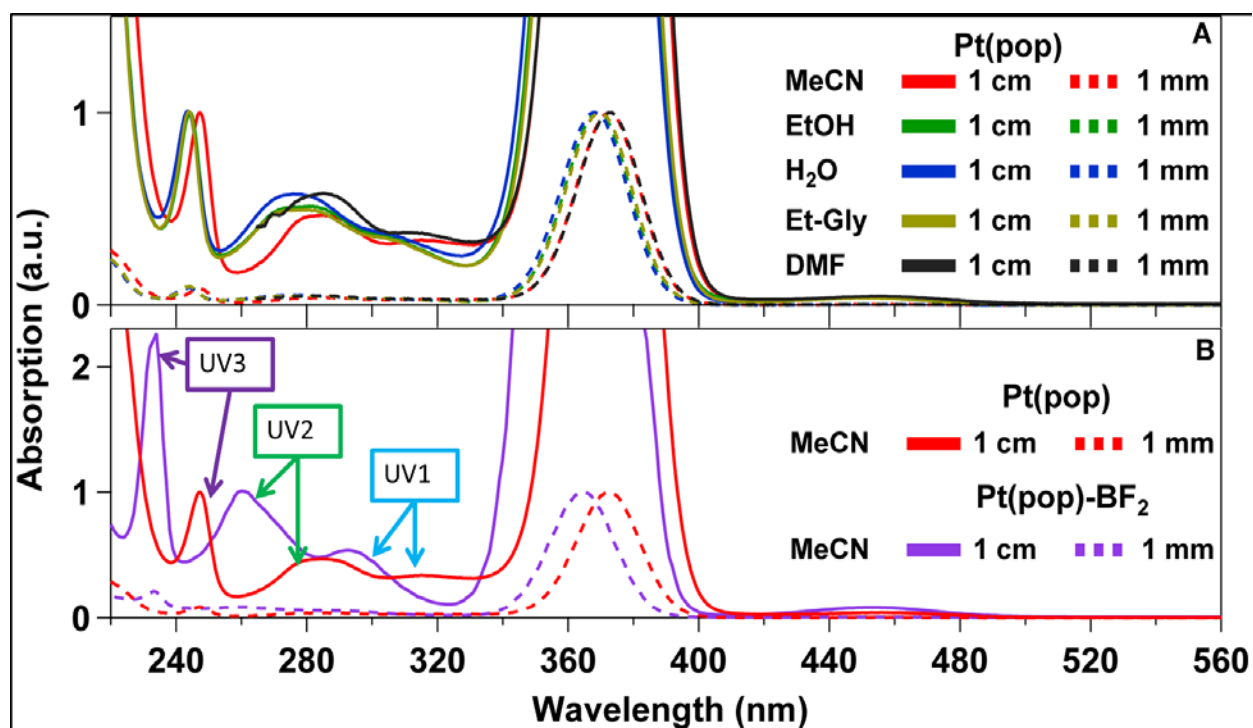


Figure 3-4 Static absorption spectra of Pt(pop) in different solvents (A) in both 1 cm and 1 mm cuvettes, to highlight strong and weak absorption bands. The spectra were normalized on the 360 nm band for the 1 cm path and on the 250 nm band for the 1 mm path. In (B) is shown the comparison between Pt(pop) and Pt(pop)-BF₂ spectra in acetonitrile; again the 1 cm path spectra were normalized on the 360 nm band while for the 1 mm path the intensity of the 260 nm band of Pt(pop)-BF₂ was normalized to the 230 nm band of Pt(pop).

Given the role of the $^3B_{2u}$ state in mediating the room temperature (RT) ISC process and its suspected solvent- and ligand-dependence, here we complement our previous study [52] by an ultrafast UV pump-Visible probe TA study on Pt(pop) and Pt(pop)-BF₂ dissolved in acetonitrile (MeCN) and water. By exciting at different wavelengths, we investigate the effect of excitation energy (of the $^1A_{2u}$ absorption and the UV bands) on the relaxation mechanisms leading to the population of the lowest excited triplet states $^3A_{2u}$ state. We find that, upon excitation of the UV bands of both complexes, the lowest triplet state is promptly populated, while the singlet state is largely bypassed. The present and previous results and those of the literature can now be rationalised by the solvent-shifts of the $^3B_{2u}$ state.

3.2 Steady state spectra

Figure 3-4 shows the UV-visible absorption spectra of Pt(pop) dissolved in various solvents (A) and Pt(pop)-BF₂ dissolved in acetonitrile (MeCN) (B). The spectra are characterized by an intense band centred around 360-370 nm, due to the strongly allowed d- σ^* \rightarrow p- σ transition ($^1A_{1g} \rightarrow ^1A_{2u}$), and a weak band around 440-460 nm, due to the $^1A_{1g} \rightarrow ^3A_{2u}$ transition.[121, 132, 144]

Table 3–1 Summary of the central frequency ($\bar{\nu}_c$) of S₁, T₁, UV1 and UV2 bands for Pt(pop) dissolved in several solvent, together with their shift ($\bar{\nu}_s$) with respect to Pt(pop) dissolved in MeCN. The last column displays the ISC times for Pt(pop) in the mentioned solvents.

Solvent	S ₁ cm ⁻¹		T ₁ cm ⁻¹		UV1 cm ⁻¹		UV2 cm ⁻¹		τ_{ISC} (ps)
	$\bar{\nu}_c$	$\bar{\nu}_s$	$\bar{\nu}_c$	$\bar{\nu}_s$	$\bar{\nu}_c$	$\bar{\nu}_s$	$\bar{\nu}_c$	$\bar{\nu}_s$	
Ethylene Glycol	27027	181	22075	169	32787	1341	36232	1144	30.3
Ethanol	27100	254	22173	267	32787	1341	36166	1078	25.6
Water	27174	328	22100	194	32680	1234	36298	1210	13.7
DMF	26810	36	21906	0	31949	503	34965	123	11.0
MeCN	26846	0	21906	0	31446	0	35088	0	0.7

The region below 320 nm is characterized by three bands that are significantly weaker than the singlet $^1A_{1g} \rightarrow ^1A_{2u}$ band, but about 5–10 times stronger than the $^1A_{1g} \rightarrow ^3A_{2u}$ transition, pointing to a partial dipole– and/or spin–forbidden character (labelled UV1, UV2 and UV3 in Figure 3-4B). Their assignment is still unclear: Stiegman *et al* [136] assigned them to $d\sigma^* \rightarrow d_{x^2-y^2}$ transitions (UV1 and UV2) and $d_{xz}, d_{yz} \rightarrow p\sigma$ transition (UV3, without specifying the spin state). In particular, the UV1 band (315 nm in Pt(Pop) dissolved in MeCN) was assigned to the $^1A_{1g} \rightarrow ^3B_{2u}$ transition. In the $^3B_{2u}$ state, the complex is expected to have significantly longer metal–ligand bond distances than in either the ground or the lowest two metal–centred (MC) singlet and triplet states. Theoretical studies [139, 145–148] identify the $^3B_{2u}$ state as a ligand–to–metal–metal–charge–transfer (LMMCT) due to a $p_{x,y} \rightarrow p_z$ transition, but it lies at much lower energy and has a negligible oscillator strength.[145] The next state of any appreciable oscillator strength in this region (about 25 times weaker than the $^1A_{1g} \rightarrow ^1A_{2u}$ band, i.e. on the order of what we observe in Figure 3-4) is the singlet equivalent of the above 3LMMCT transition, and its energy coincides well with the UV1 band. All the states calculated between the singlet and triplet LMMCT states have the same LUMO, which shows significant electron density exposed towards the solvent. Figure 3-4A shows the absorption spectrum of Pt(pop) in different solvents (investigated here and in ref. [52]), which displays a significant shift to the blue of the UV bands in water, ethanol and ethylene glycol (all protic solvents) compared to MeCN and DMF. Beside this, the singlet and triplet transitions show less significant shifts in the various solvents due to the fact that these transitions involve orbitals that are less exposed to the solvent, unlike the UV ones that involve ligand centred orbitals (see Table 3–1).

In the case of Pt(pop)–BF₂ (Figure 3-4B) the singlet and triplet transitions lie higher in energy (0.07 eV and 0.04 eV, respectively) than those of Pt(pop) in the same solvent; fact that is even more significant in the UV bands, showing typical shifts of ~0.3 eV. While this shows the solvent sensitivity of the UV bands, and therefore their proposed LMMCT character in both complexes,[139, 145–147] the shifts cannot be easily rationalised in terms of the physical properties of the solvents.

3.3 Solvent dependence

3.3.1 Sample preparation

The experiments presented in the following paragraphs were performed in different conditions if exciting at 360 nm (¹A_{2u} band) or at 270–280 nm (UV2 band).

For 360 nm excitation experiments Pt(pop) was dissolved in high–grade acetonitrile, obtaining a concentration of ~0.9 mM, and the solution was flowed with a gear pump through a 100 μm–thick jet. For 270–280 nm excitation (270 nm for Pt(pop) in water and 280 nm for Pt(pop) in MeCN) the Pt(pop) was dissolved in milliQ water or high–grade acetonitrile, respectively, obtaining a concentration of ~4.5 mM. The sample was then flowed in a 200 μm–thick thin window flow–cell.

For all the experiments the sample concentration were chosen to have absorption of ~0.3 OD at the excitation wavelength. The pump fluence was set to ~1.2 mJ/cm² and the probe polarization was set at the magic angle with respect to the pump one.

3.3.2 Experimental results

On the left side of Figure 3-5A is shown the t – λ plot of Pt(pop) upon 360 nm (¹A_{2u} band) excitation in MeCN, while on the right panel are displayed the kinetic traces at selected wavelengths. The main features of the TA are identical to those of previously reported studies:[52] i) a Ground State Bleach (GSB) centred at 372 nm, which shows a strong oscillatory pattern due to a vibrational wave–packet of the Pt–Pt stretch mode generated by Impulsive Stimulated Raman scattering (ISRS); ii) Stimulated Emission (SE, centred at ~400 nm) and; iii) the Excited State Absorption (ESA) due to the ¹A_{2u} state, which consists of two main regions: from 440 nm to 500 nm (ESA_{S1}) and below 350 nm (ESA_{S1}), due to the ¹A_{2u} state. It also exhibits coherent oscillations due to a wave–packet of the Pt–Pt stretch mode; iv) the ESA due the triplet ³A_{2u} state (ESA_T), which we had assigned to transitions from the ^{1,3}A_{2u} states to the ^{1,3}E_g ones (described by the electronic configuration (5d_{xz} 5d_{yz})⁷(6pσ)¹).[52]

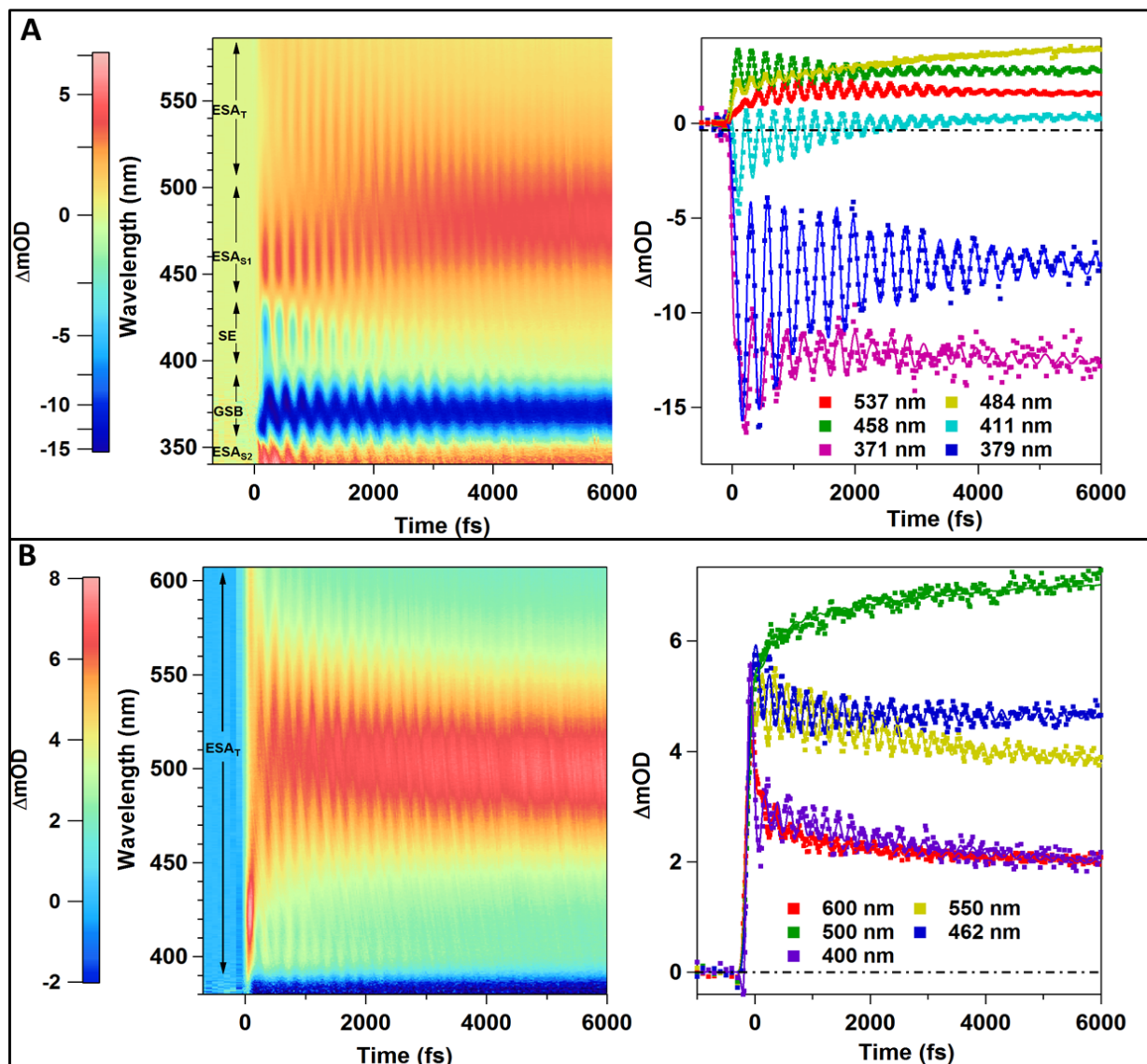


Figure 3-5 In (A) are shown the t - λ plot and kinetic traces at selected wavelengths of Pt(pop) in MeCN upon 360 nm excitation. In (B) are shown the t - λ plot with selected kinetic traces of Pt(pop) in MeCN upon 280 nm excitation.

We observe that right after time-zero only the ESA_S is present, but within few 100's fs, the ESA_T signal grows in, along with coherent oscillations. This is also clear from the time traces at 537 nm and 458 nm in Figure 3-5A (right). On the same time-scale, the SE decreases in intensity indicating a depletion of the $^1A_{2u}$ state, which is not accompanied by a recovery of the GSB. By ~ 5 ps, the $^1A_{2u}$ state is completely depopulated due to ISC, as can be seen also in the transient spectra shown in Figure 3-6A. The very short ISC time, compared to those reported in ref. [52], highlights once again its strong solvent dependence (see Table 3-1). A GF analysis was performed, in order to retrieve the time-constants along with the coherence times and the frequencies of the oscillatory pattern.

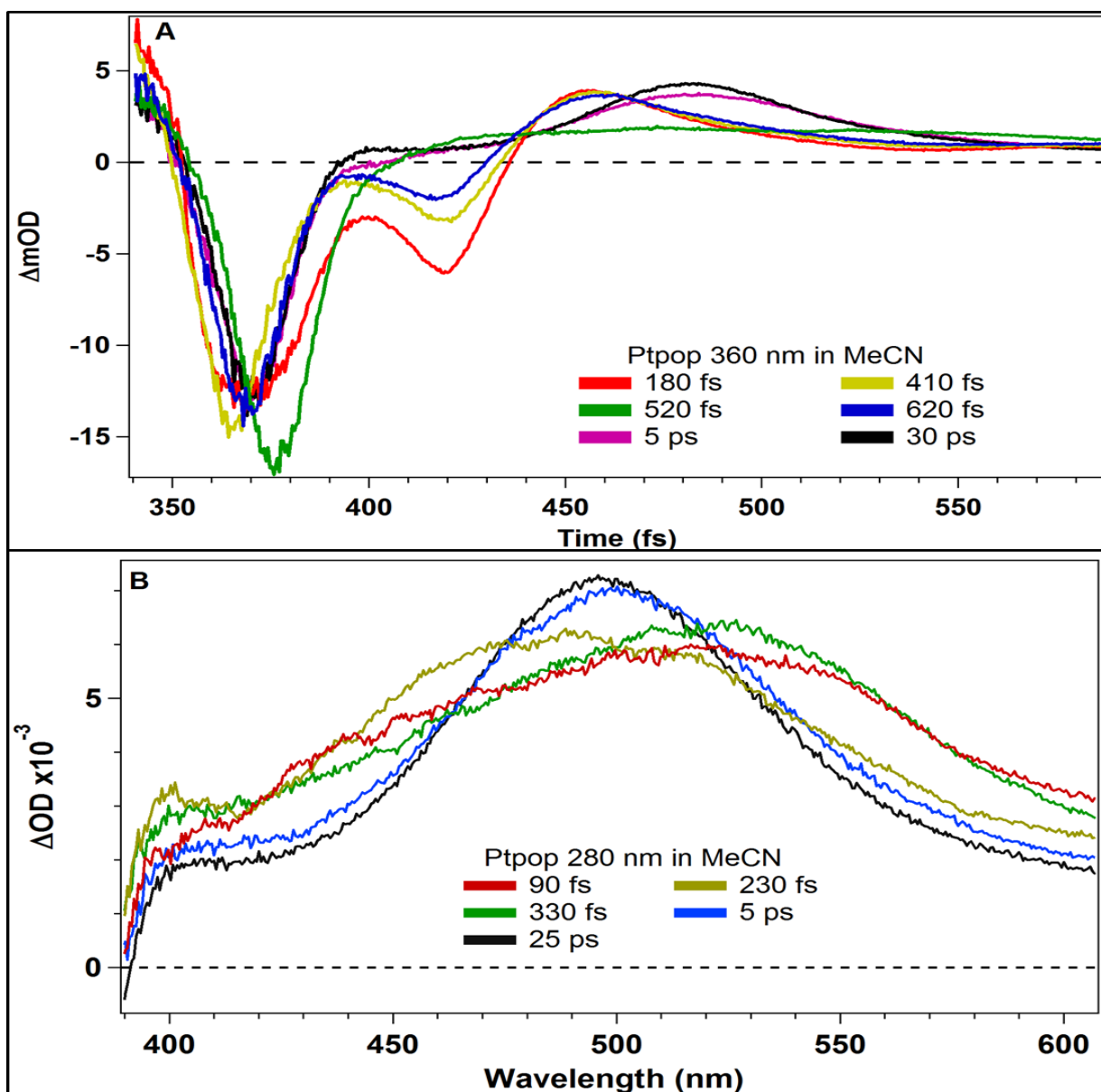


Figure 3-6 Transient spectra of Pt(pop) at selected time - delays upon 360 nm (A) and 280 nm (B) excitation. The wavelength scale in (A) is wider with respect to the one in (B) because in the latter the GSB region was blurred due to the high sample concentration.

Figure 3-5A (right) shows the fits, obtained using a tri-exponential function with three damped sine functions, all convoluted with the experimental IRF. The GF was performed letting all values as free parameters (except for the infinitely long component that was fixed to 500 ps). The fit parameters are summarized in Table 3-2 and in Table 3-3 (Section 3.5), in order to give an overview of the obtained timescales as function of solvent and ligand. In particular, population times of 700 ± 100 fs, 3.8 ± 0.4 ps (and 500 ps) are retrieved. We assigned the first value (700 fs) to the ISC time, due to the disappearance of the SE feature, and the second one (3.8 ps) to the vibrational relaxation in the ${}^3A_{2u}$ state. The former agrees with the rise time of the coherent oscillations in the ${}^3A_{2u}$ state (τ_R) of 900 ± 90 fs.

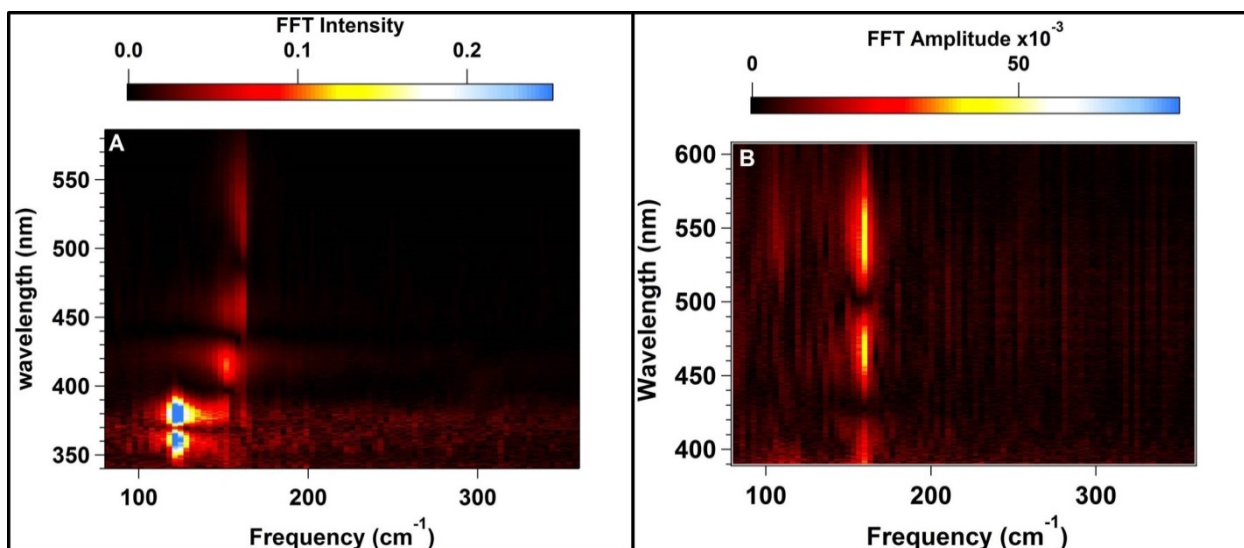


Figure 3-7 FFT map for Pt(pop) upon 360 nm (A) and 280 nm (B) excitation. The plot identifies the wavelengths at which a given frequency is present.

The retrieved oscillation frequencies agree with those of refs. [52, 124, 135, 136], but in addition we now extract the frequency in the triplet state, which is slightly larger than that of the singlet state (Table 3–3). The frequencies were further cross-checked by a Fourier Transform analysis, through which we obtained a λ - ν plot, as shown in Figure 3-7A. The oscillation period of the $^1A_{2u}$ state (223 fs) is shorter than the ISC time, thus the coherence transfer appears as a leakage of population over several cycles on the 800–900 fs rise of the oscillation in the triplet state.

In Figure 3-5B (left) is shown the t - λ plot of Pt(pop) upon 280 nm (UV2 band) excitation, which is much simpler than upon 360 nm excitation (Figure 3-5A): the GSB feature is not well reproduced because of the strong absorption of probe light by the sample (higher concentration and thicker cell used for these measurements, thus the GSB region is left outside the plot). It is important to note the absence of the SE feature, indicating that, upon 280 nm excitation, the $^1A_{2u}$ state is not populated (or only at a very small yield to be detectable). The signal is dominated by the $^3A_{2u}$ ESA band (centred at 500 nm), which appears promptly as seen also in the kinetic traces shown in Figure 3-5B right. This observation implies that the UV2 \rightarrow $^3A_{2u}$ relaxation occurs within the IRF of the measurement (< 80 fs); moreover the $^3A_{2u}$ state is in a vibrationally hot state, as can be seen from the evolution of the transient spectra shown in Figure 3-6B. Although the UV2 band lies ~ 1.6 eV higher than the triplet absorption (see Table 3–1) and the singlet state is bypassed, wave-packet oscillations still appear in the $^3A_{2u}$ state. Bypassing intermediate states is a rather uncommon behaviour in polyatomic molecules, where usually intramolecular relaxation proceeds in a stepwise fashion through all intermediate states; however, in the present

case coherence is preserved over a large energy gap (~1.6 eV, Table 3–1). In addition, the prompt rise of the triplet state population implies a very strong coupling of the initially accessed state (UV2) with the $^3A_{2u}$ state if the relaxation is direct. Alternatively, if it funnels via intermediate triplet states (possibly $^3B_{2u}$ is one of them), then these must have a strong coupling with the $^3A_{2u}$ state, but also with the initially populated UV2 state. Such strong couplings suggest that the UV2 state is a triplet state. It is interesting to observe that the signal starts quite intense around 400 nm, but quickly converges to the 500 nm centred band, around which the wave–packet oscillations can be clearly seen. This is also seen from the first peak of the kinetic trace in Figure 3-5B (right). The observed behaviour points to the passage of the wave–packet in this probe region, probably in the course of its downwards relaxation to the lowest triplet state.

By comparing the transient spectra at 25 ps upon 360 nm and 280 nm excitation (shown in Figure 3-6), it is possible to see that in the latter case the transient is red–shifted (peaking at 500 nm against 480 nm of the 360 nm excitation) and it is slightly broader. These observations hint to the presence of an appreciable excess vibrational energy that is slowly dissipated to the solvent. This slow relaxation is due to the ~1 eV energy difference between the two excitation energies and the isolation of the triplet ($^3A_{2u}$) state, which make the pathways for energy dissipation less efficient and pointing to a weak coupling of the Pt–Pt vibration to solvent modes in this state. The GF analysis with a tri–exponential function and only one damped sine function delivers the best fit as can be seen in Figure 3-5B right. The population times are 280 ± 30 fs 3.5 ± 0.3 ps and a non–decaying component, which reflect the presence of a primary cooling followed by a cooling time comparable with the 360 nm excitation. All the fit parameters are given in Table 3–2 and Table 3–3 in Section 3.5, while the mode frequencies are confirmed by the FFT analysis, as can be seen in Figure 3-7B.

The case of Pt(pop) in water under 360 nm excitation was already reported;^[52] however, here we revisit it under 270 nm (UV2 band, Figure 3-4A). Figure 3-8A (left) shows the corresponding t – λ plot. Just as above, the TA spectrum is dominated by the ESA_T feature (centred at ~475 nm) that appears within the experimental IRF and is accompanied by wave packet oscillations. More distinctly than in the previous case, we also observe the single passage of the wave packet in the 390–430 nm region prior to its localization in the triplet state, as also shown in the transient spectra of Figure 3-8A (right).

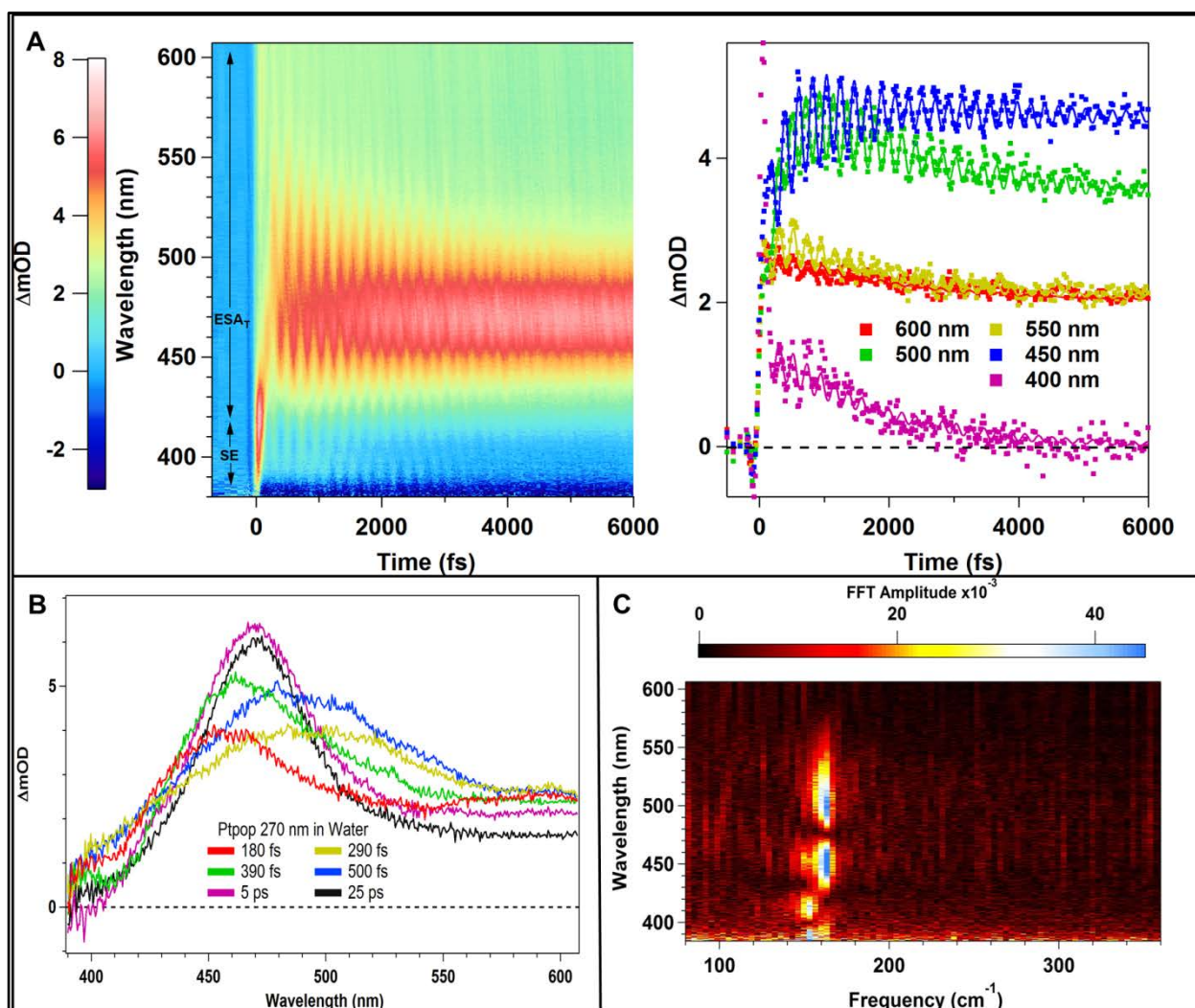


Figure 3-8 shows the $t-\lambda$ plot of Pt(pop) in water upon 270 nm (UV2) excitation, together with some kinetic traces at selected wavelengths (A). The best - fit is overlapped to the data points and, as can be seen in the picture, the GF procedure was started right after the coherent artifact present at time-zero. In (B) are shown transient spectra at selected time - delays, while in (C) is shown the FFT map that highlights the frequencies present in the oscillatory pattern

A weak SE feature around ~ 400 nm points to some population reaching the singlet state ($^1A_{2u}$) from the UV2 state, contrary to the MeCN case. These features, together with the wave-packet evolution in time, can be better observed in Figure 3-8B, which shows transient spectra at selected time-delays. To best-fit the data-points, three exponential decays and two exponentially damped sine functions were necessary, as shown by the GF analysis in Figure 3-8A (right). The retrieved population times, namely 320 ± 20 fs and 1.7 ± 0.1 ps, are very similar to the values reported in previous studies [52] and point to a primary ultrafast vibrational relaxation of the system (320 fs component), followed by a slower component (1.7 ps). The parameters obtained by the GF (population and coherence times) are summarized in Table 3-2 and Table 3-3 in Section 3.5.

Moreover the wave-packet frequencies are confirmed from the FFT analysis (see Figure 3-8C), which shows clearly the presence of the mode belonging to the $^1A_{2u}$ state in the SE region at ~ 420 nm. It is important to highlight that the coherence times are 1.7 ± 0.2 ps for the $^1A_{2u}$ state and 2.9 ± 0.2 ps for the $^3A_{2u}$. The former is in excellent agreement with the previously reported damping times,[52] while the latter is observed for the first time.

3.4 Ligand dependence

3.4.1 Sample preparation

As in the previous case, the experiments were performed exciting at two different wavelengths, namely 360 nm ($^1A_{2u}$ band) and 260 nm (UV2 band); however, since Pt(pop)-BF₂ is moisture and oxygen sensitive, the preparation of the sample, handling and measurements were done under Argon atmosphere.

For the 360 nm excitation experiments, Pt(pop)-BF₂ was dissolved in high-grade anhydrous acetonitrile with a concentration of ~ 0.9 mM. During the experiments the solution was flowed in a 100 μ m-thick thin window flow-cell in order to avoid photo-damaging of the sample. For the 260 nm excitation experiments the same procedure described above was used but the Pt(pop)-BF₂ solution was more concentrated, namely ~ 4.5 mM. The sample concentration in these experiments was set to obtain absorption of ~ 0.3 OD at the excitation wavelength. The excitation fluence was set to ~ 1.2 mJ/cm² and the probe polarization was set to the magic angle with respect to the pump polarization.

3.4.2 Experimental results

Figure 3-9A (left) shows the t - λ plot of Pt(pop)-BF₂ upon 360 nm photo-excitation, displaying the GSB at 365 nm, the SE at 390 nm and a broad ESA covering the region from 420 nm to 600 nm. In the transient signal both the SE and ESA_S features are present up to 10 ps, while no ESA_T appears, implying that in the investigated pump-probe delay time window the $^1A_{2u}$ state does not undergo ISC to the $^3A_{2u}$ state, in agreement with its reported radiative lifetime of 1.6 ns.[3] Also in this case, coherent wave-packets show up both in the ground and the excited state, as can be seen in both the t - λ plot and in the selected kinetic traces beside it (Figure 3-9A). The above-mentioned spectral features, as well as their time-evolution, can be seen also in Figure 3-10A that shows transient spectra at selected time-delays. The latter were chosen so to highlight wave-packet motion. In order to retrieve the characteristic timescales of Pt(pop)-BF₂ (both population and coherence), a GF analysis was performed.

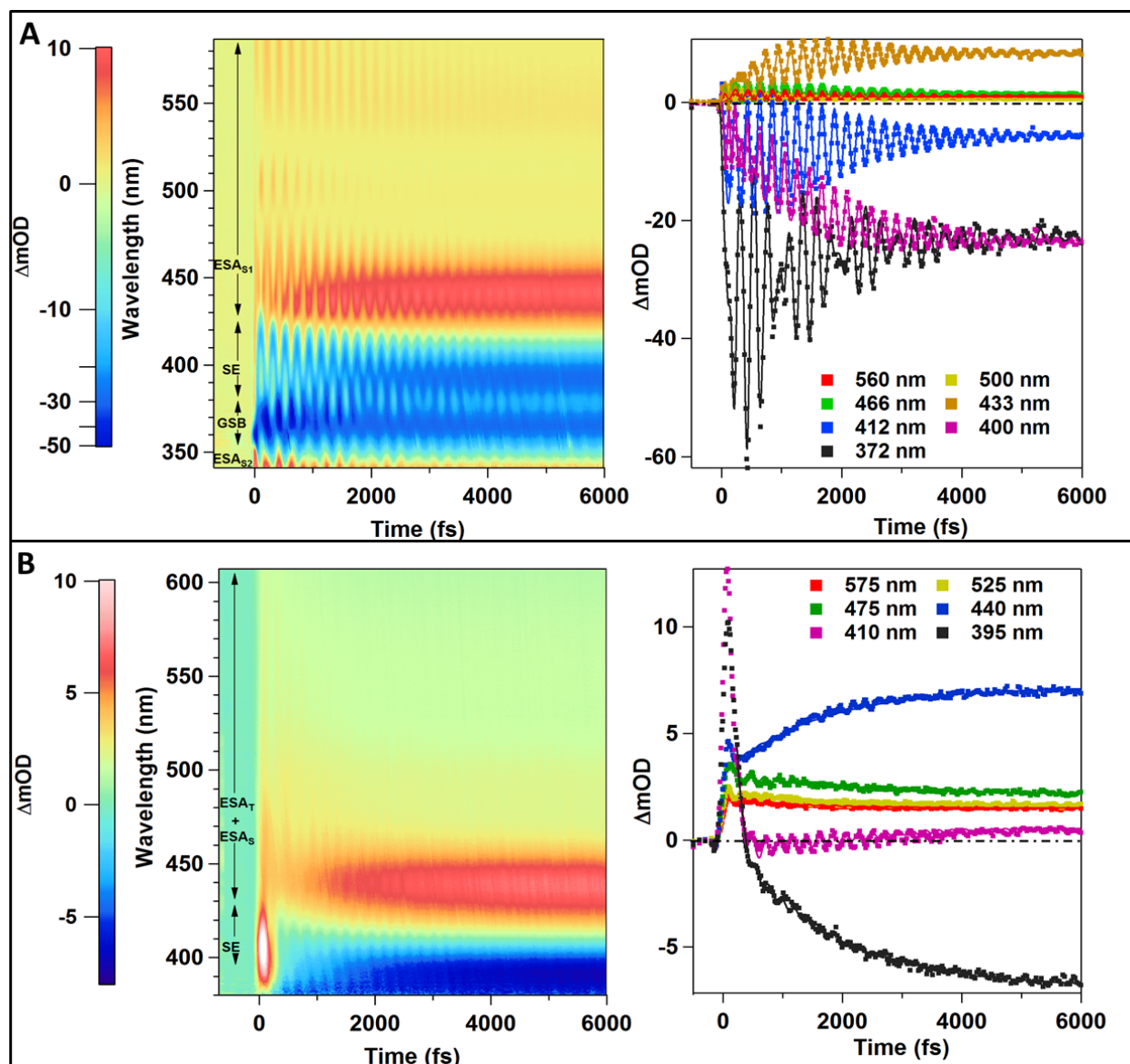


Figure 3-9 shows t - λ plot (left) and selected kinetic traces (right) of Pt(pop)-BF₂ upon 360 nm (A) and 260 nm (B) excitation.

To best-fit the data points two exponential decays (1.2 ± 0.1 ps and 500 ps accounting for the non-decaying signal) and three exponentially damped sine functions (describing the oscillations in the ${}^1A_{1g}$, ${}^1A_{2u}$ states plus the overtone of ${}^1A_{2u}$) were used. The frequencies obtained by GF were also cross-checked with FFT analysis, whose results were in excellent agreement with the GF ones, as shown in Figure 3-11A. For the sake of clarity all the results of the GF analysis are given in Table 3-2 and Table 3-3 (Section 3.5).

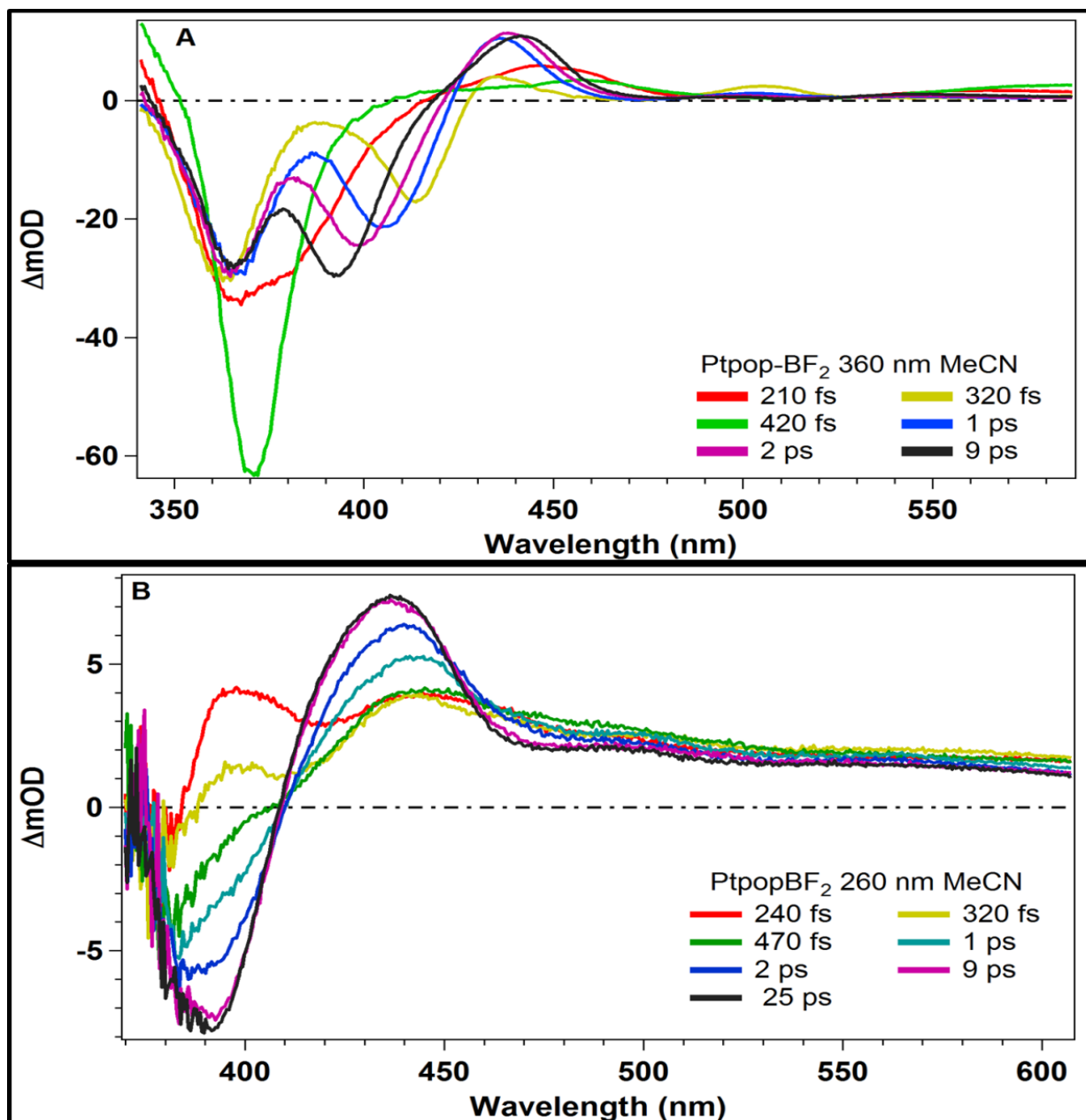


Figure 3-10 Transient spectra of Pt(pop)-BF₂ at selected time - delays upon 360 nm (A) and 260 nm (B) excitation. Also in this case the wavelength axis has been cut in the blurred GSB region.

Figure 3-9B (left) displays the $t-\lambda$ plot obtained by photo-exciting the Pt(pop)-BF₂ at 260 nm excitation, which shows the following features: i) the SE is present but grows only after some 100s fs; ii) the ESA_S is present, which implies (as the presence of the SE) that some population reaches the ¹A_{2u} state; iii) the oscillatory pattern is much weaker, as can be seen also in the kinetic traces shown in Figure 3-9B (right); iv) the first 100s of fs are characterized by an ESA feature over the entire probe region, as can be seen in the transient spectrum at 240 fs in Figure 3-10B.

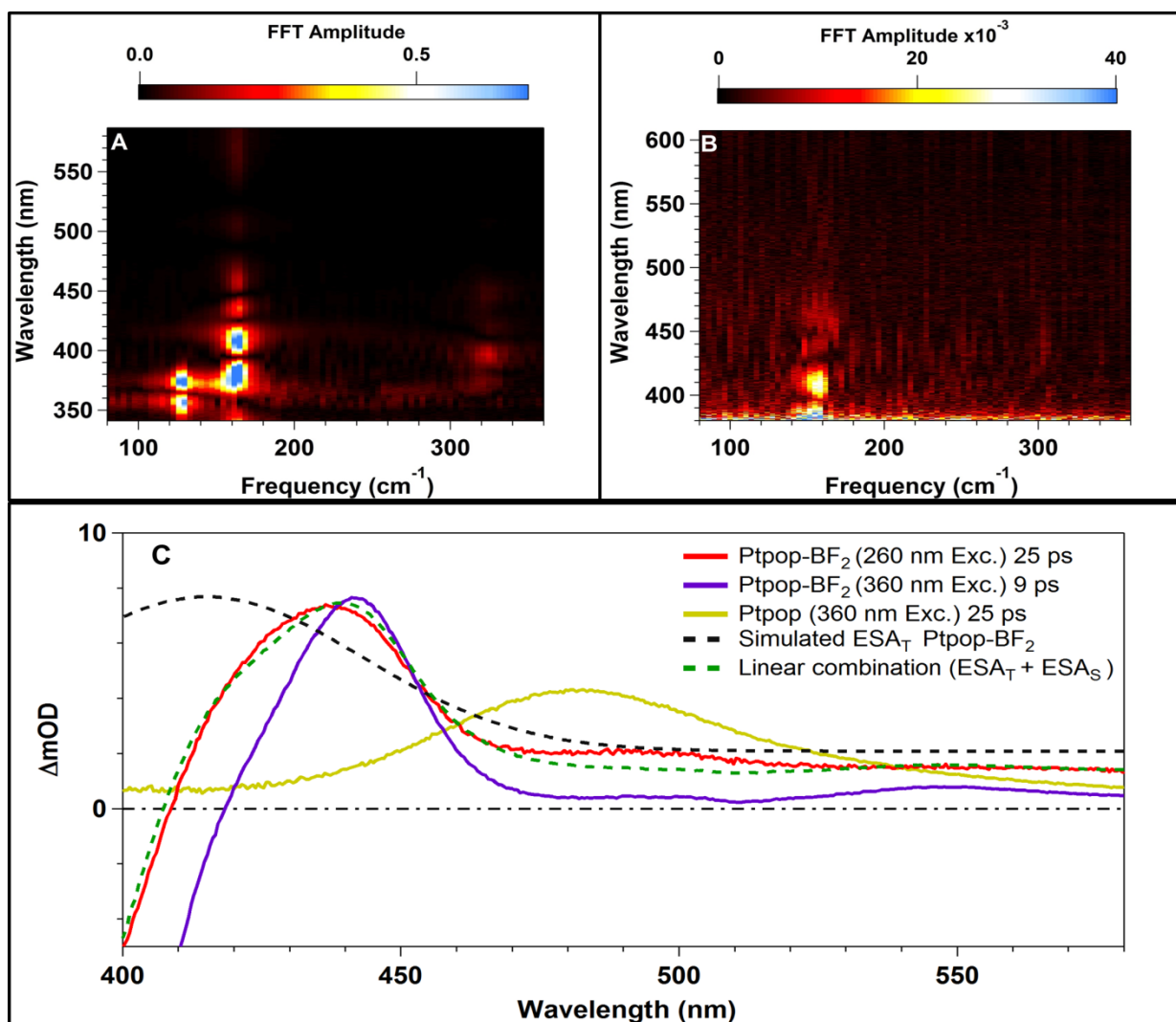


Figure 3-11 Results of FFT analysis of the oscillatory pattern in Pt(pop)-BF₂ upon 360 nm (A) and 290 nm (B) excitation. In (C) is reported the comparison between transient spectra at time – delays > 9 ps for Pt(pop) upon 360 nm, Pt(pop)-BF₂ upon 360 nm and Pt(pop)-BF₂ upon 260 nm. The simulated ESA profile of the ³A_{2u} state of Pt(pop)-BF₂ is shown in dotted black line while the linear combination between ¹A_{2u} and ³A_{2u} is shown in dotted green.

The spectral feature present at short delay–times could be due either to the UV2 state or to the ³B_{2u} state; however, based on the Pt(pop) results, the ³B_{2u} → ³A_{2u} IC should occur within our experimental IRF, suggesting that this first ESA feature is due to the depletion of the UV2 state. Similarly to the other cases, a GF analysis was performed to gather information on the characteristic timescales of the system. To best–fit the data–points four exponential decays (120 ± 15 fs, 1.3 ± 0.1 ps, 4.5 ± 0.3 ps and 500 ps) and one exponentially damped sine function (describing the ¹A_{2u} frequency) were used. The obtained frequency was cross–checked by FFT analysis, which shows the same result within the error, as can be seen in Figure 3-11B. Kinetic traces at selected wavelengths and the obtained best–fit are shown in Figure 3-9B (right), while the fit parameters are summarized in Table 3–2 and in Table 3–3 (Section 3.5).

The transient spectrum at 240 fs (Figure 3-10B) shows four ESA bands: at 400 nm, 460 nm, 510 nm and 570 nm. With increasing time–delay, the 460 nm band increases in amplitude and shifts to the blue, while the 400 nm band decreases in intensity to eventually disappear.

The ESA bands at 510 nm and 570 nm are present also upon 360 nm excitation, even if they have a very low intensity, as can be seen in Figure 3-11C. In order to identify the origin of the spectral differences between the two excitation wavelengths, we compare the transient spectra at long delay–times (> 9 ps) of Pt(pop)–BF₂ upon 260 nm and 360 nm excitation and Pt(pop) upon 360 nm excitation, as shown in Figure 3-11C.

The transient spectrum of Pt(pop)–BF₂ at 9 ps upon 360 nm excitation is entirely due to the response of the ¹A_{2u} state, while the one at 30 ps for Pt(pop) upon 360 nm excitation is entirely due to the ³A_{2u} state. This comparison shows immediately an interesting detail: the ESA band at ~435 nm of Pt(pop)–BF₂ upon 260 nm excitation is not symmetric and blue–shifted with respect to the ESA band at ~445 nm of Pt(pop)–BF₂ upon 360 nm excitation, suggesting the presence of a second band in that ESA region. To explain this difference, it is necessary to compare the static absorption spectrum of Pt(pop)–BF₂ with respect to the Pt(pop) one (Figure 3-4B). The UV bands in Pt(pop)–BF₂ are strongly shifted to higher energies with respect to the Pt(pop) case, while the ³A_{2u} band is only weakly affected by the perfluoroboration. As a consequence, the ESA due to the ³A_{2u} state in Pt(pop)–BF₂ will be strongly blue–shifted with respect to the ³A_{2u} ESA in Pt(pop). In Figure 3-11C we show also two simulated transient spectra: the simulated ³A_{2u} Pt(pop)–BF₂ ESA (black dotted line) and a linear combination of the latter with the transient spectrum of Pt(pop)–BF₂ upon 360 nm excitation (in dotted green). The former ESA band was obtained by best–fit of the ESA_T of Pt(pop) with a Gaussian function and changing the central frequency, thus assuming that the transient response is similar in both Pt(pop) and Pt(pop)–BF₂. The obtained ³A_{2u} Pt(pop)–BF₂ ESA was used to perform a linear combination with the ¹A_{2u} response of Pt(pop)–BF₂, in order to reproduce the signal obtained upon 260 nm excitation of Pt(pop)–BF₂. The result, shown in Figure 3-11C, is obtained with a ratio of $0.5 \times \text{ESA}_T + 0.5 \times \text{ESA}_S$, assuming that the amplitudes of the ESA_T and ESA_S transient signal are comparable (as in the Pt(pop) case shown in Figure 3-6A). Moreover, it was also necessary to introduce a small vertical offset in order to obtain the green dotted curve (introduced in the Gaussian curve), which hints to the absorption of a solvated electron. The agreement between the simulated transient signal with the experimental one is quite good in the entire probing region, except for the 500 nm low–intensity band that was not reproduced, suggesting that this is a typical feature of the ESA_T band in Pt(pop)–BF₂.

All these observations suggest that, upon excitation of Pt(pop)–BF₂ in the UV2 band, the system relaxes via a branching mechanism from the UV2 state to the ^{1,3}A_{2u} ones (possibly via the ³B_{2u} state).

3.5 Summary of the GF results

In this section we report all the fitting parameters obtained from the GF analysis of all the experiments. In Table 3–2 are reported the obtained population times, while in Table 3–3 are summarized the coherence timescales and frequencies of the detected oscillatory patterns. In Table 3–3 the frequencies (ω) are defined for the ground state (subscript G), ¹A_{2u} state (subscript S) and its overtone (subscript OT), and ³A_{2u} state (subscript T).

Table 3–2 Summary of the population times retrieved by GF of several kinetic traces.

Pt(pop) in MeCN				
λ_{exc} (nm)	τ_1 (fs)	τ_2 (ps)	τ_3 (ps)	
360	700 ± 100	3.8 ± 0.4	500	
280	280 ± 30	3.5 ± 0.3	500	
Pt(pop) in H₂O				
λ_{exc} (nm)	τ_1 (fs)	τ_2 (ps)	τ_3 (ps)	
270	320 ± 20	1.7 ± 0.1	500	
Pt(pop)–BF₂ in MeCN				
λ_{exc} (nm)	τ_1 (fs)	τ_2 (ps)	τ_3 (ps)	τ_4 (ps)
360	— — — —	1.2 ± 0.1	— — — —	500
260	120 ± 15	1.3 ± 0.1	4.5 ± 0.3	500

Table 3–3 Summary of the parameters describing the oscillatory patterns retrieved by GF of several kinetic traces.

Pt(pop) in MeCN							
λ_{exc} (nm)	ω_{G} (cm ⁻¹)	$\tau_{\text{D(G)}}$ (ps)	ω_{S} (cm ⁻¹)	$\tau_{\text{D(S)}}$ (ps)	ω_{T} (cm ⁻¹)	$\tau_{\text{R(T)}}$ (fs)	$\tau_{\text{D(T)}}$ (ps)
360	<i>119 ± 1</i>	<i>2.2 ± 0.2</i>	<i>149 ± 1</i>	<i>1.1 ± 0.1</i>	<i>157 ± 1</i>	<i>900 ± 90</i>	<i>2.5 ± 0.4</i>
280	---	---	---	---	<i>157 ± 1</i>	---	<i>2.5 ± 0.3</i>
Pt(pop) in H₂O							
λ_{exc} (nm)	ω_{G} (cm ⁻¹)	$\tau_{\text{D(G)}}$ (ps)	ω_{S} (cm ⁻¹)	$\tau_{\text{D(S)}}$ (ps)	ω_{T} (cm ⁻¹)	$\tau_{\text{D(T)}}$ (ps)	
270	---	---	<i>147 ± 1</i>	<i>1.7 ± 0.2</i>	<i>159 ± 1</i>		<i>2.9 ± 0.2</i>
Pt(pop)–BF₂ in MeCN							
λ_{exc} (nm)	ω_{G} (cm ⁻¹)	$\tau_{\text{D(G)}}$ (ps)	ω_{S} (cm ⁻¹)	$\tau_{\text{D(S)}}$ (ps)	ω_{OT} (cm ⁻¹)	$\tau_{\text{D(OT)}}$ (fs)	
360	<i>126 ± 1</i>	<i>2.1 ± 0.2</i>	<i>162 ± 1</i>	<i>1.2 ± 0.2</i>	<i>324 ± 1</i>		<i>550 ± 60</i>
260	---	---	<i>152 ± 10</i>	<i>1.8 ± 0.5</i>	---		---

3.6 Discussion

The results presented here reveal a number of new features: i) the solvent effect on the $^1\text{A}_{2\text{u}} \rightarrow ^3\text{A}_{2\text{u}}$ ISC rate is further confirmed;[52] ii) coherence transfer is observed during the above-mentioned ISC process in MeCN as well as in water; iii) excitation of the UV2 band in Pt(pop) leads to population of the lowest triplet state ($^3\text{A}_{2\text{u}}$) to an extent that depends on the solvent (e.g. in MeCN is detected only the $^3\text{A}_{2\text{u}}$ while in water mainly the $^3\text{A}_{2\text{u}}$ state is populated with a small percentage of $^1\text{A}_{2\text{u}}$ state); iii) the $^1\text{A}_{2\text{u}} \rightarrow ^3\text{A}_{2\text{u}}$ ISC in the case of 360 nm excitation of Pt(pop)–BF₂ is suppressed,[3] while excitation of UV2 state populates both the $^1\text{A}_{2\text{u}}$ and the $^3\text{A}_{2\text{u}}$ states equally; iv) in all cases, upon UV excitation of the system, coherent oscillations appear in the lowest populated triplet state, pointing to a conservation of coherence over a large energy range during intramolecular relaxation.

The obtained results suggest that the bluer the UV bands, the lower the probability of a $^1\text{A}_{2\text{u}} \rightarrow ^3\text{A}_{2\text{u}}$ ISC upon $^1\text{A}_{2\text{u}}$ excitation (Table 3–1). Indeed, Pt(pop)–BF₂ displays the blue-most UV bands and a strongly suppressed ISC, while Pt(pop) dissolved in water, ethanol or ethylene glycol displays ISC timescales ranging from 13 to 30 ps.[52]

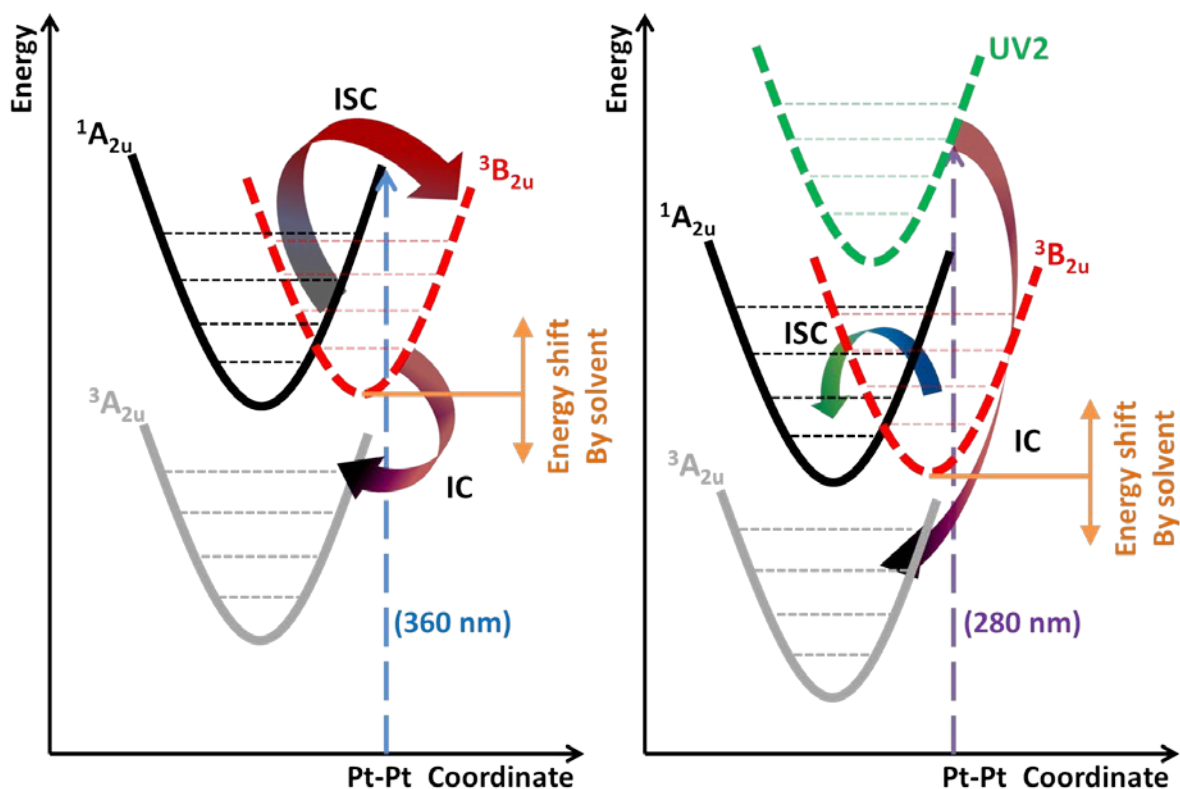


Figure 3-12 Scheme of the proposed photo-cycle for Pt(pop) and its derivatives with the $^3B_{2u}$ intermediate state for both 360 nm (left) and UV2 (right) excitation.

The latter timescales are 10–40 fold longer than Pt(pop) dissolved in MeCN, where the UV bands lie at the lowest energy and in which the ISC time is < 1 ps. Pt(pop) dissolved in DMF stands out in this trend as its ISC time is 11 ps, yet its UV bands lie at about the same energy as in MeCN. The energy shift of the UV1 band correlates quite well with the presented results, thus implying that it is due to the $^3B_{2u}$ state as already suggested by Stiegman *et al.*, [136] as well as recently reported by TDDFT studies of Zálíš *et al.* [148]. Although we did not investigate all the solvents, the above trends seem to be well correlated to the cascade of population upon excitation of Pt(pop) and Pt(pop)-BF₂ in the UV2 bands, showing a direct correlation between the energy of the UV1 band and the ISC time. As a matter of fact, when Pt(pop) is dissolved in MeCN the UV2 state lies at the lower energies than in other investigated solvents and the singlet state is completely avoided in the cascade, thus populating with unity QY the lowest excited triplet state. The more the energy of the UV1 band (and so of the $^3B_{2u}$ state) increases, the more the percentage of population in the $^1A_{2u}$ state (as seen in the Pt(pop)-BF₂ case). The above mentioned general trends confirm Milder and Brunschwig's hypothesis, [127] in which a ligand-field $^3B_{2u}$ state acts as intermediate in the $^1A_{2u} \rightarrow ^3A_{2u}$ ISC, as schematically depicted in Figure 3-12.

When the system is photo-excited in the $^1A_{2u}$ band (~ 360 nm), the $^1A_{2u} \rightarrow ^3A_{2u}$ ISC rate constant depends on the energy of the $^3B_{2u}$ state, which is modulated by the solvent as well as by the ligand. This means that the relaxation occurs in two steps: i) $^1A_{2u} \rightarrow ^3B_{2u}$ ISC, which is the rate limiting step; and ii) $^3B_{2u} \rightarrow ^3A_{2u}$ IC, which occurs on an ultrafast timescale (> 80 fs). Figure 3-12 (left) shows a schematic view of the proposed photo-cycle: in the case of Pt(pop) in MeCN the $^3B_{2u}$ state should have an energy comparable to the $^1A_{2u}$ state and a strong coupling with it, leading to a fast $^1A_{2u} \rightarrow ^3B_{2u}$ ISC rate followed by an ultrafast IC. When Pt(pop) is dissolved in Ethylene glycol (the solvent presenting the longer ISC rate in our study) the energy of the $^3B_{2u}$ state increases, thus raising the activation energy for the ISC (recall Equation (3.1)) and strongly reducing the ISC rate constant. The extreme case of Pt(pop)-BF₂ in MeCN shows the result of a strong energy shift of the $^3B_{2u}$ state, thus leading to a strong decrease of the ISC rate constant. Probably, in the latter case the ISC will be driven by slow skeletal modes and not via the $^3B_{2u}$ state. The hypothesis of the intermediate $^3B_{2u}$ state explains also the results obtained upon UV2 band excitation. Our experimental results highlight the following trend in the $^3A_{2u}$ - $^1A_{2u}$ population percentages: Pt(pop) in MeCN (100% $^3A_{2u}$) $>$ Pt(pop) in water ($\sim 90\%$ $^3A_{2u}$ and $\sim 10\%$ $^1A_{2u}$) $>$ Pt(pop)-BF₂ in MeCN ($\sim 50\%$ $^3A_{2u}$ and $\sim 50\%$ $^1A_{2u}$).

The observed trend is in excellent agreement with the results shown for the 360 nm excitation, since the higher the $^3B_{2u}$ in energy the more the $^1A_{2u}$ is populated. The photo-cycle related to the UV2 band excitation is shown in Figure 3-12 (right). In the latter scheme, two extreme situations can be identified: i) Pt(pop) in MeCN has low-lying $^3B_{2u}$ state, implying that the relaxation is mainly governed by the $^3B_{2u} \rightarrow ^3A_{2u}$ IC (in agreement with 360 nm excitation experiments in which back-ISC to the $^1A_{2u}$ state is too slow and thus not a valuable pathway); and ii) Pt(pop)-BF₂ in MeCN has high-lying $^3B_{2u}$ state, where the $^3B_{2u}$ - $^1A_{2u}$ Frank-Condon overlap is bigger than the previous case, thus leading to a faster $^3B_{2u} \rightarrow ^1A_{2u}$ ISC that competes with the $^3B_{2u} \rightarrow ^3A_{2u}$ IC. As a consequence, in the latter case a percentage of the excited population goes to the $^1A_{2u}$ state where it is trapped for ns because of the low Frank-Condon overlap and energy difference between $^1,^3A_{2u}$ states.

Another important process observed in our results, is the coherence transfer of the wave-packet to the $^3A_{2u}$ state upon excitation of the system (either in the $^1A_{2u}$ state or to the UV2 state). This process is mainly observed in Pt(pop), dissolved both in MeCN and H₂O, while in Pt(pop)-BF₂ (excited in the UV2 band) the oscillatory pattern is weak compared to the previous cases. Figure 3-13 shows the oscillatory pattern at three selected wavelengths, namely 379 nm (GSB), 411 nm (SE) and 550 nm (ESA_T).

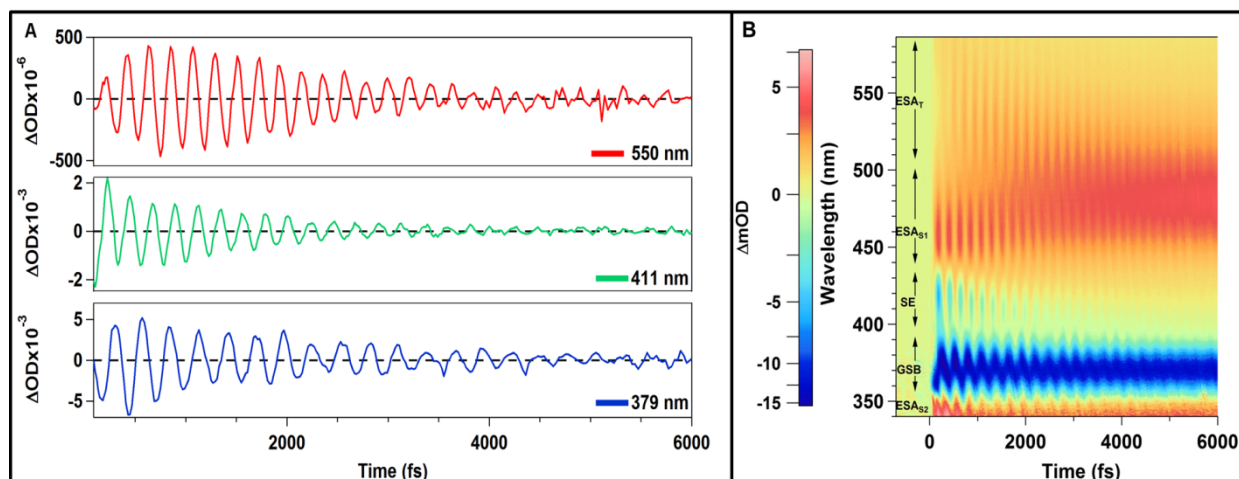


Figure 3-13 Oscillatory pattern in Pt(pop) dissolved in MeCN at selected wavelengths upon 360 nm excitation (A) and relative t - λ plot (B).

The growth of the oscillatory pattern in the ESA_T region, is in perfect agreement with the model proposed by Jean and Fleming [107] (shown in Figure 1-8C), showing the coherence transfer over several cycles of the wave-packet's oscillation. We observed the amplitude growth of the ${}^3A_{2u}$ wave-packet oscillation only in Pt(pop) in MeCN upon 360 nm excitation, since in all the other investigated cases the ${}^3A_{2u}$ state was promptly populated. Beside these results, the GSB oscillation shows the overlapping contributions of the ${}^1A_{1g}$ and ${}^1A_{2u}$ wave-packets, which is also slightly visible in the SE region.

3.7 Conclusions

In this chapter we reported on the effect of both the solvent and the ligand in the Pt(pop) photo-cycle, together with its impact on the ISC time constants. The results of the transient absorption UV pump-Visible probe experiments highlights the validity of the hypothesis formulated by Brunschwig and Milder, namely the presence of the ${}^3B_{2u}$ state between the ${}^1A_{2u}$ and ${}^3A_{2u}$ ones, which acts as an intermediate in the ${}^1A_{2u} \rightarrow {}^3A_{2u}$ ISC.

Therefore our interpretation highlights that the ISC rate constants, detected upon 360 nm (${}^1A_{2u}$) excitation, are due to the ${}^1A_{2u} \rightarrow {}^3B_{2u}$ ISC process, which is followed by an ultrafast (< 80 fs) ${}^3B_{2u} \rightarrow {}^3A_{2u}$ IC. When the system is excited at 280–260 nm (UV2) the detected process depends on the relative energy of the ${}^3B_{2u}$ state, passing from a total ${}^3B_{2u} \rightarrow {}^3A_{2u}$ IC to a competition between ${}^3B_{2u} \rightarrow {}^1A_{2u}$ ISC and ${}^3B_{2u} \rightarrow {}^3A_{2u}$ IC. We also reported on the presence of coherence transfer to the ${}^3A_{2u}$ state during relaxation through different spin states, as a leakage on several wave-packet cycles.

Chapter 4

4 Electron and Energy Transfer in Myoglobins

The use of FRET as a “*spectroscopic ruler*” has been questioned by the results of recent 2D–UV TA and UV pump–Visible probe TA experiments,[15] which reported a *Trp¹⁴–to–heme electron transfer process in ferric myoglobin complexes. Such deactivation pathway occurs in parallel with the FRET process and could lead to wrong distance estimation if not accounted for. The aim of this chapter is to investigate several myoglobin complexes, mostly ferrous ones, in order to verify if the *Trp¹⁴–to–heme electron transfer is an active process in all myoglobins and, if it is the case, to investigate its implications on tryptophan’s fluorescence quenching. Tryptophan is a naturally occurring chromophore in biological systems and, for this reason, is usually used to determine distances in biological systems via FRET.[65, 67] Therefore, a better understanding of tryptophan’s deactivation processes is crucial for the estimation of distances in all systems containing this residue.

The first part of the chapter (Section 4.1) introduces the myoglobin and its biological function, together with tryptophan dynamics, both in water and in proteins. After this brief introduction, several myoglobin complexes will be investigated via ultrafast transient absorption techniques, aiming to put the basis of a deeper understanding of the electron transfer process in heme proteins. Therefore, Section 4.2 reports the results obtained in deoxy–Mb, followed by Sections 4.3, 4.4 and 4.5 that report on the results obtained for MbCO, MbNO and MbCN, respectively. Finally, the chapter will be closed drawing individual conclusions on myoglobin and a more general view on heme proteins and the used of FRET mechanism in distance determination (Section 4.6).

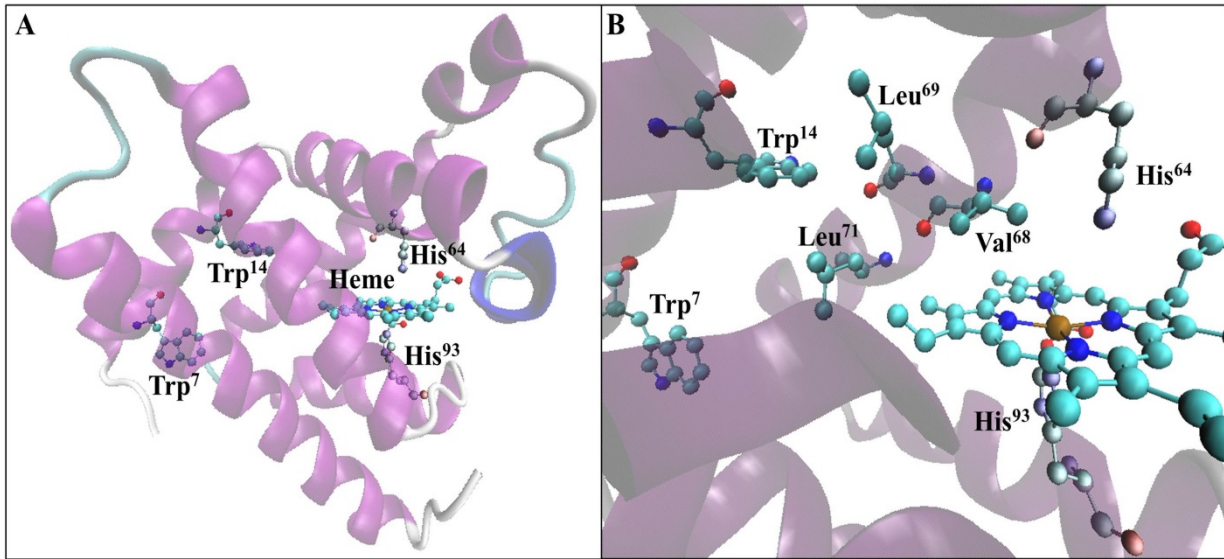


Figure 4-1 Deoxy-myoglobin structure obtained from Protein Data Bank, showing the backbone (with the α – helices in purple), the heme and the most important amino acids for the following discussion, namely the two tryptophan residues, the distal and proximal Histidine (position 64 and 93, respectively), Leucine 69 and 71 and Valine 68. In (A) is given a complete view of the deoxy – Mb, while in (B) the picture is focused on the residues between Trp¹⁴ and the heme, which identify a possible pathway for the electron transfer process.

4.1 Myoglobin and tryptophan

Myoglobin is a small globular protein composed of 153 amino-acids, which are organized in eight α -helices. The cofactor, an iron complex of the Protoporphyrin IX, is embedded within the peptide structure, as shown in Figure 4-1,[149] and it is anchored to the protein scaffold by the histidine 93 (also called proximal histidine), which coordinates the iron ion in one of the two apical positions. The second apical position is the one fulfilling myoglobin's biological functions, namely acting as a storage of molecular oxygen (O_2) inside muscles [7] and as a NO – scavenger.[6, 150, 151] Because of its conformation, myoglobin can bind various small molecules, such as carbon monoxide (CO), nitrogen monoxide (NO), cyanide (CN^-) and water, whose affinity depends on the iron's oxidation state and it is modulated by the histidine 64 (also called *distal histidine*).[152] The ferrous form of myoglobin is the oxygen binding form, which shows also high affinity for CO and NO, while the ferric form is usually coordinated by a water molecule (hereafter MetMb) and shows a strong affinity towards CN^- . The coordination of these small diatomic molecules to the iron ion is strongly reflected in the absorption spectrum, as shown in Figure 4-2, which changes dramatically depending on the myoglobin complex.

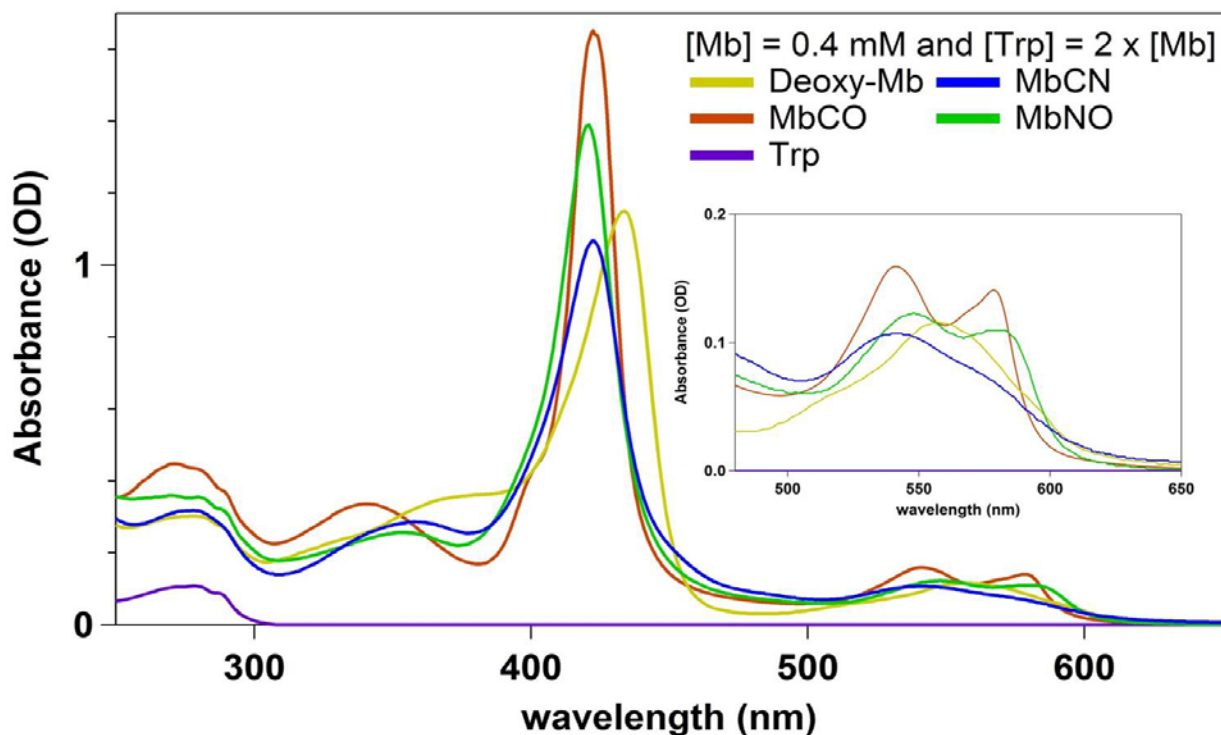


Figure 4-2 Absorption spectra of several myoglobin complexes and tryptophan dissolved in aqueous phosphate buffer solution at pH 7 with a concentration of 0.4 mM and measured in a 0.2 mm quartz cuvette. The inset gives a more detailed view of the Q-bands.

The bands in the absorption spectra are due to several π - π^* transitions, showing a moderately intense pair of bands between 500 nm and 600 nm (called Q-bands), an intense band around 430 nm (called B or Soret band) and two moderately intense bands between 250 nm and 380 nm (called L and N bands respectively).[153] As shown in Figure 4-2 the shape of the Q-bands is strongly influenced by the diatomic ligand complexing the iron ion, while the Soret band is only weakly influenced. The motivation is that Q-bands are not allowed transitions that become partially allowed via vibronic coupling, so a small perturbation in the vibrational structure will have strong influence on these bands. On the other hand, the Soret band is fully allowed, implying that variations in the vibrational levels will have a smaller impact, even if always present. The main absorbers in myoglobin (in the 250–700 nm region) are the heme and the tryptophan; as can be seen in Figure 4-2 all the absorption bands are due solely to porphyrin transitions, except the L band (250–300 nm) that is composed by the superposition of the porphyrin and the tryptophan residues absorption. In this spectral region there are two other amino acids that absorb, namely phenylalanine and the tyrosine; however, the molar extinction coefficient of tryptophan is the largest, resulting the main absorber in the 250–300 nm region, as shown in Figure 4-3.[154]

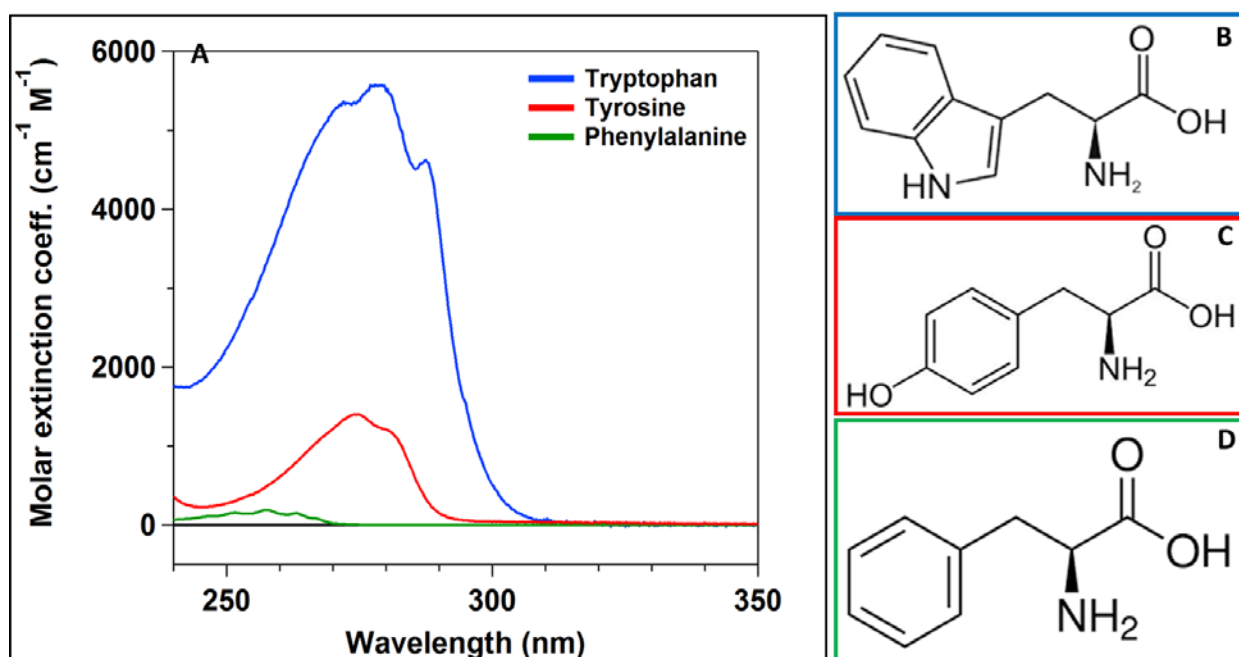


Figure 4-3 Absorption spectra of tryptophan, Tyrosine and Phenylalanine (A) with their structures (B to D, respectively). The molar extinction coefficient showed in (A) highlights the importance of the tryptophan residue with respect to Tyrosine and Phenylalanine.

As shown in Figure 4-1, horse heart (HH) myoglobin contains two tryptophan residues situated in positions 7 and 14 of the peptide chain.[155, 156] Trp⁷ is mostly exposed to the solvent and its center-to-center distance from the heme is 21 Å, while Trp¹⁴ is more embedded in the peptide environment and it is closer to the heme (15 Å).[149, 157]

Tryptophan is extremely sensitive to its environment, which strongly influences its fluorescence. For this reason it has been addressed as a natural local probe in proteins, thus allowing investigating on protein dynamics without altering their nature.[158–162] Previous time-resolved fluorescence experiments [13, 163, 164] reported that, in heme proteins, *Trp fluorescence lifetime is reduced by 1–2 orders of magnitude with respect to the 3 ns decay time of tryptophan in water.[165, 166] The common explanation to these quenching times in the protein matrix is that *Trp undergoes FRET to the heme, e.g. leading to decay times of 20 ps (*Trp¹⁴) and 120 ps (*Trp⁷) in myoglobin complexes.[13, 163, 164] However, recent 2D-UV Transient Absorption and UV pump-Visible probe TA experiments, on MetMb and ferric MbCN, demonstrated that another competing process is active other than FRET, namely the electron transfer from *Trp¹⁴ to the heme.[15] The comparison between *Trp quenching times in various myoglobin complexes does not show strong differences, as shown in Table 4-1, suggesting that a similar mechanism is present in both ferric and ferrous systems.

Table 4–1 Summary of the *Trp⁷ and *Trp¹⁴ decay times for several Mb complexes. The values refer to Sperm Whale (SW) Mb except for the Apo–Mb which refers to Horse Heart (HH). The structure of these two Mbs is very similar so the timescales can be compared.

Myoglobin complex	Trp ⁷ decay time (ps)		Trp ¹⁴ decay time (ps)	
<i>Deoxy–Mb (SW)</i>	105[13]		18[13]	
<i>MetMb (SW)</i>	135[163]	112[13]	16[163]	21[13]
<i>MbCO (SW)</i>	132[163]	125[13]	26[163]	23[13]
<i>MbCN (SW)</i>	113[13]		28[13]	
<i>MbN₃ (SW)</i>	109[13]		27[13]	
<i>MbO₂ (SW)</i>	122[13]		24[13]	
<i>Apo–Mb (HH)</i>	2840[167]		2806[167]	

The diverse quenching times between *Trp⁷ and *Trp¹⁴, are due to the Trp–heme distance and relative orientation of the tryptophan residues with respect to the heme; nevertheless, it was demonstrated that only *Trp¹⁴ undergoes both FRET and electron transfer to the heme, while *Trp⁷ undergoes only FRET to the heme.[15] Furthermore, it is interesting to highlight that *Trp’s fluorescence decay time in apo–myoglobin (myoglobin without the cofactor) shows similar values to the tryptophan dissolved in aqueous solution, which is quite surprising because *Trp is a strong electron–donor and it is known to undergo electron transfer to the backbone and nearby amino acidic residues.[168] Qiu *et al* [169] performed a site directed mutation study on apo–myoglobin (among other proteins), reporting shorter *Trp fluorescence when tryptophan was substituted by various amino acids, e.g. Lysine (positions 87 and 34) and Alanine (position 125). Therefore, when tryptophan residues are in their natural positions (7 and 14) their fluorescence is not quenched, but it is when they are in other positions of the peptide chain, suggesting that the Trp–heme interaction is crucial for *Trp’s fluorescence quenching in natural myoglobin.

The aim of this study is to investigate the tryptophan relaxation processes, in order to determine if the electron transfer process is active in both ferric and ferrous myoglobin complexes. If this is the case, the additional electron could be localized on the iron ion, delocalized on the porphyrin ring or localized on the diatomic ligand.

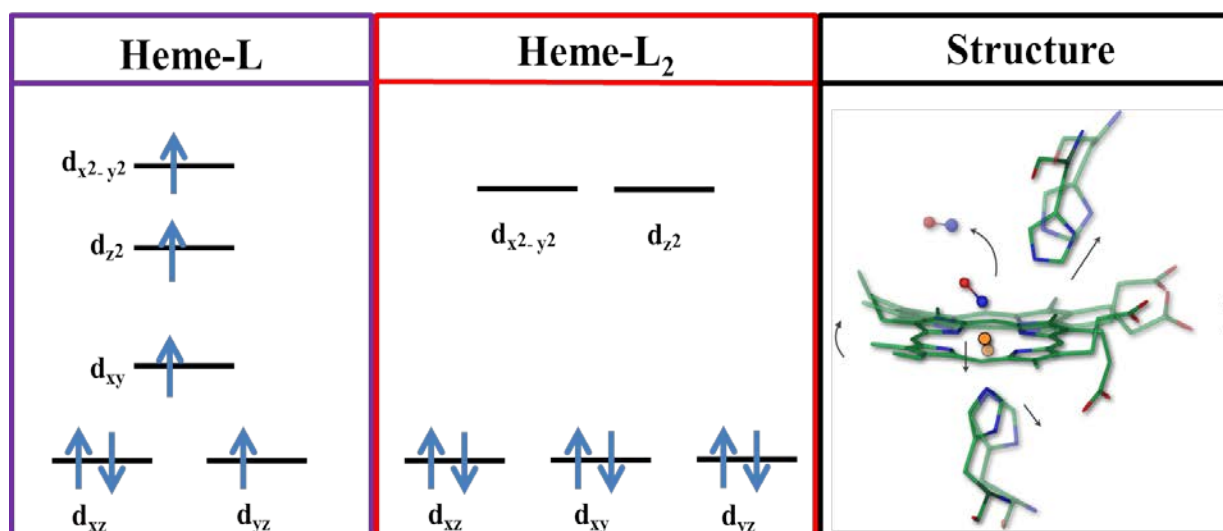


Figure 4-4 Schematic representation of the crystal-field split of Fe d orbitals in deoxy-Mb (Heme-L), ligated ferrous Mb (Heme-L₂) and the overlap of the ligated and domed structures, where L stands for ligand. The proximal histidine is depicted below the heme plane, the distal histidine above and the diatomic ligand is displayed as two spheres connected by a line. The arrows indicate the motion of the heme, of the ligand and of the histidines. The right panel is reproduced from ref. [203].

However, the absorption of tryptophan residues is completely overlapped to the heme absorption (see absorption spectra in Figure 4-2), making a selective excitation of the tryptophan residues impossible. This problem can be overcome by selective excitation of the heme (e.g. at 315 nm) and sequential comparison of the obtained results with the response of the system upon excitation of both tryptophan and heme (e.g. at 290 nm). Assuming that the heme response is similar at both excitation wavelengths, it is possible to obtain selective information on the Tryptophan residues. This approach is perfect for systems displaying a short photo-cycle compared to the *Trp lifetime, such as MetMb and deoxy-Mb with a photo-cycle < 4 ps,[12, 34, 170] but it can be more complicated for system displaying lifetimes comparable to the *Trp ones (such as ligand recombination times). As a matter of fact, the presence of diatomic ligands in myoglobin introduces more complexity in the relaxation of the system, leading to ligand photolysis upon heme excitation with quantum yield (QY) depending on the ligand itself, e.g. MbCO and MbNO.[12] After photo-detachment, the ligand can bind back to the heme (geminate recombination) or can diffuse away from the heme before recombining (non-geminate recombination). The case of MbCO shows a pure non-geminate recombination: the ligand detachment occurs with unity QY,[12] followed by sub-ps CO trapping in the closest Xenon cavity,[11] which then recombines to the heme on a 56 μ s timescale as reported by previous time resolved infrared studies.[10] Completely opposite is the case of MbCN, in which the ligand does not undergo photolysis and shows mainly the same timescales of deoxy-Mb,[12, 34, 170] namely a short photo-cycle < 4 ps.[171]

An intermediate case is represented by MbNO, in which the ligand undergoes photo-detachment with a QY of ~55% [12] and recombines non-exponentially with at least three timescales: 8–30 ps, 150–230 ps and a ns component.[12, 172–177] The photolysis of the ligand has strong consequences on the heme, since the iron ion is pulled out of the heme plane and the porphyrin ring bends as shown in Figure 4-4. The latter is known as *heme doming* and it arises from the change of spin state in the iron upon ligand photolysis, which passes from low-spin (Heme-L₂) to high-spin (Heme-L) because of the different ligand field on the iron ion (Figure 4-4). The doming of the heme initiates fluctuations in the tertiary structure of the protein, thus responding to the photolysis of the ligand; moreover, it was suggested that this process is at the origin of the structural changes leading to the cooperative transitions in hemoglobin.[178]

Several experimental techniques can be used to retrieve the afore-mentioned information, each of them targeting a given observable; however, this leads sometimes to a broad distribution of timescales that identify the same process (as shown by the MbNO case). Transient absorption allows probing in the UV-visible and in the infrared range, gathering information on both the electronic and vibrational response of the heme and of the *Trp residues.[15, 172–176] Probing in the infrared region is also useful for investigating on the ligands' vibrational modes, allowing gathering more information on the ligand dynamics themselves.[175, 176] Time-Resolved Resonance Raman (TR³) can give insights on the Raman active modes of the molecule, gathering information on the effect of ligand recombination on the proximal histidine (Fe-N(His)) as well as the Fe-N(porph) stretching modes.[177]

In this Chapter we present the comparison of TA measurements on several Mb complexes, exciting both at 315 nm and 290 nm and probing in the UV-visible (390–700 nm) and/ or in the Mid-IR (1300–2200 cm⁻¹) region. These results elucidate the dynamics of photo-excited tryptophan and its fluorescence quenching by means of interaction with the heme.

4.2 Deoxy–Myoglobin

Deoxy–Mb is the most suitable system to start with when studying excited tryptophan dynamics, because of the absence of diatomic ligands that introduce more complexity to the decay of the system. As a matter of fact deoxy–Mb only shows dynamics related to the heme relaxation, whose longest decay time is $< 4\text{--}5$ ps, giving the possibility to study the response of the system at longer time–delays without interfering processes.

The main drawback of the use of deoxy–Mb is that it is highly sensitive to molecular oxygen, thus needing to be prepared and measured under Argon (Ar) atmosphere and dissolved in degassed solvents.

4.2.1 UV pump–Visible probe

The samples for these experiments were prepared by dissolving ~ 250 mg of horse heart met–myoglobin in 40 mL of 10 mM phosphate buffer aqueous solution at $\text{pH} \approx 7$, to which was added a 2–fold excess of sodium dithionite ($\text{Na}_2\text{S}_2\text{O}_4$), with respect to equimolar quantity, in order to reduce the iron center to the ferrous state. All the reagents were flowed under Ar atmosphere for ~ 30 minutes while the buffer solution (~ 300 mL) was bubbled with Ar for ~ 1 hour. The sample was held in a bottle with a lid containing four small inlets to introduce three Teflon tubes: two to flow the sample and one to introduce an Ar overpressure (~ 1.5 bar) inside the bottle. The fourth inlet was kept free for sample withdrawal (spectroscopic analysis of sample status during the measurements) and dithionite addition if needed. These experiments were performed on the 20 kHz 2D–UV TA setup, with typical pump fluence ~ 0.8 mJ/cm² and an IRF ~ 300 fs. The optical response of the deoxy–Mb was probed in the visible region between 390 nm and 720 nm, and the polarization of the probe was set to magic angle with respect to the pump one.

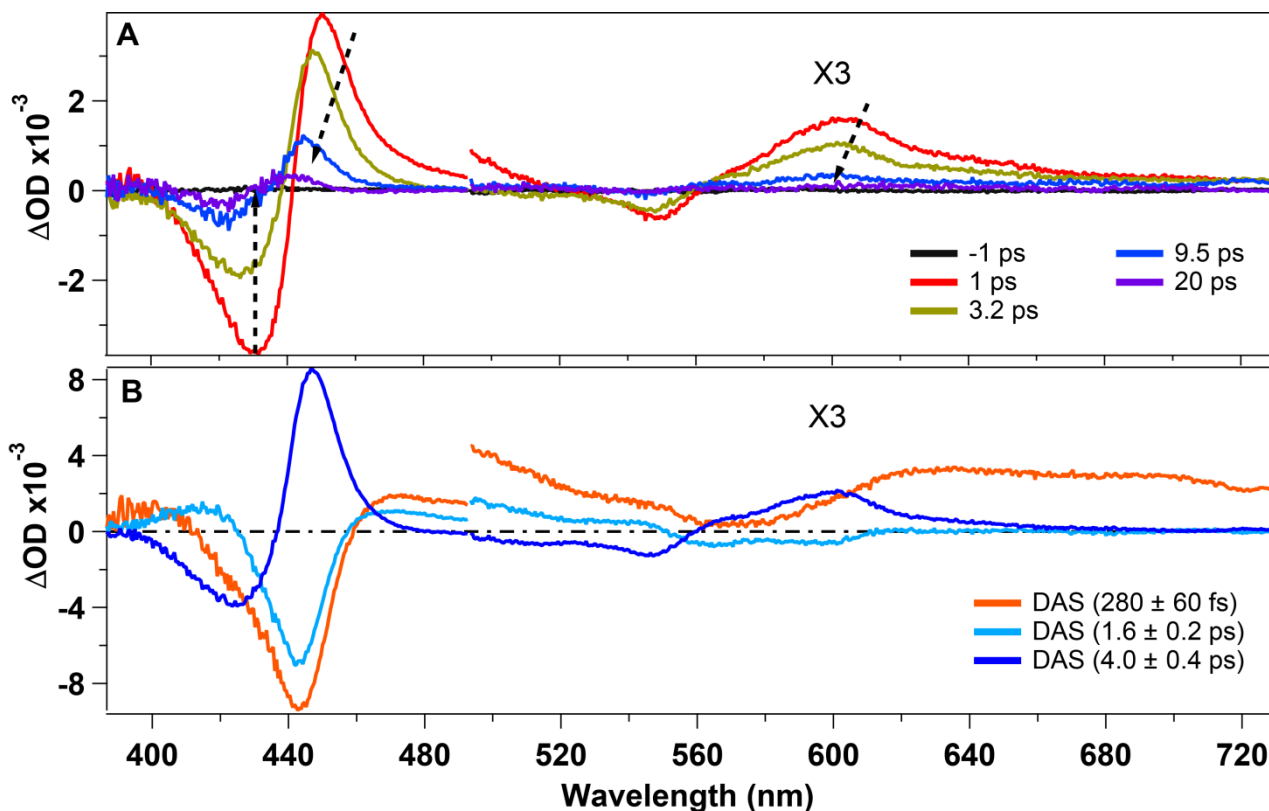


Figure 4-5 Deoxy-Mb transient spectra at selected time-delays upon 315 nm excitation (A) and DAS's related to the characteristic timescales obtained via SVD and GF analysis.

4.2.1.1 Photo-excitation at 315 nm

Figure 4-5A shows TA spectra, at selected pump-probe time delays, obtained upon 315 nm excitation of deoxy-Mb. Two negative features appear at ~430 nm and ~550 nm that are due to GSB of the Soret and Q-bands, respectively (static spectra in Figure 4-2). Positive features, due to ESA, are observed at 450 nm and 600 nm, respectively,[12, 34] which shift to the blue within the first 10–15 ps, while becoming weaker. The apparent shift of the GSB features results from the dynamics of the overlapping ESA contributions. Two mechanisms were proposed to explain the heme photo-cycle, namely the system undergoes VR [12, 34] or relaxes via cascade through spin states.[170] Nevertheless, our purpose here is not to discuss these mechanisms as they occur in the first few ps or so and do not influence the *Trp kinetics we are investigating. The timescales related to the relaxation of deoxy-Mb were retrieved by both an SVD analysis and a GF of selected kinetic traces.

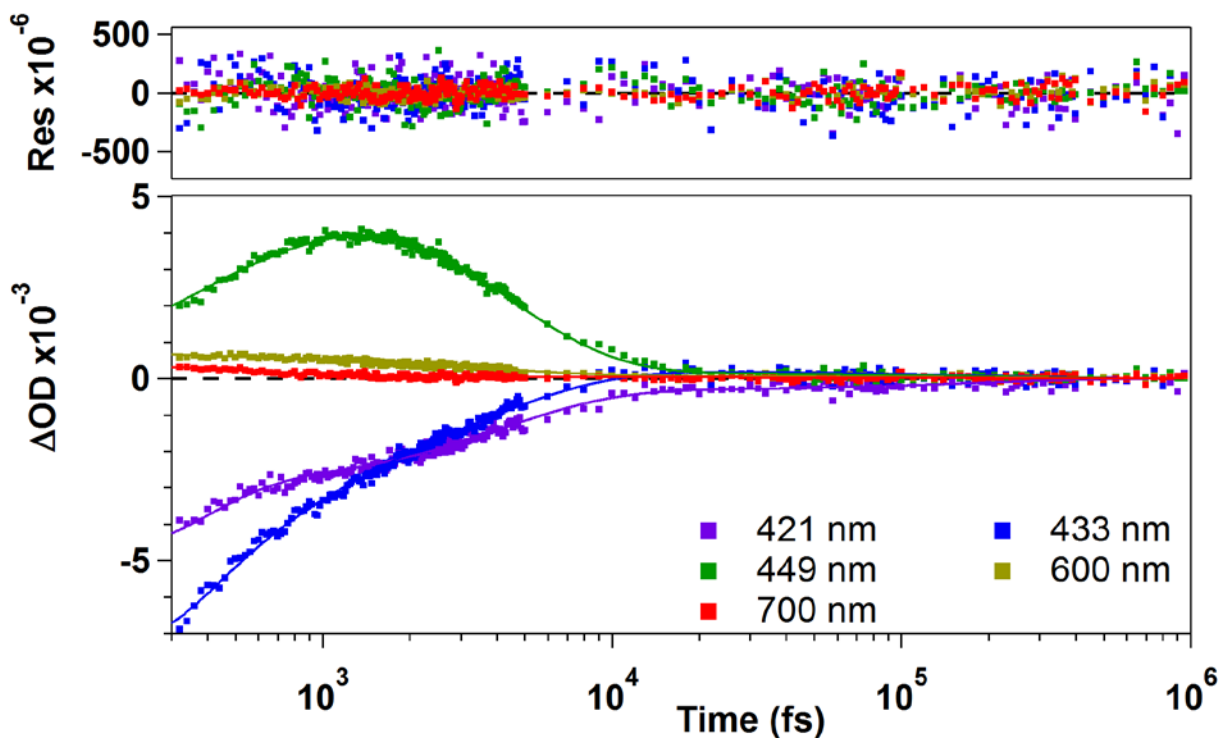


Figure 4-6 Deoxy-Mb kinetic traces at selected wavelengths (colored dots) upon 315 nm excitation, together with best-fit (solid lines). The upper panel shows the scattering of fit residuals

The fit function, used to recover the involved timescales, is a sum of exponential decays convoluted with the instrumental response function (IRF ~ 300 fs), assumed to be Gaussian. The timescales, obtained by a GF of the kinetic traces shown in Figure 4-6, are: 280 ± 60 fs, 1.6 ± 0.2 ps and 4.0 ± 0.4 ps, in agreement with the literature.[34, 170, 179] The large error for the 280 fs contribution results from its proximity to the IRF duration. In Figure 1B we show the Decay Associated Spectra (DAS) obtained from the SVD analysis. The DAS's are due to the amplitudes of the exponential decay functions used to best-fit the data points, allowing defining if a certain feature is decaying or rising. A DAS is related to a particular timescale and it can be read by comparing it with the transient spectrum at the corresponding time-delay. If the amplitude of the DAS has the same sign as the spectrum the feature is decaying, (e.g. a negative DAS in the GSB region) while if the DAS has opposite sign with respect to the spectrum the spectral feature is rising (e.g. a negative DAS in the spectral region corresponding to an ESA feature). As mentioned above, the interpretation of the mechanism related to the heme relaxation is still subject of debate.[12, 34, 170, 180–182]

Our aim here is not to discuss these mechanisms. Important is that the longest timescale in the heme photo-cycle is ~ 4 ps, which is much shorter than the *Trp decay times (~ 20 and ~ 120 ps).

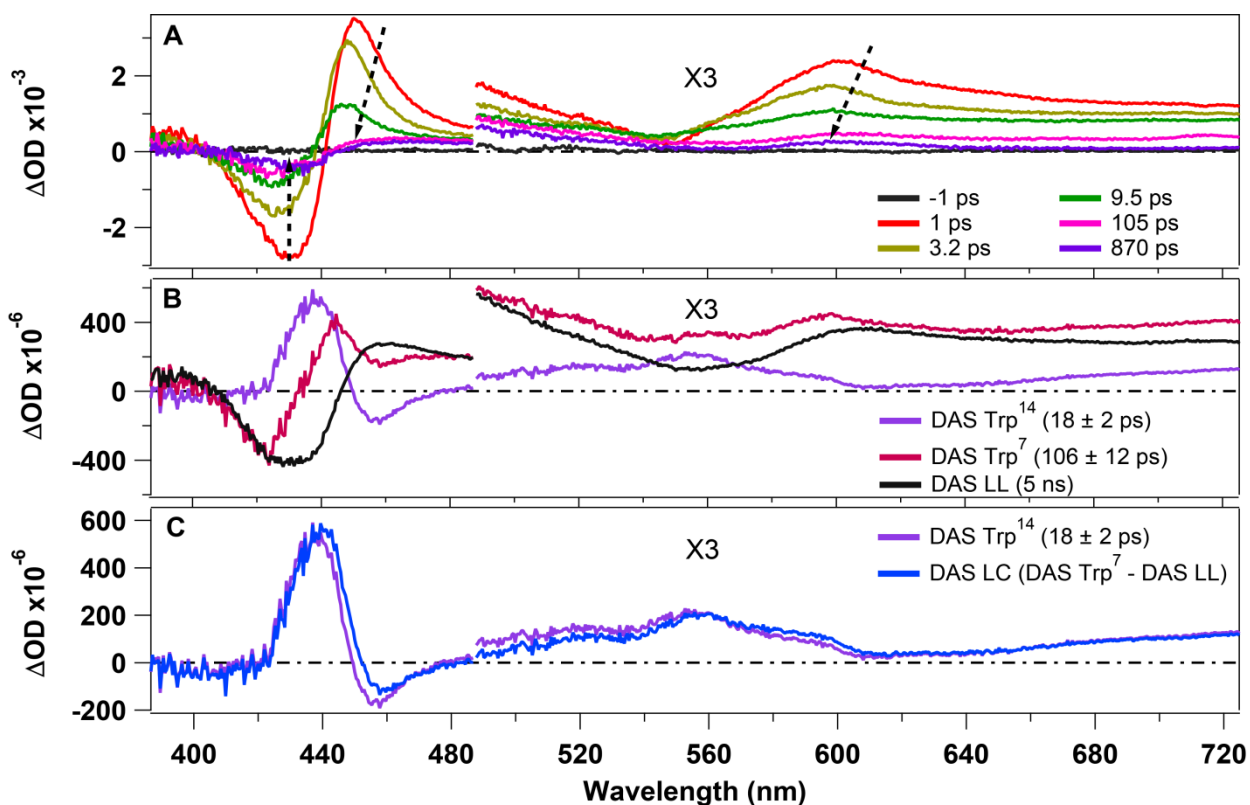


Figure 4-7 Deoxy-Mb transient spectra at selected time-delays upon 290 nm excitation (A), DAS's related to *Trp characteristic decay times (B) and comparison between *Trp¹⁴ DAS and the linear combination of *Trp⁷ and LL DAS's (C).

4.2.1.2 Photo-excitation at 290 nm

Figure 4-7A shows TA spectra at selected time delays, obtained upon 290 nm excitation. They display GSB features at ~430 nm and 550 nm due to the Soret and Q-bands, respectively. The latter is overlapped with a very broad unstructured positive contribution which we assign to ESA of the photo-excited Trp residues.[165] Additionally the two ESA features of the heme (~450 nm and ~600 nm, corresponding to the Soret and Q-band, respectively) are observed for small pump-probe delays. For time-delays < 15 ps, the TA spectra exhibit the same behaviour as upon 315 nm excitation, namely the ESA features shift to the blue and decrease in intensity while the GSB decreases in intensity. However, at longer pump-probe delays the TA signals show a remaining GSB feature at ~430 nm and two ESA features, at ~460 nm and at ~610 nm, respectively (better visible in Figure 4-9B). The TA spectra maintain the same shape from delay times of ~40 ps up to 1 ns, except for a small reduction in intensity (in the entire probe range) in the first hundred ps due to the disappearance of the *Trp¹⁴ and *Trp⁷ ESA.

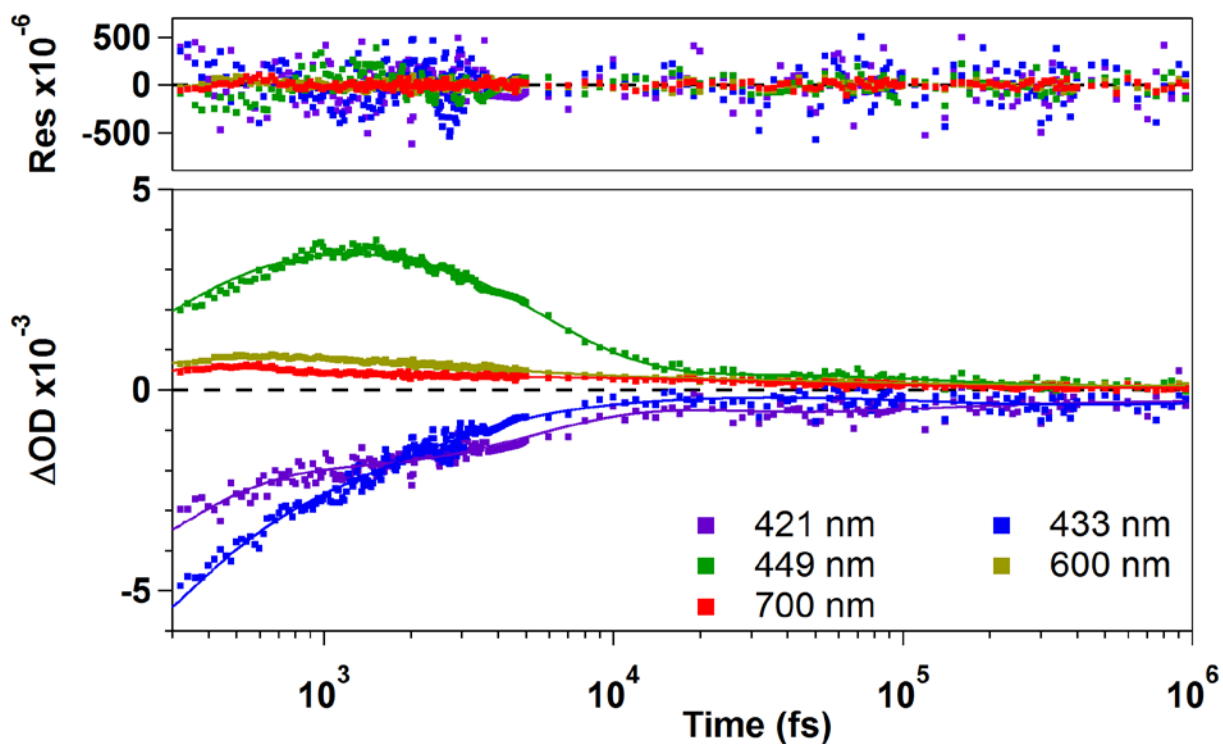


Figure 4-8 Deoxy-Mb kinetic traces at selected wavelength upon 290 nm excitation (colored dots), together with their best-fit (solid lines). The upper panel shows the scattering of the residuals upon best-fit.

Figure 4-9 compares the TA spectra at 900 ps upon 315 nm (panel A) and 290 nm (panel B) excitation. Both the shape and the amplitude of these transients differ strongly, suggesting the formation of a long-lived (LL) photo-product for 290 nm excitation. As this photo-product spectrum displays clear features in the Soret- and Q-band region, it indicates a modification of the heme group. Further it cannot result from a *Trp-heme FRET process, since the heme photo-cycle is very short. The *Trp FRET rate would be the rate limiting step and no LL photo-product would be observed. The data were analyzed both via SVD and GF analysis, in order to determine the kinetics of the spectral evolution. To best-fit the data points six exponential components were used as shown in Figure 4-8, yielding to time constants of: 230 ± 60 fs, 1.5 ± 0.2 ps, 4.4 ± 0.4 ps, 18 ± 2 ps, 106 ± 12 ps and a long component (set to 5 ns) which accounts for the LL signal. All time constants (except for the 5 ns) were free parameters of the fit and the results are in excellent agreement with the decay times for the heme obtained upon 315 nm excitation (see above) and with the literature values for the *Trp decay times.[13, 163] Figure 4-7B shows the DAS's obtained for the *Trp⁷ and *Trp¹⁴ decay times (18 and 106 ps, respectively), together with the DAS corresponding to the LL photo-product. The DAS's assigned to *Trp⁷ and *Trp¹⁴ decays differ significantly, indicating different relaxation pathways.

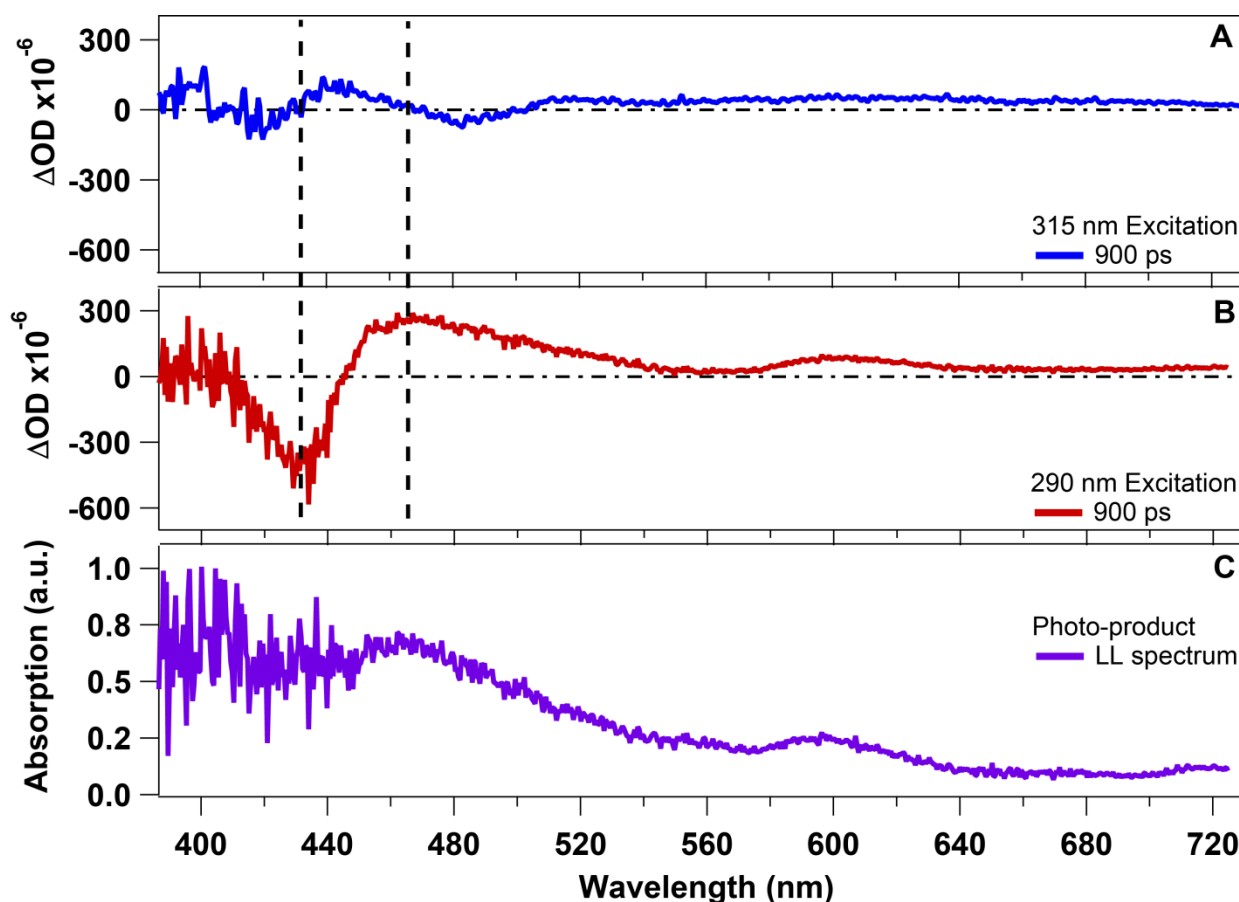
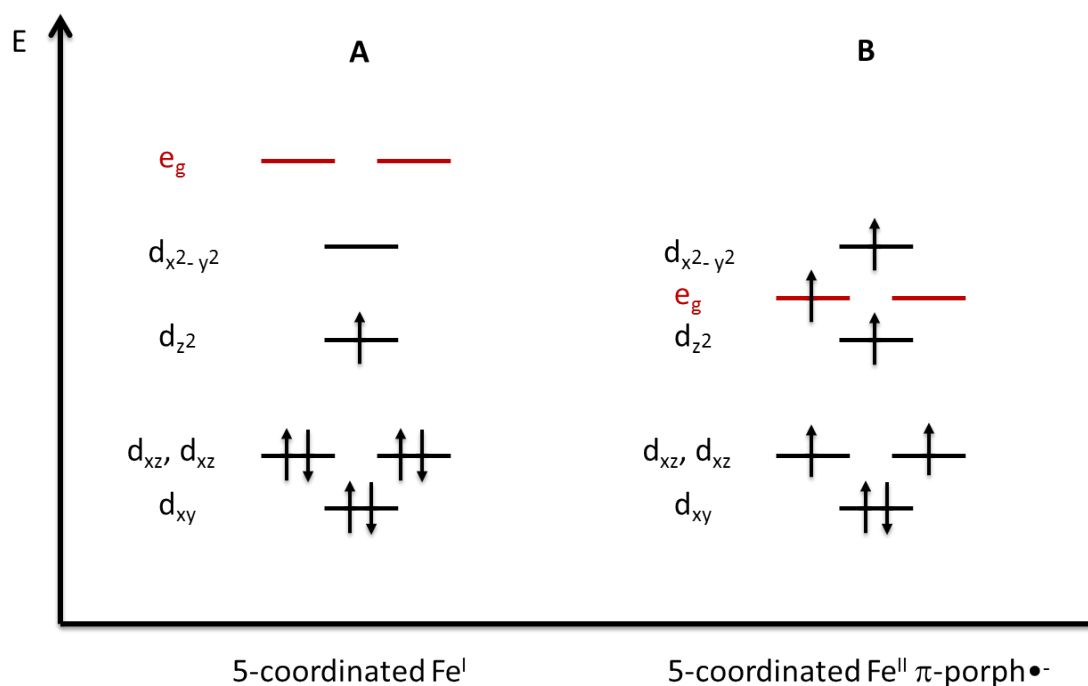


Figure 4-9 Transient spectra at 900 ps of Deoxy-Mb upon 315nm (A) and 290 nm (B) excitation. In (C) is shown the spectrum of the long-lived photo-product obtained by subtracting the GSB to the transient spectrum shown in (B).

The former contains a decay of the *Trp ESA as well as a response of the heme observed on the same timescale, since FRET is the rate-limiting step. The 18 ps DAS (Trp¹⁴) is almost a mirror image of the LL DAS. More precisely, around 430 nm the positive feature in the Trp¹⁴ DAS mirrors the negative feature present in the LL DAS, although it is somewhat narrower. Furthermore, the two DAS mirror each other in the entire range from 460 nm to 730 nm, bearing in mind an overall small positive offset in the Trp¹⁴ DAS. This strongly suggests that *Trp¹⁴ decay feeds the LL photo-product population. The spectral response to excitation of the two Trp residues is likely similar, except for the rise of the photo-product spectrum only occurring upon excitation of the Trp¹⁴ residue. Thus it should be possible to reproduce the Trp¹⁴ DAS with a linear combination (LC) of the Trp⁷ DAS, which represents the response from Trp excitation, and the inverted LL spectrum representing the rise of the photo-product. This is shown in Figure 4-7C, where we compare the linear combination $-LL\ DAS + Trp^7\ DAS$ with the Trp¹⁴ DAS and find excellent agreement demonstrating that indeed, the LL state grows out of relaxation of the *Trp¹⁴ residue.



Scheme 4-1 Schematic representation of metal and porphyrin orbital energies in the case of penta-coordinated Fe^{I} (A) and penta-coordinated Fe^{II} porphyrin π -anion radical (B). The d orbitals of the iron are drawn in black while the e_g orbitals of the porphyrin ring are in red.

As mentioned above, the LL photoproduct must be related to a change of the heme group and is not due to a $^*\text{Trp}$ -to-heme FRET. Since a photo-triggered Trp^{14} to heme electron transfer was already reported for ferric Mbs [15] and since the $^*\text{Trp}$ decay times are almost invariant for all Mbs (Table 4-1), this suggests that a photo-induced Trp^{14} to heme electron transfer also occurs in the ferrous deoxy-Mb. The resulting low-valent heme could either be an Fe^{I} heme or a Fe^{II} -porphyrin π -anion radical ($\text{Fe}^{\text{II}}(\text{porph}^{\bullet-})$) complex, if the additional electron resides on the porphyrin ring.[183-187]

Several studies were performed, with a wide variety of techniques, on low-valent iron complexes, both as Fe^{I} -porphyrin and $\text{Fe}^{\text{II}}(\text{porph}^{\bullet-})$.[184-191] However, a large part focusses on tetraphenyl-porphyrins (TPP) and octaethyl-porphyrins (OEP) in organic solvents.[185, 190] It was concluded that formation of Fe^{I} -porph or $\text{Fe}^{\text{II}}(\text{porph}^{\bullet-})$ depends sensitively on the relative energy of the iron $d_{x^2-y^2}$ orbitals and the porphyrin e_g orbitals, as shown in Scheme 4-1 (reported from ref.[186]). One way to experimentally affect the relative energies of these orbitals, is substitution of the hydrogens in the porphyrin meso positions (e.g. in TPP and OEP).[186]

If electron-withdrawing substituents are introduced in the ring, the energy of e_g orbitals will decrease making the π -anion radicals more likely.[186] On the other hand, if electron-donor groups are present in the ring, the energy of the e_g orbitals will become higher, leading to Fe^I complexes.[186, 187, 192] In the case of the $Fe^{II}(\text{porph}^{\bullet-})$ species, absorption spectra display a broad band centered ~ 700 nm and around ~ 450 nm, and the Q- and Soret bands disappear.[186] The LL photo-product absorption spectrum is shown in Figure 4-9C and it is obtained by subtracting the GSB contribution to the transient signal at 900 ps (Figure 4-9B). It is comparable to the absorption spectrum of the reduced $Fe^{II}(\text{NO}_2\text{-OEP})$, which generates a porphyrin π -anion radical,[186] bearing in mind that this comparison is qualitative as the porphyrin, the solvent and the environment differ. In Figure 4-9C, the Soret- and Q-band are nearly vanished and new bands arise around 450 nm and 600 nm. This comparison leads us to conclude that the anion radical $Fe^{II}(\text{porph}^{\bullet-})$ is formed. This is further supported by cryo-radiolysis experiments [191, 193]. EPR/ENDOR studies show that at ~ 70 K a mixture of $Fe^I\text{-Mb}$ and $Fe^{II}(\text{porph}^{\bullet-})\text{ Mb}$ is generated, in a 9:1 ratio, upon γ -ray irradiation.[191] The authors suggested that different conformations in the frozen protein complexes might explain the simultaneous observation of both species. Annealing experiments hint to the possibility that the decay of Fe^I species could involve intra-molecular electron transfer, leading to the formation of $Fe^{II}(\text{porph}^{\bullet-})$. [191] The latter results suggest that the e_g and $d_{x^2-y^2}$ orbitals are close in energy, leading to the $Fe^{II}(\text{porph}^{\bullet-})$ when the system has the possibility to relax. Low-valent heme species, their nature and relevance under physiological conditions, were also investigated in theoretical studies,[194–196] which also suggest formation of an $Fe^{II}(\text{porph}^{\bullet-})$.

The photoproducts of $^*\text{Trp}^{14}$ -to-heme electron transfer are the protonated Trp π -cation radical ($\text{TrpH}^{\bullet+}$ or $^*\text{TrpH}^{\bullet+}$, for its ground or excited state) and $Fe^{II}(\text{porph}^{\bullet-})$ (or $^*Fe^{II}(\text{porph}^{\bullet-})$). Since the transient spectra at delay times > 40 ps do not display any changes (except for a small vertical offset due to $^*\text{Trp}^7$ and $^*\text{Trp}^{14}$ ESA) it is safe assuming that the $Fe^{II}(\text{porph}^{\bullet-})$ is generated. In the opposite case (generation of $^*Fe^{II}(\text{porph}^{\bullet-})$) different spectral features would have been present in the transient spectra, together with their evolution. Further, if $\text{TrpH}^{\bullet+}$ is generated an ESA feature at 560 nm (absorption band of $\text{TrpH}^{\bullet+}$ [197]) should rise with the $^*\text{Trp}^{14}$ decay time. If instead $^*\text{TrpH}^{\bullet+}$ is generated, some transient features should appear somewhere in the probing region (note that no information is available on $^*\text{TrpH}^{\bullet+}$ absorption bands, but it should show at least an ESA feature in the probed region).

Despite this, the transient spectra do not display any ESA feature around 560 nm, suggesting that the molar extinction coefficient of the generated $\text{TrpH}^{\bullet+}$ (or $^*\text{TrpH}^{\bullet+}$) is too small to detect the produced species. This is in-line with the results on MbCN and met-Mb, in which the Trp radical cation was not detected either in its ground or excited state.[15]

To estimate the QY for the electron transfer, the deoxy-Mb static spectrum (Figure 4-2) has been rescaled to the GSB amplitude of the LL transient spectrum at 900 ps, allowing a rough estimate of the proportion of Mb's with a $\text{Fe}^{\text{II}}(\text{porph}^{\bullet-})$ heme. In this way it was possible to obtain an indirect estimation of the total number of molecules undergoing reduction ($\text{Molec}_{\text{RED}}$), the total number of excited molecules ($\text{Molec}_{\text{EXC}}$) and the excited Trp^{14} percentage ($\text{Exc}_{\text{Trp14}}$). With these three parameters it is possible to obtain the quantum yield for the generation of the photo-reduced species with respect to the total number of excited molecules (QY_{RED}) and with respect to the Trp^{14} (QY_{ET}), as shown in equation(4.1).

$$\text{QY}_{\text{RED}} = \frac{\text{Molec}_{\text{RED}}}{\text{Molec}_{\text{EXC}}} \qquad \text{QY}_{\text{ET}} = \frac{\text{QY}_{\text{RED}}}{\text{Exc}_{\text{Trp14}}} \qquad (4.1)$$

The total number of excited molecules was obtained by summing up all the DAS's and rescaling the absorption spectrum (in the same experimental condition of the measurement) to the GSB amplitude. A similar procedure was followed to account for the number of molecules undergoing photo-reduction: the spectrum was rescaled to the GSB amplitude of the transient signal at 900 ps. The scaling values obtained for the total number of excited molecules was $\text{Molec}_{\text{EXC}} = 0.0257$, while the number of reduced molecules was $\text{Molec}_{\text{RED}} = 0.00112$. To estimate the number of excited Trp^{14} molecules we compare the molar extinction coefficient of heme and Trp at 290 nm, finding that the heme accounts for ~70 % of the total absorption and the two Trp account for ~30%. This implies that ~15% of the excited molecules are Trp^{14} , leading to $\text{Exc}_{\text{Trp14}} = 0.15$. Inserting the numbers in equation (4.1) we can obtain the quantum yield for the total reduction and for the electron transfer process, finding:

$$\text{QY}_{\text{RED}} = 4.4\% \qquad \text{QY}_{\text{ET}} = 29\%$$

The obtained value was divided by the total amount of excited Trp^{14} residues. We find that ~30 % of photo-excited Trp^{14} 's relax via electron transfer to the heme while the remaining relaxes via FRET. Since there are only these two parallel relaxation mechanisms, we can apply the relationship $\text{QY} = k_{\text{et}}/(\sum_i k_i)$ in order to obtain an estimate of the k_{et} , which leads to $k_{\text{et}} = 1/\tau_{\text{et}} = 1.7 \cdot 10^{-10} \text{ s}^{-1}$ ($\tau_{\text{et}} = 60 \text{ ps}$). These values are similar to the ferric Mbs, where the QY was found to be ~60%, [15] implying $k_{\text{et}} = 1/\tau_{\text{et}} = 3.3 \cdot 10^{-10} \text{ s}^{-1}$ ($\tau_{\text{et}} = 30 \text{ ps}$).

4.2.2 UV pump–IR probe

More insights on the nature of the generated photo–product due to *Trp¹⁴–to–heme electron transfer can be obtained by probing in the fingerprint region, which is sensitive to the vibrational modes of the porphyrin ring. As in the previously presented measurements, all the sample handling (from preparation to measuring) was done under inert gas. These experiments were performed at the RAL laser facility.

Lyophilized horse heart met–Mb and Na₂S₂O₄, were purchased from Sigma Aldrich and used as delivered without any further purification. The deoxy–Mb was prepared under inert gas environment, by flowing N₂ in a portable glove box, to avoid presence of hydrogen in the D₂O, oxidation of the reagents and consequent formation of the oxy–Mb complex. The met–Mb was flowed with N₂ in the glove box for ~30 min and then dissolved in freshly prepared degassed phosphate buffer solution (20 mM) at pD 7. A 2–fold excess of sodium dithionite, with respect to the equimolar ratio, was added to the met–Mb solution to obtain the deoxy–Mb. The sample was kept inside an air tight container with an inlet–outlet system to flow the sample through a Harrick cell, which was additionally kept rastering in the x–y plane when measuring so to avoid photo–damaging of the sample. The experiments were performed with a fluence of ~0.8 mJ/cm² and an IRF ≈180 fs. In order to avoid dynamics related to rotational diffusion all the measurements were performed with probe polarization at magic angle with respect to the pump.

4.2.2.1 Comparison of 315 nm and 290 nm photo–excitation

In Figure 4-11 is shown the comparison between transient spectra at selected time–delays obtained upon 315 nm (A) and 290 nm (B) excitation of deoxy–Mb. Recent experiments of Lim et al.[198] on MbCO report on the information obtainable in the fingerprint region (1300–1800 cm⁻¹), which is extremely rich and gives information on the response of the protein’s amide structure[198] and on the heme stretching frequencies.[199] The aim here is to find a marker that allows us to confirm our hypothesis of Fe^{II}(porph^{-•}) generation. All the bands in the 1300–1800 cm⁻¹ probing range show only decaying kinetics upon both 315 nm and 290 nm excitation, except one band (centered at 1720 cm⁻¹) that is present only upon 290 nm excitation, as shown in Figure 4-11B. The transient spectra of Figure 4-11B show that the ESA band rises on a ~20 ps timescale and decays on a much longer timescale than our experimental time–delay (> 3 ns), implying that it derives from the *Trp¹⁴–to–heme electron transfer process.

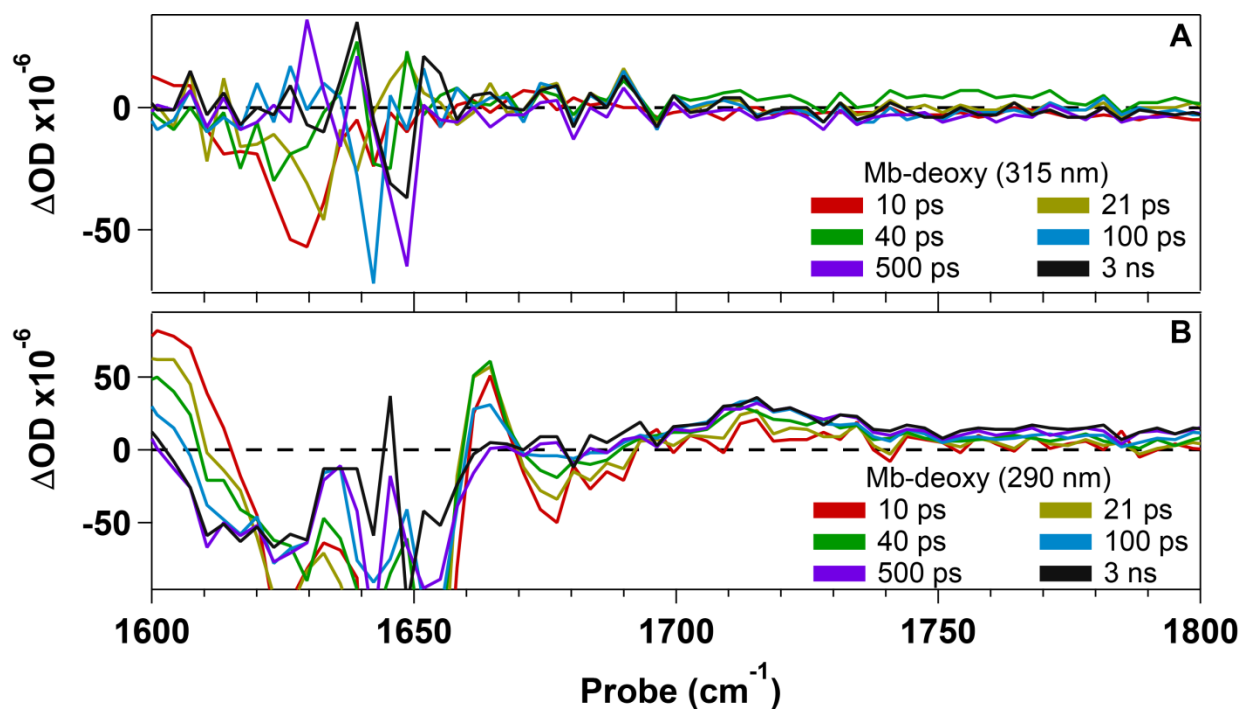


Figure 4-10 Comparison of transient spectra at selected time delays obtained upon 315nm (A) and 290 nm (B) excitation of deoxy-Mb. The selected probe region highlights the band at 1720 cm^{-1} .

The assignment of the 1720 cm^{-1} band can be done by analyzing the previously reported stretching modes in MetMb by Hu *et al.*, [200] which assigned the symmetric $\text{C}_\alpha\text{-C}_m$ to the 1483 cm^{-1} (ν_3) band, the $\text{C}_\beta\text{-C}_\beta$ to 1544 cm^{-1} (ν_2) – 1563 (ν_{11}) cm^{-1} bands and the asymmetric $\text{C}_\alpha\text{-C}_m$ stretching frequency to 1608 (ν_{10}) cm^{-1} (see heme structure in Figure 4-10). The latter modes have a lower frequency than the observed transient band and the presence of an additional electron on the porphyrin ring would lead to the reduction of the reported stretching frequencies, due to the population of a π^* orbital of the porphyrin. However, the C=O stretching frequency of the carboxylic groups present in the porphyrin (see Figure 4-10) is supposed to fall in this region, thus suggesting that the C=O frequency changes because of the change in the nearby electric field due to the additional electron on the heme.

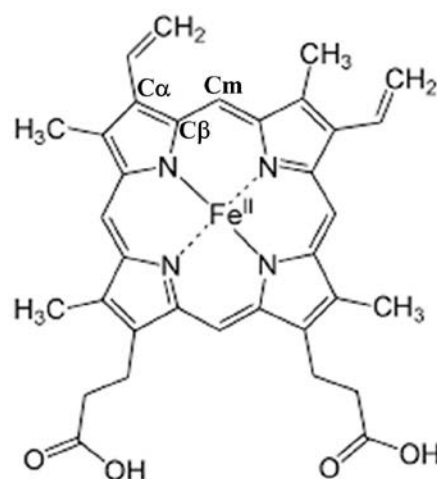


Figure 4-11 Heme representation with C_α , C_β and C_m labelled.

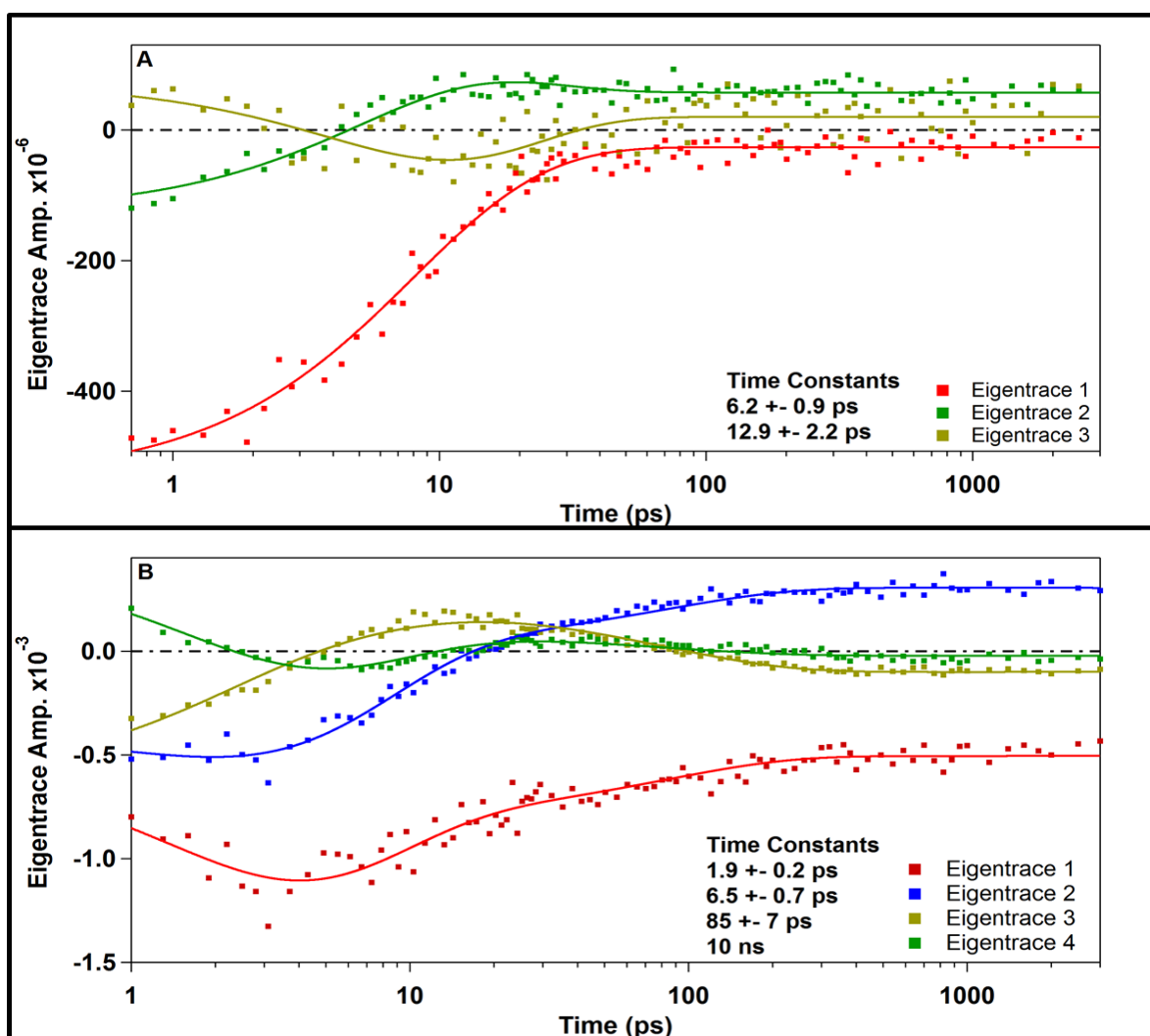


Figure 4-12 GF of the eigentraces obtained upon SVD analysis of the deoxy-Mb data matrix upon 315 nm (A) and 290 nm (B) excitation.

Further, the presence of an additional electron on the heme could lead to structural changes in both the heme and the protein scaffold, thus changing the environment of the carboxylic groups (e.g. more embedded in the hydrophobic environment of the protein) and therefore influencing the C=O stretching frequency. The presence of the 1720 cm⁻¹ ESA band, together with the flat transient absorption in the visible range, suggests the formation of a Fe^{II}(porph^{-•}) in place of a Fe^I-heme. The generation of the latter would strongly influence the Fe-N stretching modes (~400 cm⁻¹), while weakly the C-C frequencies. To investigate the characteristic time constants involved in the heme relaxation process, both an SVD and GF analysis were performed. In Figure 4-12 are shown the best-fit of the most important eigentraces obtained by SVD of the entire data matrix for both 315 nm (A) and 290 nm (B) excitation. When deoxy-Mb is excited at 315 nm, the system recovers non-exponentially with timescales: 6.2 ± 0.9 ps and 12.9 ± 2.2 ps, in perfect agreement with previous experiments.[198]

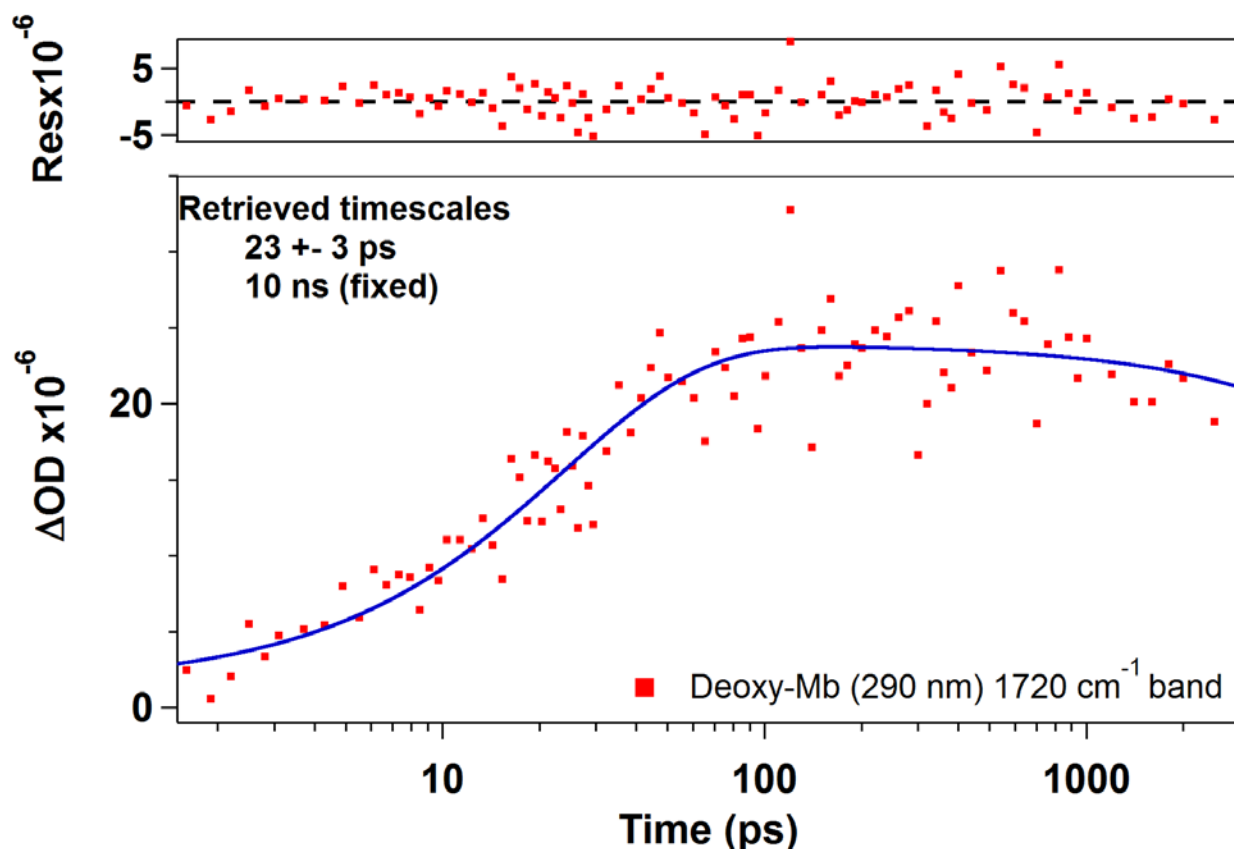


Figure 4-13 Best-fit of the kinetic trace obtained by integrating the entire 1720 cm^{-1} band, together with the scattering of the residual (upper panel).

The rigid offset in the eigentraces 1, 2 and 3, shown in Figure 4-12A, is due to background subtraction problems, interpreted by the SVD as a signal, since we do not expect any LL species upon 315 nm excitation of deoxy-Mb (in agreement Visible probe TA).

Photo-excitation of the system at 290 nm complicates the data, since also some stretching frequencies of the tryptophan residues fall in this probing region. Thus, the GF of the most important eigentraces results in four exponential decays: 1.9 ± 0.2 ps, 6.5 ± 0.7 ps, 85 ± 7 ps and 10 ns (fixed to account for non-decaying signal). The difference in timescales between 315 nm and 290 nm excitation is due to two main reasons: i) upon 290 nm excitation also *Trp contributes to the transient signal in the probed region (1.9 ps and 85 ps) and ii) the formation of LL photo-product accounts for the observed non-decaying component. The 1.9 ps component was not present upon 315 nm excitation (see Figure 4-12), suggesting its correlation to the *Trp . Hence, the latter timescale was assigned to a cooling process of both $^*Trp^7$ and $^*Trp^{14}$. Further, we suggest that the 85 ps component is the sum of several timescales that are impossible to disentangle (in these data), namely: i) the 12.9 ps relaxation of the heme; ii) the 20 ps due to the decay of the $^*Trp^{14}$ and the rise of the photo-product; and iii) the 106 ps relaxation of $^*Trp^7$.

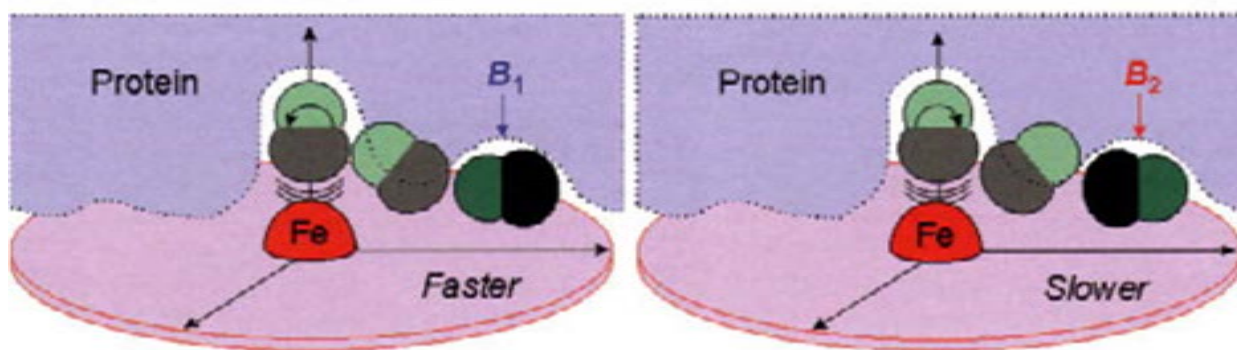
To clearly assess the photo-product generation and its kinetics, we performed the best-fit of a kinetic trace obtained by integrating the 1720 cm^{-1} ESA band (Figure 4-11B). The result of the latter is shown in Figure 4-13, where it is clearly visible that the 1720 cm^{-1} ESA band grows with a ~ 20 ps timescale and does not decay within the experimental pump-probe delay, namely 3 ns. This result is in excellent agreement with the ones obtained from our UV pump-Visible probe transient absorption studies, in which a broad ESA feature (covering the entire visible range) was observed growing on a ~ 20 ps timescale and non-decaying within 1 ns.

More insights on the $^*\text{Trp}^{14}$ -to-heme electron transfer reaction in deoxy-Mb could be obtained by using Marcus theory;^[87] however, many parameters are unknown in the present case (such as estimates of λ and ΔG°), making impossible (at this stage) a deeper analysis of the Marcus region in which this electron transfer occurs.

4.2.3 Deoxy-Mb conclusions

The combination of UV pump-visible probe and UV pump-IR probe transient absorption spectroscopy allowed recognizing the quenching processes of the $^*\text{Trp}^{14}$ in deoxy-Mb, highlighting the formation of a $\text{Fe}^{\text{II}}(\text{porph}^{\bullet-})$ in favor of the Fe^{I} -heme. The transient spectra of the generated photo-product show clear signatures of a porphyrin anion radical in the visible region (Figure 4-9), due to the loss of the intense Soret band. These results coupled with the band at 1720 cm^{-1} detected in the IR region (Figure 4-11), provides a marker to recognize the formation of a π - anion radical through the study of C-C stretching frequencies.

In deoxy-Mb the $^*\text{Trp}^{14}$ -to-heme electron transfer process accounts for $\sim 30\%$ of the quenching, (obtained by the GSB amplitude centered at 430 nm at 1 ns) which is about half of what was calculated in the MbCN case. This result is expected since the standard reduction potential for the couple $\text{Fe}^{\text{II}}/\text{Fe}^{\text{II}}(\text{porph}^{\bullet-})$ is -0.8 V against the $+0.049\text{ V}$ of the $\text{Fe}^{\text{III/II}}$ couple.^[185, 187, 201]



Scheme 4-2 Schematic representation of the heme pocket in MbCO and the CO rotation upon photolysis. The carbon atom is depicted in green while the oxygen atom is depicted in black. This picture is adapted from ref [11].

4.3 Carboxy–myoglobin (MbCO)

MbCO is the best ferrous system to start with when studying the ligand dependence of electron transfer process, since: i) the CO is photolyzed with a unity quantum yield and ii) the CO does not display recombination dynamics in the ps to ns range.[10, 12] Upon CO photolysis the ligand gets trapped in a binding pocket close to the heme in < 1 ps, as reported by previous Time-Resolved IR (TR-IR) experiments from Lim *et al.*[11] In the latter studies they showed that the CO ligand turns both clockwise (B_2) and anti-clockwise (B_1) upon photolysis, being trapped (in both ways) inside a binding pocket close to the heme, as shown in Scheme 4-2 (reproduced from ref. [11]). This gives rise to two metastable states, which are separated by an energy barrier of 1.2–1.5 kcal/mol.[202] The different orientation inside the pocket affects the CO stretching frequency, giving rise to two transient ESA bands peaked at 2120 cm^{-1} (B_2) and 2130 cm^{-1} (B_1), which were investigated via polarization anisotropy.[11] As shown pictorially in Scheme 4-2 the ligand rotates $\sim 90^\circ$ and it is blocked inside the binding pocket parallel to the heme plane; however, the B_1 rotation has to overcome a smaller energy barrier than B_2 , which explains the timescales of 0.2 ps and 0.5 ps, respectively. After this process the protein's scaffold nearby the heme rearranges itself on a 1.6 ps timescales, establishing a potential energy barrier that inhibits the CO geminate recombination process. It is important to mention that in Scheme 4-2 the CO is represented bound to the iron perpendicularly to the heme plane; this is an approximation, since the CO angle, with respect to the normal to the heme plane, is modulated by the distal histidine.[152] Lima *et al* reported the Fe–C bond to have an inclination of 22° with respect to the normal of the heme plane, with the CO inclined 5° with respect to the Fe–C line.[171, 203]

4.3.1 UV pump–IR probe

To investigate the $^*Trp^{14}$ -to-heme electron transfer (in MbCO) two spectral windows were probed: i) the CO stretching frequency (highly sensitive to changes in the environment) and ii) the finger print region (gives information on porphyrin's vibrational modes). The sample was handled and prepared under inert gas, so to avoid deuterium/hydrogen exchange. Lyophilized horse heart met-Mb and $Na_2S_2O_4$, were purchased from Sigma Aldrich and used as delivered without any further purification. The preparation of MbCO was performed in two steps: 1) preparation of deoxy-Mb and 2) introduction of an overpressure of CO gas in the container. The first step is already described in paragraph 4.2.2, which is followed by the introduction of an overpressure of 2.5 bar of gaseous CO for ~5 minutes. The typical change of color and the absorption spectrum (see Figure 4-2) ensures the formation of the MbCO complex. The experiments, both 315 nm and 290 nm excitation, were performed with a fluence of ~ 0.8 mJ/cm², an IRF \approx 180 fs and magic angle polarization between pump and probe pulses.

4.3.1.1 Comparison of 315 nm and 290 nm photo-excitation

Figure 4-14 shows the comparison between transient spectra, at selected time-delays, upon 315 nm (A) and 290 nm (B) photo-excitation. When MbCO is photo-excited at 315 nm, the CO is photo-detached within the IRF with unity QY,[11] thus leading to deoxy-Mb. The transient spectrum in the 1900–2150 cm⁻¹ is composed by a GSB feature (due to the CO stretching) and an ESA feature with a typical double-peak structure. The GSB is detected at 1942 cm⁻¹ with a shoulder at 1933 cm⁻¹ and a low intensity peak at 1966 cm⁻¹ (Figure 4-14A), in agreement with previous measurements.[10, 11, 204] The ESA feature corresponds to the docked CO (Figure 4-14A), which is detected at 2120 cm⁻¹ and 2132 cm⁻¹, in excellent agreement with previous TR-IR measurements.[10, 11] Since the CO recombination is in the order of μ s and the maximum experimental pump-probe delay is 3 ns, we do not expect any evolution of the signal above 1–2 ps. The double peak ESA feature in Figure 4-14A, due to free CO, is not well visible because of the low MbCO concentration in the presented experiments ($[MbCO] \approx 4$ mM) with respect to the one used by Lim *et al* [11] ($[MbCO] \approx 15$ mM).

The transient spectral response of MbCO, upon 290 nm excitation, displays a new ESA band (centered at 1915 cm⁻¹) and the growth of the GSB amplitude with increasing time-delay.

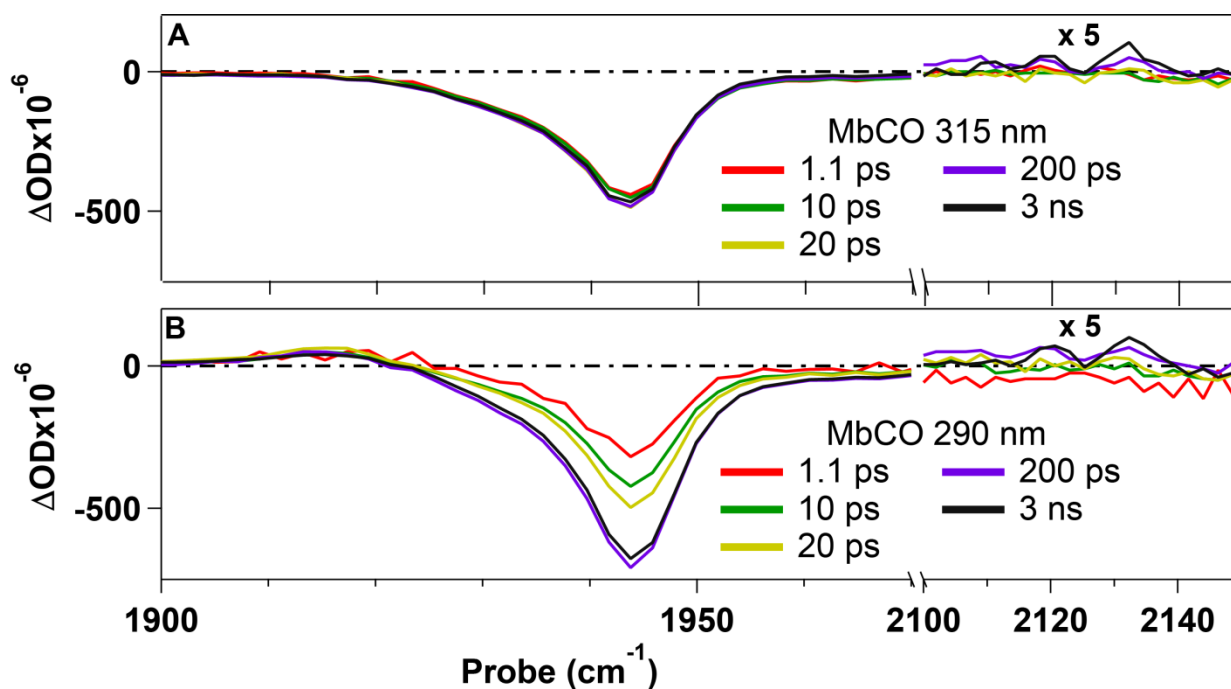


Figure 4-14 Comparison between transient spectra at selected time-delays for MbCO upon 315 nm (A) and 290 nm (B) excitation. The inset in (B) shows the evolution of the 1915 cm^{-1} band. The transient spectra in the 2100-2150 cm^{-1} are multiplied by 5.

A careful analysis of the transient spectra shows that the GSB amplitude grows within the first 100–200 ps, after which the transient spectra do not evolve anymore (see transient spectra at 200 ps and at 3 ns in Figure 4-14). We suggest that the latter is due to the $^* \text{Trp}^{14}$ -to-heme electron transfer process, which induces a change in the CO stretching frequency, thus affecting the GSB amplitude. The electron transfer process induces also the growth of a new spectral feature, namely an ESA band centered at 1915 cm^{-1} (shown in Figure 4-14B), which overlaps (at least partially) with the GSB. The appearance of the 1915 cm^{-1} ESA band only upon 290 nm, as well as its kinetics, suggests that it is related to the $^* \text{Trp}^{14}$ -to-heme electron transfer. If the additional electron is localized on the heme (generating a porphyrin π -anion radical as in the deoxy-Mb case), the CO stretching frequency will be influenced by the different electric field nearby, which leads to a change in frequency and therefore to the ESA band at 1915 cm^{-1} . Beside this, probing in the fingerprint region (upon 290 nm excitation) shows the presence of a broad and unstructured background to which is superimposed a weak band peaking at 1720 cm^{-1} . This result, compared with the deoxy-Mb one, suggests the generation of a Fe^{II} -heme π -anion radical also in the MbCO case. In order to have more information on the kinetics of the system, a GF analysis of the 1915 cm^{-1} , 1945 cm^{-1} and 1720 cm^{-1} bands was performed (only the transients upon 290 nm were analyzed since it is known that upon 315 nm the system does not show any interesting kinetics in the investigated time-delay).

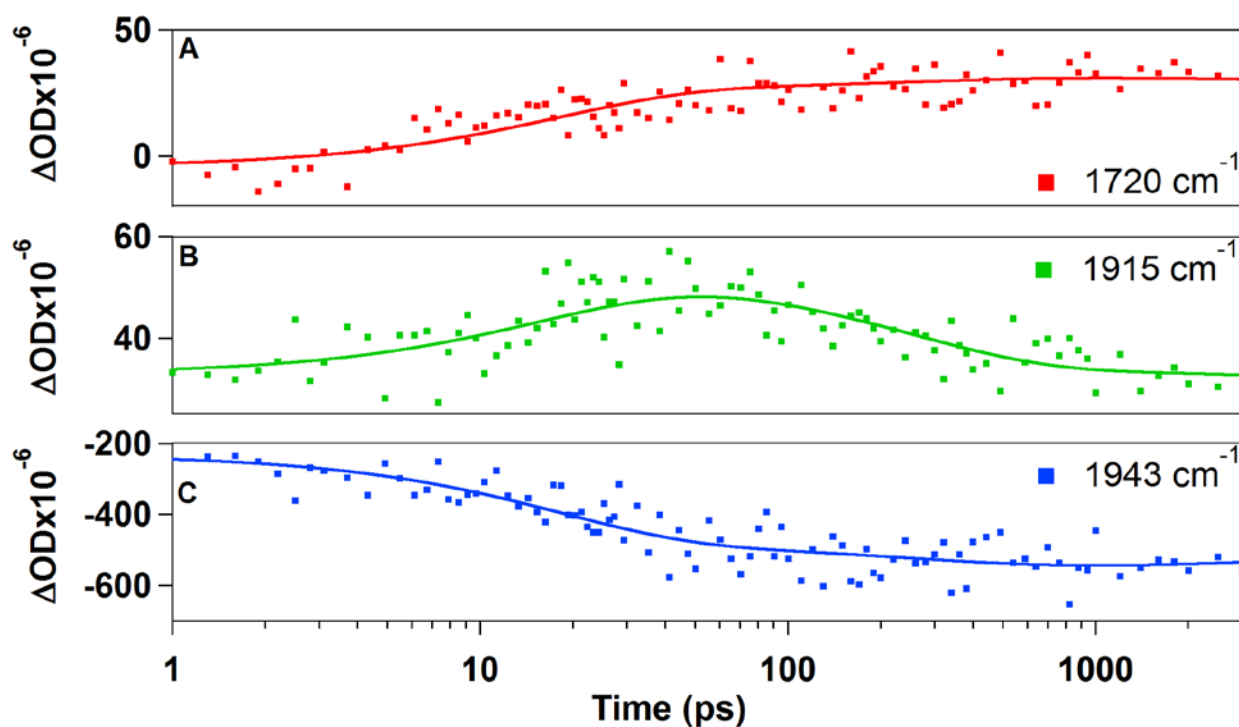


Figure 4-15 Best-fit of the three main bands arising from 290 nm excitation of MbCO: 1720 cm^{-1} (porphyrin π anion radical band) in (A), 1915 cm^{-1} (perturbed CO band) in (B) and 1943 cm^{-1} (CO GSB band) in (C). The kinetic traces are obtained by integration of the above-mentioned bands, in order to obtain a better S/N.

The best-fit of the latter traces is shown in Figure 4-15, displaying a rise on 18 ± 3 ps, in all three cases, followed by a different evolution of the 1915 cm^{-1} band than the GSB and $\text{Fe}^{\text{II}}(\text{porph}^{\bullet})$. While the latter do not show any evolution, the 1915 cm^{-1} band decays on a 260 ± 50 ps timescale. The observed behavior suggests that the $^*\text{Trp}^{14}$ -to-heme electron transfer generates a $\text{Fe}^{\text{II}}(\text{porph}^{\bullet})$, with a lifetime longer than our experimental window, and that this process leads to the CO release. The latter observation stems for a change in the tertiary structure of the protein, maybe due to a structural change of the heme, which implies the detachment of the CO. If this is the case, a rise of the free CO docked in the distal pocket (B₁ and B₂ bands) on a comparable timescale than the decay of the 1915 cm^{-1} band should be observed. Indeed, as shown in Figure 4-16, the B₁ and B₂ bands display a rise of the transient signal on a 223 ± 36 ps timescale, in excellent agreement with the decay of the 1915 cm^{-1} band observed.

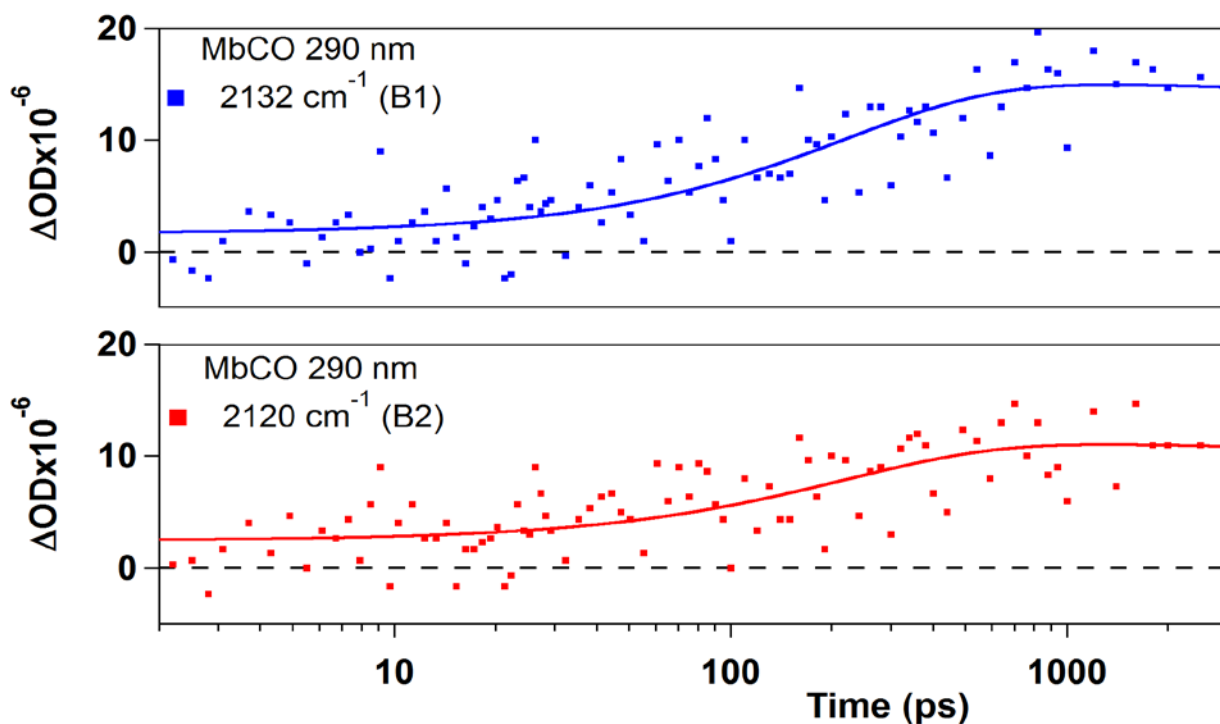


Figure 4-16 Kinetic traces of the free CO bands B₁ at 2132 cm⁻¹ (A) and B₂ at 2120 cm⁻¹ (B) upon 290 nm excitation of MbCO, together with the obtained best-fit.

In order to have more insights on the nature of the generated photo-product, we recall the mechanism of CO coordination with the iron ion and then compare the CO frequency (ν_{CO}) shift in our results (ESA (1915 cm⁻¹) –GSB (1945 cm⁻¹)) with the shift due to reduction of the iron center in some Fe–carbonyl complexes. Comparing such different systems is surely a qualitative approach, but can help suggesting which photo-product is generated upon *Trp¹⁴–to–heme electron transfer. The CO coordination to the metal is given by the sum of two main contributions: 1) a first σ bond occurs through the 2p_z (σ) electron pair of the CO and 2) a d_{π} – p_{π} back-bonding from the metal d orbitals to the π^* (2p_x,2p_y) CO orbitals is established, both decreasing ν_{CO} . In Fe–carbonyl complexes this is quite important, leading to a ν_{CO} shift of ~240 cm⁻¹ between [Fe⁽⁰⁾(CO)₅] (ν_{CO} = 2029 cm⁻¹) and [Fe⁽²⁻⁾(CO)₄]²⁻ (ν_{CO} is 1790 cm⁻¹).^[205] Previous theoretical investigations ^[206] reported smaller ν_{CO} shifts (~120–140 cm⁻¹) between [Fe⁽²⁺⁾(CO)₅]²⁺ (ν_{CO} = 2151 cm⁻¹, 2168 cm⁻¹) and [Fe⁽⁰⁾(CO)₅] (ν_{CO} = 2029 cm⁻¹). In our results the ESA band at ν_{CO} = 1915 cm⁻¹ is shifted by ~30 cm⁻¹ with respect to the GSB peak, as shown in the transient spectra of Figure 4-14B. The latter seems to be too small to account for the generation of a pure Fe^I–heme complex upon *Trp¹⁴– to–heme electron transfer, which would give a ν_{CO} shift \approx 70 cm⁻¹. Beside this, the presence of the weak 1720 cm⁻¹ band suggests some degree of delocalization of the additional electron between the Fe ion and the porphyrin ring.

4.3.2 MbCO conclusions

By comparing the transient signal of MbCO upon 315 nm and 290 nm excitation, we gathered information on the *Trp¹⁴-to-heme electron transfer process. The presence of the 1915 cm⁻¹ ESA band, together with the evolution of the GSB feature of the CO and the 1720 cm⁻¹ ESA band, suggest that the additional electron is delocalized on the heme generating an Fe^{II}(porph^{-•}) that influences the stretching frequency of the bound CO. The latter is confirmed by the small CO frequency shift (~30 cm⁻¹) compared with the ones obtained by the reduction of iron-carbonyl complexes. This is not an unexpected result, since a similar result was obtained in the deoxy-Mb case and it was also predicted by previous EPR-ENDOR measurements of Davydov *et al.*[191, 193] Moreover, these results highlight that the *Trp¹⁴-to-heme electron transfer induces some structural changes in the protein, leading to the dissociation (and immediate docking in the distal pocket) of the CO within 260 ps. Nonetheless, other experiments are needed to completely assess the *Trp¹⁴-to-heme electron transfer process, such as the QY of the process.

4.4 Nitrosyl–myoglobin (MbNO)

As mentioned in Section 4.1, upon MbNO photo–excitation the NO ligand is photolyzed with a QY \approx 50 %.[12] The rebinding kinetics of NO has been investigated by several time–resolved techniques, exciting either in the Soret or Q–bands and probing using TA in the UV–Visible region,[12, 172–174, 207–210] in the Near–IR (NIR),[211, 212] in the Mid–IR [175, 213, 214] and with TR³ spectroscopy.[177] All these studies reported non–exponential rebinding kinetics attributed to NO geminate recombination, whose timescales can be grouped in two main ranges: 10–40 ps and 130–300 ps. (see Table 4–2) Ye *et al* [12] proposed that the fast recombination kinetic is due to a barrier–less NO rebinding from the center of the distal pocket, which lies close to the heme. They argued that this recombination occurs because of the formation of a transition state involving the unpaired NO electron and the Fe’s anti–bonding d_{z^2} orbitals, without distortions in the protein’s matrix.[210] Moreover, the slower component (130 –280 ps) was assigned to the NO recombination from the Xe4 pocket.[155]

Table 4–2 Summary of the NO recombination timescales reported in literature, with the pump wavelength and probing region used. The upper case numbers refers to: 1) single wavelength detection experiments at 480 nm (Soret band); 2) single wavelength detection experiments at 435 nm (Soret band); 3) single wavelength detection experiments at 615 nm (Q bands) and 4) white light super–continuum detection experiments.

Probe region	τ_1 (ps)	τ_2 (ps)	τ_3 (ps)	λ Pump	Ref.
<i>UV-Vis</i> ¹	27.6 (52%)	279.3 (48%)	—————	574 nm	[172]
<i>UV-Vis</i> ²	9.1 (40%)	200 (50%)	∞ (10%)	570 nm	[208]
<i>UV-Vis</i> ¹	13 (40%)	148 (50%)	∞ (10%)	564 nm	[177]
				560–570	
<i>Res. Raman</i> ²	30 \pm 10	—————	—————	nm	[177]
<i>NIR- (Band III)</i> ³	27.5 (42%)	293 (33%)	∞ (25%)	560–570 nm	[211]
<i>Visible</i> ³	12 (40%)	205 (37 %)	∞ (23%)	564 nm	[211]
<i>Mid-IR</i>	42 (29%)	238 (36%)	—————	400 nm	[214]
<i>Mid-IR</i>	—————	133 (46%)	—————	580 nm	[175]
<i>UV-Vis</i> ⁴	13.8 (23%)	200 (33%)	∞ (<3%)	400 nm	[12]
<i>UV-Vis</i> ⁴	8 (30%)	170 (20%)	—————	580 nm	[12]
<i>UV-Vis</i>	13.8 (41%)	200 (59%)	—————	400 nm	[210]
<i>UV-Vis</i>	8 (60%)	170 (40%)	—————	580 nm	[210]

The NO photolysis leads to an impulsive heme *doming*, which is followed by ligand docking in the Xe4 cavity. The protein scaffold reacts to the conformational changes in the heme by rearranging itself, thus giving rise to a small time-dependent energy barrier (~3 kJ/mol).[210] More recent TR³ [177] and NIR (band III absorption) [211] studies reported the presence of an additional 30 ps component, which was interpreted as the time needed for the *domed* → planar transition of the heme. The latter observation suggests that the NO rebinds to a domed heme and the structure remains distorted for some time before going back to the planar configuration.

4.4.1 UV pump-visible probe

The samples for these experiments were prepared by dissolving ~450 mg of horse heart met-myoglobin in 40 mL of 10 mM phosphate buffer aqueous solution at pH ≈ 7, to which was added a 1.5 fold excess to the stoichiometric quantity of sodium nitrite (NaNO₂). To this solution was added a 2-fold excess of Na₂S₂O₄, with respect to the total equimolar quantity needed to reduce both myoglobin and nitrite to nitrogen monoxide (NO). At this point, the NO generated *in situ* binds with the myoglobin generating the MbNO complex. All the reagents were flowed in Ar for ~30 minutes, while the buffer solution (~300 mL) was bubbled with Ar for ~1 hour. The sample was held in a bottle with a lid containing four small inlets to introduce three Teflon tubes: two to flow the sample and one to introduce an Ar overpressure (~1.5 bar) inside the bottle. The fourth was kept free for sample withdrawal (spectroscopic analysis of sample status) and dithionite addition if needed.

These experiments were performed on the 20 kHz 2D-UV TA setup, with typical pump fluence of ~0.8 mJ/cm² and IRF ~120 fs. The optical response of the MbNO was probed in the visible region between 380 nm and 620 nm, where the most important features of the Soret- and Q-bands are present. Finally the polarization of the probe was set at the magic angle with respect to the pump polarization.

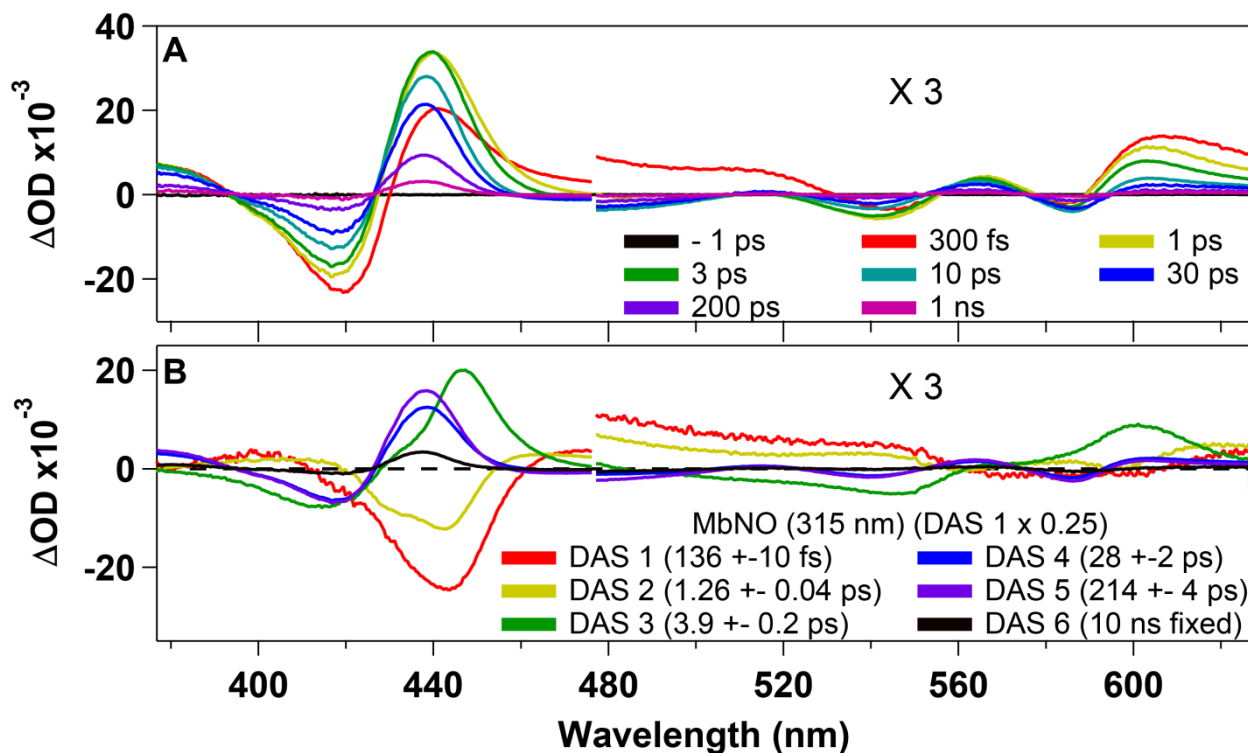


Figure 4-17 Transient spectra at selected time-delays of MbNO upon 315 nm excitation (A) with Q-bands' region multiplied by 3. In (B) are shown the DAS's related to the heme characteristic times (1-3) and to the NO recombination (4-6). DAS 1 is divided by four for the sake of clarity in graph.

4.4.1.1 Photo-excitation at 315 nm

In Figure 4-17 are shown transient spectra of MbNO at selected time-delays upon 315 nm excitation, together with the DAS's obtained by SVD analysis of the data matrix. The transient spectra, shown in Figure 4-17A, display three GSB features at 420 nm, 540 nm and 590 nm and four ESA features at < 390 nm, 440 nm, 570 nm and > 600 nm. The transient features around 400 nm belong to the Soret band, while the ones in the 500–600 nm region belong to the Q-band (Figure 4-17A). As can be seen in Figure 4-17A, the most intense changes occur in the Soret ESA band, whose transient spectrum at 300 fs is very broad and narrows non-exponentially while blue-shifting. As already shown in deoxy-Mb (Section 4.2.1) the short timescales (< 4 ps) are characteristic of the heme dynamics, while all the rest are due to the recombination of the photolyzed NO molecules. In order to retrieve the characteristic decay-times of the system, both SVD and GF analysis of selected kinetic traces were performed. In both cases six timescales were used to best-fit the data points as can be seen in Figure 4-18, where it is shown the best-fit of the most important eigentraces. In the fitting procedure all the amplitudes were let free to change as all the timescales, except the 10 ns component that was used to describe the non-decaying transient signal and thus was fixed.

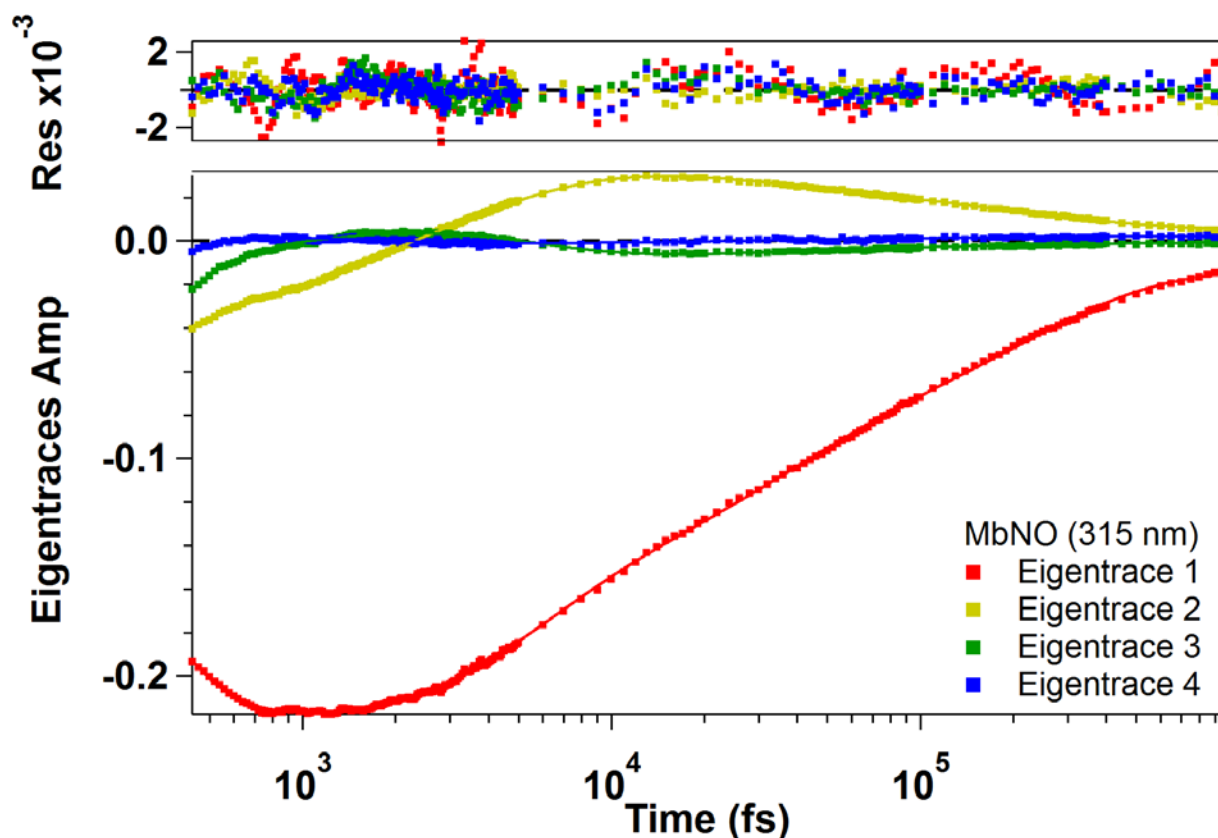


Figure 4-18 Best-fit of the most important eigentraces obtained by the SVD analysis of the MbNO data matrix upon 315 nm excitation, with scattering of the residuals shown in the upper panel.

The timescales obtained by this procedure are: 136 ± 10 fs, 1.26 ± 0.04 ps, 3.9 ± 0.2 ps, 28 ± 2 ps, 214 ± 4 ps and 10 ns, as shown in Figure 4-18. The obtained heme decay constants (136 fs, 1.26 ps and 3.9 ps) are in excellent agreement with the ones in literature, as well as with the deoxy-Mb ones presented in Section 4.2.1.1. The retrieved NO recombination times (28 ps, 214 ps and 10 ns) give some interesting information, showing a slightly longer timescale for the fast recombination dynamics (28 ps) with respect to the results presented in literature using the same technique (8 ps to 18 ps).[12, 172, 176] However, Kruglik *et al* [177] reported the presence of a 30 ps component in their TR³ experiments (sensitive to the Fe-N(Im) stretching of the proximal histidine). They interpreted the latter result as the NO geminate recombination to a *domed* heme.[177] The 214 ps timescale is also comparable to the one reported in other visible probe TA experiments,[12, 172, 176] as well as previous transient X-ray absorption measurements.[171] Finally, by comparing the amplitudes of the 28 ps, 214 ps and 10 ns DAS's at 438 nm, it is possible to obtain the rebinding ratio between the photolyzed NO molecules, namely 40 %, 50 % and 10 %, respectively. The latter observation is in good agreement with the ratios reported in literature (see Table 4-2).

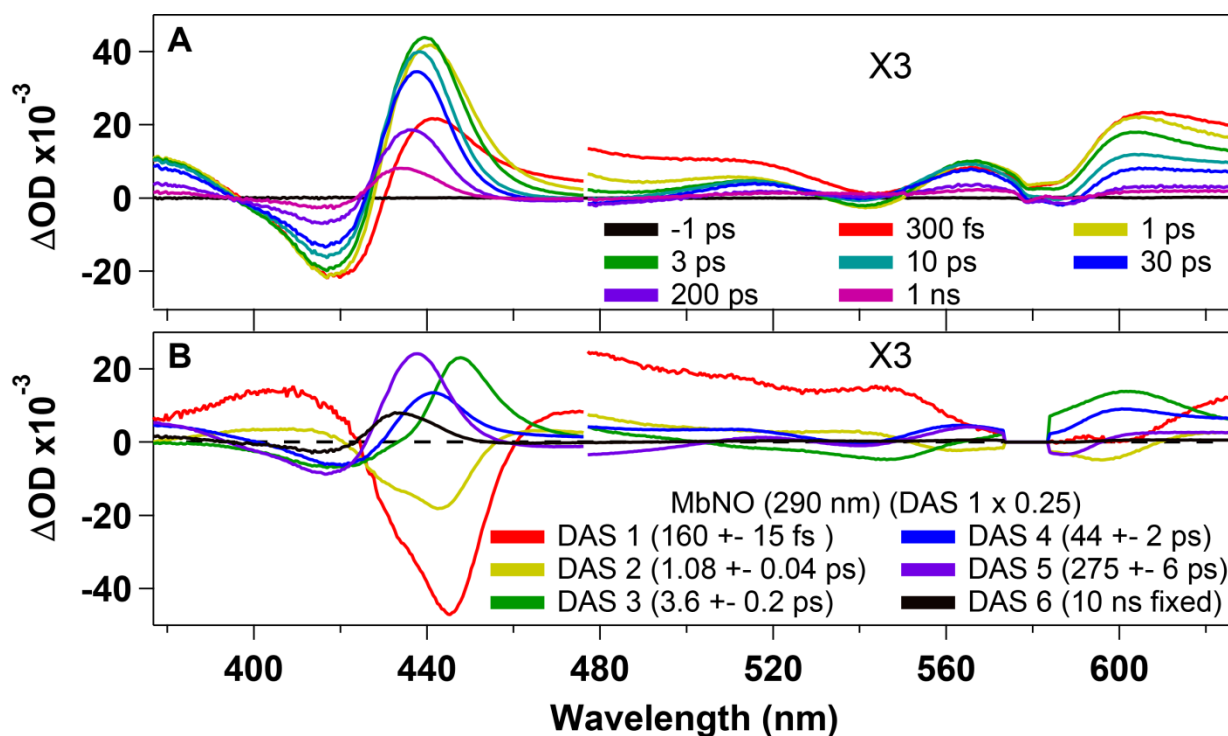


Figure 4-19 Transient spectra at selected time-delays of MbNO upon 290 nm (A), together with a zoom of the Q-band region. In (B) are shown the DAS's obtained by the SVD analysis of the data matrix. DAS 1 is divided by four for the sake of clarity in the graph.

4.4.1.2 Photo-excitation at 290 nm

In Figure 4-19A are shown the transient spectra obtained upon 290 nm excitation of MbNO, which display (within the first 10–15 ps) a similar transient response with respect to the results obtained upon 315 nm excitation. However, several differences can be observed: i) the presence of broad and unstructured ESA band (spanning the entire visible region) due to the $^*Trp^7$ and $^*Trp^{14}$ ESA; ii) the amount of non-decaying transient signal is larger than the 315 nm excitation case; and iii) a blue-shift (~ 4 nm) of the ESA band in the Soret region occurring on a timescale ≈ 350 ps. To estimate the latter value, several transient spectra were normalized at the maximum of the 438 nm ESA band and the obtained points were plotted against the time-delay. The points were best-fit with an exponential function, thus retrieving a timescale of 345 ± 150 ps, as shown in Figure 4-20. The large error on the latter estimation is due to the scattering of the last points, which is related to the larger noise on the signal at long delay-times. The small feature, peaking at 580 nm, in the Q-bands region is not a transient change due to the response of the sample, but a residue of the fundamental wavelength used to generate the 290 nm pump that was not successfully removed via background subtraction.

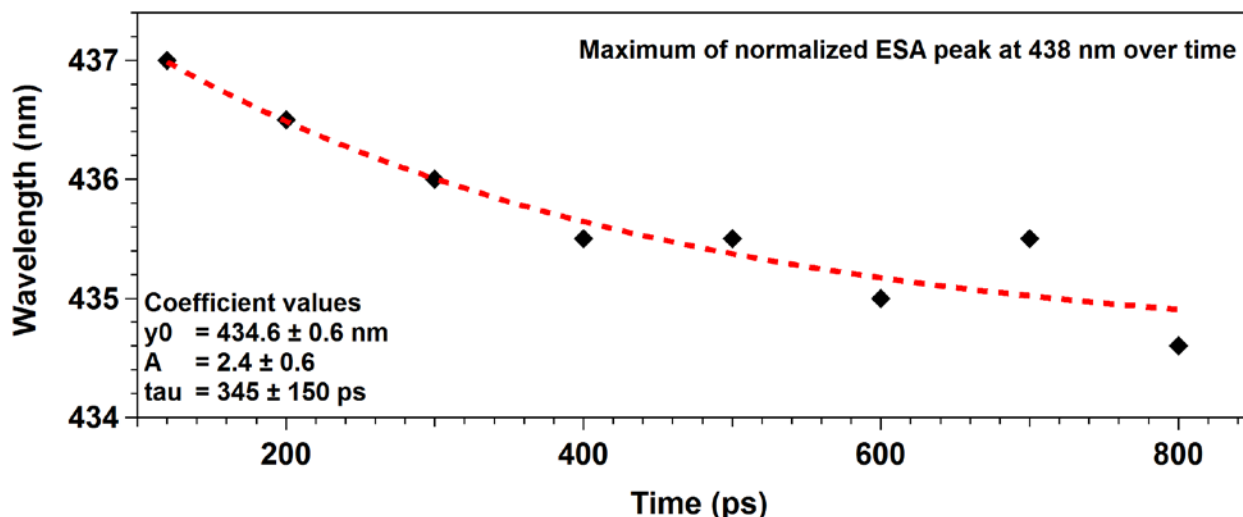


Figure 4-20 Exponential fit of the 438 nm ESA band's shift as function of time - delay. Transient spectra at several time-delays were normalized at the maximum of the Soret ESA band and its maximum was plot as function of time. The function used to best-fit the points is an exponential decay: $y = y_0 + A \exp(-(x - x_0)/\tau)$, where $x_0 = 120$ ps and indicates the position in time of the first point.

As in the 315 nm excitation case, the characteristic timescales were retrieved via both SVD and GF analysis, as shown in Figure 4-21. In order to satisfactorily best-fit the data points six exponential decays were used, while both amplitudes and timescales of each exponential function were let as free parameters (except the 10 ns component). The results obtained by the best-fit are: 160 ± 15 fs, 1.08 ± 0.04 ps, 3.6 ± 0.2 ps, 44 ± 2 ps (*Trp¹⁴ + NO recombination) and 275 ± 4 ps (*Trp⁷ + NO recombination), as shown in Figure 4-19B. The similarity of the retrieved timescales with the 315 nm excitation is not surprising, since the *Trp⁷ and *Trp¹⁴ decays are in the same range as the NO geminate recombination. Nonetheless, a careful analysis of the correlated DAS's reveals some details: 1) the blue-shift observed in the transient spectra is present in the DAS's (from the DAS at 44 ps to the DAS at 10 ns); 2) the different shape of the 44 ps DAS (*Trp¹⁴) with respect to the 275 ps DAS (*Trp⁷) does not involve a simple blue-shift of the latter, thus suggesting the occurrence of some other process on the 44 ps timescale that is not present in the 275 ps DAS; and 3) the ratio between the maxima of the 44 ps, 275 ps and 10 ns DAS's is different with respect to the 315 nm excitation case, being 30 %, 53 % and 17 %, respectively. These observations altogether suggest that, also in this case, a *Trp¹⁴-to-heme electron transfer process occurs; however, the absence of more prominent features does not give hints on the nature of the generated photo-product. Nonetheless, the shape of the transient spectra at long time-delays allows excluding the generation of a Fe^{II}(porph^{•-}), which would lead to strong changes in the Soret-band region (see deoxy-Mb case in Section 4.2.1.2).

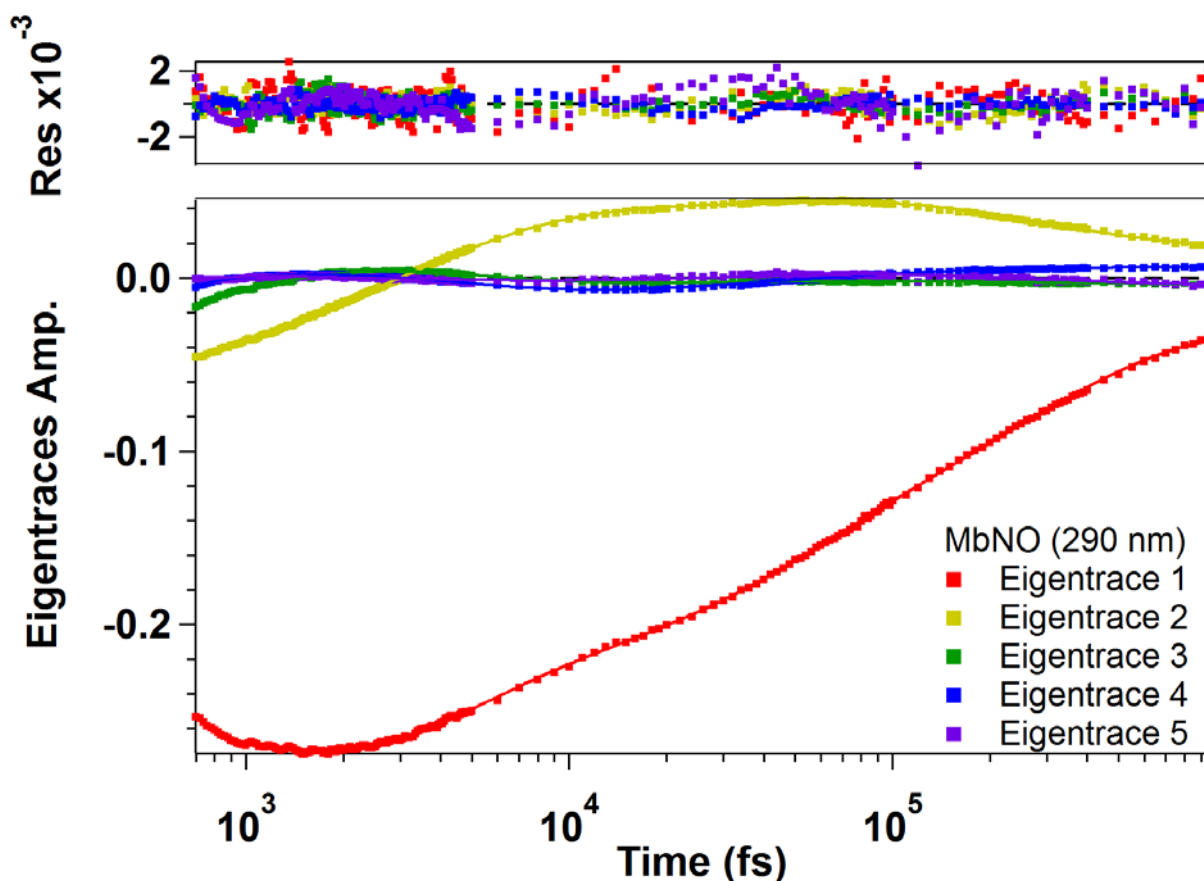


Figure 4-21 GF analysis of the most important eigentraces obtained by the SVD analysis of MbNO upon 290 nm excitation, together with the scattering of the residuals shown in the upper panel.

Therefore, the additional electron of the $^*Trp^{14}$ electron transfer process should reside either on the Fe ion or on the NO ligand. The latter seems more probable, since an involvement of the ligand would not lead to big spectral changes in the visible spectrum, while a reduction of the Fe ion would. Finally, the presence of several processes occurring on a timescale longer than the experimental pump–probe delay does not allow the estimation of the QY for the electron transfer process from the GSB amplitude at 1 ns.

4.4.2 UV pump–IR probe

More information on the $^*Trp^{14}$ electron transfer process in MbNO can be gathered by probing in the Mid–IR region, thus clarifying if the additional electron goes to the ligand or to the heme. The preparation of the sample is similar to the UV pump–visible probe experiments, but deuterated water was used in order to detect clearly the NO stretching frequency.

Moreover, the sample was handled and prepared under inert gas, so to avoid both deuterium/hydrogen exchange and MbNO \rightarrow MetMb degradation.

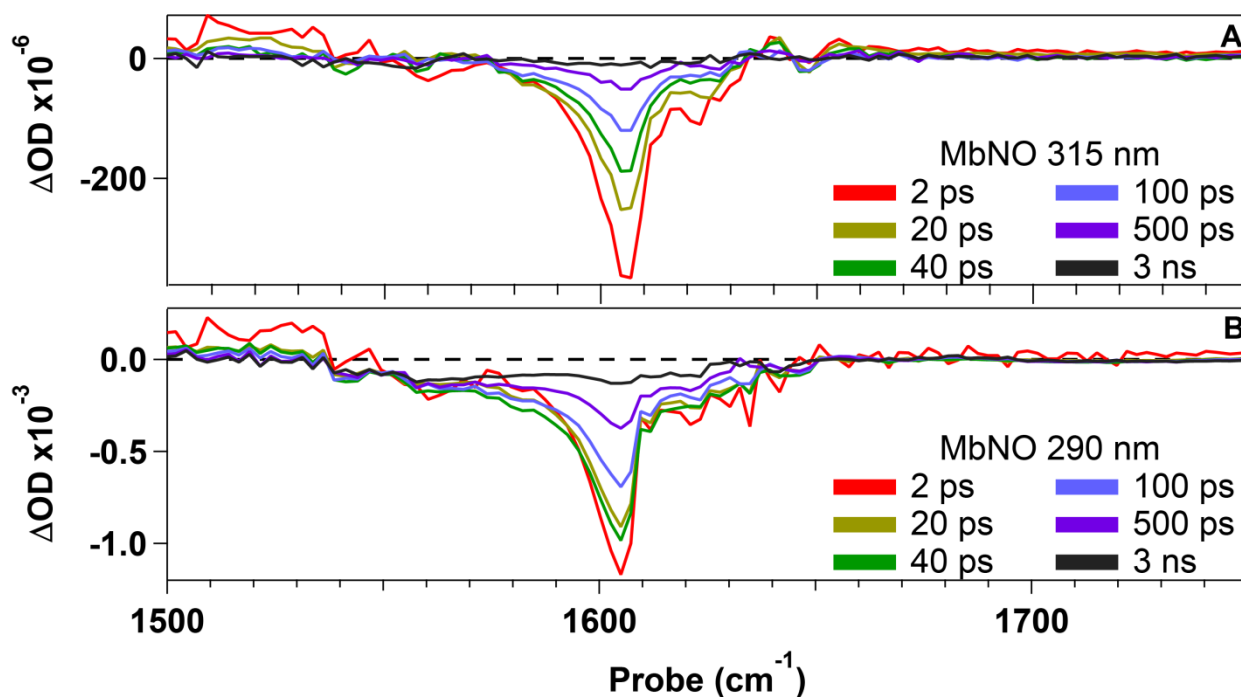


Figure 4-22 Transient spectra at selected time delays upon 315 nm (A) and 290 nm (B) excitation of MbNO.

The experiments were performed with a fluence $\sim 0.8 \text{ mJ/cm}^2$, an IRF $\approx 180 \text{ fs}$ and with the probe polarization set to the magic angle with respect to the pump. The sample was flowed through a $50 \mu\text{m}$ thick flow-cell in a close circuit and kept rastering in the x-y plane.

4.4.2.1 Comparison between 315 nm and 290 nm excitation

Figure 4-22 shows transient spectra, at selected time-delays, upon 315 nm (A) and 290 nm (B) excitation of MbNO. The transient spectra in the $1500\text{--}1750 \text{ cm}^{-1}$ region, upon 315 nm excitation of MbNO, (Figure 4-22) show a broad GSB feature composed of two bands centered at 1607 cm^{-1} (with a shoulder at $\sim 1595 \text{ cm}^{-1}$) and 1621 cm^{-1} that were assigned to different NO conformation inside the protein, as previously reported for 580 nm excitation.[175, 176] At higher frequencies two weak ESA features, centered at 1640 cm^{-1} and 1660 cm^{-1} , can be observed, with a GSB feature between them (centered at 1650 cm^{-1}). The latter features were attributed to the amide I and II bands,[175, 198, 213] thus being not important for the aim of our work. The characteristic timescales of the NO geminate recombination were retrieved by both SVD and GF analysis.

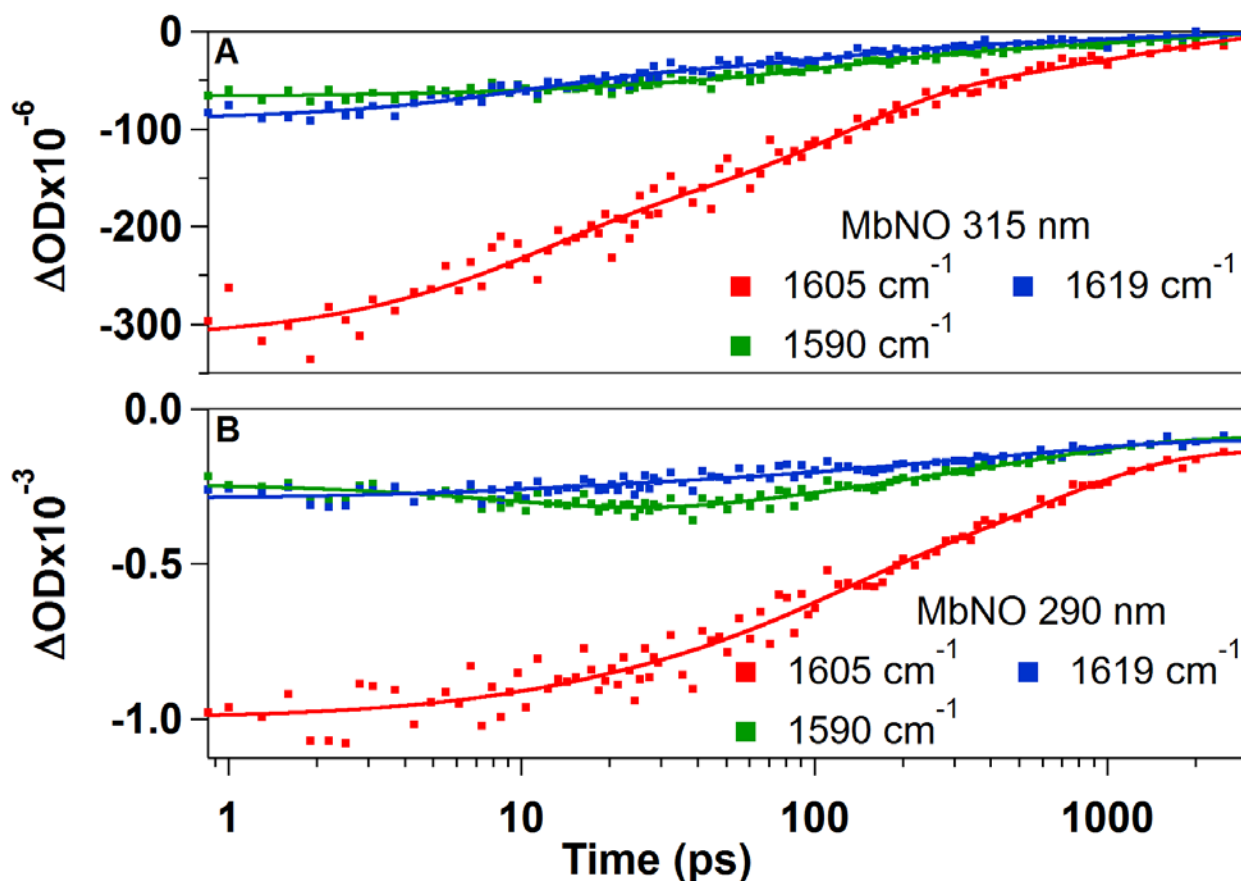


Figure 4-23 GF analysis of three kinetic traces taken in three regions of the GSB feature in the NO stretching region upon 315 nm (A) and 290 nm (B) excitation of MbNO.

The result obtained by GF analysis of three kinetic traces in the NO GSB region is shown in Figure 4-23A. The traces were best-fit by using three exponential decays with timescales of 8.4 ± 0.7 ps, 108 ± 10 ps and 1.7 ± 0.3 ns, in excellent agreement with the NO geminate recombination timescales reported by previous time-resolved IR studies ($\lambda_{exc} = 580$ nm).[175, 213]

The transient spectra of MbNO upon 290 nm excitation (Figure 4-22B), are very interesting since they do not reflect the presence of new spectral features that could allow an immediate recognition of the $^*Trp^{14}$ -to-heme electron transfer process. The latter process seem to be present also in this case, since the comparison of the GSB recovery between 315 nm and 290 nm excitation of MbNO shows interesting differences in the first 50 ps (see 2 ps, 20 ps and 40 ps transient spectra in Figure 4-22). The differences observed in the GSB recovery are due to the overlapping contributions of NO geminate recombination and $^*Trp^{14}$ electron transfer, which occur on comparable timescales, thus leading to a plateau.

Beside the latter observation, it is also important to highlight the absence of the ESA band at 1720 cm^{-1} ; thus suggesting that the porphyrin π -anion radical is not generated during the $^*Trp^{14}$ electron transfer process. In order to retrieve the characteristic timescales of MbNO upon 290 nm excitation, both SVD and GF analysis were performed as displayed in Figure 4-23B. The decay times of $^*Trp^{14}$ and $^*Trp^7$ are very close to the NO geminate recombination timescales, thus the NO recombination's decay times (set to the ones obtained upon 315 nm excitation) were fixed. The 1.8 ns component is incorporated within the 10 ns component, which accounts for the non-decaying signal. The GF procedure converged to the following values: 8 ps (fixed), 16 ± 6 ps, 110 ps (fixed), 580 ± 100 ps and 10 ns (fixed). The 8 ps and 110 ps decays are due to NO recombination, while the 10 ns component accounts for the non-decaying signal (composed of NO recombination plus electron transfer photo-product). The 16 ps timescale matches quite well with the $^*Trp^{14}$ decay-time (and thus the rise of the photo-product due to electron transfer), while the 580 ps timescale could be due to partial back-electron transfer to the $TrpH^{+\bullet}$ (even though we do not have any spectral marker to be sure of it). The latter results highlight the presence of a $^*Trp^{14}$ electron transfer process upon 290 nm excitation of MbNO, showing the presence of two additional timescales. Moreover, the absence of additional ESA features, in the probed spectral region, implies a strong shift of the NO stretching frequency, thus suggesting its shift outside the probe region. The latter case is highly probable since, along all the investigated diatomic ligands, the NO shows the strongest dependence on its environment and on the metal oxidation state.[215] Further, the NO stretching frequency (ν_{NO}) in MbNO varies significantly, showing ν_{NO} shifts of $\sim 300\text{ cm}^{-1}$ from $Mb^{III}NO$ ($\nu_{NO} = 1927\text{ cm}^{-1}$) to $Mb^{II}NO$ ($\nu_{NO} = 1613\text{ cm}^{-1}$) [176, 215] and to $Mb(HNO)$ ($\nu_{NO} = 1385\text{ cm}^{-1}$).[215] The latter case leads also to small changes in the visible spectrum, showing a red-shifted Soret-band with respect to the $Mb^{II}NO$. [215] This observation is in clear contrast with the $\sim 4\text{ nm}$ blue-shift observed in the visible probe experiments, thus allowing us to discard the formation of the $Mb^{II}(HNO)$ complex. Beside these observations, the absence of the 1720 cm^{-1} band implies that no porphyrin π -anion radical is generated. Since both $Fe^{II}(\text{heme}^{\bullet-})$ and $Fe^I\text{-heme}$ are two extreme electromers of the same specie (see paragraph 4.2.2), the absence of the 1720 cm^{-1} band implies (indirectly) that the additional electron is not localized on the Fe ion. Therefore, from our results we suggest the localization of the additional electron on the NO ligand. If this is the case, an $Mb^{II}NO^-$ would be generated via a $^*Trp^{14}$ -to-ligand electron transfer process and, because of the high sensitivity of NO stretching frequency on external perturbations, the transient features of the generated photo-product would be (most probably) shifted outside the probe region.

This hypothesis is in perfect agreement with the cyclic voltammetry results reported by Bayachou *et al.*, [201] which showed the preferential ligand reduction in Mb^{II}NO (embedded in dimethyl–didodecyl–ammonium bromide (ddab) films). They reported two reduction potentials for Mb^{II}NO: i) the reduction potential of the NO (– 0.63 V vs NHE) [201] and ii) the reduction potential of the heme (– 0.85 V vs NHE). [201] The NO value constitutes most probably a better optimized pathway for the *Trp¹⁴ electron transfer process with respect to the *Trp¹⁴ → heme one.

Reduced Fe^{II}–NO complexes [216, 217] (commonly addressed as nitroxyl: NO[–] and HNO) have been recently reported and are described using Enemark–Feltham notation for M–NO complexes (M = generic metal), [218, 219] which reads the number of free electrons on the NO plus the *d* electrons on the Fe, as strongly delocalized on the FeNO fragment (e.g. Mb^{II}NO[–] is a [FeNO]⁸ system). In order to better understand the biological importance of these [FeNO]⁸ complexes (and in general M–NO complexes), their properties have been investigated both experimentally [201, 217, 219–221] and theoretically. [218, 222] Recently, the crucial role of [FeNO]⁸ complexes, in both myocardial [223] and vascular [224] pharmacology, has been pointed out. Hence, the hypothesis of a *Trp¹⁴–to–ligand electron transfer process in nitrosyl– myoglobin might be also an important step in the biological function of MbNO.

4.4.3 MbNO conclusions

The UV pump–Visible probe transient absorption experiments showed that, upon 290 nm excitation of MbNO, the ESA at 430 nm blue–shifts ~4 nm on a 350 ps timescale, showing only a tiny spectral difference in this probe region. Beside this, UV pump–IR probe experiments (NO stretching region) show the absence of any ESA band associated to the generated photo–product frequency, thus underlying the absence of a porphyrin π –anion radical. Further, the generation of a pure Fe^I–heme seems unlikely because of two reasons: i) it should be less stable than the porphyrin π –anion radical [191, 196] and ii) it should lead to strong changes in the visible region, which is not the case of our experimental results. The last possibility is that the additional electron is localized on the ligand, hypothesis that is validated by the strong biological relevance of [FeNO]⁸ complexes [201, 217, 219–221] and the observation of NO reduction in MbNO–ddab thin films. [201] An electron localized on the NO ligand should lead to a strong shift of the NO stretching frequency; however, it is difficult to determine the entity and the direction (lower or higher frequencies) of the shift.

Finally, if $\text{Mb}^{\text{II}}\text{NO}^-$ is the primary photo-product generated by the $^*\text{Trp}^{14}$ electron transfer process, the ligand should undergo some rearrangement (or modification) in order to explain the 350 ps timescale Soret ESA shift. Unfortunately, we do not have the possibility to determine irrefutably the origin of the shift as well as the final product. In order to assess these questions, experiments sensitive to the Fe oxidation state, as well as the NO electronic state, should be performed.

4.5 Cyano–myoglobin (MbCN)

As already mentioned in Section 4.1, MbCN displays a short photo–cycle and the complete absence of ligand photolysis, thus reflecting a transient response similar to the un–ligated forms (e.g. MetMb and deoxy–Mb). Helbing *et al* [225] performed TA experiments exciting in the Soret band and probing both in the visible and in the MIR regions, reporting a photo–cycle < 4 ps.[225] Probing in the CN stretching region gives more insights on the ligand response, displaying the GSB of the CN stretching frequency (ν_{CN}) centered at 2126 cm^{-1} and two ESA bands centered at 2118 cm^{-1} (band **1**) and 2096 cm^{-1} (band **2**).[225] The ESA features in the transient spectra were attributed to a vibrationally hot CN (2118 cm^{-1}) and to a loosely bound CN to the iron (2096 cm^{-1}). Recent 2D–UV and UV pump–visible probe TA experiments by Consani *et al* [15] demonstrated the presence (in both MetMb and MbCN) of a competing pathway in the deactivation of $^* \text{Trp}^{14}$, namely $^* \text{Trp}^{14}$ –to–heme electron transfer process. Their results highlighted that $\sim 60\%$ of excited Trp^{14} undergo electron transfer, while the rest undergoes FRET to the heme. The electron transfer process leads to the generation of a ferrous MbCN, as demonstrated by the static difference between $\text{Mb}^{\text{II}}\text{CN}$ and $\text{Mb}^{\text{III}}\text{CN}$, which partially recovers through back–electron transfer on a ~ 200 ps timescale. On the basis of these experiments, we explore the effect of the $^* \text{Trp}^{14}$ –to–heme electron transfer process on the ligand.

4.5.1 UV pump–IR probe

MbCN was obtained by dissolving the necessary amount of MetMb in 40 mL of deuterated phosphate buffer ($\text{pD} \approx 7$) to obtain a concentration of ~ 4 mM. A 1.5–fold excess with respect to the equimolar quantity of sodium cyanide (NaCN) was added to the MetMb solution in order to obtain the MbCN. Also in this case handling and preparation were performed under nitrogen atmosphere and the obtained solution was flowed through a $50\text{ }\mu\text{m}$ Harrick cell, which was kept rastering in the x–y plane to reduce cumulative photo–damage.

4.5.1.1 Comparison between 315 nm and 290 nm photo–excitation

Figure 4-24 compares the transient spectra of MbCN, at selected time–delays, upon 315 nm (A) and 290 nm (B) excitation. The transient spectra obtained upon 315 nm excitation (Figure 4-24A) show a GSB feature at 2126 cm^{-1} and two ESA features at 2118 cm^{-1} and 2096 cm^{-1} , in excellent agreement with the previous TR–IR studies.[225, 226] In order to retrieve the characteristic timescales of the system, both SVD and GF analysis of selected kinetic traces were performed.

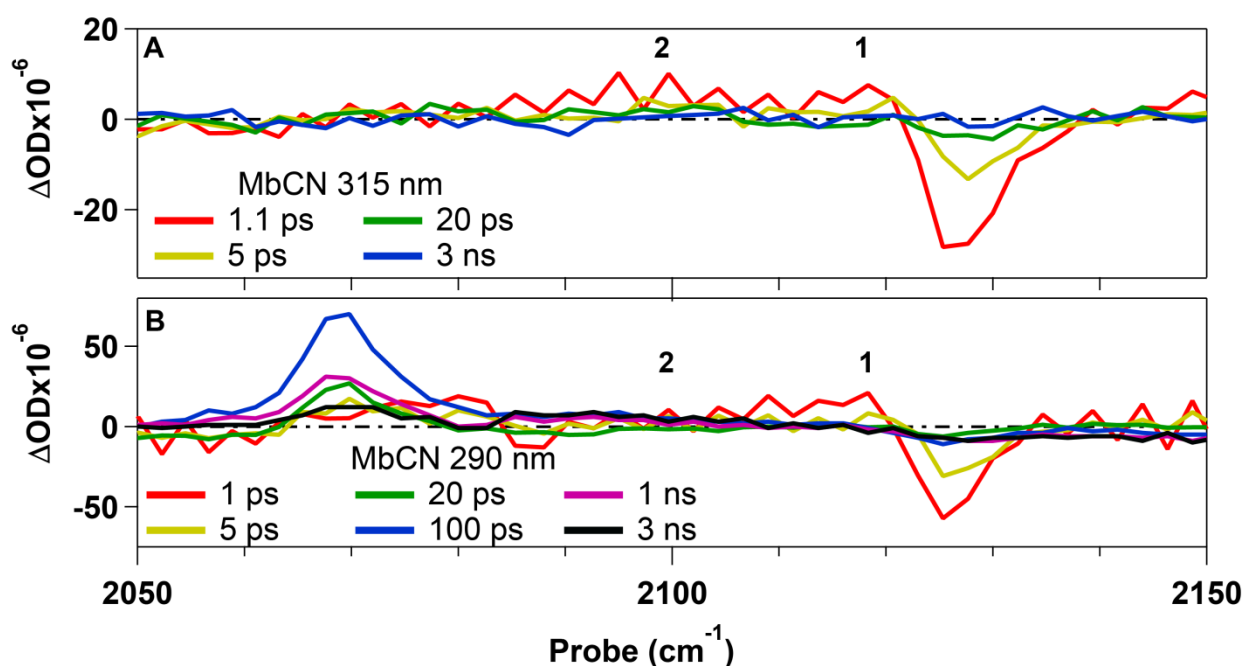


Figure 4-24 Transient spectra at selected time-delays upon 315 nm (A) and 290 nm (B) excitation of MbCN. The numbers 1 and 2 identify the ESA bands at 2118 cm^{-1} and 2096 cm^{-1} , respectively.

The results of SVD analysis are shown in Figure 4-25A, which display an exponential decay of 7.5 ± 1.0 ps; in very good agreement with the values obtained for the other systems (in this work), while it is slightly longer than the 3–4 ps previously reported [225, 226] (previous experiments excited the sample at 400 nm and 575 nm, respectively, which implies a large difference in photon energy between our experiments and the ones reported in literature). The DAS related to the 7.5 ps timescale is displayed in Figure 4-25C, showing a decay of all the features. As shown in Figure 4-24B, the excitation of MbCN at 290 nm shows similar features with respect to the 315 nm excitation during the first 10 ps; however, an additional ESA band centered at $\nu_{\text{CN}} = 2068 \text{ cm}^{-1}$ grows on the timescale of $^* \text{Trp}^{14}$ decay. To obtain more information on the kinetics of the system, the timescales were retrieved via both GF and SVD analyses, as shown in Figure 4-25B. The latter analysis converged on five characteristic timescales: 350 ± 50 fs, 6 ± 1.5 ps, 22 ± 4 ps, 620 ± 180 ps and 100 ns (fixed value accounting for non-decaying signal), with all the decay times (except the 100 ns component) and amplitudes left as free parameters during the fitting procedure. As can be seen in the DAS's shown in Figure 4-25D, the 350 fs decay time appears as decay in the GSB feature and in the ESA bands at 2118 cm^{-1} and 2098 cm^{-1} , suggesting a primary relaxation mechanism of the CN.

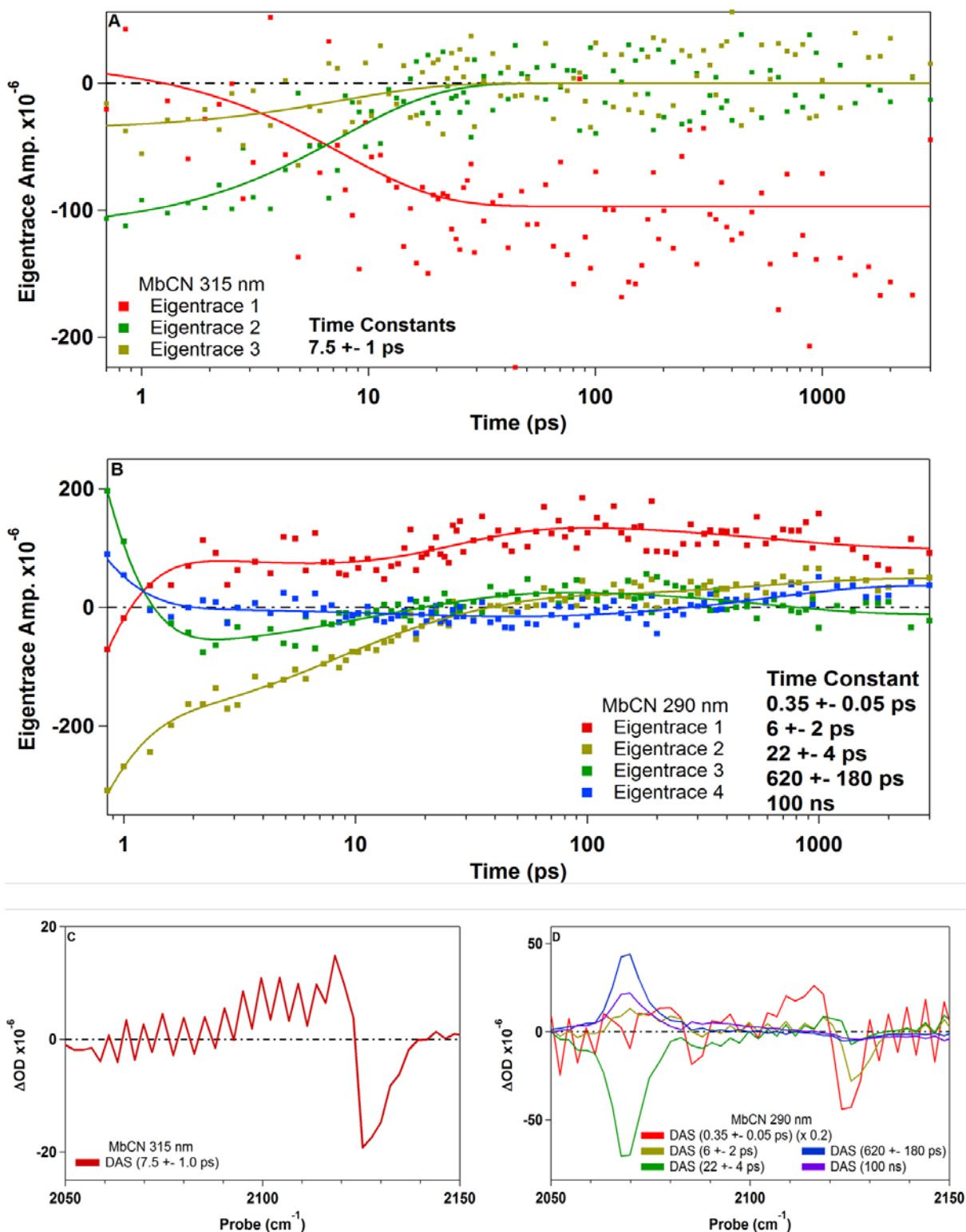


Figure 4-25 GF of the most important Eigentraces obtained via SVD of the MbCN data matrix upon 315 nm (A) and upon 290 nm (B) excitation. The amplitudes obtained from the GF are used to generate the DAS's, which are shown in (C) for 315 nm excitation and in (D) for the 290 nm excitation.

Since these dynamics were not observed upon 315 nm excitation, and since they are on a sub-ps time scale, we suggest that they are due to the extra energy introduced in the system upon 290 nm excitation.

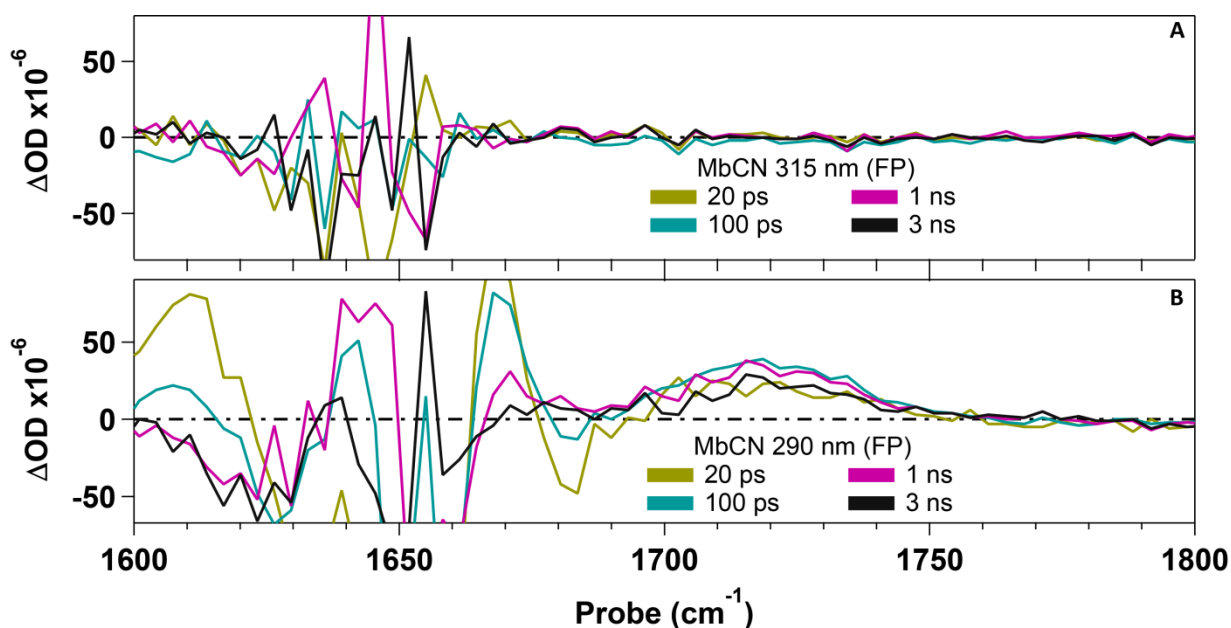


Figure 4-26 Comparison of fingerprint region upon 315 nm (A) and 290 nm (B) MbCN excitation

The 6 ps time scale overlaps within the error with the 7.5 ps found for the 315 nm excitation, pointing to the CN relaxation. Further, the 22 ps timescale is due to the $^*Trp^{14}$ quenching, which leads (partly) to the growth of the ESA band at $\nu_{CN} = 2068 \text{ cm}^{-1}$, in perfect agreement with the previous 2D-UV TA results.[15] Finally, the 620 ps timescale is attributed to a partial back-electron transfer from the reduced haem to the $Trp^{14}H^{+\bullet}$, while the rest decays on a much longer timescale than our experimental pump-probe delay. The 620 ps value is about three times larger than the one found by previous UV pump-Visible probe experiments (~ 200 ps).[15] By comparing the amplitudes of the 620 ps and 100 ns DAS's it is possible to estimate the amount of photo-reduced hemes undergoing back-electron transfer with 620 ps, accounting for $\sim 64\%$ of the total decay of the ESA band (Figure 4-25B). The ESA band due to the electron transfer process ($\nu_{CN} = 2068 \text{ cm}^{-1}$) gives more insight on the photo-product's nature. The detected $\nu_{CN} = 2068 \text{ cm}^{-1}$ does not match with that of free CN ($\nu_{CN_{free}} = 2046 \text{ cm}^{-1}$), HCN ($\nu_{HCN} = 2094 \text{ cm}^{-1}$), or CN^- ($\nu_{CN^-} = 2080 \text{ cm}^{-1}$),[225, 227] allowing us to disregard the generation of these species. Previous 2D-UV TA and UV pump-Visible probe experiments,[15] reported the generation of $Mb^{II}CN$ via the electron transfer process; however, $Mb^{II}CN$ shows $\nu_{CN} = 2057 \text{ cm}^{-1}$,[227] with a shoulder at $\nu_{CN} = 2078 \text{ cm}^{-1}$ that appears at pH 5.6.[227]

The $\sim 10 \text{ cm}^{-1}$ shift, detected in our experiments, shows that the Mb^{III}CN reduction (due to the *Trp¹⁴ electron transfer) does not generate a pure Mb^{II}CN specie, thus suggesting a small percentage of delocalization on the porphyrin ring. This hypothesis is confirmed by probing the 1300–1800 cm^{-1} region, which displays the marker of the porphyrin π -anion radical (1720 cm^{-1} band), as shown in Figure 4-26.

4.5.2 Application of Marcus' theory of electron transfer on MbCN

Marcus' theory of electron transfer (described in Chapter 1 and recalled here) can be used in order to obtain more information on the investigated system, such as the value of the donor–acceptor coupling and if the products are in their ground or excited state. Equation (4.2) relates the electron transfer rate to the coupling element between donor and acceptor ($|H_{AB}|^2$), to the temperature (T), to the free energy of the reaction (ΔG°) and to the total reorganization energy (λ).

$$(4.2) \quad k_{et} = \sqrt{\frac{4\pi^3}{h^2 \lambda k_B T}} |H_{AB}|^2 e^{-\frac{(\Delta G^\circ + \lambda)^2}{4\lambda k_B T}}$$

$$(4.3) \quad \Delta G^\circ = O_{x_D} - Red_A - E_{D^*} + E_{Prod.} - \frac{e^2}{\epsilon} (d_{AD})$$

Equation (4.3) shows that ΔG° depends on the oxidation potential of the electron donor in the excited state (the term $O_{x_D} + E_{D^*}$), the reduction potential of the electron acceptor (Red_A), the energy of generated products (the term $E_{Prod.}$) and the Columbic interaction between products. It is clear from equations (4.2) and (4.3) that, in order to apply Marcus' theory, several parameters need to be estimated, such as the ΔG° , the λ and the $|H_{AB}|^2$. In the case of MbCN the ΔG° and the λ values can be easily obtained, since the self–exchange reorganization energy is well known for the ferric Mb \rightarrow ferrous Mb transition. Using the ΔG° and λ values it is possible to calculate $k_{et}/|H_{AB}|^2$, which can be combined with the experimental k_{et} to obtain an estimation of the $|H_{AB}|^2$ value. The values for direct donor–acceptor coupling depend on the donor–acceptor distance and are usually small for an average center–to–center distance of 15 Å (0.02 cm^{-1}). [85] However, the latter can be strongly modulated by the protein environment and by the presence of residues between donor and acceptor.

Table 4–3 Summary of the λ , ΔG° and $k_{et}/(|H_{AB}|^2)$ values obtained for all the possible scenarios of the ${}^*\text{Trp}^{14}$ -to-heme electron transfer process in MbCN.

	$\text{Mb}^{\text{II}}\text{CN (ES)}$ $+ \text{TrpH}^{\bullet+} \text{(GS)}$	$\text{Mb}^{\text{II}}\text{CN (GS)} +$ $\text{TrpH}^{\bullet+} \text{(ES)}$	$\text{Mb}^{\text{II}}\text{CN (ES)}$ $+ \text{TrpH}^{\bullet+} \text{(ES)}$	$\text{Mb}^{\text{II}}\text{CN (GS)} +$ $\text{TrpH}^{\bullet+} \text{(GS)}$
λ (eV)	0.8	0.8	0.8	0.8
ΔG° (eV)	-1.77	-0.70	0.42	-2.91
$k_{et}/(H_{AB} ^2)$ ($\text{eV}^{-2} \text{s}^{-1}$)	1.96×10^{11}	1.65×10^{16}	2.18×10^8	8.28×10^{-8}

To estimate ΔG° is necessary to determine if the products are generated in their ground state (GS) or excited state (ES); therefore, four main scenarios are possible: 1) $\text{Mb}^{\text{II}}\text{CN (ES)} + \text{TrpH}^{\bullet+} \text{(GS)}$; 2) $\text{Mb}^{\text{II}}\text{CN (GS)} + \text{TrpH}^{\bullet+} \text{(ES)}$; 3) $\text{Mb}^{\text{II}}\text{CN (ES)} + \text{TrpH}^{\bullet+} \text{(ES)}$; and 4) $\text{Mb}^{\text{II}}\text{CN (GS)} + \text{TrpH}^{\bullet+} \text{(GS)}$. There is no experimental or theoretical evidence suggesting one of the proposed scenarios, thus the best option is to calculate the ΔG° value for all the possible scenarios by using the following values: $\text{Trp}_{\text{ox}} = +1$ eV vs NHE,[228] $\text{Fe}^{3+/2+} = +0.046$ eV vs NHE,[229] $E^*_{\text{Trp}} = +3.85$ eV (from Trp fluorescence), $E^*_{\text{TrpH}^{\bullet+}} = +2.19$ eV (from $\text{TrpH}^{\bullet+}$ absorption[197]), $E^*_{\text{Mb}^{\text{II}}\text{CN}} = +1.13$ eV (from $\text{Mb}^{\text{II}}\text{CN}$ absorption[227]) and assuming that the Columbic interaction is negligible with respect to the total value of ΔG° .

The reorganization energy for the donor–acceptor pair (λ_{12}) electron transfer process can be obtained by using Marcus cross relation $\lambda_{12} = \frac{1}{2}(\lambda_{11} + \lambda_{22})$ (where λ_{11} and λ_{22} are the self-exchange reorganization energies for donor and acceptor molecules). The $\text{Fe}^{3+/2+}$ self-exchange reorganization energy has been proposed to be ~ 0.9 eV in cytochrome c,[230, 231] while the $\text{TrpH}^{0/\bullet+}$ self-exchange was estimated to be ~ 0.7 eV within an hydrophobic environment.[232, 233] Therefore, we estimate $\lambda_{12} \approx 0.8$ eV and use it to get the value of $k_{et}/(|H_{AB}|^2)$ for the four scenarios mentioned above (see Table 4–3). As can be seen in Table 4–3, the scenario (3) is the less likely because the electron transfer reaction is endoergonic ($\Delta G^\circ > 0$), while scenario (4) is too exoergonic and falls in the inverse region, thus decreasing the rate of the process. Scenarios (1) and (2) are more likely to occur, as can be seen by the ΔG° and $k_{et}/(|H_{AB}|^2)$ values; however, the evaluation of the $k_{et}/(|H_{AB}|^2)$ shows that (2) has a $k_{et}/(|H_{AB}|^2)$ value orders of magnitude smaller than (1), implying a huge $|H_{AB}|^2 \approx 3000 \text{ cm}^{-1}$. The latter value does not seem reasonable, thus implying that scenario (2) is the best option. Comparison of the λ and ΔG° values in the scenario (2) highlights that the ${}^*\text{Trp}^{14}$ -to-heme electron transfer process (in $\text{Mb}^{\text{III}}\text{CN}$) occurs in the barrier-less region, in which $\lambda \approx -\Delta G^\circ$, as shown in Figure 1-6.

Finally, combining the $k_{et}/(|H_{AB}|^2)$ value obtained by Marcus theory with the experimental value of k_{et} ($\tau_{et} \approx 30$ ps, $k_{et} \approx 3 \times 10^{10}$ s⁻¹), it is possible to estimate a value of $\sim 1.36 \times 10^{-3}$ eV (or ~ 10.5 cm⁻¹) for H_{AB} . The retrieved value highlights the key role of the amino-acid lying between donor and acceptor molecules and how the environment can increase the amplitude of the otherwise small donor-acceptor direct coupling.

4.5.3 MbCN conclusions

The *Trp¹⁴-to-heme electron transfer process in ferrous Mbs was already reported by Consani *et al* [15] that investigated it with both 2D-UV and UV pump-Visible probe TA techniques. However, our UV pump-IR probe experiments show additional details of the process, such as the nature of the generated photo-product and the partial delocalization of the additional electron on the porphyrin ring. Moreover, the selective study of the CN stretching frequency, together with the longer pump-probe delay used, allowed obtaining a more precise value for the back-electron transfer timescale.

Finally, in this case it has been possible to apply Marcus' theory of electron transfer to estimate the value of the donor-acceptor coupling in MbCN. The direct donor-acceptor coupling at a distance of ~ 15 Å is in the order of 0.02 cm⁻¹, [85] with respect to the ~ 10 cm⁻¹ estimated by Marcus calculation. We suggest that this large coupling enhancement is due to the residues lying between the donor and acceptor and that it should be similar in all the myoglobin complexes, thus introducing another piece of information in the wide scenario of the *Trp¹⁴-to-heme electron transfer process in myoglobins.

4.6 General conclusions

The combination of UV pump-Visible probe and UV pump-IR probe TA experiments allowed a deeper understanding on the *Trp¹⁴-to-heme electron transfer process in myoglobins. If the electron transfer from an extremely strong electron donor (*Trp) to a ferric heme seems expected, the same is not for the case of ferrous hemes, which display a much more negative reduction potential (-0.83 V against $+0.05$ V in the ferric case, both vs NHE). [201] Nonetheless, the existence of these low-valent heme species was proposed by both theoretical [195, 196] and experimental [186, 191, 193] studies, but they were never detected in physiological conditions. Our results demonstrate that the electron transfer is indeed an active process in ferrous Mbs (both ligated and un-ligated ones), and that it generates mainly (and most probably exclusively) the Fe^{II}-heme^{-•} electromer.

Moreover, the MbCN results showed that, also in ferric myoglobins, the additional electron is not completely situated on the Fe ion, but it is delocalized between the Fe ion and porphyrin ring. Probing in the ligand stretching region highlighted that the electron transfer process in ferrous Mbs induces some structural changes that influence the tertiary structure of the protein, thus leading to ligand detachment as shown in the MbCO case. This result suggests that the *Trp-to-heme electron transfer process produces a ground state myoglobin in all the studied cases. Comparison of these results with the fluorescence lifetimes of *Trp¹⁴ in Apo-myoglobin and mutated Mbs [167, 169] strongly suggests that the Trp-heme interaction is crucial, but not the sole important parameter in the electron transfer process, e.g. presence of residues or α -helices between donor and acceptor. The latter hypothesis is farther demonstrated by previous investigations on ferric and ferrous cytochrome c (Cyt c), [180, 181] where the Trp residue is at Van der Waals distance with the heme. [234, 235] Consani *et al* reported that the FRET process accounts for 50–70 %, respectively, of the excited tryptophan fluorescence quenching. [180] At Van der Waals distance both FRET ($1/R^6$ scaling), Dexter energy transfer and electron transfer scale (both scaling exponentially with the distance) are quite important, but only a small percentage of long-lived photo-products was reported. Hence, in the Cyt c case it is most likely that Dexter energy transfer process competes with the FRET to quench *Trp fluorescence, while the electron transfer process has a marginal role. Therefore, the factors regulating the *Trp¹⁴-to-heme electron transfer mechanism are (at least): i) the donor-acceptor distance; ii) the amino acids between the Trp residue and the heme; and iii) the presence of the heme and its interaction with the *Trp. An exception to this discussion is the MbNO case, in which the additional electron is localized on the NO ligand. This behavior is due to the reduction potential of the NO (-0.63 V vs NHE), which is bigger than the potential needed to reduce the Fe^{II}(heme) to a Fe^{II}(heme^{•-}) (-0.83 V vs NHE). Moreover, localization of the additional electron on the NO requires less reorganization energy overall, thus creating a more energetically favored pathway for the electron transfer.

Finally, it is imperative to stress the importance of these results in the use of FRET as a “*spectroscopic ruler*”. [64, 65, 70, 236, 237] The latter is indeed a useful tool in distance determination between chromophores, which is the reason why it is largely used in various fields of research, such as biomedical sciences, [238, 239] biochemistry [240, 241] and material science. [242, 243] These results, show important implications in the use of FRET as spectroscopic ruler when tryptophan residues are used as chromophores; nonetheless, in a wider vision, the use of this technique requires more knowledge on the donor deactivation pathways (independent on the system).

As in the case of tryptophan the electron transfer process competes with FRET, other donors could display additional quenching pathways that compete with the FRET, thus leading to wrong distance evaluations.

Chapter 5

5 Prion proteins and their biological role

Prion proteins are responsible for several animal diseases, such as mad cow disease, scrapie in sheep and goats and chronic wasting disease in deer and elk.[244] Prion diseases are found also in humans, such as kuru and Creutzfeldt–Jakob disease (CJD);[16, 245] however, these diseases are quite rare, accounting for about one in a million deaths. Prion–related diseases are generally called transmissible spongiform encephalopathies (TSE), with the prions being present at high concentrations in the central nervous system, although they are expressed in the entire body.[16] Human prions consist of 253 amino acids, containing two attached carbohydrates and a glycosyl–phosphatidylinositol (GPI) anchor in the C–terminal domain, as shown in Figure 5-1A. The NMR structure of the full length protein (residues 23–231)[246] reveals three main regions: i) a flexible region in the N–terminal domain (23–124); ii) a globular domain (125–228) and iii) a short flexible part in the C–terminal domain (229–231), as shown in Figure 5-1B (reproduced from ref. [247]). NMR and X–ray crystallography measurements reported a high α –helical content in the globular region.[246, 248, 249] The misfolding of the globular region in the cellular form of prions (hereafter PrP^C) generates the scrapie isoform (hereafter PrP^{SC}), which is at the origin of prion diseases.[244, 250, 251] The latter shows high β –sheet content together with a high proteinase resistance, but it has an equivalent amino–acid sequence of PrP^C; moreover, the PrP^{SC} works as a template for additional PrP^C \rightarrow PrP^{SC} conversion, thus facilitating a build–up of misfolded protein. The latter mechanism leads to neurodegeneration (Figure 5-1A) and identifies PrP^{SC} as the infecting agent. [247, 251] Both PrP^C and PrP^{SC} are usually anchored to the cell surface through the GPI moiety and introduced in the cell through endocytosis of the membrane, as shown in Figure 5-1A. Previous experiments through genetic techniques on knockout mice,[17, 252] showed that the most important step in contracting the prion diseases is exactly the PrP^C \rightarrow PrP^{SC} conversion and remarked that the biological function of prions has to be subtle.[17, 252] The growing interest in prions and their biological role in animals and humans is due to several factors: i) the transmission of prion–related diseases through contaminating food, transplant tissues or blood could lead to it becoming wide–spread among humans, as in the case of individuals who, upon consumption of infected beef, showed a new–variant of CJD;[245] ii) prion diseases involve deposits of misfolded proteins, thus

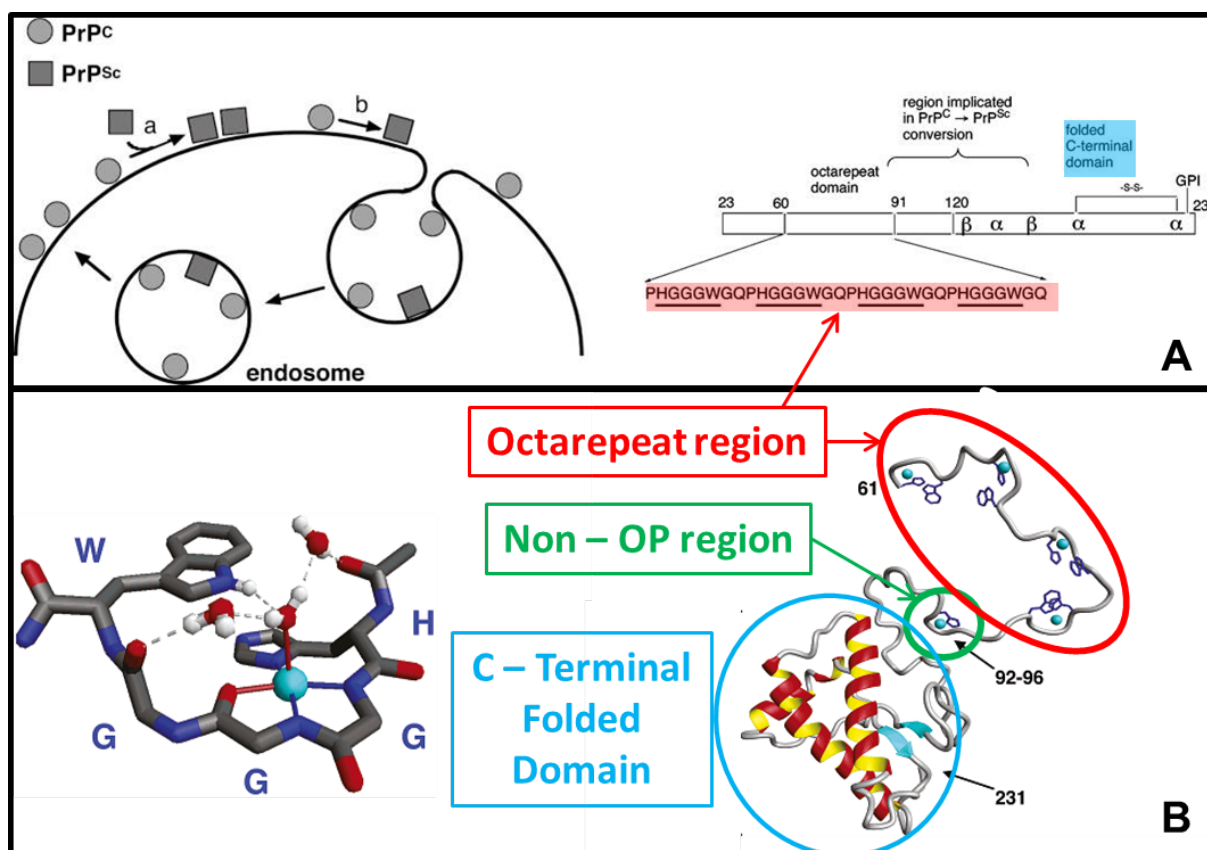


Figure 5-1 In (A) is shown a schematic representation of the cycle of PrP inside the cell by endocytosis, together with a linear scheme of the PrP that highlights the position of the octarepeat region with respect to the folded domain and the region that is responsible for the PrP^C → PrP^{Sc} conversion. The GPI in position 231 indicates the glycoposphatidylinositol membrane anchor that keeps the PrP protein anchored to the cell membrane. In (B) is shown the binding structure of the minimum copper binding moiety HGGGW, together with a more detailed NMR structure of the entire protein. In the latter is highlighted a fifth copper coordination site between residues 92 to 96, defined as the Non - Octapeptide (OP) region. Both figures are adapted from ref. [247]

resulting in the deterioration of nearby neurons; and iii) the prions have an infectious nature, representing a new form of transmission for neurological infections.[247]

Hornshaw *et al* [253, 254] proposed the possible implication of PrP^C in Cu²⁺ binding, which is performed via a domain composed by four or five copies of the amino-acid sequence PHGGGWGQ (P = Proline, H = Histidine, G = Glycine, W = Tryptophan and Q = Glutamine), generally called octarepeat region (hereafter OP4) (Figure 5-1A). This binding moiety is situated in the N-terminal side of the protein and is its most conserved part, thus pointing to its importance in prion biological function.[253, 254] Recently, the presence of other five binding sites in PrPs has been reported (Figure 5-1B): i) two sites between the octarepeat region and the globular region; [255, 256] ii) two sites in the C-terminal region [257] and iii) one non-specific binding site that can bind Cu^{II} when present at high concentrations.[258, 259]

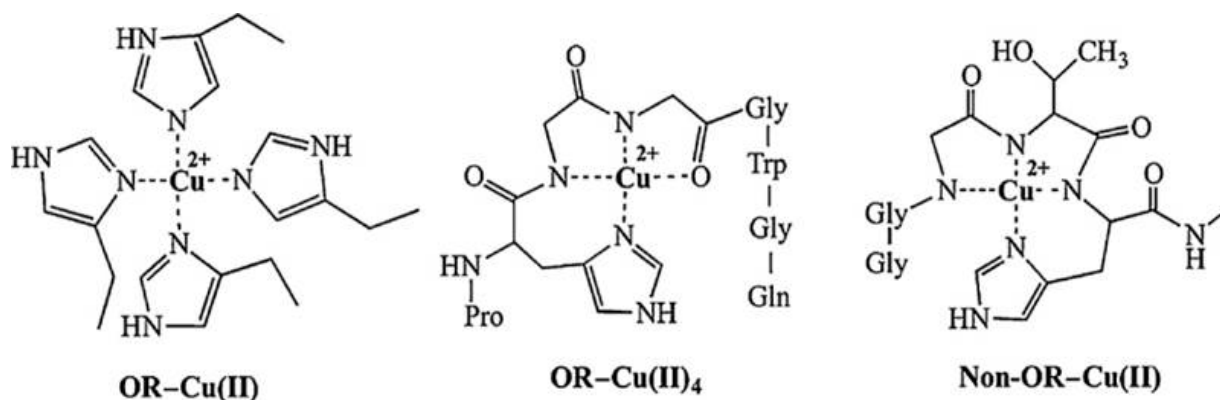


Figure 5-2 Possible complexing modes of copper from the octarepeat region (OR), where OR is equivalent to OP4 used in the text. The first structure from the left (OR-Cu(II)) is the copper complexing mode in a low- occupancy regime, while the central (OR-Cu(II)₄) is the complexing mode in a high-occupancy regime. The Non-OR-Cu(II) is the complexing mode of a different sequence, namely GGGTH (T = threonine). This figure is reproduced from ref. [289]

Brown *et al* [260] reported on the biological importance of Cu binding, showing how the Cu concentration in the brain of PrP-knockout mice is lower than in the wild type. They reported also a highly cooperative Cu binding in PrPs,[260] showing dissociation constants varying from the μM to the nM range at pH 7.4.[261, 262] Previous experiments reported also that Cu^{II} binding in PrPs is pH dependent, displaying the coordination of only two Cu^{2+} ions at pH 6 instead of four–five depending on the PrP.[261, 262] Aronoff–Spencer *et al* [263] performed EPR experiments to identify the smallest binding unit of the octarepeat region, reporting the HGGGW (hereafter OPS) as the fundamental unit that can bind Cu^{2+} in a 1:1 ratio, as shown in Figure 5-1B. More information about the conformation of the binding unit upon copper complexation were obtained by both Raman spectroscopy[264] and X–ray scattering [265] on single crystals, showing that Cu is coordinated by the nitrogen of the imidazole in the histidine, the two nitrogen atoms of the first and second glycines and by the carbonyl group of the second glycine, as shown in Figure 5-1B and Figure 5-2(center). Moreover, the indole NH of tryptophan hydrogen bonds to a water molecule coordinating on the axial position of the Cu ion, thus creating a strongly organized Cu binding unit (Figure 5-1B). The amount of Cu ions bound by the OP4 depends on the pH, thus influencing the binding mode; however, also the Cu–OP4 ratio in solution determines the binding mode of OP4, as shown in Figure 5-2. In a low–occupancy regime only one Cu ion per OP4 unit is present, forming a $\text{Cu}-(\text{N-His})_4$ complex, while in a high–occupancy regime the formed complex is the one shown above for the HGGGW moiety (Figure 5-1B and Figure 5-2). Finally, X–ray absorption spectroscopy measurements on the Cu K–edge, performed by Morante *et al*,[266] have shown inter–molecular copper binding modes at low Cu^{II} concentrations, in which the Cu^{II} ion is complexed by two different OP4 peptides.

Despite the high affinity for Cu^{2+} ions, PrPs display binding affinities for other divalent anions, such as Zn^{2+} , Mn^{2+} , Fe^{2+} , Ni^{2+} , Cd^{2+} and Ca^{2+} . [19, 261, 267] The PrP binding affinity for the Zn^{2+} is 2–3 orders of magnitude lower than to Cu; however, the Zn^{2+} –PrP interaction has garnered attention because 5–15% of the total Zn^{2+} content in the brain is present in pre-synaptic vesicles, where it reaches mM levels. [268] In the neuronal synapses PrP concentration is high, making it a possible candidate in Zn^{2+} homeostasis. [269]

Brown *et al* [270] reported interesting results on Mn^{2+} , showing that Mn^{2+} can replace Cu^{2+} in PrP and that the Mn^{2+} –PrP complex displays a similar SOD activity as the Cu–PrP complex. They also reported that the Mn^{2+} –PrP complex displays a protease resistance (exactly as the PrP^{SC} form), assuming a similar structure as the PrP^{SC} one that suggest the involvement of Mn^{2+} in prion-related diseases.

Fernaues *et al* [271] reported interesting results on the importance of Fe^{2+} in neurodegenerative diseases as well as the Fe^{2+} –PrP relationship. They reported that infection by PrP^{SC} is connected to a change in Fe^{2+} homeostasis, even if a value for the binding constant of Fe^{2+} to PrPs is not known yet. Finally, Ni^{2+} , Cd^{2+} and Ca^{2+} show a very weak binding to PrPs and very little is known on their physiological function related to PrPs. [267, 272]

Although a definitive demonstration of the physiological function of PrPs remains elusive, several hypothesis were proposed: i) PrP could work as a protection to neurons from reactive oxygen species, thus acting as a superoxide dismutase (hereafter denoted as SOD); [273] ii) PrP could act as a Cu^{2+} transporter from outside the cell to its interior [261, 265, 274] and; iii) PrP could act as a copper buffer, thus sequestering the excess of copper that could have deleterious redox activity in the body. [275] All these hypotheses seem plausible and are supported by experimental evidence, leading to several possible scenarios that do not allow proper determination of the principal role of prions in humans and animals. Miura *et al* [276] reported the reduction of the copper in the complex and its pH dependence by Raman spectroscopy. The latter is in good agreement with the work of Ruiz *et al* [20] that reported on the role of the tryptophan residue in the $\text{Cu}^{\text{II}} \rightarrow \text{Cu}^{\text{I}}$ reduction, showing that the absence of tryptophan diminishes the above-mentioned reduction by 76 %. Previous studies reported on the property of PrPs as Cu^{II} transporters, showing that copper transport does not depend on the level of PrP expression. [275, 277] However, the pH dependence of Cu^{II} binding strongly suggests the involvement of PrPs in binding Cu^{II} outside the cellular membrane ($\text{pH} \approx 7.4$) and its release inside the cell ($\text{pH} \approx 6.8$). [275, 277]

Previous experiments on PrP knockout cells demonstrate that cells infected with PrP^{SC} are more prone to oxidative stress; thus showing a strong decrease in the copper binding ability with respect to the normal PrP^C. [278]

Nowadays, very few time-resolved studies have been performed on PrPs [279–281] and those available in literature are on the minutes–hours timescales. Indeed protein activity (e.g. Cu reduction from Trp, PrP^C → PrP^{SC} transition, trigger for agglomeration, etc.) occurs on the latter timescales; nonetheless, ultrafast time-resolved experiments allow gathering information on the nature of the active intra- and inter-molecular processes in prions upon tryptophan excitation (e.g. quenching timescales and mechanism of *Trp as well as interaction between *Trp and the complexed Cu ion). In order to investigate the photo-cycle of the *Trp we focus our experiments on the octarepeat region, which has been suggested to have an important role in the biological task of prion proteins as well as the main one responsible for Cu binding. [16, 19, 245, 247, 282]

Here we present an ultrafast UV pump–Visible probe transient absorption study on the octarepeat region, from the smallest binding peptide moiety OPS to the entire octarepeat region found in human PrP, namely OP4. The study presented here aims at investigating the transient response of the OPS and OP4 in solution, as well as the impact of Cu^{II} binding on the dynamics of the afore-mentioned systems. Probing in the visible range (380–600 nm) allows the investigation of the tryptophan ESA response (when OPS or OP4 are dissolved in buffer solution) but also a possible response of the complexed Cu^{II} or eventual photo-products in case of a *Trp–Cu electron transfer. As mentioned above the ability of prions to bind Cu^{II}, as well as the binding mode, strongly depends on pH; therefore, using a buffer is mandatory when studying this kind of peptides.

5.1 Sample preparation

The pH dependence of Cu bonding by prion proteins has already been discussed, but another crucial aspect is the choice of a suitable buffer for the experiment to succeed. Several buffers (such as the phosphate) complex the Cu^{II} avoiding its binding by the PrPs; [262] thus a Cu^{II} non-complexing buffer is needed for these experiments. The best choice, for the pH range needed, is 2-(N-morpholino) ethanesulphate (hereafter denoted as MES). [283, 284] The static spectra were measured in a 1 cm thick cuvette, while the transient absorption measurements were performed flowing the sample in a 1 mm thick flow-cell.

For time-resolved experiments (as well as static) the OPS sample was prepared by dissolving ~4 mg in 10 mL of buffer solution at pH 7, in order to reach a [OPS] = 0.4–0.5 mM. [258]

In the OP4 case, four tryptophan residues are present in the same peptide chain; thus, for static absorption and emission experiments a $[OP4] \approx 0.13$ mM, while for time-resolved experiments a $[OP4] \approx 0.5$ mM was used. This is because in static spectroscopy all four chromophores contribute to the signal, while in time-resolved spectroscopy the most probable scenario is the excitation of one chromophore per molecule, as determined by Poisson distribution.

Preparation of the PrP-Cu complexes requires the pH control of the Cu^{II} solution, because Cu^{II} precipitates as hydroxide (low solubility in water) at $pH > 5$. Therefore the Cu^{II} solution needs to be slightly acidic and also at high concentration because, upon PrP- Cu^{II} complex formation, the absorption band of Trp broadens (slightly reducing the absorption at 280 nm).[285] Since this work is based on a comparison between the time-resolved response of PrP and PrP-Cu, it is important to add the minimal volume of Cu^{II} solution during the preparation of the PrP-Cu complex, so that the OD at 280 nm (for the static and time-resolved experiments) does not differ much upon Cu solution addition. For this reason, a 100 mM stock solution of aqueous $CuCl_2$ was prepared, thus implying the addition of ~ 50 μL aliquots for a 1:1 PrP/Cu ratio (in the case of OPS that contains only one Trp, for OP4 the quantity is 4-fold the OPS one).

The excitation pulses in transient absorption measurements were set at 280 nm (2 nm FWHM), with fluence ≈ 0.8 mJ/cm² and IRF ≈ 130 fs FWHM. The polarization of the probe pulse was set to magic angle (by a $\lambda/2$ plate) with respect to the pump, so to avoid the detection of timescales related to rotational diffusion.

The OPS was purchased from the UNIL peptide facility (purity 74–81 %), while the OP4 was purchased from NeoBiolab (purity 98–99 %). All the samples were used as received without any further purification. The $CuCl_2 \cdot 2 H_2O$ and MES were purchased by Sigma Aldrich and used as received.

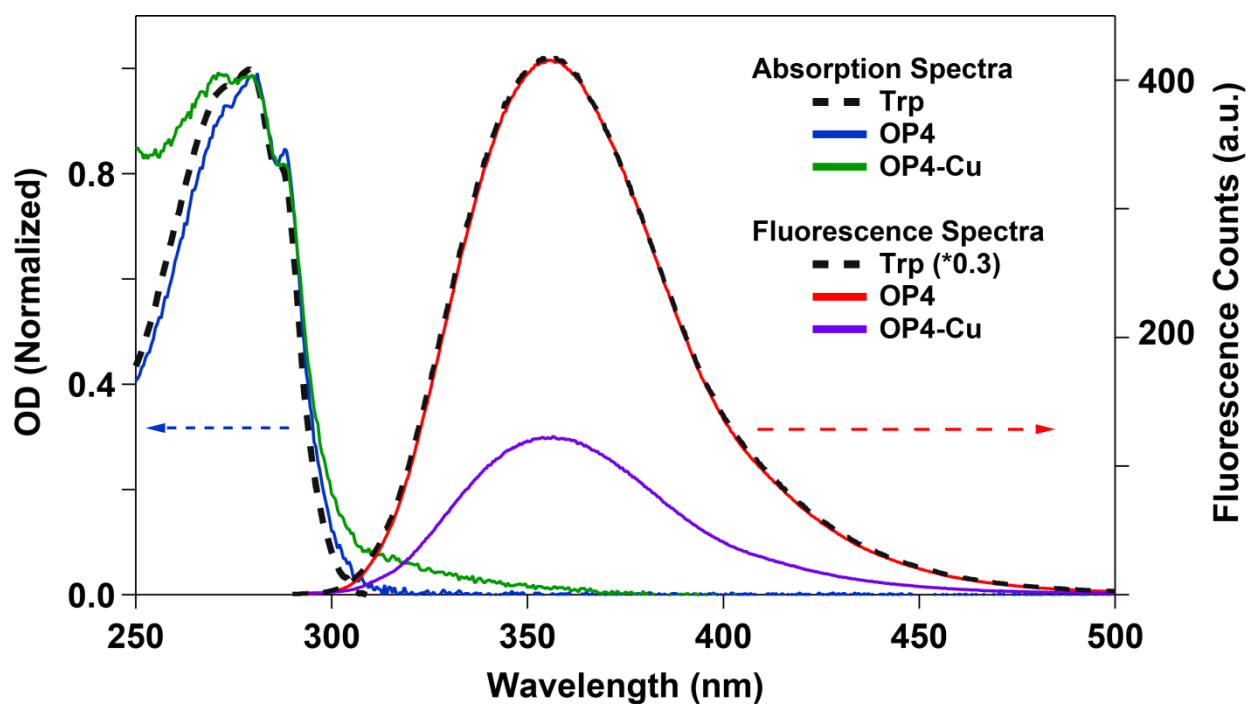


Figure 5-3 Static absorption spectra of Trp, OP4 and OP4-Cu together with their fluorescence spectra. All the spectra were acquired in a 1 cm cuvette and the background given by the buffer solution was subtracted to obtain only the spectrum of the species (only needed for the absorption spectra). The absorption spectra were normalized at 280 nm in order to compare the band shape. The concentration of Trp in water was set to 0.5 mM while the concentration of OP4 was 0.13 mM, since four Trp residues are present in one peptide molecule.

5.2 Static spectra of PrPs

Figure 5-3 shows both the absorption and fluorescence spectra of Trp, OP4 and OP4-Cu solutions. The absorption spectra are normalized at 280 nm for comparison. There is a slight red-shift of the Trp in OP4 and a broadening of the absorption band when the PrP complexes the Cu^{II} . Upon Cu addition the solution becomes slightly milky, in agreement with the reported solubility reduction of the PrP-Cu complex with respect to the PrP,[258] and its color changes from colorless to straw yellow. The OP4-Cu static absorption spectrum does not show bands above 350 nm, thus suggesting that the color difference is due to the band between 300 nm and 350 nm, which is typical of the PrP-Cu complexed form. As far as the fluorescence is concerned, the emission spectrum shows the same shape for Trp, OP4 and OP4-Cu, but a ~0.5 mM Trp solution in 10 mM MES shows a fluorescence ~3 times more intense than the one of a ~0.13 mM OP4 solution in 10 mM MES (recalling that OP4 contains four Trp residues). The reduction of the fluorescence intensity becomes more drastic upon copper complexation, showing a ~4-fold reduction of the fluorescence intensity in presence of a 3-fold excess of Cu^{II} with respect to the Trp/Cu equimolar quantity.

The only investigation on the static electronic spectroscopy of octarepeat human PrP segments is the work of dos Santos *et al.*,[285] who reported a broadening of the Trp absorption band upon Cu^{II} complexation as we observe here. However, in their static absorption spectrum, they highlight a band centered at 320 nm (even in the OP4 without copper in solution). However, the OP4 absorption spectrum in the 250–400 nm range displays only one band due to tryptophan absorption, as shown in Figure 5-3, thus suggesting the presence of impurities in their samples.

5.3 Transient absorption experiments on HGGGW (OPS)

This section reports on the UV pump–Visible probe transient absorption experiments on OPS, comparing the response of the latter with that of its Cu^{II} complex.

5.3.1 Investigation of OPS dynamics

Figure 5-4(A) shows the t – λ plot obtained upon 280 nm excitation of the Trp residue contained in the OPS. In order to highlight the response of the system at early times, the t – λ plot shows the first 5 ps after time–zero, even though the maximum delay time was 1 ns. The 350–590 nm range displays the *Trp ESA, in agreement with previous measurements reporting the dynamics of Trp in water.[165] The t – λ plot in Figure 5-4(A) displays an intensity growth on the red–side of the broad ESA band within the first ps. The latter evolution can be observed better in Figure 5-4(B), where the kinetic trace at 550 nm grows on a sub–ps timescale narrows and the kinetic trace at 400 nm decays on the same timescale. Hence, the observed sub–ps dynamics suggest the detection of a primary cooling process, in which the initially broad ESA feature narrows down in < 1 ps. Figure 5-4(C) shows the time evolution of selected kinetic traces till 900 ps, highlighting the difference between the kinetics of *Trp within the peptide and *Trp dissolved in water, recalling that the latter displays a non–exponential decay with timescales of 0.5 ns and 3 ns.[165] The characteristic timescales of OPS were retrieved by a GF analysis of single traces, which converged to three main timescales: 392 ± 27 fs, 18.7 ± 1.7 ps and 1.5 ± 0.2 ns.

Figure 5-5 shows selected transient spectra at characteristic time–delays (A), and the DAS's obtained by the GF analysis (B). Comparing the transient spectra at 150 fs and 400 fs displays the above–mentioned narrowing of the broad ESA feature; interpretation that is validated also by the DAS at 390 fs, which shows a decay of the transient signal in the 360–440 nm range and a growth in the 440–590 nm range. The second timescale (~ 19 ps) shows instead a small decay of the excited state population, followed by a more pronounced decay on a 1.5 ns timescale.

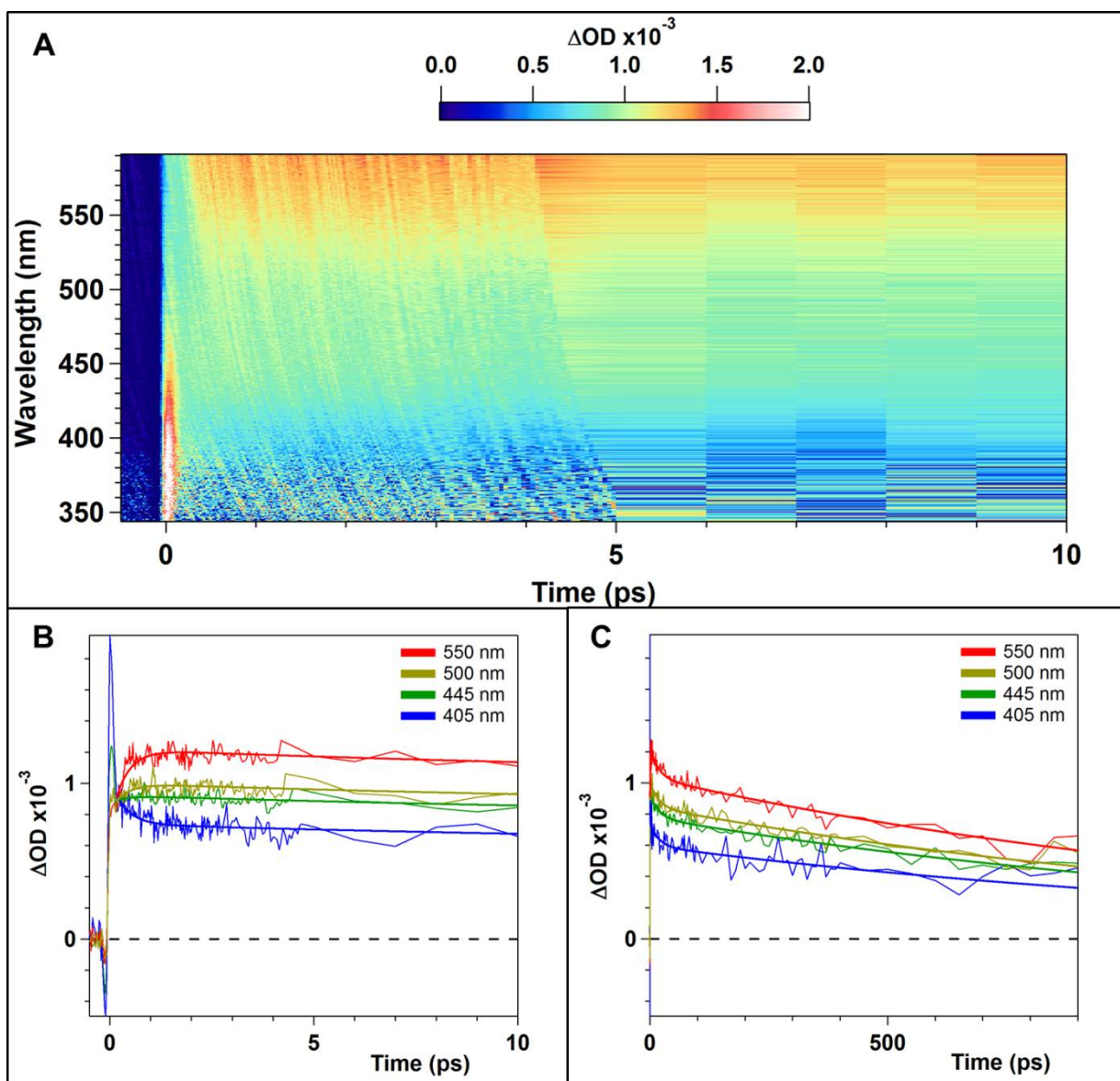


Figure 5-4 t - λ plot of OPS upon 280 nm excitation (A). In (B) are shown selected kinetic traces and their best-fit within the first 10 ps time – delay, while in (C) is shown the entire time – course till 900 ps.

The 19 ps decay represents the non-radiative quenching of the excited Trp and, by comparing the amplitude of the DAS at 19 ps and at 1.5 ns, it is possible to see that it accounts for the 3–4 fold reduction of fluorescence. The 1.5 ns value (obtained by GF analysis) is half the 3 ns component observed in the *Trp in water;[165] however, it is important to highlight that this value is obtained from a data-set whose longest time-delay is 900 ps. Therefore, it identifies more a lower limit for the radiative process than its correct determination; thus we suggest that the 1.5 ns component identifies the radiative decay of the excited state population.

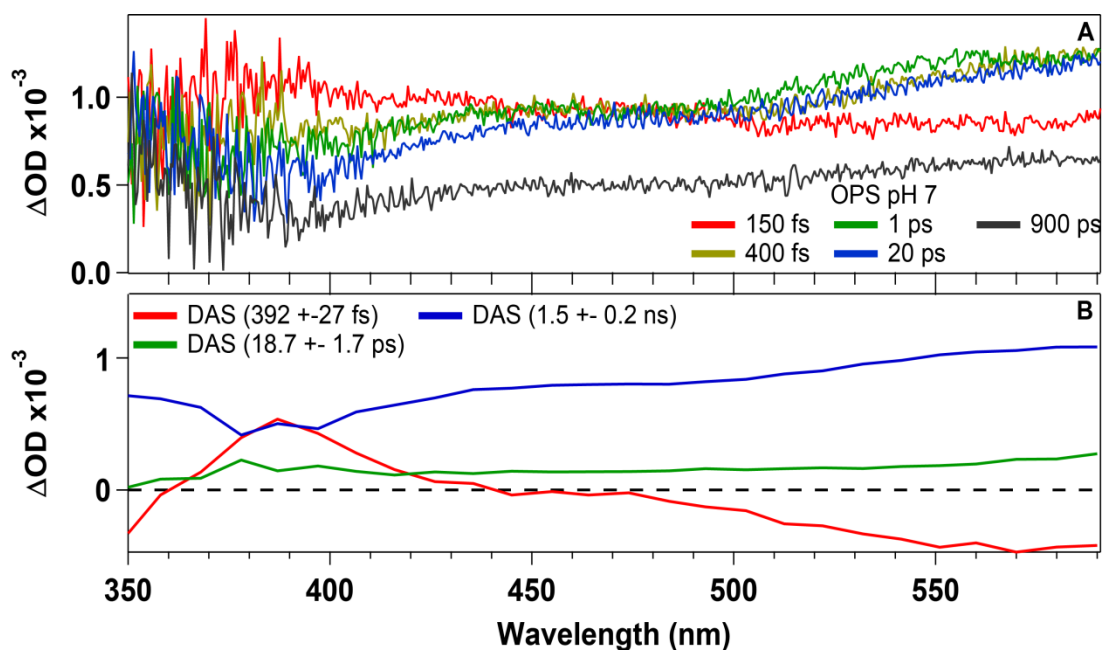


Figure 5-5 Selected transient spectra at characteristic time-delays (A) and DAS's related to the retrieved timescales via GF analysis (B).

To identify the nature of the non-radiative quenching process, it is sufficient to analyze the system and its absorption spectrum: the lack of an acceptor chromophore displaying an absorption spectrum that overlaps (at least partially) with the donor emission, rules out the FRET (Förster energy transfer) process. A similar condition is necessary for Dexter energy transfer, since energy must be conserved in the process, thus leaving the electron transfer process as the most probable one. Furthermore, tryptophan residues are known to undergo electron transfer to the backbone of the protein or to nearby residues.[81, 168, 169, 286, 287] Yu *et al* [288] reported that Glycine quenches the *Trp fluorescence via proton transfer, while Histidine does it via electron transfer.[287] Hence, we suggest that the 19 ps timescale is due to electron transfer from *Trp to H or G residues, even if the $TrpH^{+\bullet}$ (absorbing at 560 nm [197]), is not detected in our experiments.

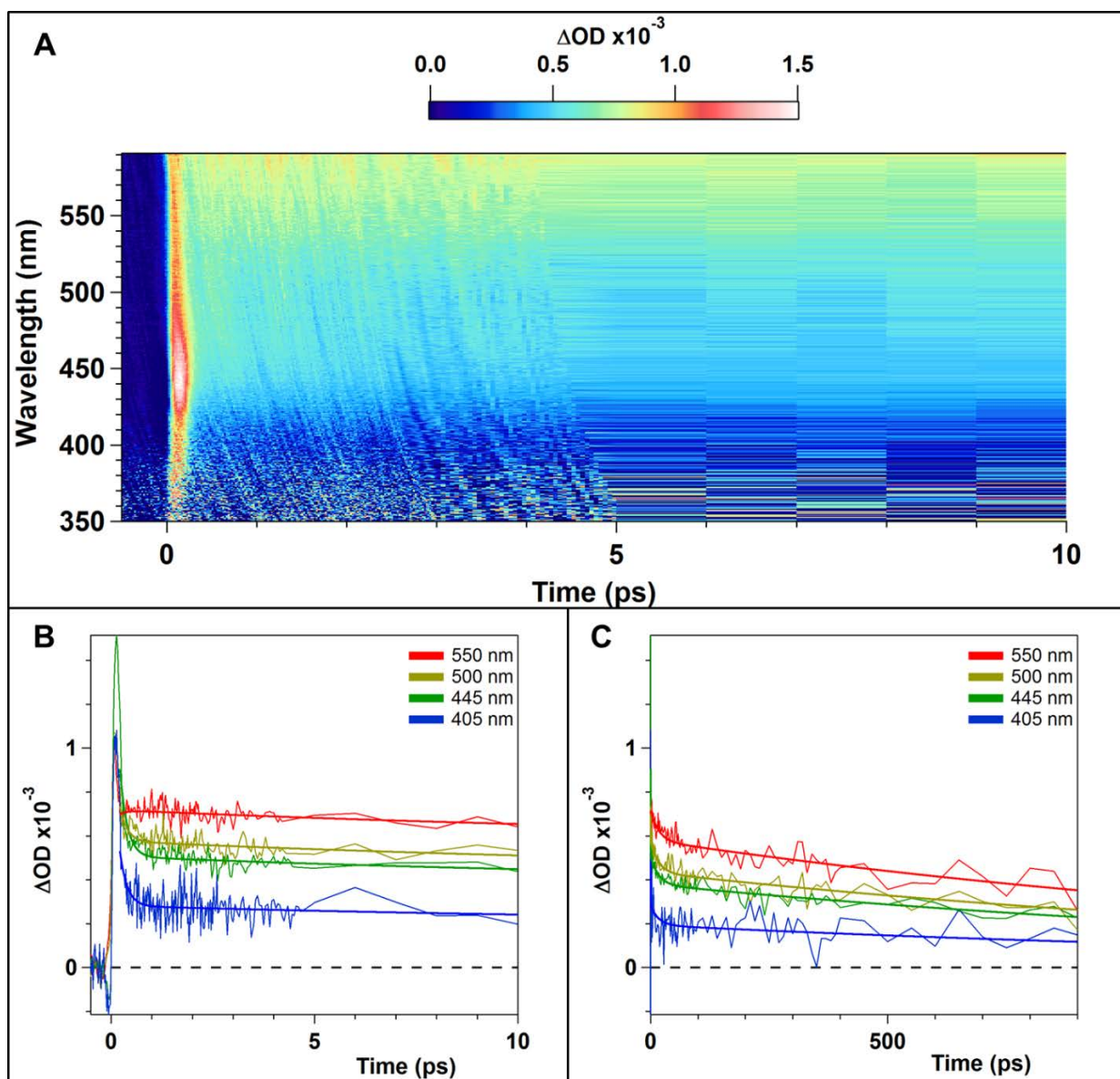


Figure 5-6 t - λ plot of OPS – Cu upon 280 nm excitation (A). In (B) are shown selected kinetic traces and their best-fit within the first 10 ps time – delay, while in (C) is shown the entire time – course till 900 ps.

5.3.2 Investigation of OPS–Cu dynamics

Figure 5-6 shows the t - λ plot of OPS–Cu, upon 280 nm excitation, (A) together with some kinetic traces selected at wavelengths (B,C). This experiment was performed right after the OPS alone, by adding to the original solution a 3-fold excess of Cu^{II} , namely $\sim 150 \mu\text{L}$ of a 100 mM CuCl_2 aqueous solution (see sample preparation 5.1). The t - λ plot shown in Figure 5-6 displays an extra feature centered at 450 nm, which decays on a timescale < 500 fs and strongly quenches the $^* \text{Trp}$ fluorescence. In order to retrieve the characteristic timescales of the system, a GF analysis on several kinetic traces was performed, leading to the following values: 180 ± 20 fs, 17.0 ± 2.6 ps and 1.8 ± 0.2 ns.

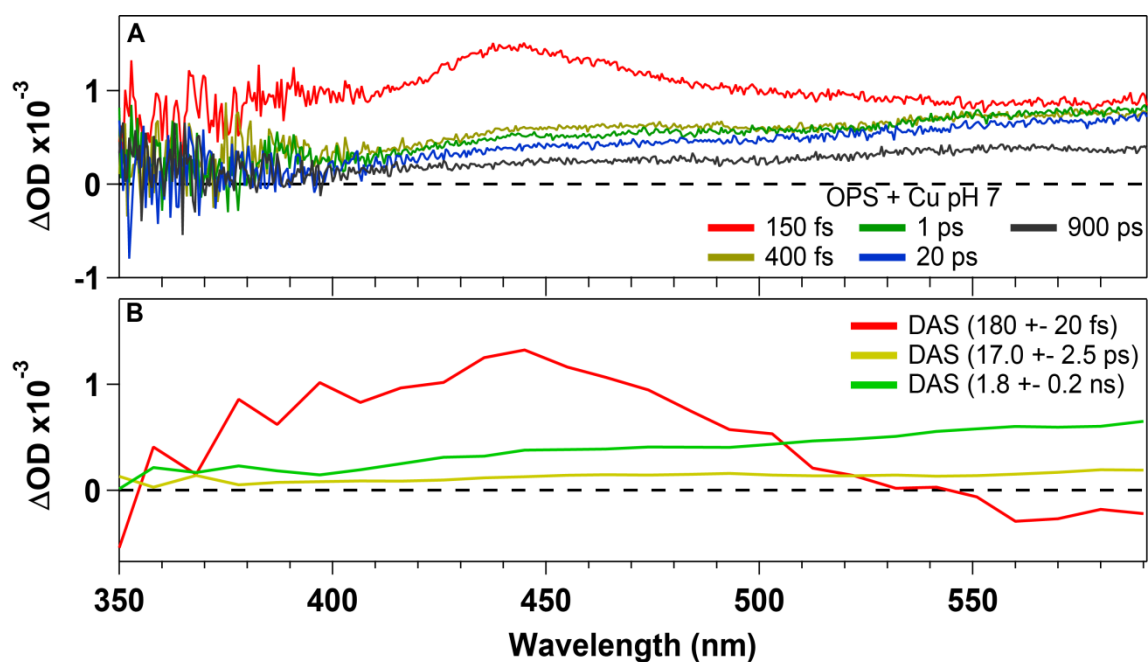


Figure 5-7 Selected transient spectra at characteristic time-delays (A) and DAS's associated to the retrieved time constants for the complex OPS-Cu.

The direct comparison of the transient spectrum at 150 fs with the 180 fs DAS clearly shows that the new feature disappears promptly after the excitation. Since the experimental conditions are the same as for the un-complexed OPS, it is clear that another deactivation mechanism is active upon copper complexation. We can safely exclude FRET from the additional quenching processes, because the band at 320 nm in the OPS-Cu absorption spectrum is too weak to allow good FRET coupling. Moreover, the Trp residue is hydrogen bonding to a water molecule situated in the fifth coordination site of the copper, as shown in Figure 5-1B. Photo-excited Trp is known to be a strong donor for electron transfer [73, 74, 81, 169] and proton-coupled electron transfer [286] with water molecules and other suitable acceptors. Beside this, the reduction potential for the couple $\text{Cu}^{\text{II/I}}$ is +0.17 V vs NHE in the completely complexed octarepeat peptide,[289, 290] thus suggesting that a $^*\text{Trp-to-Cu}$ electron transfer process is active. However, we do not detect the growth of the transient ESA band at 450 nm, implying that the $^*\text{Trp-to-Cu}^{\text{II}}$ electron transfer occurs on a timescale $\ll 130$ fs. Hence, we suggest that the detected ESA band at 450 nm is due to the $\text{Cu}^{\text{I-to-TrpH}}^{\bullet}$ back-electron transfer, which occurs on 180 fs timescale. This hypothesis is qualitatively validated by comparing the 450 nm ESA band (detected in our experiments) with the absorption spectrum of the Cu^{I} -bathocuproine disulphonate (BCS) complex. Bathocuproine disulphonate is a Cu^{I} indicator (shown in Figure 5-8), which displays an absorption band at 480 nm upon Cu^{I} complexation.[20]

Since Cu^{I} is a d^{10} ion, the latter transition should have a metal-to-ligand charge transfer character, similarly to the back-electron transfer proposed in the PrP-Cu complex. Even though the Cu^{I} -BCS and the photo-excited PrP-Cu complexes contain different ligands

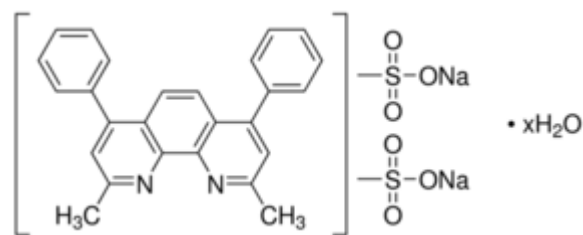


Figure 5-8 Schematic structure of the bathocuproine disulphonate.

share the central ion as well as a similar absorption band position. Interestingly, the presence of the additional quenching pathway does not influence the 17 ps component, which is still present and with a similar amplitude as the un-complexed OPS. This behavior can be explained invoking the presence of different conformations in the PrP-Cu complex, in which the $^*\text{Trp}$ is further apart from the Cu^{II} and does not undergo electron transfer. The 1.8 ns is attributed to the radiative decay of the $^*\text{Trp}$ in agreement with the results shown for the un-complexed OPS.

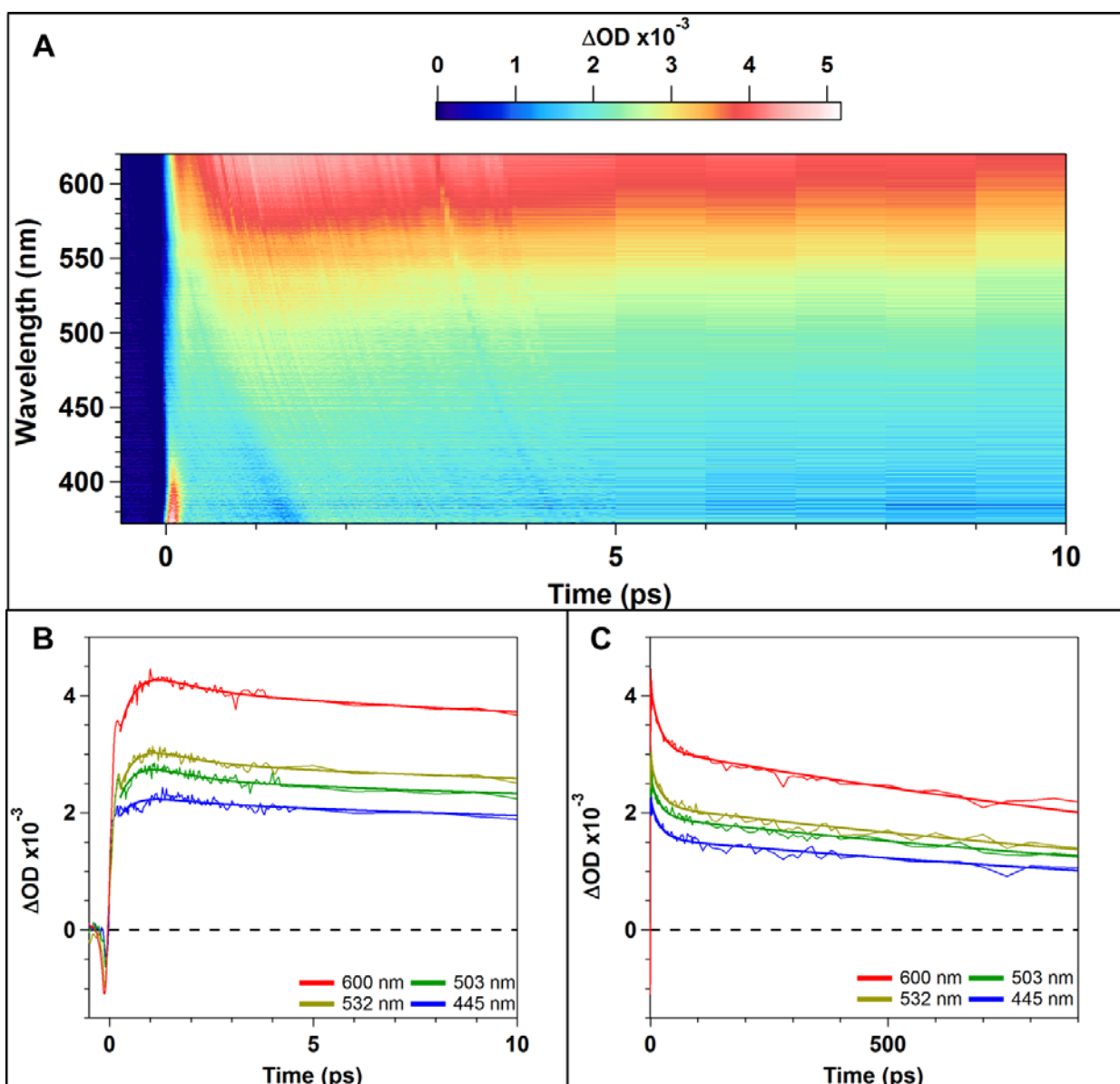


Figure 5-9 t - λ plot of OP4 upon 280 nm excitation (A). In (B) are shown selected kinetic traces and their best-fit within the first 10 ps time – delay, while in (C) is shown the entire time – course till 900 ps.

5.4 Transient absorption experiments on (PHGGGWGQ)₄ (OP4)

This paragraph is based on the same methodology used for the OPS, but reports on the full octarepeat region (OP4), containing four tryptophan residues in each peptide molecule.

5.4.1 Investigation of OP4 dynamics

Figure 5-9 shows the t - λ plot of OP4 (upon 280 nm excitation) (A) together with selected kinetic traces (B, C). The layout of the t - λ plot is similar to the OPS one, displaying a broad ESA feature due to the *Trp residues narrowing on a sub-ps timescale, as shown in Figure 5-9. However, the reduction of the transient signal in the blue-side of the spectrum is stronger in the OPS than in OP4, as can be seen from the kinetic traces shown in Figure 5-9.

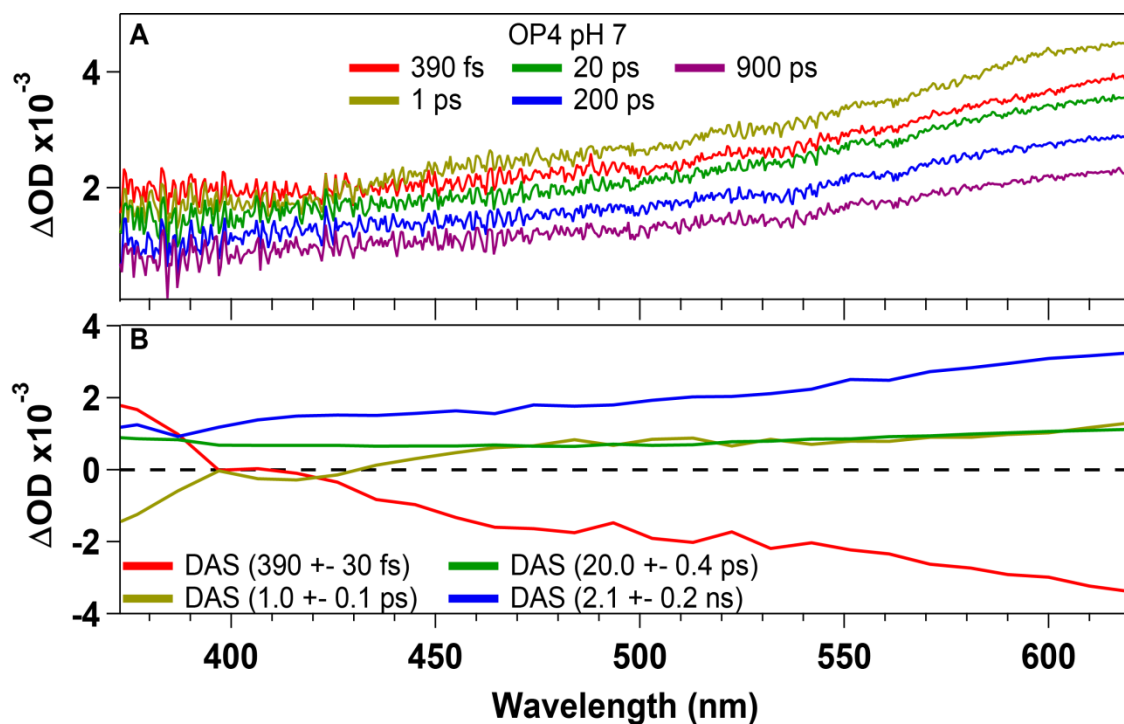


Figure 5-10 Selected transient spectra at characteristic time-delays (A) and DAS's related to the decay times obtained by GF analysis (B) of OP4.

Comparison of the transient spectra at 390 fs and 1 ps shows an overall increase in the transient signal over the 420–620 nm range, followed by a decay of the transient signal on different exponential timescales. The latter were retrieved via GF analysis of kinetic traces (selected ones shown in Figure 5-9), which converged to four characteristic timescales: 390 ± 30 fs, 1.0 ± 0.1 ps, 20.0 ± 0.4 ps and 2.1 ± 0.2 ns. The sub-ps dynamics are characterized by a growth of the transient signal in the red-side of the spectrum and a weak decay in the blue-side, thus suggesting a narrowing of the wide ESA band on the 390 fs as shown in Figure 5-10A. The 1 ps timescale is detected in OP4 but not in OPS, thus suggesting the implication of the additional amino acids (e.g. Glutamine and Proline). Photo-excited tryptophan is known to undergo electron transfer towards Glutamine and in the OP4 the two residues are separated by a Glycine residue; therefore, we suggest that the 1 ps timescale is due to *Trp-to-Glutamine electron transfer quenching. The 20 ps decay time is the same as the 19 ps observed in the OPS case, thus pointing to the same quenching mechanism of *Trp as the one proposed in the OPS, namely *Trp undergoing electron transfer to H or G residues. Finally the 2 ns component again identifies the *Trp's radiative decay, comparable to that of the *Trp in water.

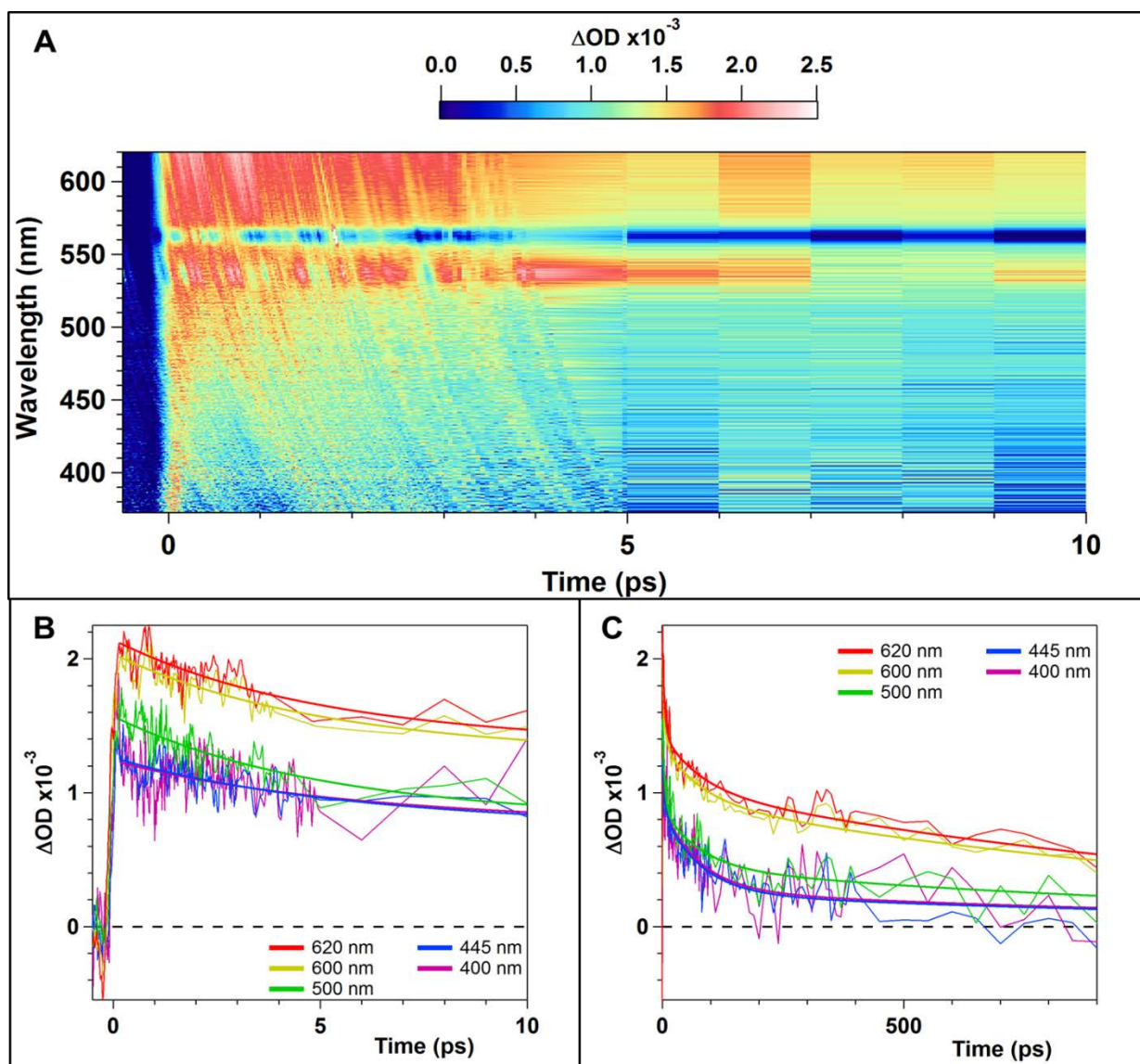


Figure 5-11 shows the t - λ plot of OP4 – Cu upon 280 nm excitation (A). In (B) are shown selected kinetic traces and their best-fit within the first 10 ps time – delay, while in (C) is shown the entire time – course till 900 ps.

5.4.2 Investigation of OP4–Cu dynamics

Figure 5-11 (A) shows the t - λ plot obtained upon 280 nm excitation of the OP4–Cu. As in the OPS case, a 3-fold excess (with respect to the equimolar Trp–Cu quantity) of Cu^{II} was added to the OP4 solution (600 μL of a 100 mM CuCl_2 solution) in order to be sure of the saturation of the OP4 binding sites. In the 530–570 nm region, the scattering of the visible light used to generate the UV pump does not allow to get information on the spectral and kinetic response of the sample, thus it is removed from the data analysis (missing points in Figure 5-12). A general overview of the t - λ plot shows much weaker amplitude of the transient signal with respect to the OP4 and, more interestingly, does not display the sub-ps timescales observed in the OP4 case (Figure 5-9).

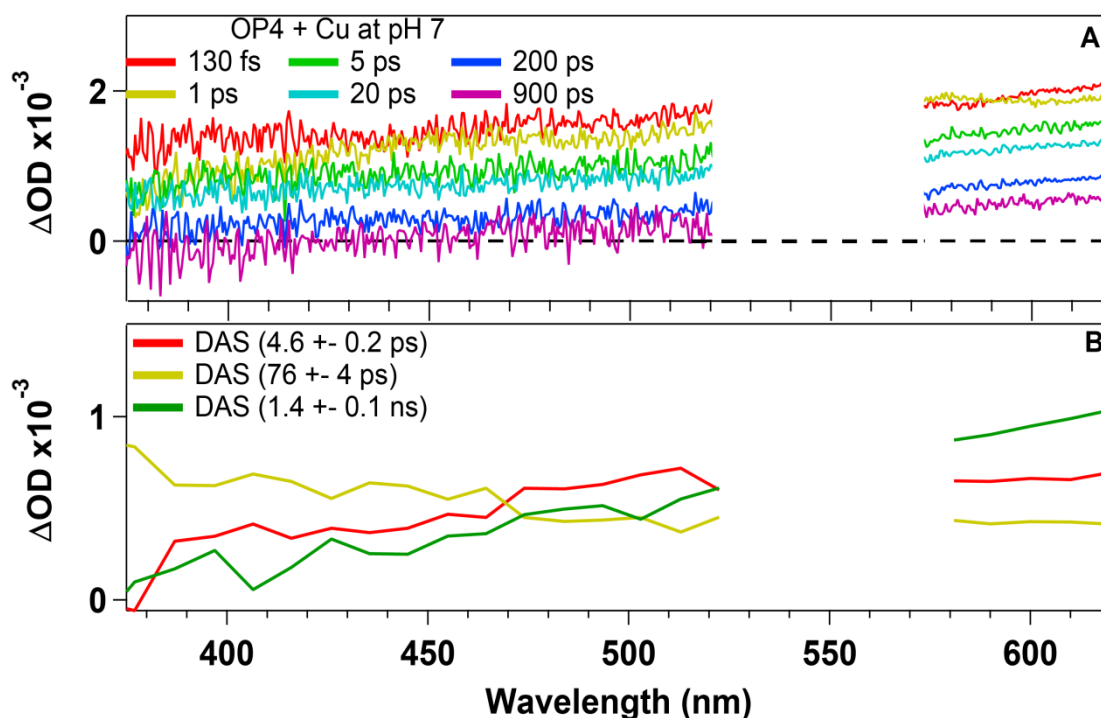


Figure 5-12 Transient spectra at selected time-delays (A) and DAS's related to the GF analysis of the OP4-Cu complex upon 280 nm excitation.

A first comparison between the $t-\lambda$ plots of OPS-Cu and OP4-Cu shows that in the latter is not present the additional feature centered at 450 nm, which was assigned to the Cu^{I} -to- TrpH^{\bullet} back-electron transfer. This observation is reflected in the characteristic timescales retrieved through the GF analysis of multiple kinetic traces, which converged on the following decay times: 4.6 ± 0.2 ps, 76 ± 4 ps and 1.4 ± 0.1 ns. As can be seen in the DAS's shown in Figure 5-12B, the three exponential timescales are associated to decays of the transient signal. The 1 ps component observed in the un-complexed OP4 is not present, being replaced by a 5 ps component in the OP4-Cu; however, both of them show a similar DAS. Since the formation of the copper complex introduces more constraints on the peptide chain, the residues cannot move as freely as in the un-complexed form, thus retarding the interaction with nearby residues that quenches the $^*\text{Trp}$ fluorescence. As already mentioned above, the ESA band due to the back-electron transfer to the TrpH^{\bullet} is not present, thus implying that in OP4 the peptide chain tends to adopt conformations in which the Trp residue is distant from the copper. Therefore, $^*\text{Trp}$ is preferably quenched by the interaction with other residues, such as glutamine, histidine or glycine residues, instead of interacting with the Cu^{II} ion.

The same elongation in the decay kinetics is observed in the 76 ps timescale, which is ~4 times longer than the 20 ps observed in the un-complexed OP4. Also in this case the DAS's are very similar, implying a smaller degree of flexibility for the protein to reach the right conformation needed to undergo electron transfer, which is reflected in longer quenching timescales. Finally, the 1.4 ns component is again related to the radiative timescale of the *Trp.

5.5 Discussion

The smallest binding sequence (OPS) and the octapeptide region (OP4) show several similarities in their non-radiative quenching of *Trp, but also some strong differences on the observed timescales probably due to the different size of the peptide chains. The two un-complexed peptides show three common timescales (summarized in Table 5–1): 400 fs (assigned to vibrational cooling), 20 ps (assigned to electron transfer) and 1.5–2 ns (assigned to the lower limit of *Trp's radiative decay). Beside these timescales, the longer OP4 peptide displays an additional timescale, namely 1 ps, suggesting both the interaction with the glutamine residue and the presence of additional conformers in which the Trp residues are closer to histidine or glycine, allowing a faster electron transfer process. The latter observations are confirmed by NMR studies of prions in solution,[246] which show the backbone flexibility and the lack of any regular secondary structure in the octarepeat region. Thus, we identify two main causes for the additional 1 ps timescale, namely: i) OP4 is more flexible and longer than OPS, displaying higher probability of *Trp interaction with histidine and glycine and; ii) the presence of glutamine close to the Trp in the OP4 sequence, which is an electron acceptor and Trp quencher.[287] In all cases the main quenching mechanism, in the investigated peptides, is more likely to be electron transfer.

Table 5–1 Summary of the retrieved decay times of the investigated PrPs

	τ_1 (fs)	τ_2 (ps)	τ_3 (ps)	τ_4 (ns)
OPS	392 ± 27	————	18.7 ± 1.7	1.5 ± 0.2
OPS–Cu	180 ± 20	————	17.0 ± 2.5	1.8 ± 0.2
OP4	390 ± 30	1.0 ± 0.1	20.0 ± 0.4	2.1 ± 0.2
OP4–Cu	————	4.6 ± 0.2	76 ± 4	1.4 ± 0.1

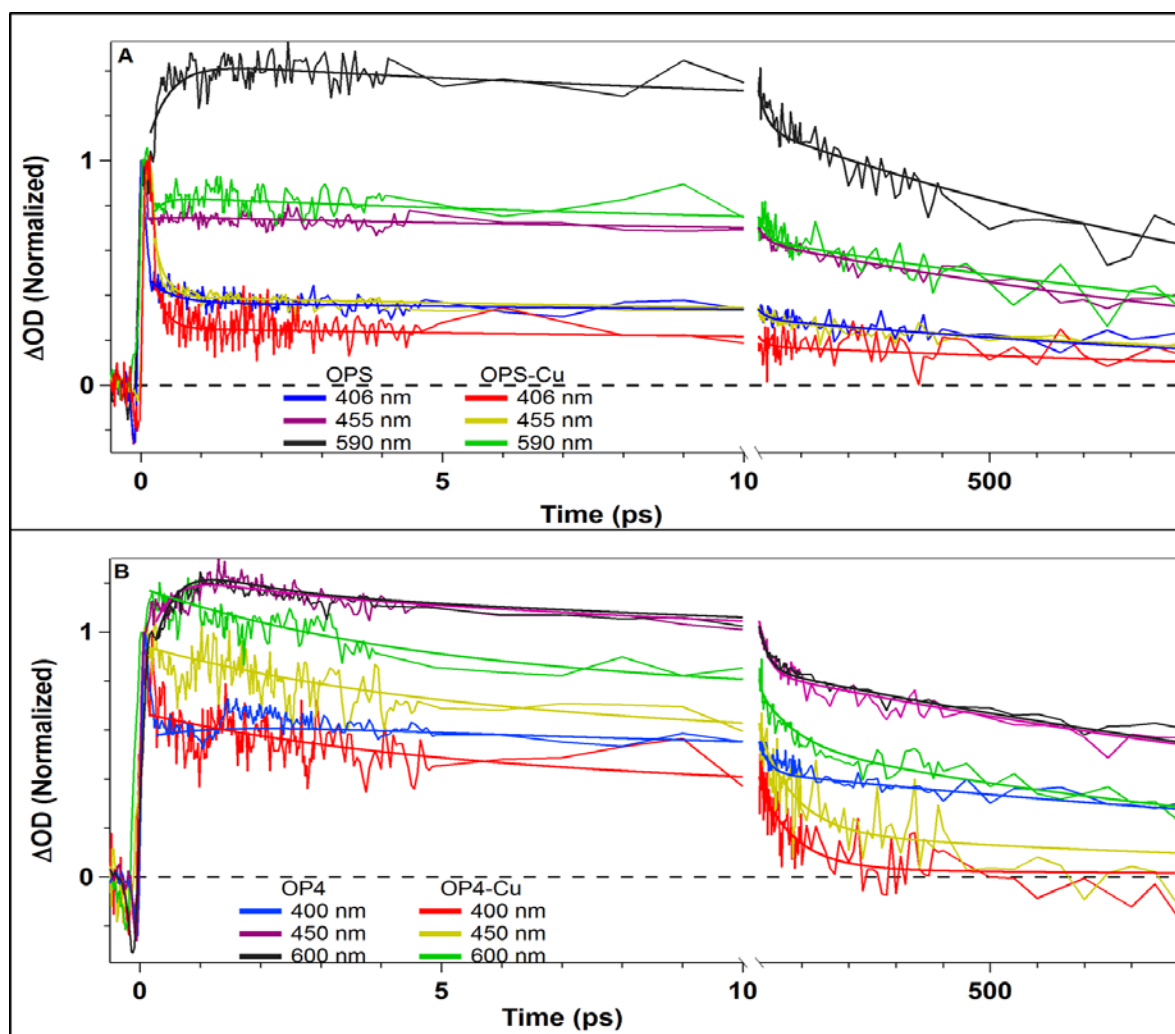


Figure 5-13 Comparison of selected kinetic traces of OPS (A) and OP4 (B), both in their free-form and in the fully occupied Cu-complex.

Upon Cu complexation the *Trp quenching dynamics differ strongly between the OPS and OP4, as shown in Figure 5-13 (A) and (B), where selected kinetic traces of OPS and OP4, respectively, (both with and without Cu) are normalized at the cross-phase modulation maximum. Normalization of the traces allows direct comparison of the dynamics upon copper complexation removing the differences in fluence and concentration between samples. As mentioned in Paragraph 5.3.2, in the OPS-Cu case (Figure 5-13A) a *Trp -to- Cu^{II} electron transfer occurs on a timescale $\ll 130$ fs, generating a Cu^I species that undergoes a back-electron transfer to the $TrpH^{+\bullet}$ on a 180 fs timescale. The Cu^I species complexed by the prion peptide give rise to a band centered at 450 nm, which has been qualitatively compared to the absorption band of the Cu-BCS complex (centered at 480 nm).[20] The 180 fs decay component accounts for $\sim 50\%$ of the *Trp transient signal amplitude (Figure 5-13A), which is the same amount of quenching observed in the static fluorescence measurements.

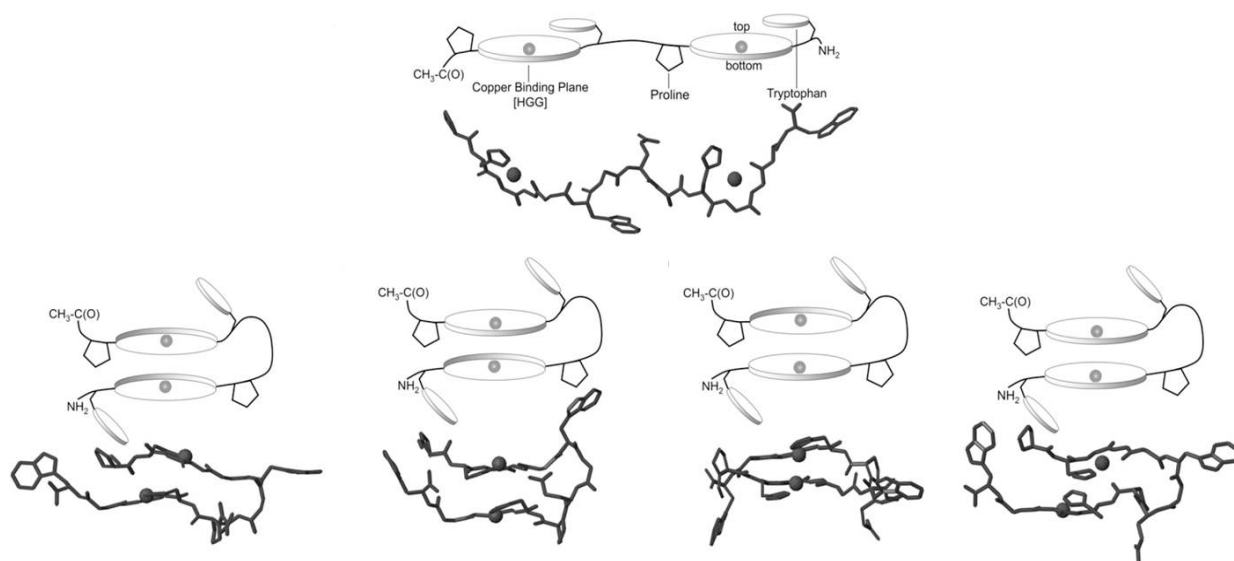


Figure 5-14 Schematic representations of possible Cu-bound OP2 obtained by DFT calculations. In all cases the tryptophan residues are far from the Cu center, oppositely to what is observed in the OPS complex. This figure is reproduced from ref. [291]

In the OP4 case (Figure 5-13B) no sub-ps quenching has been observed, thus pointing to the absence of direct interaction with the copper ion. The strongest quenching occurs on a 70–80 ps timescale, which can be explained by the conformation assumed by the peptide upon Cu complexation. As shown in Figure 5-14 the peptide tends to wrap itself around the Cu ion, with the Cu-L₄ (L = Ligand = N, O) planes facing each other, as reported by previous DFT calculations on OP2.[291] These conformations confine the Trp residues away from the Cu ion and from the nearby glutamine; therefore, since the electron transfer rate scales exponentially with the donor–acceptor distance, the quenching time becomes longer (from 20 ps in OP4 to 70 ps in OP4–Cu). Hence, the more constrained structure of OP4–Cu reduces the possibility of *Trp movement to be in the right conformation needed for the electron transfer to histidine, glycine or glutamine, thus causing the elongation of quenching rates (OP4 = 1 ps and 20 ps, while OP4–Cu = 5 ps and 76 ps).

Therefore, the results of this work contain also useful structural information that show the different conformations adopted by the peptide when using the OPS or the OP4 system. The latter results can help understanding the different behavior observed in previous investigations,[20, 276] which reported the reduction of Cu^{II} by the Trp residues on the minute–hour timescale under physiological conditions (without UV–light illumination at low occupancies).

Despite the latter experimental evidences, during our measurements we did not observe any feature related to a non photo-induced Trp-to-Cu electron transfer (e.g. features of the $\text{TrpH}^{+\bullet}$), even though several static absorption spectra were performed to check sample damaging. This discordance can be explained by taking into account the different PrP: Cu ratio; the non-photo-induced Trp-to-Cu electron transfer was observed at low-occupancies, while our experiments were performed at high-occupancies of the octarepeat region. This explanation agrees with Liu *et al.*, [289] which reported the importance of the OP4-Cu binding mode on the Cu redox cycle and suggested the importance of both pH and peptide: Cu ratio, highlighting the importance of the experimental conditions and how they affect the geometry of the protein itself. Redecke *et al* [292] reported on the aggregation of mouse prion proteins (in aqueous solution) under continuous UV irradiation (302 nm), by monitoring the sample with both circular dichroism and UV-Visible spectroscopy. Their results were obtained after 5–15 minutes of continuous illumination of the sample with different fluence values. In our case, no photo-damage was observed during the measurement; nonetheless, the results of Redecke *et al* are important to understand the formation of PrPs aggregates. These observations altogether, point to the involvement of the N-terminal part of the prion in the $\text{PrP}^{\text{C}} \rightarrow \text{PrP}^{\text{SC}}$ conversion. The reported agglomeration upon 300 nm illumination and the non-photo-induced Trp-Cu electron transfer, are strong evidences of the pivotal role of Trp residues in the physiology of prion proteins.

5.6 Conclusions

The physiological role of prion proteins, as well as the $\text{PrP}^{\text{C}} \rightarrow \text{PrP}^{\text{SC}}$ conversion, remains elusive even after 30 years from their discovery. Their capability to bind Cu^{II} ions seem to have a central role in the physiological function of these proteins, since the part of the sequence that binds the largest amount of Cu^{II} ions is also the most conserved along different species. The dynamics observed in the minutes-hours timescales are often triggered by the ones occurring in the fs-ps range.

With the aim of investigating the Trp ultrafast dynamics and understanding its photo-cycle, as well as the interaction of $^*\text{Trp}$ with nearby residues, we report the first (to our knowledge) ultrafast UV pump-Visible probe transient absorption study on the octarepeat sequence present in the natural human prion protein. In both OPS and OP4 the excited state population of Trp is quenched via nearby amino acids, even if on different timescales, thus pointing to the importance of the interaction between Trp and histidine, glycine and glutamine. Upon Cu addition the protein wraps around the metallic ion, introducing more constraints in the possible peptide conformations.

Moreover, in the OPS the Trp is a terminal residue and it can approach the Cu^{II} ion being close enough to undergo electron transfer. This is not the case of the OP4, in which the Trp points farther, inhibiting the electron transfer to the Cu^{II} ion detected in the smaller OPS. Nonetheless, the excited state population of Trp is quenched on two timescales (5 ps and 70 ps), highlighting again the importance of the nearby residues (also in wrapped conformations of the peptide).

Chapter 6

6 Conclusions and Perspectives

In this thesis three different metallic complexes were investigated with UV pump–Visible (or IR) probe Transient Absorption spectroscopy. Several aspects of these complexes were studied: from the Intersystem crossing and coherence transfer of the highly harmonic potential energy surfaces of Pt(pop) and Pt(pop)–BF₂, to the competing processes of Tryptophan’s fluorescence quenching in biological systems (Myoglobin and prion proteins).

The Pt(pop) is a case–study molecule, which has the peculiarity to form a σ –bond between the two Platinum ions upon excitation.[120, 136] The interest in this inorganic complex has been focused mostly on the lowest excited singlet ($^1A_{2u}$) and triplet ($^3A_{2u}$) states, mainly because of the high reactivity of the latter.[120, 125, 129, 136] The most important mode in Pt(pop) is the Pt–Pt stretching, which allows to describe the system via potential energy curves on the Energy vs Pt–Pt coordinate plane. Moreover, investigation on the Pt–Pt stretching showed that the frequency of the latter in the $^{1,3}A_{2u}$ states is similar (150 cm^{-1} and 155 cm^{-1} ,[52, 135] respectively), suggesting a nested parabola representation of the $^{1,3}A_{2u}$ states. Brunshwig and Milder [127] proposed that another triple state ($^3B_{2u}$) works as intermediate in the relaxation pathway, defining a total decaying pathway of the type: $^1A_{2u} \rightarrow ^3B_{2u} \rightarrow ^3A_{2u}$ (first step is the rate determining). Recently, Van der Veen *et al* [52] reported the solvent–dependent $^1A_{2u} \rightarrow ^3A_{2u}$ Intersystem crossing via transient absorption experiments. They reported Intersystem crossing times spanning from 11 ps in DMF to 30 ps in Ethylene glycol. Our experiments add more information to the latter, reporting a < 1 ps Intersystem crossing in acetonitrile and show the presence of coherence transfer between the $^{1,3}A_{2u}$ states by detecting the arrival of the wave–packet (generated in the $^1A_{2u}$ state) in the $^3A_{2u}$ state. The transient response upon excitation of higher–lying states (UV2), in both Pt(pop) (dissolved in acetonitrile and water) and Pt(pop)–BF₂ (dissolved in acetonitrile), agrees perfectly with the proposed $^3B_{2u}$ intermediate state suggested by Brunshwig and Milder. In order to have a deeper understanding of both Pt(pop) and Pt(pop)–BF₂, it would be interesting to perform some more experiments, such as: i) Time–resolved X–ray absorption probing the phosphorous, which would give information on the cage deformation and; ii) Transient absorption experiments exciting at different wavelengths, such as different regions of UV1, UV2 and UV3 bands, and in different solvents so to compare the transient response.

The other two investigated metal complexes involve either a Fe ion (myoglobin) or a Cu ion (prions). These two proteins share the presence of tryptophan residues in the peptide chain, which is often used as a natural chromophore in the study of protein's dynamics. Since tryptophan is naturally present in proteins [158] and its fluorescence is strongly affected by its environment,[158, 162] it is often used in FRET distance measurements.[62, 157–159] However, the presence of parallel relaxation mechanisms would lead to wrong distance estimates, e.g. the competition between FRET and electron transfer in ferric myoglobins. Therefore, we are interested in determining the active mechanisms in the relaxation pathway of excited tryptophan residues (both in myoglobin and prion proteins).

In myoglobin there are two tryptophan residues (Trp^7 and Trp^{14}), whose center-to-center distance from the heme is $\sim 20 \text{ \AA}$ and $\sim 15 \text{ \AA}$, respectively.[169] The case of ferric myoglobins (MetMb and MbCN) has been previously investigated via 2D-UV and UV pump-Visible probe by Consani *et al.*,[15] which reported a $^*\text{Trp}^{14}$ -to-heme electron transfer occurring with a 60% quantum yield. Our UV pump-IR probe experiments on MbCN (probing in the CN region) confirmed the $^*\text{Trp}^{14}$ -to-heme electron transfer process previously reported. Moreover, probing in the fingerprint region of the porphyrin added valuable information, showing the formation of a porphyrin π -anion radical (band at 1720 cm^{-1}). Thus, the latter results highlight the partial delocalization of the additional charge on the porphyrin, which was not detected previously via 2D-UV and UV pump-Visible probe TA experiments. The invariance in $^*\text{Trp}^{14}$ decay times [13, 14, 163] suggests that a similar mechanism is also active in ferrous myoglobins, even if the reduction potential in ferrous myoglobin is much more negative (-0.85 V (NHE) in the ferrous heme vs $+0.049 \text{ V}$ (NHE) in the ferric one).[201] In this thesis, it has been reported the surprising evidence of a $^*\text{Trp}^{14}$ -to-heme electron transfer in ferrous myoglobins (deoxy-Mb and MbCO) and the peculiar case of MbNO, in which the electron is transferred to the ligand. Since tryptophan cannot be excited selectively, the excitation of the heme at 315 nm has been compared with the one at 290 nm, where both heme and tryptophan absorb. The case of deoxy-Mb is the most suitable to begin with, since the absence of apical ligands attached to the sixth coordination site of the Fe ion assures a short photo-cycle, e.g. $< 4 \text{ ps}$.[12, 34] Interestingly enough, upon 290 nm excitation a broad ESA feature was detected by probing in the visible region. The absorption spectrum of the photo-product, obtained by subtracting the GSB feature from the transient spectrum at 1 ns, showed the absence of the Soret band. Comparison of the obtained results with previous studies on low-valent porphyrins [186, 191, 195, 196] suggested that the generated photo-product, through $^*\text{Trp}^{14}$ -to-heme electron transfer, to be a porphyrin π -anion radical.[186]

The latter hypothesis was then validated by UV pump–IR probe experiments, which showed the growth of a band in the C–C stretching region of the porphyrin ring (1720 cm^{-1}). The MbCO case is quite similar to the deoxy–Mb, showing the generation of a porphyrin π –anion radical. In this case, the 1720 cm^{-1} band is not as well–defined as in deoxy–Mb or MbCN cases, which can be due to the overlap with another broad positive feature. Nonetheless, the MbCO case shows an important aspect that was not observed before, namely the structural changes of the protein scaffold upon the $^*\text{Trp}^{14}$ –to–heme electron transfer that leads to the CO dissociation on a 260 ps timescale. Moreover, it is important to highlight that the $\text{Fe}^{\text{II}}\text{–heme}^{\bullet-}$ and the $\text{Fe}^{\text{I}}\text{–heme}$ are two extreme electromers of the same species,[191, 196] implying the possibility of detecting a small percentage of $\text{Fe}^{\text{I}}\text{–heme}$ depending on the system. A particular case is constituted by the MbNO, being both the most interesting one as well as the most complex to understand. The absence of the 1720 cm^{-1} band, suggests that the porphyrin π –anion radical is not generated. Moreover, the absence of a clear feature in the ligand region (as shown in MbCN and MbCO) implies that the ligand is strongly influenced. Previous cyclic voltammetry experiments by Bayachou *et al* [201] on MbNO reported that the NO reduction potential is bigger than the $\text{Fe}^{\text{II}}\text{–heme}$ one, thus suggesting that the NO could be reduced by the $^*\text{Trp}^{14}$ electron transfer. Moreover, probing in the visible region shows a shift of the Soret ESA feature on a 350 ps timescale (only upon 290 nm), whose cause was not identified.

The results presented in this thesis raise more questions on the nature of the photo–products and the importance of the electromerism between the $\text{Fe}^{\text{II}}\text{–heme}^{\bullet-}$ and the $\text{Fe}^{\text{I}}\text{–heme}$. In order to answer these questions additional experiments could be performed, such as: i) time–resolved X–ray absorption exciting the tryptophan residue and probing the Fe ion would give information on the possible change of Fe oxidation state; ii) in the MbNO case, probing at frequencies $< 1300\text{ cm}^{-1}$ and $> 1800\text{ cm}^{-1}$ would allow to detect the ESA feature of the reduced NO; and iii) a spectro – electrochemical analysis would give the static spectra of the reduced myoglobin species, allowing comparison with the spectra associated to the generated photo–products.

With respect to myoglobin, prion proteins are smaller and less understood both from a point of view of physiological relevance and disease–relationship.[16, 244, 245] Prion proteins contain four tryptophan residues in the octarepeat region (N–terminal side) and bind Cu^{II} ions with high selectivity.[258, 261, 263] The peptides investigated in this thesis possess either one or four tryptophan residues, e.g. OPS (sequence HGGGW) and OP4 (sequence (PHGGGWGQ)₄), respectively. The transient signal obtained upon 280 nm photo–excitation of OPS is due to the $^*\text{Trp}$, which was probed in the 380–600 nm range.

The latter region is characterized mainly by the broad and unstructured *Trp ESA band, whose time evolution was described by three time constants: ~390 fs (assigned to cooling), ~19 ps (assigned to electron transfer to nearby residues, such as H or G) and ~1.5 ns (assigned to a lower limit for *Trp radiative decay). Addition of a 3-fold excess of CuCl₂ solution, with respect to equimolar quantity, leads to the formation of the OPS–Cu complex, which shows the presence of a new ESA band centered at 450 nm and decaying on a 180 fs timescale. The latter feature was assigned to a Cu^I–to–TrpH^{•+} back–electron transfer, by comparing the ESA band with the absorption band of the Cu^I–bathocuproine sulphonate (BCS) complex. If this is the case, the *Trp–to–Cu^{II} forward electron transfer should occur on a timescale \ll 130 fs (the experimental IRF) since we do not detect the rise of the transient ESA band. The proposed deactivation mechanism is possible since the Trp is hydrogen bonding a water molecule that is directly bound to the Cu ion, therefore having a preferential pathway for the electron transfer. Beside the 180 fs timescale were detected a 17 ps and a 1.8 ns components, thus suggesting that different molecular conformations are present in the probed peptide, some of which have the Trp residue far away from the Cu ion and closer to other amino acid residues.

The results on the un–complexed OP4 show similar features to the un–complexed OP4 except an additional timescale of 1 ps, which was assigned either to the *Trp–to–Glutamine electron transfer or to the *Trp–to–histidine (or glycine) electron transfer. In the latter case, the shorter timescale could be due to the folding of the peptide chain, since OP4 has a much longer sequence than OPS and can lead the *Trp closer to other amino acids that are not its neighbors in the peptide sequence. The presence of the ~390 fs, ~20 ps and 2 ns suggest that, also in this case, the peptides acquire different conformations, some of which have the Trp residue much closer to histidine, glycine and glutamine (responsible for the additional 1 ps timescale observed). Addition of a 3-fold excess of CuCl₂ solution, with respect to Trp: Cu equimolar quantity, leads to the formation of the OP4–Cu complex. Interestingly, the OP4–Cu kinetics are completely different from the OP4 or OPS–Cu ones, showing three decay times: 4.6 ps, 76 ps and 1.4 ns. The latter value was again assigned to the *Trp radiative decay, while the 4.6 ps and 76 ps were assigned to electron transfer from the *Trp to nearby amino acids. We suggested that the different timescales, with respect to the free peptide, are due to the lower flexibility of the peptide induced by the Cu complexation, which causes the peptide to wrap around the metallic ion.[247] The absence of *Trp–to–Cu electron transfer suggests that in OP4–Cu the Trp is far away from the Cu, in agreement with recent DFT calculations.[294] Therefore these results highlight the importance of peptide conformations on the Trp excited state population quenching, but also display the key role of Trp in prion proteins.

These preliminary results open to a series of other possible ultrafast experiments, such as measuring the transient response as function of the pH, modifying the proportion between metal center and binding moieties or even use different metal centers. Varying the pH of the solution (e.g. from pH = 5 to pH = 8) used for transient absorption experiments, allows understanding the impact of residues' protonation on the observed kinetics and on Cu complexation. Modifying the Cu: OP ratio would give also more information, since the Cu-binding forms are different at low and high-occupancy of the Cu-binding sites.[247, 289, 290] Combining the latter measurements with the investigation of longer parts of the sequence, maybe introducing the fifth coordination site (so called Non-Octarepeat region), would give even more information on the prion behavior. Beside the reported results, investigation of the ultrafast kinetics of OP upon Zn^{2+} , Mn^{2+} or Fe^{2+} complexation would be interesting,[269, 272, 294–296] adding more value to the observed OP–Cu kinetics. Therefore, it would be useful to perform both TA (probing both in the UV and in the visible regions) and fluorescence Up–Conversion experiments with different experimental conditions. TA experiments, exciting the Trp residue and probing in the IR region, would also be interesting, since they allow gathering information on the change of vibrational modes' frequency. The latter could show the marker of the $TrpH^{\bullet+}$ generated upon the electron transfer process from the *Trp to nearby residues.

Moreover, time–resolved X–ray absorption and emission (exciting the Trp residue) could be performed, so to investigate deeply on Cu reduction (even if short pulses are required). Finally, it would be extremely important to investigate the impact of residue exchange, determining the kinetics of *Trp in absence of histidine, glutamine or proline, as well as the capability of complex different metal ions with slight changes in the sequence, performing transient absorption exciting at 280 nm and probing in the IR region.

List of Abbreviations

2D	Two Dimensional
A	Acceptor
BBO	β -Barium Borate
BCS	Bathocuproine Sulphonate
bpy	2,2'- bipyridine
CCD	Charged-Coupled Device
CMOS	Complementary Metal-Oxide Semiconductor
CW	Continuous Wave
Cyt	Cytochrome
D	Donor
DAS	Decay Associated Spectrum
ddab	dimethyl-didodecyl ammonium bromide
DFT	Density Functional Theory
dimen	1,8-diisocyano-p-menthane
dmbp	4,4'-dimethyl-2,2'- bipyridine
dpp	2,3-dipyridil pyrazine
EN	Electronic Noise
ES	Excited State
ESA	Excited State Absorption
FFT	Fast Fourier Transform
FRET	Förster Energy Transfer

FS	Fused Silica
FWHM	Full Width at Half Maximum
G	Glycine
GF	Global Fit
GPI	Glycosyl-Phosphatidylinositol
GS	Ground State
GSB	Ground State Bleach
GVD	Group Velocity Dispersion
H	Histidine
HH	Horse Heart
IC	Internal Conversion
Im	Imidazole
IRF	Instrumental Response Function
ISC	Intersystem Crossing
LL	Long-Lived
LMCT	Ligand-to-Metal Charge Transfer
LMMCT	Ligand-to-Metal-Metal Charge Transfer
Mb	Myoglobin
MES	2-(N-Morpholino) EthaneSulphate
MLCT	Metal-to-Ligand Charge Transfer
NHE	Normal Hydrogen Electrode
NOPA	NON-Collinear Optical Parametric Amplifier
OEP	Octa-ethyl Porphyrin

P	Proline
PD	Photo Diode
porph	Porphyrin
PrP	Prion Protein
PrP ^C	Cellular PrP
PrP ^{SC}	Scrapie PrP
Q	Glutamine
QY	Quantum Yield
SE	Stimulated Emission
S / N	Signal-to-Noise Ratio
SVD	Singular Value Decomposition
SW	Sperm Whale
T	Temperature
TA	Transient Absorption
TDDFT	Time-Dependent DFT
TPP	Tetra Phenyl Porphyrin
Trp (W)	Tryptophan
TSE	Transmissible Spongiform Encephalopathies
VR	Vibrational relaxation

Acknowledgments

At the end of this thesis, as at the end of my Ph. D. period, I want to thank all the people that made this work possible and all the friends that spent with me these beautiful years.

In the first place I would like to express my deepest gratitude to Prof. *Majed Chergui*, which gave me the opportunity to join the LSU group and begin the journey that brought me here. Your support and encouragement, as well as your wide knowledge in the field of time-resolved spectroscopy, have been of great help and inspiration during my Ph. D. thesis! Even though I was a “*tabula rasa*” on laser technology and ultrafast spectroscopy you gave me the opportunity to learn and build up a successful Ph. D. and for this I am extremely grateful to you.

I would like to thank the committee members: Prof. *Antonìn Vlček*, Dr. *Jan Helbing*, Prof. *Kai Johnsson* and Prof. *Jacques-Edouard Moser* for accepting to evaluate this work, their very interesting comments and the fruitful discussion.

I would like to thank twice Prof. *Antonìn Vlček* for the great collaboration and instructive discussions on Pt(pop) molecular complexes, as well as his constant support and emphasis on this argument.

A special thank goes to *Esther von Arx* and *Monique Bassin*, the two secretaries that helped me in the bureaucratic jungle that concerned not only work-related information but any information related to life in Switzerland.

I am grateful to *Andrea Cannizzo*, which I nicknamed “*the machinegun*” for his ability of “shooting” an incredible amount of words in a short lapse of time. Is seared in my memories one of the first days after my arrival in Lausanne, when you explained me everything I needed to know about lasers keeping me four consecutive hours in the lab. At the end I was tired and you were not even thinking to drink a glass of water! Anyways, even if you left the group six months after my arrival, you taught me so many things about lasers and I am grateful for that.

I thank *Frank van Mourik* and *Gerald Auböck*. You have both been a reference point in the laboratory life during these years of Ph. D. and helped me in my scientific growth. Beside your scientific and experimental knowledge, I have to admit that you surprised me, *Frank*, when I saw you moving so fast on the squash field!

A special thanks goes to *Andre al Haddad*, colleague and friend that shared with me both uphill and downhill moments of these four years. From the running trials to the Libanese food, from the Top Gear shows to the Italian food and from two days of continuous measurements to the BBQs at the lake, these were four years full of fun.

I would like to thank my former and new office mates: *Maria Teresa Scarongella, Ahmed El Zohry, Josè Andara Ojeda* and *Malte Oppermann*. It was really great to share the office with you! You have set a high quality standard for future office mates!

I am very grateful to *Adrien Chauvet*, which double-checked my thesis. You just came out of the blue and proposed yourself to take on yourself the burden of reading a full thesis, even if it was not your duty. I deeply appreciate your gesture and thank you again!

Special thanks to all the group members, former and new-comers: *Fabrizio Messina, Marco Reinhard, Ahmad Odeh, Cristina Consani, Enrico Pomarico, Christopher Arrel, Edoardo Baldini, Gloria Capano, Mahsa Silatani, Fabio Santomauro, Grilj Jakob, Janina Löffler, Lars Mewes, Thomas Rossi and Tania Palmieri*. It has been really nice spending these years in a beautiful environment as the LSU. Thank you all for the great cake/coffee/drink times spent together!

I want to thank also all the friends I met along this path and the ones known from before, that came all the way to here to visit me and enjoy fantastic moments. Thanks to *Riccardo Piras, Elisa Sessini, Luca Pilia, Davide Espa, Antonio Papa, Francesco Angioni, Antonio Bosa, Marta Mameli Giulia Mancini, Francesco Pennacchio, Luca Piazza, Massimo Vespignani and Stefano Andreozzi*. Some of you are still here and some of you already left but I am very grateful for all the beautiful moments spent together here in Switzerland and in Italy.

Last but not least I thank my family! Non penso ci siano delle parole che riescano ad esprimere l'aiuto, la pazienza ed il bene che mi avete dato perciò dirò semplicemente GRAZIE! Ringrazio specialmente i miei genitori, che hanno fatto sì che tutto ciò potesse avvenire! Parlando di famiglia un ringraziamento profondo va anche a te, Fabiana, che mi sei stata sempre vicina durante tutti questi anni e soprattutto negli ultimi mesi, con tutti i miei alti e bassi. Senza di voi, *la mia famiglia*, non sarei mai riuscito ad arrivare fin qui con cotanta sportiveggianza!

Bibliography

1. Esswein, A.J. and D.G. Nocera, Hydrogen production by molecular photocatalysis. *Chemical Reviews*, 2007. 107(10): p. 4022–4047.
2. Vlcek, A., *The life and times of excited states of organometallic and coordination compounds*. *Coordination Chemistry Reviews*, 2000. 200: p. 933–977.
3. Durrell, A.C., et al., Structural Control of (1)A(2u)–to–(3)A(2u) Intersystem Crossing in Diplatinum(II,II) Complexes. *Journal of the American Chemical Society*, 2012. 134(34): p. 14201–14207.
4. Kaltashov, I.A., et al., Investigation of structure, dynamics and function of metalloproteins with electrospray ionization mass spectrometry. *Analytical and Bioanalytical Chemistry*, 2006. 386(3): p. 472–481.
5. Sawicki, K.T., H.C. Chang, and H. Ardehali, Role of Heme in Cardiovascular Physiology and Disease. *Journal of the American Heart Association*, 2015. 4(1).
6. Wittenberg, J.B. and B.A. Wittenberg, Myoglobin function reassessed. *Journal of Experimental Biology*, 2003. 206(12): p. 2011–2020.
7. Ordway, G.A. and D.J. Garry, Myoglobin: an essential hemoprotein in striated muscle. *Journal of Experimental Biology*, 2004. 207(20): p. 3441–3446.
8. Fogel, U., A. Fago, and T. Rassaf, Keeping the heart in balance: the functional interactions of myoglobin with nitrogen oxides. *Journal of Experimental Biology*, 2010. 213(16): p. 2726–2733.
9. Chauvet, A.A.P., et al., Photo-induced dynamics of the heme centers in cytochrome bc(1). *Physical Chemistry Chemical Physics*, 2015. 17(3): p. 2143–2151.
10. Jackson, T.A., M. Lim, and P.A. Anfinrud, Complex Nonexponential Relaxation in Myoglobin after Photodissociation of Mbco – Measurement and Analysis from 2–Ps to 56–Mu–S. *Chemical Physics*, 1994. 180(2–3): p. 131–140.
11. Lim, M.H., T.A. Jackson, and P.A. Anfinrud, Ultrafast rotation and trapping of carbon monoxide dissociated from myoglobin. *Nature Structural Biology*, 1997. 4(3): p. 209–214.
12. Ye, X., A. Demidov, and P.M. Champion, Measurements of the photodissociation quantum yields of MbNO and MbO(2) and the vibrational relaxation of the six-coordinate heme species. *Journal of the American Chemical Society*, 2002. 124(20): p. 5914–5924.
13. Willis, K.J., et al., Fluorescence Decay Kinetics of the Tryptophyl Residues of Myoglobin – Effect of Heme Ligation and Evidence for Discrete Lifetime Components. *Biochemistry*, 1990. 29(22): p. 5270–5275.
14. Willis, K.J., A.G. Szabo, and D.T. Krajcarski, Fluorescence Decay Kinetics of the Tryptophyl Residues of Myoglobin Single-Crystals. *Journal of the American Chemical Society*, 1991. 113(6): p. 2000–2002.
15. Consani, C., et al., Ultrafast Tryptophan–to–Heme Electron Transfer in Myoglobins Revealed by UV 2D Spectroscopy. *Science*, 2013. 339(6127): p. 1586–1589.
16. Prusiner, S.B., Prions. *Proceedings of the National Academy of Sciences of the United States of America*, 1998. 95(23): p. 13363–13383.
17. Sailer, A., et al., No Propagation of Prions in Mice Devoid of Prp. *Cell*, 1994. 77(7): p. 967–968.
18. Huang, Z.W., S.B. Prusiner, and F.E. Cohen, Scrapie prions: A three-dimensional model of an infectious fragment. *Folding & Design*, 1996. 1(1): p. 13–19.
19. Stockel, J., et al., Prion protein selectively binds copper(II) ions. *Biochemistry*, 1998. 37(20): p. 7185–7193.

20. Ruiz, F.H., E. Silva, and N.C. Inestrosa, *The N-terminal tandem repeat region of human prion protein reduces copper: Role of tryptophan residues*. *Biochemical and Biophysical Research Communications*, 2000. 269(2): p. 491–495.
21. *The Nobel Prize in Chemistry 1967*. [cited 2015 10 March]; Available from: http://www.nobelprize.org/nobel_prizes/chemistry/laureates/1967/.
22. Tollin, G., et al., *Use of Laser Flash-Photolysis Time-Resolved Spectrophotometry to Investigate Interprotein and Intraprotein Electron-Transfer Mechanisms*. *Biophysical Chemistry*, 1993. 48(2): p. 259–279.
23. Holten, D. and M.W. Windsor, *Picosecond Flash-Photolysis in Biology and Biophysics*. *Annual Review of Biophysics and Bioengineering*, 1978. 7: p. 189–227.
24. Nibbering, E.T.J., H. Fidder, and E. Pines, *Ultrafast chemistry: Using time-resolved vibrational spectroscopy for interrogation of structural dynamics*. *Annual Review of Physical Chemistry*, 2005. 56: p. 337–367.
25. Bressler, C. and M. Chergui, *Ultrafast X-ray absorption spectroscopy*. *Chemical Reviews*, 2004. 104(4): p. 1781–1812.
26. Bucksbaum, P.H., *The future of attosecond Spectroscopy*. *Science*, 2007. 317(5839): p. 766–769.
27. Cannizzo, A., et al., *Femtosecond fluorescence upconversion setup with broadband detection in the ultraviolet*. *Optics Letters*, 2007. 32(24): p. 3555–3557.
28. Aubock, G., et al., *Femtosecond pump/supercontinuum-probe setup with 20 kHz repetition rate*. *Review of Scientific Instruments*, 2012. 83(9).
29. Aubock, G., et al., *Ultrabroadband femtosecond two-dimensional ultraviolet transient absorption*. *Optics Letters*, 2012. 37(12): p. 2337–2339.
30. Greetham, G.M., et al., *ULTRA: A Unique Instrument for Time-Resolved Spectroscopy*. *Applied Spectroscopy*, 2010. 64(12): p. 1311–9.
31. Ekvall, K., et al., *Cross phase modulation artifact in liquid phase transient absorption spectroscopy*. *Journal of Applied Physics*, 2000. 87(5): p. 2340–2352.
32. Polli, D., et al., *Effective temporal resolution in pump-probe spectroscopy with strongly chirped pulses*. *Physical Review A*, 2010. 82(5).
33. Owrutsky, J.C., D. Raftery, and R.M. Hochstrasser, *Vibrational relaxation dynamics in solutions*. *Annual Review of Physical Chemistry*, 1994. 45: p. 519–55.
34. Kholodenko, Y., et al., *Energy dissipation and relaxation processes in deoxy myoglobin after photoexcitation in the Soret region*. *Chemical Physics*, 2000. 259(1): p. 71–87.
35. Fidder, H., M. Rini, and E.T.J. Nibbering, *The role of large conformational changes in efficient ultrafast internal conversion: Deviations from the energy gap law*. *Journal of the American Chemical Society*, 2004. 126(12): p. 3789–3794.
36. Kasha, M., *Characterization of electronic transitions in complex molecules*. *Discussions of the Faraday Society*, 1950. 9(0): p. 14–19.
37. Wilkinson, A.D.M.a.A. *Kasha's rule*. IUPAC, *Compendium of Chemical Terminology*, 2nd ed. 1997 2014–02–24; Available from: <http://goldbook.iupac.org/K03370.html>.
38. Zhang, Y.X., et al., *Metal-enhanced S₂ fluorescence from azulene*. *Chemical Physics Letters*, 2006. 432(4–6): p. 528–532.
39. Wagner, B.D., D. Tittelbach-Helmrich, and R.P. Steer, *Radiationless decay of the S₂ states of azulene and related compounds: solvent dependence and the energy gap law*. *The Journal of Physical Chemistry*, 1992. 96(20): p. 7904–7908.
40. Geldof, P.A., R.P.H. Rettschnick, and G.J. Hoytink, *Fluorescence from the second excited singlets of pyrene and 3,4-benzopyrene*. *Chemical Physics Letters*, 1969. 4(2): p. 59–61.

41. Wannier, P., P.M. Rentzepis, and J. Jortner, Resonance fluorescence from the second excited singlet state of naphthalene. *Chemical Physics Letters*, 1971. 10(2): p. 193–196.
42. Deinum, T., et al., Relative quantum yield of the S2 emission of naphthalene vapour. *Chemical Physics Letters*, 1973. 19(1): p. 29–31.
43. Loi, M.A., et al., Encapsulation of Conjugated Oligomers in Single-Walled Carbon Nanotubes: Towards Nanohybrids for Photonic Devices. *Advanced Materials*, 2010. 22(14): p. 1635–1639.
44. Yanagi, K. and H. Kataura, CARBON NANOTUBES Breaking Kasha's rule. *Nature Photonics*, 2010. 4(4): p. 200–201.
45. Solovyov, K.N. and E.A. Borisevich, Intramolecular heavy-atom effect in the photophysics of organic molecules. *Physics–Uspekhi*, 2005. 48(3): p. 231–253.
46. Chergui, M., On the interplay between charge, spin and structural dynamics in transition metal complexes. *Dalton Transactions*, 2012. 41(42): p. 13022–13029.
47. Gawelda, W., et al., Light-induced spin crossover probed by ultrafast optical and X-ray spectroscopies. *Chimia*, 2007. 61(4): p. 179–183.
48. Cannizzo, A., et al., Femtosecond fluorescence and intersystem crossing in rhenium(I) carbonyl–bipyridine complexes. *Journal of the American Chemical Society*, 2008. 130(28): p. 8967–8974.
49. Bressler, C., et al., Femtosecond XANES Study of the Light-Induced Spin Crossover Dynamics in an Iron(II) Complex. *Science*, 2009. 323(5913): p. 489–492.
50. Cannizzo, A., et al., Light-induced spin crossover in Fe(II)-based complexes: The full photocycle unraveled by ultrafast optical and X-ray spectroscopies. *Coordination Chemistry Reviews*, 2010. 254(21–22): p. 2677–2686.
51. El Nahhas, A., et al., X-ray Absorption Spectroscopy of Ground and Excited Rhenium–Carbonyl–Diimine Complexes: Evidence for a Two-Center Electron Transfer. *The Journal of Physical Chemistry A*, 2013. 117(2): p. 361–369.
52. van der Veen, R.M., et al., Vibrational Relaxation and Intersystem Crossing of Binuclear Metal Complexes in Solution. *Journal of the American Chemical Society*, 2011. 133(2): p. 305–315.
53. Cannizzo, A., et al., Broadband femtosecond fluorescence spectroscopy of [Ru(bpy)(3)](2+). *Angewandte Chemie–International Edition*, 2006. 45(19): p. 3174–3176.
54. Gawelda, W., et al., Ultrafast nonadiabatic dynamics of [Fe–II(bpy)(3)](2+) in solution. *Journal of the American Chemical Society*, 2007. 129(26): p. 8199–8206.
55. Consani, C., et al., Vibrational Coherences and Relaxation in the High-Spin State of Aqueous [Fe–II(bpy)(3)](2+). *Angewandte Chemie–International Edition*, 2009. 48(39): p. 7184–7187.
56. Bram, O., et al., Ultrafast Relaxation Dynamics of Osmium–Polypyridine Complexes in Solution. *Journal of Physical Chemistry C*, 2013. 117(31): p. 15958–15966.
57. Chergui, M., Ultrafast Photophysics of Transition Metal Complexes. *Accounts of Chemical Research*, 2015. 48(3): p. 801–808.
58. Turro, N.J., Ramamurthy, V. and Scaiano, J.C., Principles of Molecular Photochemistry An Introduction 2009: University Science Books. 36.
59. Turro, N.J., Ramamurthy, V. and Scaiano, J.C., Principles of Molecular Photochemistry 2009. 195–200.
60. Mirkovic, T. and G. Scholes, Photosynthetic Light Harvesting, in *Photobiology*, L.O. Björn, Editor 2015, Springer New York. p. 231–241.
61. Olaya-Castro, A. and G.D. Scholes, Energy transfer from Forster–Dexter theory to quantum coherent light-harvesting. *International Reviews in Physical Chemistry*, 2011. 30(1): p. 49–77.

62. Masters, B.R., *Paths to Förster's resonance energy transfer (FRET) theory. The European Physical Journal H*, 2014. 39(1): p. 87–139.
63. Dexter, D.L., *A Theory of Sensitized Luminescence in Solids. Journal of Chemical Physics*, 1953. 21(5): p. 836–850.
64. Stryer, L., *Fluorescence Energy–Transfer as a Spectroscopic Ruler. Annual Review of Biochemistry*, 1978. 47: p. 819–846.
65. Truong, K. and M. Ikura, *The use of FRET imaging microscopy to detect protein–protein interactions and protein conformational changes in vivo. Current Opinion in Structural Biology*, 2001. 11(5): p. 573–578.
66. Polley, N., et al., *Ultrafast FRET at fiber tips: Potential applications in sensitive remote sensing of molecular interaction. Sensors and Actuators B: Chemical*, 2015. 210(0): p. 381–388.
67. Gustiananda, M., et al., *Conformation of prion protein repeat peptides probed by FRET measurements and molecular dynamics simulations. Biophysical Journal*, 2004. 86(4): p. 2467–2483.
68. Hadar, I., et al., *Dimensionality Effects on Fluorescence Resonance Energy Transfer between Single Semiconductor Nanocrystals and Multiple Dye Acceptors. Journal of Physical Chemistry C*, 2015. 119(7): p. 3849–3856.
69. DAHAN, M., *Fluorescence microscopy for biological imaging, in Physics and Biology. p. 31–48.*
70. Winkler, J.R., *FRETting over the Spectroscopic Ruler. Science*, 2013. 339(6127): p. 1530–1531.
71. Gray, H.B. and J.R. Winkler, *Long–range electron transfer. Proceedings of the National Academy of Sciences of the United States of America*, 2005. 102(10): p. 3534–3539.
72. Cordes, M., et al., *Influence of amino acid side chains on long–distance electron transfer in peptides: Electron hopping via "Stepping Stones". Angewandte Chemie–International Edition*, 2008. 47(18): p. 3461–3463.
73. Cordes, M. and B. Giese, *Electron transfer in peptides and proteins. Chemical Society Reviews*, 2009. 38(4): p. 892–901.
74. Farver, O. and I. Pecht, *Electron transfer in blue copper proteins. Coordination Chemistry Reviews*, 2011. 255(7–8): p. 757–773.
75. Lancaster, K.M., et al., *Electron Transfer Reactivity of Type Zero Pseudomonas aeruginosa Azurin. Journal of the American Chemical Society*, 2011. 133(13): p. 4865–4873.
76. Farver, O., et al., *Structure–function correlation of intramolecular electron transfer in wild type and single–site mutated azurins. Chemical Physics*, 1996. 204(2–3): p. 271–277.
77. Gray, H.B. and J.R. Winkler, *Electron transfer in proteins. Annual Review of Biochemistry*, 1996. 65: p. 537–561.
78. Mines, G.A., et al., *Cytochrome c folding triggered by electron transfer. Chemistry & Biology*, 1996. 3(6): p. 491–497.
79. Pascher, T., et al., *Protein folding triggered by electron transfer. Science*, 1996. 271(5255): p. 1558–1560.
80. Byrdin, M., et al., *Intraprotein electron transfer and proton dynamics during photoactivation of DNA photolyase from E–coli: review and new insights from an "inverse" deuterium isotope effect. Biochimica Et Biophysica Acta–Bioenergetics*, 2004. 1655(1–3): p. 64–70.
81. Wang, M., et al., *Electron Transfer in Peptides with Cysteine and Methionine as Relay Amino Acids. Angewandte Chemie–International Edition*, 2009. 48(23): p. 4232–4234.

82. Gray, H.B. and J.R. Winkler, *Electron flow through proteins. Chemical Physics Letters*, 2009. 483(1–3): p. 1–9.
83. Warren, J.J., et al., *Electron hopping through proteins. Coordination Chemistry Reviews*, 2012. 256(21–22): p. 2478–2487.
84. Siddarth, P. and R.A. Marcus, *Correlation between Theory and Experiment in Electron–Transfer Reactions in Proteins – Electronic Couplings in Modified Cytochrome–C and Myoglobin Derivatives. Journal of Physical Chemistry*, 1993. 97(50): p. 13078–13082.
85. Siddarth, P. and R.A. Marcus, *Electron–Transfer Reactions in Proteins – Electronic Coupling in Myoglobin. Journal of Physical Chemistry*, 1993. 97(23): p. 6111–6114.
86. Schichman, S.A., T.E. Meyer, and H.B. Gray, *Kinetics of electron transfer in Pseudomonas aeruginosa cytochrome cd(1)–nitrite reductase. Inorganica Chimica Acta*, 1996. 243(1–2): p. 25–31.
87. Marcus, R.A., *On the Theory of Oxidation–Reduction Reactions Involving Electron Transfer .1. Journal of Chemical Physics*, 1956. 24(5): p. 966–978.
88. Marcus, R.A., *Chemical + Electrochemical Electron–Transfer Theory. Annual Review of Physical Chemistry*, 1964. 15: p. 155–&.
89. Marcus, R.A., *Theory of Oxidation–Reduction Reactions Involving Electron Transfer .5. Comparison and Properties of Electrochemical and Chemical Rate Constants. Journal of Physical Chemistry*, 1963. 67(4): p. 853–&.
90. Marcus, R.A., *On the Theory of Electrochemical and Chemical Electron Transfer Processes. Canadian Journal of Chemistry–Revue Canadienne De Chimie*, 1959. 37(1): p. 155–163.
91. Libby, W.F., *Theory of Electron Exchange Reactions in Aqueous Solution. Journal of Physical Chemistry*, 1952. 56(7): p. 863–868.
92. Grampp, G., *The Marcus Inverted Region from Theory to Experiment. Angewandte Chemie–International Edition in English*, 1993. 32(5): p. 691–693.
93. Koch, M., et al., *Bimolecular Photoinduced Electron Transfer in Imidazolium–Based Room–Temperature Ionic Liquids Is Not Faster than in Conventional Solvents. Journal of the American Chemical Society*, 2012. 134(8): p. 3729–3736.
94. Rosspeintner, A., et al., *Spurious Observation of the Marcus Inverted Region in Bimolecular Photoinduced Electron Transfer. Journal of the American Chemical Society*, 2012. 134(28): p. 11396–11399.
95. Ohmori, K., *Wave–Packet and Coherent Control Dynamics. Annual Review of Physical Chemistry*, 2009. 60: p. 487–511.
96. Garraway, B.M. and K.A. Suominen, *Wave–Packet Dynamics – New Physics and Chemistry in Femto–Time. Reports on Progress in Physics*, 1995. 58(4): p. 365–419.
97. Doncheski, M.A. and R.W. Robinett, *Wave packet revivals and the energy eigenvalue spectrum of the quantum pendulum. Annals of Physics*, 2003. 308(2): p. 578–598.
98. Averbukh, I.S. and N.F. Perelman, *Fractional Revivals of Wave–Packets in the Course of Long–Term Evolution of Highly Excited Quantum–Systems. Zhurnal Eksperimentalnoi I Teoreticheskoi Fiziki*, 1989. 96(3): p. 818–827.
99. Averbukh, I.S. and N.F. Perelman, *Fractional Revivals – Universality in the Long–Term Evolution of Quantum Wave–Packets Beyond the Correspondence Principle Dynamics. Physics Letters A*, 1989. 139(9): p. 449–453.
100. Sudheesh, C., S. Lakshmibala, and V. Balakrishnan, *Manifestations of wave packet revivals in the moments of observables. Physics Letters A*, 2004. 329(1–2): p. 14–21.
101. Pollard, W.T., et al., *Quantum–Mechanical Theory for 6–Fs Dynamic Absorption–Spectroscopy and Its Application to Nile Blue. Chemical Physics Letters*, 1990. 168(3–4): p. 239–245.

102. Rose, T.S., M.J. Rosker, and A.H. Zewail, *Femtosecond Real-Time Probing of Reactions .4. The Reactions of Alkali-Halides*. *Journal of Chemical Physics*, 1989. 91(12): p. 7415–7436.
103. Dantus, M., R.M. Bowman, and A.H. Zewail, *Femtosecond Laser Observations of Molecular Vibration and Rotation*. *Nature*, 1990. 343(6260): p. 737–739.
104. Mokhtari, A., et al., *Direct Femtosecond Mapping of Trajectories in a Chemical-Reaction*. *Nature*, 1990. 348(6298): p. 225–227.
105. Cong, P., A. Mokhtari, and A.H. Zewail, *Femtosecond Probing of Persistent Wave Packet Motion in Dissociative Reactions – up to 40 Ps*. *Chemical Physics Letters*, 1990. 172(2): p. 109–113.
106. Scherer, N.F., D.M. Jonas, and G.R. Fleming, *Femtosecond Wave-Packet and Chemical-Reaction Dynamics of Iodine in Solution – Tunable Probe Study of Motion Along the Reaction Coordinate*. *Journal of Chemical Physics*, 1993. 99(1): p. 153–168.
107. Jean, J.M. and G.R. Fleming, *Competition between Energy and Phase Relaxation in Electronic Curve Crossing Processes*. *Journal of Chemical Physics*, 1995. 103(6): p. 2092–2101.
108. Baum, P., S. Lochbrunner, and E. Riedle, *Generation of tunable 7-fs ultraviolet pulses: achromatic phase matching and chirp management*. *Applied Physics B–Lasers and Optics*, 2004. 79(8): p. 1027–1032.
109. Baum, P., S. Lochbrunner, and E. Riedle, *Tunable sub-10-fs ultraviolet pulses generated by achromatic frequency doubling*. *Optics Letters*, 2004. 29(14): p. 1686–1688.
110. Zheltikov, A.M., *Let there be white light: supercontinuum generation by ultrashort laser pulses*. *Physics–Uspekhi*, 2006. 49(6): p. 605–628.
111. Chin, S.L., et al., *Advances in intense femtosecond laser filamentation in air*. *Laser Physics*, 2012. 22(1): p. 1–53.
112. Ghosh, G., *Sellmeier coefficients and dispersion of thermo-optic coefficients for some optical glasses*. *Applied Optics*, 1997. 36(7): p. 1540–1546.
113. Polyanskiy, M. *RefractiveIndex.Info*. 2008–2015; Available from: <http://refractiveindex.info/?shelf=glass&book=BK7&page=SCHOTT>.
114. optics, G., 2015.
115. Moon, J.A., *Optimization of Signal-to-Noise Ratios in Pump-Probe Spectroscopy*. *Review of Scientific Instruments*, 1993. 64(7): p. 1775–1778.
116. Dobryakov, A.L., et al., *Femtosecond pump/supercontinuum-probe spectroscopy: Optimized setup and signal analysis for single-shot spectral referencing*. *Review of Scientific Instruments*, 2010. 81(11).
117. Henry, E.R., *The use of matrix methods in the modeling of spectroscopic data sets*. *Biophysical Journal*, 1997. 72(2): p. 652–673.
118. Ruckebusch, C., et al., *Comprehensive data analysis of femtosecond transient absorption spectra: A review*. *Journal of Photochemistry and Photobiology C–Photochemistry Reviews*, 2012. 13(1): p. 1–27.
119. Galo, A.L. and M.F. Colombo, *Singular Value Decomposition and Ligand Binding Analysis*. *Journal of Spectroscopy*, 2013.
120. Roundhill, D.M., H.B. Gray, and C.M. Che, *Pyrophosphito-Bridged Diplatinum Chemistry*. *Accounts of Chemical Research*, 1989. 22(2): p. 55–61.
121. Smith, D.C. and H.B. Gray, *Photochemistry of Binuclear D8 Complexes*. *Coordination Chemistry Reviews*, 1990. 100: p. 169–181.
122. Miskowski, V.M., et al., *Spectroscopy and Photophysics of Rh₂(Dimen)₄(2+) (Dimen = 1,8-Diisocyanomenthane) – Exceptional Metal-Metal Bond Shortening in the Lowest Electronic Excited-States*. *Inorganic Chemistry*, 1994. 33(13): p. 2799–2807.

123. Smith, D.C., et al., *Electronic Absorption and Mcd Spectra of $M_2(Tmb)_4(2+)$, $M = Rh$ and Ir – a Valence–Bond Description of the Upper Electronic Excited–States.* *Journal of the American Chemical Society*, 1990. 112(10): p. 3759–3767.
124. Bryan, S.A., M.K. Dickson, and D.M. Roundhill, *Thermal, Photochemical, and Electrochemical Reactions Involving Binuclear Platinum(Ii) and Platinum(Iii) Pyrophosphite Complexes – Reaction Chemistry of $Pt_2(P_2O_5H_2)_4^{4-}$ and the Halide–Complexes $Pt_2(P_2O_5H_2)_4^{2-}$.* *Journal of the American Chemical Society*, 1984. 106(6): p. 1882–1883.
125. Bryan, S.A., M.K. Dickson, and D.M. Roundhill, *Synthesis, Reactivity, Kinetics, and Photochemical Studies on Tetrakis(Mu–Pyrophosphito)Diplatinate(Ii) and Dihalotetrakis(Mu–Pyrophosphito)Diplatinate(Iii) Complexes – Comparison of the Substitution Mechanisms of the Diplatinum(Iii) Complexes with Those of Monomeric Platinum(Ii) and Platinum(Iv) Compounds.* *Inorganic Chemistry*, 1987. 26(23): p. 3878–3886.
126. Fordyce, W.A., J.G. Brummer, and G.A. Crosby, *Electronic Spectroscopy of a Diplatinum(Ii) Octaphosphite Complex.* *Journal of the American Chemical Society*, 1981. 103(24): p. 7061–7064.
127. Milder, S.J. and B.S. Brunschwig, *Factors Affecting Nonradiative Decay – Temperature–Dependence of the Picosecond Fluorescence Lifetime of $Pt_2(POP)_4(4-)$.* *Journal of Physical Chemistry*, 1992. 96(5): p. 2189–2196.
128. Che, C.M., et al., *Photoreactions of Organic Halides, Alcohols, and Olefins with Tetrakis(Pyrophosphito)Diplatinate(Ii).* *Journal of Physical Chemistry*, 1989. 93(8): p. 3095–3099.
129. Roundhill, D.M., S.J. Atherton, and Z.P. Shen, *Hydrogen–Atom Abstraction from C–H, P–H, Si–H, and Sn–H Bonds by the Triplet Excited–State of the Tetrakis(Mu–Pyrophosphito)Diplatinum(Ii) Tetraanion – Spectroscopic Observation of the Mixed–Valence Hydride Complex $Pt_2(Mu–P_2O_5H_2)_4^{4-}$.* *Journal of the American Chemical Society*, 1987. 109(20): p. 6076–6079.
130. Roundhill, D.M., Z.P. Shen, and S.J. Atherton, *Reactivity of the Triplet–State of the Tetrakis(Mu–Pyrophosphito)Diplatinate(Ii) Tetraanion with Alkenes and Alkynes – Comparison with the Energy–Transfer Photosensitizer and Diradical Chemistry of Ketone Triplets.* *Inorganic Chemistry*, 1987. 26(23): p. 3833–3835.
131. Smith, D.C. and H.B. Gray, *Catalysis of the Oxidation of 1,4–Cyclohexadiene to Benzene by Electroactive Binuclear Rhodium Complexes.* *Catalysis Letters*, 1990. 6(2): p. 195–199.
132. Roundhill, D.M., M.K. Dickson, and S.J. Atherton, *Thermal and Photochemical Addition of Alkyl and Aryl Halides to Tetrakis(Mu–Pyrophosphito)Diplatinum(Ii) Tetraanion.* *Journal of Organometallic Chemistry*, 1987. 335(3): p. 413–422.
133. Smith, D.C., et al., *Synthesis and Characterization of $[Ir_2(Tmb)_4h_2][B(C_6H_5)_4]_2 \cdot CH_3C_6H_5$.* *Inorganic Chemistry*, 1990. 29(3): p. 534–538.
134. Rice, S.F. and H.B. Gray, *Electronic Absorption and Emission–Spectra of Binuclear Platinum(Ii) Complexes – Characterization of the Lowest Singlet and Triplet Excited–States of $Pt_2(H_2P_2O_5)_4^{4-}$.* *Journal of the American Chemical Society*, 1983. 105(14): p. 4571–4575.
135. Che, C.M., et al., *Metal–Metal Interactions in Binuclear Platinum(Ii) Diphosphite Complexes – Resonance Raman–Spectra of the $1a_{1g}(D–Sigma Star)_2$ and $3a_{2u}(D–Sigma Star P–Sigma Star)$ Electronic States of $Pt_2(P_2O_5H_2)_4^{4-}$.* *Journal of the American Chemical Society*, 1983. 105(16): p. 5492–5494.
136. Stiegman, A.E., et al., *Electronic Spectroscopy of D8–D8 Diplatinum Complexes – $1a_{2u}(Dsigma Star–JP–Sigma)$, $3e_u(Dxz, Dyz–JP–Sigma)$, and $3,1b_{2u}(Dsigma Star–J$*

- Dx₂-Y₂) Excited-States of Pt₂(P₂O₅H₂)₄⁴⁻. *Inorganic Chemistry*, 1987. 26(7): p. 1112–1116.*
137. van der Veen, R.M., et al., EXAFS structural determination of the Pt-2(P₂O₅H₂)₄⁴⁻ anion in solution. *Chimia*, 2008. 62(4): p. 287–290.
 138. van der Veen, R.M., et al., Structural Determination of a Photochemically Active Diplatinum Molecule by Time-Resolved EXAFS Spectroscopy. *Angewandte Chemie-International Edition*, 2009. 48(15): p. 2711–2714.
 139. Stoyanov, S.R., J.M. Villegas, and D.P. Rillema, Spectroscopic properties of [Pt-2(μ -P₂O₅H₂)₄]⁴⁻: A time-dependent density functional theory and conductor-like polarizable continuum model investigation. *Journal of Physical Chemistry B*, 2004. 108(32): p. 12175–12180.
 140. El Nahhas, A., et al., Ultrafast Excited-State Dynamics of [Re(L)(CO)₃(bpy)]⁽ⁿ⁾ Complexes: Involvement of the Solvent. *Journal of Physical Chemistry A*, 2010. 114(22): p. 6361–6369.
 141. Cho, S., et al., Coherence in Metal-Metal-to-Ligand-Charge-Transfer Excited States of a Dimetallic Complex Investigated by Ultrafast Transient Absorption Anisotropy. *The Journal of Physical Chemistry A*, 2011. 115(16): p. 3990–3996.
 142. Hartsock, R.W., et al., Characterizing the Deformational Isomers of Bimetallic Ir-2(dimen)₄(2+) (dimen=1,8-diisocyano-p-menthane) with Vibrational Wavepacket Dynamics. *Journal of Physical Chemistry A*, 2011. 115(14): p. 2920–2926.
 143. Dohn, A.O., et al., Direct Dynamics Studies of a Binuclear Metal Complex in Solution: The Interplay Between Vibrational Relaxation, Coherence, and Solvent Effects. *Journal of Physical Chemistry Letters*, 2014. 5(14): p. 2414–2418.
 144. Ikeyama, T., S. Yamamoto, and T. Azumi, Vibrational Analysis of Sublevel Phosphorescence Spectra of Potassium Tetrakis(Mu-Diphosphonato)Diplatinate(II) – Mechanism of Radiative Transition for the Electronically Forbidden-A_{1u} Spectrum. *Journal of Physical Chemistry*, 1988. 92(24): p. 6899–6901.
 145. Novozhilova, I.V., A.V. Volkov, and P. Coppens, Theoretical analysis of the triplet excited state of the [Pt-2(H₂P₂O₅)₄]⁴⁻ ion and comparison with time-resolved x-ray and spectroscopic results. *Journal of the American Chemical Society*, 2003. 125(4): p. 1079–1087.
 146. Pan, Q.J., et al., Theoretical insight into electronic structures and spectroscopic properties of [Pt-2(pop)₄]⁴⁻, [Pt-2(pcp)₄]⁴⁻, and related derivatives (pop = P₂O₅H₂²⁻ and pcp = P₂O₄CH₂⁻). *Inorganic Chemistry*, 2006. 45(21): p. 8729–8735.
 147. Shimizu, Y., Y. Tanaka, and T. Azumi, Assignment of the Lower Electronic States of Potassium Tetrakis(Mu-Diphosphonato)Diplatinate(II). *Journal of Physical Chemistry*, 1984. 88(11): p. 2423–2425.
 148. Zális, S., et al., Spin-Orbit TDDFT Electronic Structure of Diplatinum(II,II) Complexes. *Inorganic Chemistry*, 2015.
 149. Hersleth, H.P., et al., Crystallographic and spectroscopic studies of peroxide-derived myoglobin compound II and occurrence of protonated Fe^{IV}O. *J Biol Chem*, 2007. 282(32): p. 23372–86.
 150. Fogel, U., et al., Myoglobin: A scavenger of bioactive NO (vol 98, pg 735, 2001). *Proceedings of the National Academy of Sciences of the United States of America*, 2001. 98(7): p. 4276–4276.
 151. Brunori, M., et al., Nitric oxide and cellular respiration. *Cellular and Molecular Life Sciences*, 1999. 56(7–8): p. 549–557.
 152. Olson, J.S. and G.N. Phillips, Myoglobin discriminates between O₂, NO, and CO by electrostatic interactions with the bound ligand. *Journal of Biological Inorganic Chemistry*, 1997. 2(4): p. 544–552.

153. Mack, J., Stillman, M.J., *Phtalocyanines: spectroscopical and electrochemical characterization. The porphyrin Handbook*, ed. K.M. Kadish, Smith, K.M. and Guillard, R. Vol. 16. 2003: Academic Press. 46.
154. Du, H., et al., *PhotochemCAD: A computer-aided design and research tool in photochemistry. Photochemistry and Photobiology*, 1998. 68(2): p. 141–142.
155. Tilton, R.F., I.D. Kuntz, and G.A. Petsko, *Cavities in Proteins – Structure of a Metmyoglobin–Xenon Complex Solved to 1.9–Å. Biochemistry*, 1984. 23(13): p. 2849–2857.
156. Evans, S.V. and G.D. Brayer, *Horse Heart Metmyoglobin – a 2.8–Å Resolution 3–Dimensional Structure Determination. Journal of Biological Chemistry*, 1988. 263(9): p. 4263–4268.
157. Stevens, J.A., et al., *Ultrafast Dynamics of Resonance Energy Transfer in Myoglobin: Probing Local Conformation Fluctuations. Journal of Physical Chemistry B*, 2010. 114(3): p. 1498–1505.
158. Lakowicz, J.R., *Protein Fluorescence*, in *Principles of Fluorescence Spectroscopy 2004*, Springer: U.S. p. 446–480.
159. Lakowicz, J.R., *Protein Folding Measured by RET*, in *Principles of Fluorescence Spectroscopy 2004*, Springer. p. 374–378.
160. Pan, C.P. and M.D. Barkley, *Conformational effects on tryptophan fluorescence in cyclic hexapeptides. Biophysical Journal*, 2004. 86(6): p. 3828–3835.
161. Beechem, J.M. and L. Brand, *Time-Resolved Fluorescence of Proteins. Annual Review of Biochemistry*, 1985. 54: p. 43–71.
162. Ghisaidoobe, A.B.T. and S.J. Chung, *Intrinsic Tryptophan Fluorescence in the Detection and Analysis of Proteins: A Focus on Forster Resonance Energy Transfer Techniques. International Journal of Molecular Sciences*, 2014. 15(12): p. 22518–22538.
163. Hochstrasser, R.M. and D.K. Negus, *Picosecond Fluorescence Decay of Tryptophans in Myoglobin. Proceedings of the National Academy of Sciences of the United States of America–Biological Sciences*, 1984. 81(14): p. 4399–4403.
164. Janes, S.M., et al., *Fluorescence and Energy-Transfer of Tryptophans in Aplysia Myoglobin. Biophysical Journal*, 1987. 51(4): p. 653–660.
165. Leonard, J., et al., *Formation dynamics and nature of tryptophan's primary photoproduct in aqueous solution. Physical Chemistry Chemical Physics*, 2010. 12(48): p. 15744–15750.
166. Engh, R.A., L.X.Q. Chen, and G.R. Fleming, *Conformational Dynamics of Tryptophan – a Proposal for the Origin of the Nonexponential Fluorescence Decay. Chemical Physics Letters*, 1986. 126(3–4): p. 365–371.
167. Glandieres, J.M., et al., *Resolved fluorescence of the two tryptophan residues in horse apomyoglobin. Photochemistry and Photobiology*, 2000. 71(4): p. 382–386.
168. Tang, J., et al., *Intramolecular electron transfer in cyclopeptide involving tryptophan and tyrosine and corrected two-sphere model for solvent reorganization energy. Chemical Physics*, 2005. 312(1–3): p. 21–29.
169. Qiu, W.H., et al., *Ultrafast quenching of tryptophan fluorescence in proteins: Interresidue and intrahelical electron transfer. Chemical Physics*, 2008. 350(1–3): p. 154–164.
170. Consani, C., et al., *A cascade through spin states in the ultrafast haem relaxation of met-myoglobin. Journal of Chemical Physics*, 2014. 140(2).
171. Lima, F.A., et al., *Probing the electronic and geometric structure of ferric and ferrous myoglobins in physiological solutions by Fe K-edge absorption spectroscopy. Physical Chemistry Chemical Physics*, 2014. 16(4): p. 1617–1631.

172. Petrich, J.W., et al., *Ligand–Binding and Protein Relaxation in Heme–Proteins – a Room–Temperature Analysis of No Geminate Recombination*. *Biochemistry*, 1991. 30(16): p. 3975–3987.
173. Petrich, J.W., et al., *Ultrafast Measurements of Geminate Recombination of No with Site–Specific Mutants of Human Myoglobin*. *Journal of Molecular Biology*, 1994. 238(3): p. 437–444.
174. Kholodenko, Y., et al., *Heme protein dynamics revealed by geminate nitric oxide recombination in mutants of iron and cobalt myoglobin*. *Biochemistry*, 1999. 38(18): p. 5918–5924.
175. Kim, S., G. Jin, and M. Lim, *Dynamics of geminate recombination of NO with myoglobin in aqueous solution probed by femtosecond mid–IR spectroscopy*. *Journal of Physical Chemistry B*, 2004. 108(52): p. 20366–20375.
176. Nienhaus, K., P. Palladino, and G.U. Nienhaus, *Structural dynamics of myoglobin: FTIR–TDS study of NO migration and binding*. *Biochemistry*, 2008. 47(3): p. 935–948.
177. Kruglik, S.G., et al., *Picosecond primary structural transition of the heme is retarded after nitric oxide binding to heme proteins*. *Proceedings of the National Academy of Sciences of the United States of America*, 2010. 107(31): p. 13678–13683.
178. Franzen, S., et al., *Functional aspects of ultra–rapid heme doming in hemoglobin, myoglobin, and the myoglobin mutant H93G*. *J Biol Chem*, 1995. 270(4): p. 1718–20.
179. Tian, W.D., et al., *Relaxation Dynamics of Myoglobin in Solution*. *Physical Review Letters*, 1992. 68(3): p. 408–411.
180. Consani, C., et al., *Energy transfer and relaxation mechanisms in Cytochrome c*. *Chemical Physics*, 2012. 396: p. 108–115.
181. Bram, O., et al., *Femtosecond UV Studies of the Electronic Relaxation Processes in Cytochrome c*. *Journal of Physical Chemistry B*, 2011. 115(46): p. 13723–13730.
182. Fajer, J., et al., *Pi–Cation Radicals and Dications of Metalloporphyrins*. *Journal of the American Chemical Society*, 1970. 92(11): p. 3451–&.
183. Peychalho, G. and G.S. Wilson, *Electrochemical Studies of Some Porphyrin Ix Derivatives in Aprotic Media*. *Analytical Chemistry*, 1971. 43(4): p. 545–&.
184. Cohen, I.A., Lichtens, B., and D. Ostfeld, *Characterization of a D7 Iron System – Tetraphenylporphineiron(I) Anion*. *Journal of the American Chemical Society*, 1972. 94(13): p. 4522–&.
185. Lexa, D., Momentea, M., and Mispelte, J., *Characterization of Reduction Steps of Fe(III) Porphyrins*. *Biochimica Et Biophysica Acta*, 1974. 338(1): p. 151–163.
186. Yamaguchi, K. and I. Morishima, *Low–Valent Iron Porphyrins – Nmr Evidence for Pi–Anion–Radical Character in 2–Electron–Reduced Iron(III) Mesosubstituted or Beta–Pyrrole–Substituted Porphyrins*. *Inorganic Chemistry*, 1992. 31(15): p. 3216–3222.
187. Balducci, G., et al., *Electrochemistry of Iron(I) Porphyrins in the Presence of Carbon–Monoxide – Comparison with Zinc Porphyrins*. *Inorganic Chemistry*, 1994. 33(9): p. 1972–1978.
188. Kadish, K.M. and G. Larson, *Study of Redox Potentials and Electron–Transfer Rates of Several Naturally Occurring Nd Synthetic Iron Porphyrins in Dmf*. *Bioinorganic Chemistry*, 1977. 7(2): p. 95–105.
189. De Silva, C., K. Czarnecki, and M.D. Ryan, *Visible and resonance Raman spectra of low valent iron porphyrins*. *Inorganica Chimica Acta*, 1999. 287(1): p. 21–26.
190. Donohoe, R.J., M. Atamian, and D.F. Bocian, *Characterization of Singly Reduced Iron(II) Porphyrins*. *Journal of the American Chemical Society*, 1987. 109(19): p. 5593–5599.

191. Davydov, R. and B.M. Hoffman, *EPR and ENDOR studies of Fe(II) hemoproteins reduced and oxidized at 77 K*. *Journal of Biological Inorganic Chemistry*, 2008. 13(3): p. 357–369.
192. Kadish, K.M. and L.A. Bottomley, *Substituent Effects on Formation–Constants of Iron(III) and Iron(II) Tetraphenylporphyrin–Pyridine Complexes*. *Journal of the American Chemical Society*, 1977. 99(7): p. 2380–2382.
193. Davydov, R., et al., *EPR and ENDOR studies of cryoreduced compounds II of Peroxidases and myoglobin. Proton–coupled electron transfer and protonation status of ferryl*. *Biochemistry*, 2008. 47(18): p. 5147–5155.
194. Porro, C.S., D. Kumar, and S.P. de Visser, *Electronic properties of pentacoordinated heme complexes in cytochrome P450 enzymes: search for an Fe(I) oxidation state*. *Physical Chemistry Chemical Physics*, 2009. 11(43): p. 10219–10226.
195. Kis, Z. and R. Silaghi–Dumitrescu, *The Electronic Structure of Biologically Relevant Fe(0) Systems*. *International Journal of Quantum Chemistry*, 2010. 110(10): p. 1848–1856.
196. Silaghi–Dumitrescu, R. and S.V. Makarov, *A computational analysis of electromerism in hemoprotein Fe(I) models*. *Journal of Biological Inorganic Chemistry*, 2010. 15(6): p. 977–986.
197. Bellina, B., et al., *Spectroscopic Signatures of Peptides Containing Tryptophan Radical Cations*. *Angewandte Chemie–International Edition*, 2011. 50(48): p. 11430–11432.
198. Kim, S., G. Jin, and M. Lim, *Structural dynamics of myoglobin probed by femtosecond infrared spectroscopy of the amide band*. *Bulletin of the Korean Chemical Society*, 2003. 24(10): p. 1470–1474.
199. Owens, J.W. and C.J. Oconnor, *Comparison of the Electronic and Vibrational–Spectra of Complexes of Protoporphyrin–IX, Hemeoctapeptide, and Heme–Proteins*. *Coordination Chemistry Reviews*, 1988. 84: p. 1–45.
200. Hu, S.Z., K.M. Smith, and T.G. Spiro, *Assignment of protoheme Resonance Raman spectrum by heme labeling in myoglobin*. *Journal of the American Chemical Society*, 1996. 118(50): p. 12638–12646.
201. Bayachou, M., et al., *Electrochemical reduction of NO by myoglobin in surfactant film: Characterization and reactivity of the nitroxyl (NO–) adduct*. *Journal of the American Chemical Society*, 1998. 120(38): p. 9888–9893.
202. Meuwly, M., *On the influence of the local environment on the CO stretching frequencies in native myoglobin: Assignment of the B–States in MbCO*. *Chemphyschem*, 2006. 7(10): p. 2061–2063.
203. Lima, F.A., *Investigation of Physiological Solutions of Metalloproteins in a High–Repetition Rate Picosecond X–ray Absorption Experiment*, 2011, EPFL.
204. Moore, J.N., P.A. Hansen, and R.M. Hochstrasser, *Iron Carbonyl Bond Geometries of Carboxymyoglobin and Carboxyhemoglobin in Solution Determined by Picosecond Time–Resolved Infrared–Spectroscopy*. *Proceedings of the National Academy of Sciences of the United States of America*, 1988. 85(14): p. 5062–5066.
205. Sathyanarayana, D.N., *Vibrational Spectroscopy: theory and applications 2005*: New Age International Publisher.
206. Tsalavoutis, J.T. and M.P. Sigalas, *Density Functional Investigation and Bonding Analysis of Pentacoordinated Iron Complexes with Mixed Cyano and Carbonyl Ligands*. *Journal of Computational Chemistry*, 2010. 31(10): p. 1969–1978.
207. Cornelius, P.A., R.M. Hochstrasser, and A.W. Steele, *Ultrafast Relaxation in Picosecond Photolysis of Nitrosylhemoglobin*. *Journal of Molecular Biology*, 1983. 163(1): p. 119–128.

208. Shreve, A.P., et al., Dependence of NO recombination dynamics in horse myoglobin on solution glycerol content. *Journal of Physical Chemistry B*, 1999. 103(37): p. 7969–7975.
209. Rosca, F., et al., Wavelength selective modulation in femtosecond pump–probe spectroscopy and its application to heme proteins. *Journal of Chemical Physics*, 2001. 114(24): p. 10884–10898.
210. Ionascu, D., et al., Temperature–dependent studies of NO recombination to heme and heme proteins. *Journal of the American Chemical Society*, 2005. 127(48): p. 16921–16934.
211. Yoo, B.K., et al., Absorption Band III Kinetics Probe the Picosecond Heme Iron Motion Triggered by Nitric Oxide Binding to Hemoglobin and Myoglobin. *Journal of Physical Chemistry B*, 2012. 116(13): p. 4106–4114.
212. Kim, J., et al., Dynamics of Geminate Rebinding of NO with Cytochrome c in Aqueous Solution Using Femtosecond Vibrational Spectroscopy. *Journal of Physical Chemistry B*, 2012. 116(46): p. 13663–13671.
213. Kim, S. and M. Lim, Protein Conformation–Controlled Rebinding Barrier of NO and Its Binding Trajectories in Myoglobin and Hemoglobin at Room Temperature. *Journal of Physical Chemistry B*, 2012. 116(20): p. 5819–5830.
214. Zemojtel, T., et al., NO–bound myoglobin: Structural diversity and dynamics of the NO ligand. *Journal of the American Chemical Society*, 2004. 126(7): p. 1930–1931.
215. Sulc, F., Palmer, S.C., *The Smallest Biomolecules: Diatomics and their interaction with heme proteins* 2008: Elsevier. 445–450.
216. Montenegro, A.C., et al., Three Redox States of Nitrosyl: NO⁺, NO center dot, and NO–/HNO Interconvert Reversibly on the Same Pentacyanoferrate(II) Platform. *Angewandte Chemie–International Edition*, 2009. 48(23): p. 4213–4216.
217. Sanders, B.C., M.A. Rhine, and T.C. Harrop, Properties of {FeNO}(8) and {CoNO}(9) Metal Nitrosyls in Relation to Nitroxyl Coordination Chemistry. *Molecular Design in Inorganic Biochemistry*, 2014. 160: p. 57–88.
218. Radon, M., E. Broclawik, and K. Pierloot, Electronic Structure of Selected {FeNO}(7) Complexes in Heme and Non–Heme Architectures: A Density Functional and Multireference ab Initio Study. *Journal of Physical Chemistry B*, 2010. 114(3): p. 1518–1528.
219. Patra, A.K., et al., A thermally stable {FeNO}(8) complex: properties and biological reactivity of reduced MNO systems. *Chemical Science*, 2012. 3(2): p. 364–369.
220. Speelman, A.L. and N. Lehnert, Heme versus Non–Heme Iron–Nitroxyl {FeN(H)O}(8) Complexes: Electronic Structure and Biologically Relevant Reactivity. *Accounts of Chemical Research*, 2014. 47(4): p. 1106–1116.
221. Goodrich, L.E., et al., Electronic Structure and Biologically Relevant Reactivity of Low–Spin {FeNO}(8) Porphyrin Model Complexes: New Insight from a Bis–Picket Fence Porphyrin. *Inorganic Chemistry*, 2013. 52(13): p. 7766–7780.
222. Serres, R.G., et al., Structural, spectroscopic, and computational study of an octahedral, non–heme {Fe–NO}(6–8) series: [Fe(NO)(cyclam–ac)](2+ / + / O). *Journal of the American Chemical Society*, 2004. 126(16): p. 5138–5153.
223. Miranda, K.M., et al., Comparison of the NO and HNO donating properties of diazeniumdiolates: Primary amine adducts release HNO in vivo. *Journal of Medicinal Chemistry*, 2005. 48(26): p. 8220–8228.
224. Andrews, K.L., et al., A role for nitroxyl (HNO) as an endothelium–derived relaxing and hyperpolarizing factor in resistance arteries. *British Journal of Pharmacology*, 2009. 157(4): p. 540–550.

225. Helbing, J., et al., *Time-resolved visible and infrared study of the cyano complexes of myoglobin and of hemoglobin I from Lucina pectinata*. *Biophysical Journal*, 2004. 87(3): p. 1881–91.
226. Kim, J., et al., *Picosecond Dynamics of CN—Ligated Ferric Cytochrome c after Photoexcitation Using Time-resolved Vibrational Spectroscopy*. *Bulletin of the Korean Chemical Society*, 2010. 31(12): p. 3771–3776.
227. Reddy, K.S., et al., *Infrared spectroscopy of the cyanide complex of Iron(II) myoglobin and comparison with complexes of microperoxidase and hemoglobin*. *Biochemistry*, 1996. 35(17): p. 5562–5570.
228. Defelippis, M.R., et al., *Pulse Radiolytic Measurement of Redox Potentials – the Tyrosine and Tryptophan Radicals*. *Biochemistry*, 1989. 28(11): p. 4847–4853.
229. Chang, R., *Physical chemistry for the Bioscience2005, United States of America: University Science Books*.
230. Moser, C.C., C.C. Page, and P.L. Dutton, *Darwin at the molecular scale: selection and variance in electron tunnelling proteins including cytochrome c oxidase*. *Philosophical Transactions of the Royal Society B–Biological Sciences*, 2006. 361(1472): p. 1295–1305.
231. Muegge, I., et al., *The reorganization energy of cytochrome c revisited*. *Journal of Physical Chemistry B*, 1997. 101(5): p. 825–836.
232. Petrich, J.W., J.W. Longworth, and G.R. Fleming, *Internal Motion and Electron-Transfer in Proteins – a Picosecond Fluorescence Study of 3 Homologous Azurins*. *Biochemistry*, 1987. 26(10): p. 2711–2722.
233. Solov'yov, I.A., T. Domratcheva, and K. Schulten, *Separation of photo-induced radical pair in cryptochrome to a functionally critical distance*. *Sci Rep*, 2014. 4: p. 3845.
234. Banci, L., et al., *Solution structure of oxidized horse heart cytochrome c*. *Biochemistry*, 1997. 36(32): p. 9867–9877.
235. Banci, L., et al., *Solution structure of reduced horse heart cytochrome c*. *Journal of Biological Inorganic Chemistry*, 1999. 4(1): p. 21–31.
236. Schuler, B., et al., *Polyproline and the "spectroscopic ruler" revisited with single-molecule fluorescence*. *Proceedings of the National Academy of Sciences of the United States of America*, 2005. 102(8): p. 2754–2759.
237. Sahoo, H., et al., *A 10-angstrom spectroscopic ruler applied to short polyprolines*. *Journal of the American Chemical Society*, 2007. 129(31): p. 9762–9772.
238. Richert, L., et al., *Monitoring HIV-1 Protein Oligomerization by FLIM FRET Microscopy, in Advanced Time-Correlated Single Photon Counting Applications, W. Becker, Editor 2015, Springer International Publishing. p. 277–307*.
239. Rudkouskaya, A., et al., *Imaging Tumor Targeted Delivery using FRET in vivo*. *The FASEB Journal*, 2015. 29(1 Supplement).
240. Fernandes, F., et al., *Electrostatically driven lipid-protein interaction: Answers from FRET*. *Biochimica et Biophysica Acta (BBA) – Biomembranes*, (0).
241. Coban, O., et al., *Effect of Phosphorylation on EGFR Dimer Stability Probed by Single-Molecule Dynamics and FRET/FLIM*. *Biophysical Journal*, 2015. 108(5): p. 1013–1026.
242. Mohapatra, M., et al., *Photoluminescence properties of 'red' emitting La₂Zr₂O₇:Eu pyrochlore ceramics for potential phosphor application*. *Journal of Luminescence*, (0).
243. Jo, D.-H., et al., *Optical properties of TiO₂ and disperse red-19 composite*. *Optical Materials*, 2015. 39(0): p. 86–89.
244. Aguilar-Calvo, P., et al., *Prion and prion-like diseases in animals*. *Virus Research*, (0).

245. Prusiner, S.B., *Prion diseases and the BSE crisis*. *Science*, 1997. 278(5336): p. 245–51.
246. Zahn, R., et al., *NMR solution structure of the human prion protein*. *Proceedings of the National Academy of Sciences of the United States of America*, 2000. 97(1): p. 145–150.
247. Millhauser, G.L., *Copper binding in the prion protein*. *Accounts of Chemical Research*, 2004. 37(2): p. 79–85.
248. Abskharon, R.N.N., et al., *Probing the N-Terminal beta-Sheet Conversion in the Crystal Structure of the Human Prion Protein Bound to a Nanobody*. *Journal of the American Chemical Society*, 2014. 136(3): p. 937–944.
249. Knaus, K.J., et al., *Crystal structure of the human prion protein reveals a mechanism for oligomerization*. *Nature Structural Biology*, 2001. 8(9): p. 770–774.
250. Morales, R., K. Callegari, and C. Soto, *Prion-like features of misfolded A β and tau aggregates*. *Virus Research*, (0).
251. Caughey, B. and B. Chesebro, *Prion protein and the transmissible spongiform encephalopathies*. *Trends in Cell Biology*, 1997. 7(2): p. 56–62.
252. Bueler, H., et al., *Mice Devoid of Prp Are Resistant to Scrapie*. *Cell*, 1993. 73(7): p. 1339–1347.
253. Hornshaw, M.P., et al., *Copper-Binding to the N-Terminal Tandem Repeat Region of Mammalian and Avian Prion Protein – Structural Studies Using Synthetic Peptides*. *Biochemical and Biophysical Research Communications*, 1995. 214(3): p. 993–999.
254. Hornshaw, M.P., J.R. Mcdermott, and J.M. Candy, *Copper-Binding to the N-Terminal Tandem Repeat Regions of Mammalian and Avian Prion Protein*. *Biochemical and Biophysical Research Communications*, 1995. 207(2): p. 621–629.
255. Qin, K.F., et al., *Mapping Cu(II) binding sites in prion proteins by diethyl pyrocarbonate modification and matrix-assisted laser desorption ionization–time of flight (MALDI–TOF) mass spectrometric footprinting*. *Journal of Biological Chemistry*, 2002. 277(3): p. 1981–1990.
256. Klewpatinond, M., et al., *Deconvoluting the Cu(2+) binding modes of full-length prion protein*. *Journal of Biological Chemistry*, 2008. 283(4): p. 1870–1881.
257. Cereghetti, G.M., et al., *Electron paramagnetic resonance evidence for binding of Cu²⁺ to the C-terminal domain of the murine prion protein*. *Biophysical Journal*, 2001. 81(1): p. 516–525.
258. Viles, J.H., et al., *Copper binding to the prion protein: Structural implications of four identical cooperative binding sites*. *Proceedings of the National Academy of Sciences of the United States of America*, 1999. 96(5): p. 2042–2047.
259. Davies, P. and D.R. Brown, *The chemistry of copper binding to PrP: is there sufficient evidence to elucidate a role for copper in protein function?* *Biochemical Journal*, 2008. 410: p. 237–244.
260. Brown, D.R., et al., *The cellular prion protein binds copper in vivo*. *Nature*, 1997. 390(6661): p. 684–687.
261. Whittal, R.M., et al., *Copper binding to octarepeat peptides of the prion protein monitored by mass spectrometry*. *Protein Science*, 2000. 9(2): p. 332–343.
262. Hong, L.A. and J.D. Simon, *Insights into the thermodynamics of copper association with amyloid-beta, alpha-synuclein and prion proteins*. *Metallomics*, 2011. 3(3): p. 262–266.
263. Aronoff-Spencer, E., et al., *Identification of the Cu²⁺ binding sites in the N-terminal domain of the prion protein by EPR and CD spectroscopy*. *Biochemistry*, 2000. 39(45): p. 13760–13771.

264. Miura, T., et al., Raman spectroscopic study on the copper(II) binding mode of prion octapeptide and its pH dependence. *Biochemistry*, 1999. 38(35): p. 11560–11569.
265. Burns, C.S., et al., Molecular features of the copper binding sites in the octarepeat domain of the prion protein. *Biochemistry*, 2002. 41(12): p. 3991–4001.
266. Morante, S., et al., Inter- and intra-octarepeat Cu(II) site geometries in the prion protein – Implications in Cu(II) binding cooperativity and Cu(II)-mediated assemblies. *Journal of Biological Chemistry*, 2004. 279(12): p. 11753–11759.
267. Rana, A., et al., Prion metal interaction: Is prion pathogenesis a cause or a consequence of metal imbalance? *Chemico-Biological Interactions*, 2009. 181(3): p. 282–291.
268. Weiss, J.H., S.L. Sensi, and J.Y. Koh, Zn²⁺: a novel ionic mediator of neural injury in brain disease. *Trends in Pharmacological Sciences*, 2000. 21(10): p. 395–401.
269. Watt, N.T. and N.M. Hooper, The prion protein and neuronal zinc homeostasis. *Trends in Biochemical Sciences*, 2003. 28(8): p. 406–410.
270. Brown, D.R., et al., Consequences of manganese replacement of copper for prion protein function and proteinase resistance. *Embo Journal*, 2000. 19(6): p. 1180–1186.
271. Fernaeus, S., et al., Changed iron regulation in scrapie-infected neuroblastoma cells. *Molecular Brain Research*, 2005. 133(2): p. 266–273.
272. Jackson, G.S., et al., Location and properties of metal-binding sites on the human prion protein. *Proceedings of the National Academy of Sciences of the United States of America*, 2001. 98(15): p. 8531–8535.
273. Brown, D.R., et al., Normal prion protein has an activity like that of superoxide dismutase. *Biochemical Journal*, 1999. 344: p. 1–5.
274. Pauly, P.C. and D.A. Harris, Copper stimulates endocytosis of the prion protein. *Journal of Biological Chemistry*, 1998. 273(50): p. 33107–33110.
275. Rachidi, W., et al., Expression of prion protein increases cellular copper binding and antioxidant enzyme activities but not copper delivery. *Journal of Biological Chemistry*, 2003. 278(11): p. 9064–9072.
276. Miura, T., et al., Copper reduction by the octapeptide repeat region of prion protein: pH dependence and implications in cellular copper uptake. *Biochemistry*, 2005. 44(24): p. 8712–8720.
277. Waggoner, D.J., et al., Brain copper content and cuproenzyme activity do not vary with prion protein expression level. *Journal of Biological Chemistry*, 2000. 275(11): p. 7455–7458.
278. Rachidi, W., et al., Prion infection impairs copper binding of cultured cells. *Journal of Biological Chemistry*, 2003. 278(17): p. 14595–14598.
279. Ollesch, J., et al., Prion protein alpha-to-beta transition monitored by time-resolved Fourier transform infrared spectroscopy. *Applied Spectroscopy*, 2007. 61(10): p. 1025–1031.
280. Schlepckow, K. and H. Schwalbe, Molecular Mechanism of Prion Protein Oligomerization at Atomic Resolution. *Angewandte Chemie-International Edition*, 2013. 52(38): p. 10002–10005.
281. Wang, Y. and T. Goodson, Early aggregation in prion peptide nanostructures investigated by nonlinear and ultrafast time-resolved fluorescence spectroscopy. *Journal of Physical Chemistry B*, 2007. 111(2): p. 327–330.
282. Lau, A., et al., Octarepeat region flexibility impacts prion function, endoproteolysis and disease manifestation. *Embo Molecular Medicine*, 2015. 7(3): p. 339–356.
283. Kandegedara, A. and D.B. Rorabacher, Noncomplexing tertiary amines as "better" buffers covering the range of pH 3–11. Temperature dependence of their acid dissociation constants. *Analytical Chemistry*, 1999. 71(15): p. 3140–3144.

284. Ferguson, W.J., et al., *Hydrogen–Ion Buffers for Biological–Research*. *Analytical Biochemistry*, 1980. 104(2): p. 300–310.
285. dos Santos, N.V., et al., *Copper(II) complexation to 1–octarepeat peptide from a prion protein: Insights from theoretical and experimental UV–visible studies*. *Journal of Inorganic Biochemistry*, 2012. 114: p. 1–7.
286. Zhang, M.T. and L. Hammarstrom, *Proton–coupled electron transfer from tryptophan: a concerted mechanism with water as proton acceptor*. *Journal of the American Chemical Society*, 2011. 133(23): p. 8806–9.
287. Chen, Y. and M.D. Barkley, *Toward understanding tryptophan fluorescence in proteins*. *Biochemistry*, 1998. 37(28): p. 9976–9982.
288. Yu, H.T., et al., *Fluorescence Quenching in Indoles by Excited–State Proton–Transfer*. *Journal of the American Chemical Society*, 1992. 114(22): p. 8449–8454.
289. Liu, L., et al., *Copper Redox Cycling in the Prion Protein Depends Critically on Binding Mode*. *Journal of the American Chemical Society*, 2011. 133(31): p. 12229–12237.
290. Zhou, F.M. and G.L. Millhauser, *The rich electrochemistry and redox reactions of the copper sites in the cellular prion protein*. *Coordination Chemistry Reviews*, 2012. 256(19–20): p. 2285–2296.
291. Pushie, M.J. and H.J. Vogel, *Molecular dynamics simulations of two tandem octarepeats from the mammalian prion protein: Fully Cu²⁺–bound and metal–free forms*. *Biophysical Journal*, 2007. 93(11): p. 3762–3774.
292. Redecke, L., et al., *UV–light–induced conversion and aggregation of prion proteins*. *Free Radical Biology and Medicine*, 2009. 46(10): p. 1353–1361.
293. Rogers, M., et al., *Conversion of Truncated and Elongated Prion Proteins into the Scrapie Isoform in Cultured–Cells*. *Proceedings of the National Academy of Sciences of the United States of America*, 1993. 90(8): p. 3182–3186.
294. Pushie, M.J., et al., *Prion protein expression level alters regional copper, iron and zinc content in the mouse brain*. *Metallomics*, 2011. 3(2): p. 206–214.
295. Singh, N., et al., *Prion Protein and Metal Interaction: Physiological and Pathological Implications*. *Current Issues in Molecular Biology*, 2010. 12: p. 99–107.
296. Watt, N.T., et al., *Prion protein facilitates uptake of zinc into neuronal cells*. *Nature Communications*, 2012. 3.

Appendix A (*Pt(pop)*)

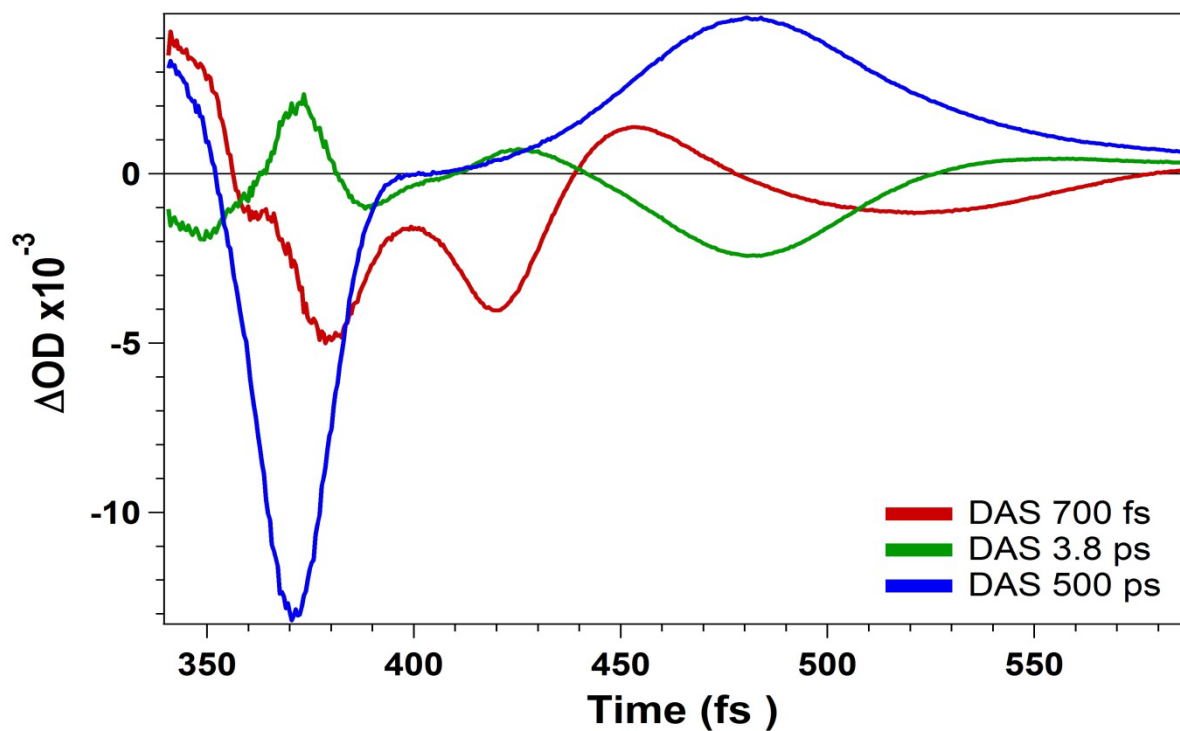


Figure 6-1 DAS's obtained by best-fit of the most important eigentraces obtained by the data of Pt(pop) in MeCN upon 360 nm excitation

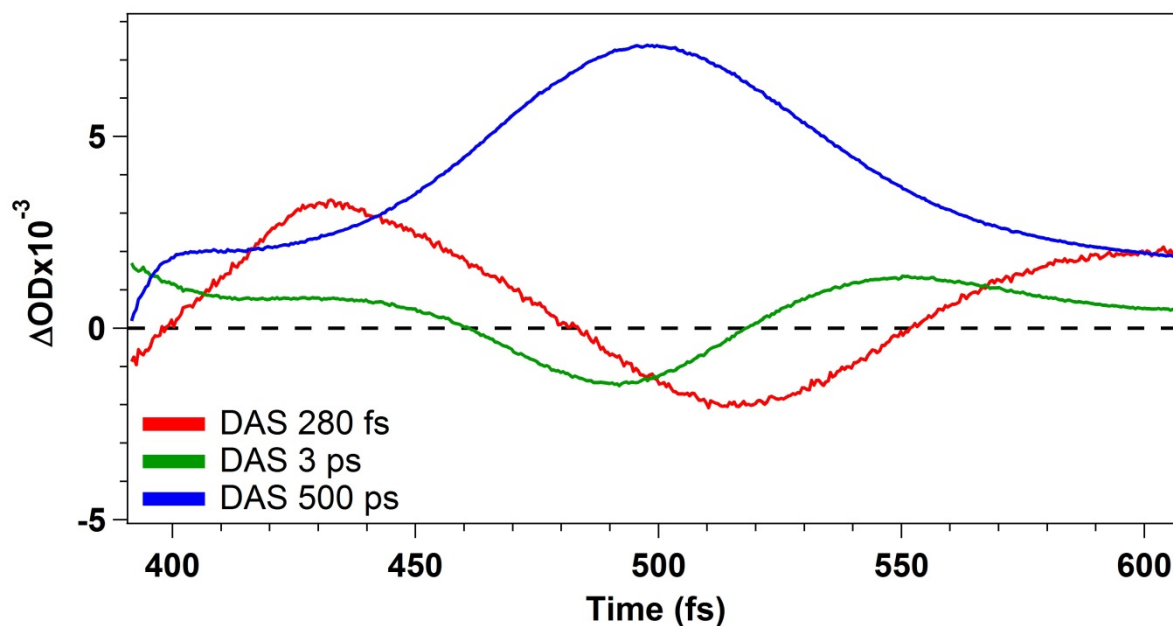


Figure 6-2 DAS's obtained by best-fit of the most important eigentraces obtained by the data of Pt(pop) in MeCN upon 280 nm excitation

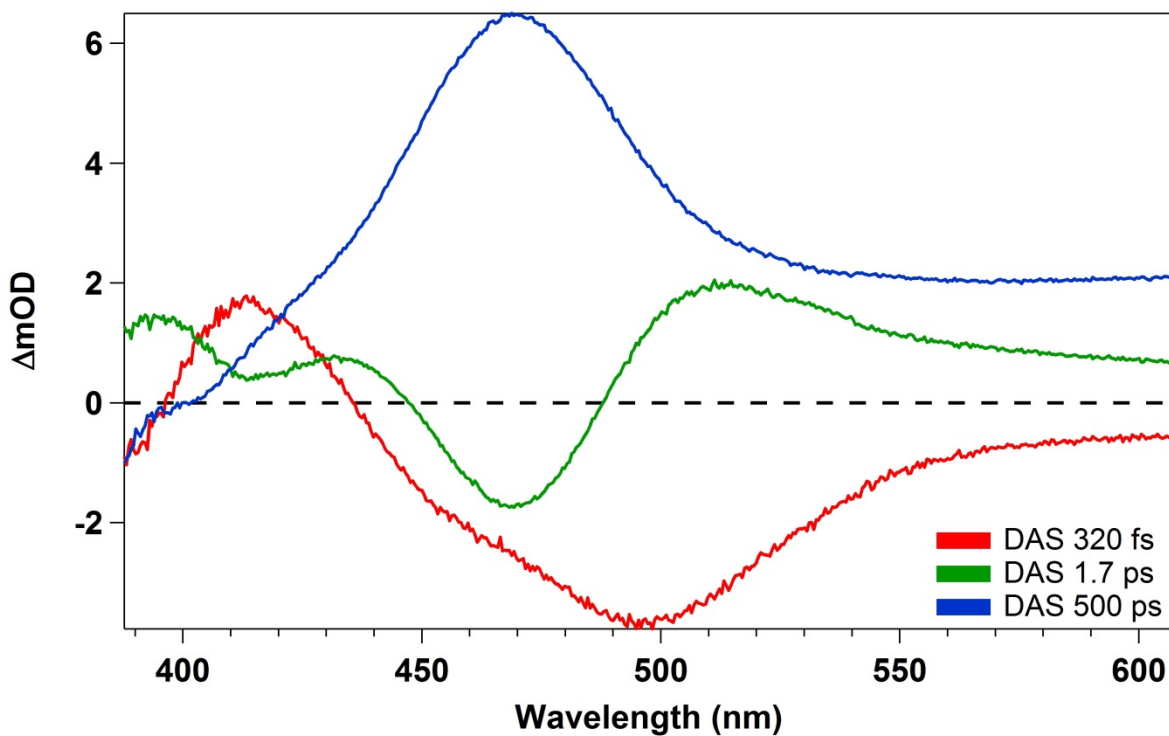


Figure 6-4 DAS's obtained by best-fit of the most important eigentraces obtained by the data of Pt(pop) in water upon 270 nm excitation

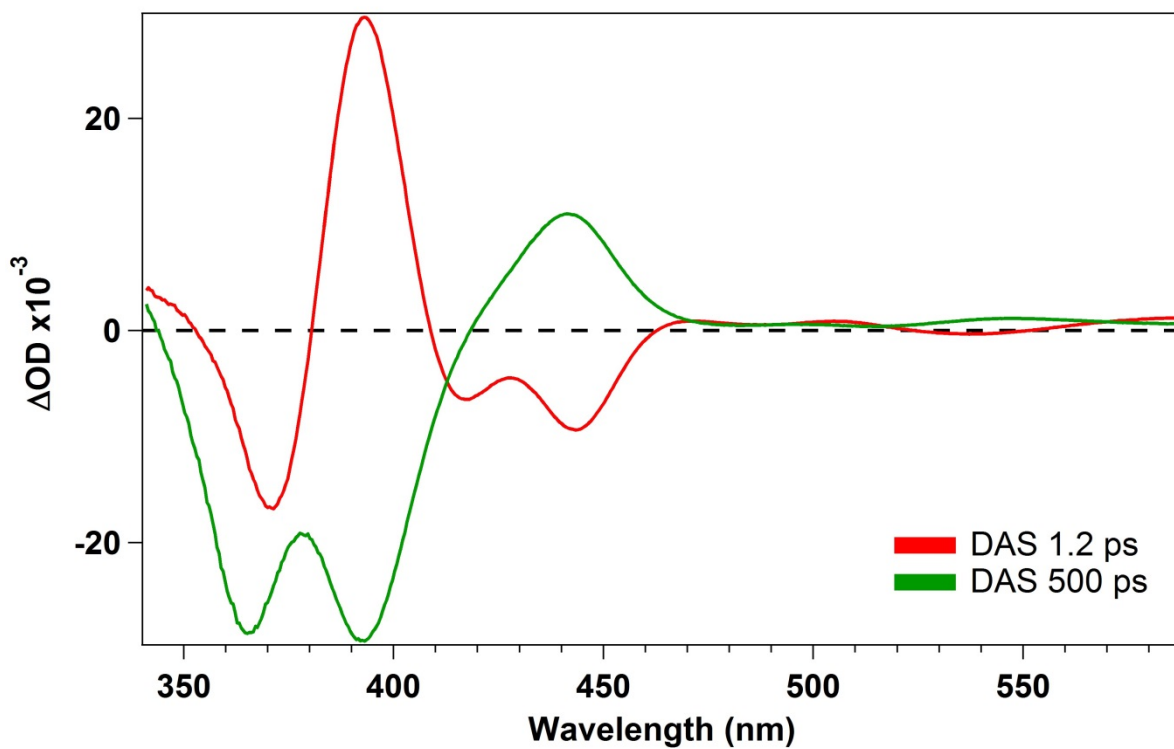


Figure 6-3 DAS's obtained by best-fit of the most important eigentraces obtained by the data of Pt(pop)-BF₂ in MeCN upon 360 nm excitation

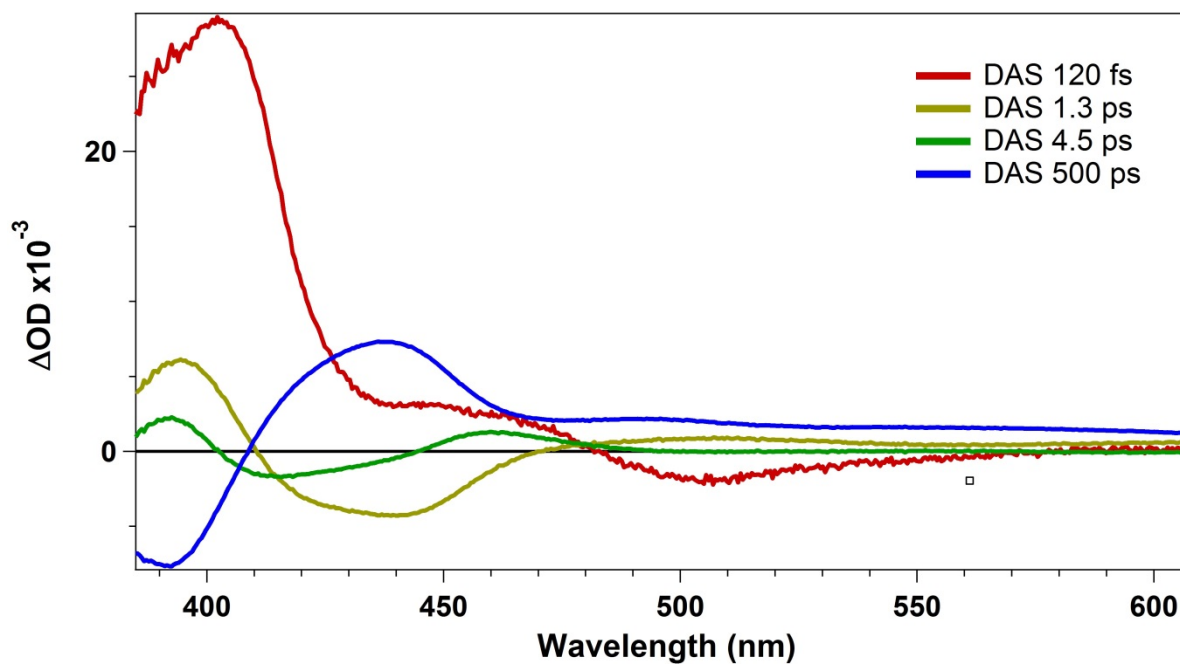




Figure 6-5 DAS's obtained by best-fit of the most important eigentraces obtained by the data of Pt(pop)-BF₂ in MeCN upon 260 nm excitation

Curriculum Vitae

Roberto Monni

EPFL–LSU
Lausanne–1015
Switzerland

 +41 78 965 76 06

 +41 (0) 21 69 304 53

 roberto.monni@epfl.ch

Education and Training

Jan. 2011–June 2015

Ph.D. in *Photonics* at EPFL

Supervisor: *Prof. Majed Chergui*

Title: “*Ultrafast photo–induced processes in metal–containing molecular complexes and in proteins*”

Nov. 2009–Dec. 2010

Specialization school on *material science* at IUSS Pavia

“*Materials for micro and nano–technologies*”

Feb. 2009–Oct. 2009

Internship project within 3R–Metals

Oct. 2006–Dec. 2008

Master degree in *Inorganic Chemistry* at University of Cagliari

Supervisor: *Prof. Paola Deplano*

Title: “*Alternative recovery methods of noble metals from electronic wastes*”

Jul. 2003–Jul. 2004

Erasmus Program: internship at TU Braunschweig (DE)

Oct. 2001–Sept. 2006

Bachelor degree in *Chemistry* at University of Cagliari

Supervisor: **Prof. Francesco Devillanova**

Title: “*Synthesis and characterization of Phospho–Indigo and Alchil–Sylil Phosphalkenes*”

Scientific Conferences

2015 ISPPCC *Krakow*

2014 Fall Meeting of the Swiss Chemical Society *Zurich*

2013 MUST Meeting *Engelberg*

2012 Ultrafast Phenomena *Lausanne*

2012 Conference on Multi–Dimensional Spectroscopy *Berlin*

2012 MUST Meeting *Lenk*

2011 MUST Meeting *Lenk*

Papers

- **Monni R.**, al Haddad A., Auböck G. and Chergui M. (2015) “*Ultrafast Tryptophan relaxation in prion proteins*” in preparation
- **Monni R.**, Horvath R., Auböck G., Towrie M., George M. and Chergui M. (2015) “*Effect of Tryptophan–to–heme electron transfer on diatomic ligands in ferrous Myoglobins*” in preparation
- **Monni R.**, Aziz–Lange K., Auböck G., Vlček A. and Chergui M. (2015) “*Ligand and solvent effect on the intramolecular relaxation of di–platinum complexes*” in preparation
- **Monni R.**, al Haddad A., van Mourik F., Auböck G. and Chergui M. (2015) “*Tryptophan–to–heme electron transfer in ferric Myoglobins*” PNAS **112**(18), 5606–5606.

- Auböck G., Consani C., **Monni R.**, Cannizzo A., van Mourik F. and Chergui M. (2012) "Femtosecond pump/supercontinuum–probe setup with 20 kHz repetition rate" Review of Scientific Instruments **83**(9).

Languages

<i>Italian</i>	Mother tongue	<i>German</i>	Basic knowledge
<i>English</i>	Full work proficiency	<i>Spanish</i>	Basic knowledge
<i>French</i>	Limited work proficiency		